Mandal, Parna (2025) Mathematical modelling of antibiotic release from medical implants to counteract biofilm formation. PhD thesis.

https://theses.gla.ac.uk/85250/

Mathematical modelling of antibiotic release from medical implants to counteract biofilm formation

Parna Mandal

Submitted in fulfilment of the requirements for the
Degree of Doctor of Philosophy

School of Mathematics and Statistics
College of Science and Engineering
University of Glasgow

June 2025

Abstract

A biofilm is a community of bacteria embedded in a self-produced extracellular matrix (EPS) that adheres to surfaces like medical implants. Biofilms are highly resistant to antibiotics due to the protective EPS barrier and dormant persister cells, leading to chronic infections that are difficult to eradicate and often require surgical intervention. This resistance, along with the increase in antibiotic resistant bacteria, underscores the need for new strategies to manage biofilm-related infections. This thesis aims to address this challenge by investigating the dynamics of biofilm growth under various conditions, including nutrient availability and antibiotic exposure. The goal is to provide insights for developing more effective therapeutic strategies. A simple mathematical model of biofilm growth is introduced, progressively incorporating complexities such as different bacterial phenotypes, nutrient-dependent transition rates between proliferative and persister bacteria, and controlled antibiotic release from porous implant. Before exploring the mathematical models in detail, this thesis introduces a hierarchy of adaptable models tailored to the needs of different studies.

The key findings of this thesis reveal the critical role of nutrient availability and antibiotic distribution in controlling biofilm growth. In nutrient-rich environments, biofilms grew rapidly but were more vulnerable to collapse under antibiotic treatment, while nutrient-poor conditions promoted persister cells, leading to thinner and more resilient biofilms that were harder to eliminate. Controlled antibiotic release from porous implants provided initial biofilm suppression but was insufficient for long-term control without sustained release, as biofilms regrew after antibiotic depletion. It is also clear from the results that higher initial antibiotic concentrations delayed biofilm regrowth but did not ensure complete eradication. Finally, spatially optimised antibiotic loading, which has a higher antibiotic concentration near the implant-biofilm interface, worked better for short-term suppression but resulted in poorer long-term biofilm control. In contrast, distributing the antibiotic farther from the implant-biofilm interface led to more sustained suppression over time. These findings underscore the need for strategies that balance sustained antibiotic presence with nutrient manipulation for effective biofilm control in clinical settings.

This work lays the foundation for several future avenues in optimising antibiotic delivery, including spatially variable implant porosity, pulse dosing, and systemic administration. The final model can also be extended to include environmental factors such as temperature and pH and can be expanded to higher-dimensional biofilm structures.

Contents

List of Tables

List of Figures

Acknowledgements

I would like to express my deepest gratitude to all those who have supported me throughout the completion of this thesis.

First and foremost, my sincere thanks go to the Engineering and Physical Sciences Research Council (EPSRC) for their generous sponsorship of my research (grant EP/V519984/1).

I am deeply grateful to my supervisors, Prof. Nigel Mottram and Dr. Sean McGinty, for their guidance, expertise, and support throughout this journey. Your mentorship has been pivotal in shaping my research and fostering both my academic and personal growth. Thank you for the opportunities, advice, and encouragement during these four years.

I would also like to express my gratitude to both former and current members of the 'Mathematical and Computational Biomedical Engineering' research group for upholding high standards and nurturing an environment of support and collaboration. I am thankful to all the professors, researchers, and colleagues I have had the pleasure of meeting at the university and during conferences. Your dedication and enthusiasm have been a constant source of inspiration.

On a more personal note, I would like to extend special thanks to my friends. Your companionship brought balance, offering breaks from work and something to look forward to during busy times. Thank you for staying connected while I was buried in writing.

To my partner, Karl, your presence has been my greatest source of strength throughout this journey. Thank you for your unwavering support, for always knowing when I needed encouragement or simply a moment of laughter, and for patiently listening to me through countless discussions about my work.

To my family, whose unwavering support has carried me through, I cannot thank you enough. To my grandparents, Atul and Rama, your love and encouragement have meant the world to me. To my sister, Prama, thank you for always bringing joy and laughter into my life, and for reminding me to take breaks and smile.

Finally, my deepest gratitude goes to my parents. To my mum, Tuhina, your endless support has been the cornerstone of everything I have accomplished. And to my dad, Prashanta, you have been my greatest source of motivation. Thank you for your hard work supporting our family, for always encouraging me to strive for excellence, and for believing in me. None of this would have been possible without both of you.

Declaration

With the exception of Chapter 1, which contains necessary introductory material, all work in this thesis was carried out by the author unless otherwise explicitly stated.

Chapter 1

Introduction

Bacteria are among the most ubiquitous and tenacious microorganisms, invading and thriving in almost every environment. Their remarkable survival mechanisms enable them to colonise diverse environments by adhering to surfaces and forming complex communities called biofilms. Biofilm formation begins when bacteria adhere to a surface. The adherent bacteria that form biofilms can be found in various environments, including the natural environment, the human body, industrial settings, and medical devices [3,30,33,64,76,138]. Although biofilms consisting of a single species are much less common and are usually found in specific infection sites such as the surfaces of medical implants, biofilms made up of numerous species can be found in most natural environments [137]. Their widespread presence poses challenges in healthcare and industry, making biofilm control strategies an essential area of research.

1.1 Biofilm growth mechanism

To understand biofilm-related issues, it is crucial to examine how these structures form and develop over time. The biofilm formation process involves several stages, including initial attachment, extracellular polymeric substance (EPS) production, maturation, and detachment (see Fig. 1.1). In the first stage, the initial bacterial population on the implant produces sensing molecules that attract the other proliferative bacteria in the bulk fluid. As the population of bacteria grows, these molecules become considerably concentrated. These molecules diffuse radially outward from the proliferative bacteria, and upon reaching the surface, they are reflected back. Eventually, the bacteria detect their approach to the surface and continue moving towards the closest surface, where they become stuck, producing more sensing molecules at the boundary. The increased production causes an increase in the recruitment of bacteria to the pioneering colonies, which eventually merge to form the biofilm [47].

In the second stage, an acidic environment surrounds the bacterial cells created by anaerobic glycolysis and hypoxia. The secreted EPS, comprising lipids, proteins, nucleic acids, and polysaccharides, encircle this. EPS envelops the bacteria and fungi to protect them from exter-

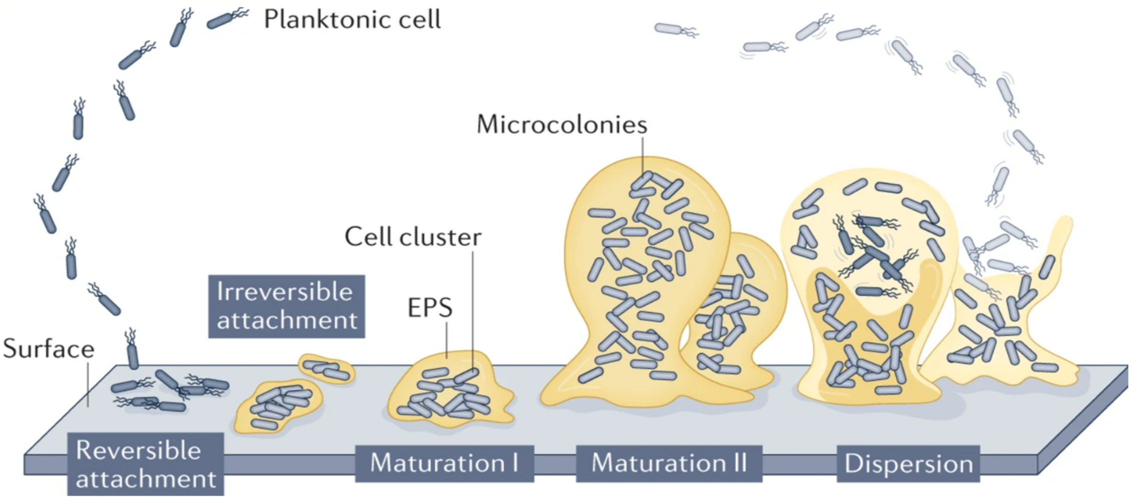

Figure 1.1: Schematic of biofilm formation [110]. This figure illustrates the stages of biofilm development: 'Reversible Attachment' represents the initial attachment process.'Irreversible Attachment' and 'Maturation I' indicate the EPS production phase.'Maturation II' refers to the maturation phase. Finally,'Dispersion' denotes the detachment phase.

nal stimuli [50]. The bacterial population within the matrix expands due to consuming nutrients from the surroundings. EPS also aids in forming the biofilm by facilitating quorum sensing systems communication and the passage of nutrients through channels to different layers. The attachment of bacteria to a surface and the subsequent development of a biofilm are believed to be facilitated by the EPS. In contrast, the diffusion of pharmacological agents is hindered through the EPS, which eventually promotes antimicrobial resilience [102].

The third stage of biofilm development is the maturation phase, during which the biofilm expands and stabilises. In this stage, new proliferative bacteria adhere to the biofilm and are encapsulated by the EPS matrix. This phase not only promotes biofilm growth but also leads to the development of persister cells, which are critical for biofilm survival under stress. These cells are metabolically inactive phenotypes that demonstrate persistent survival even after repeated environmental stress and can withstand high concentrations of antibiotics [18, 74]. While bacterial growth, natural death, and antibiotic-induced death occur within the biofilm, persister bacteria experience significantly lower death rates. The biofilm acts as a porous medium, containing extracellular fluid (ECF) that carries both bacteria and nutrients, with the EPS modulating the diffusion of these components from the surrounding bulk fluid [110].

The final stage of biofilm development involves detachment, which occurs through processes such as erosion, sloughing, and abrasion as the biofilm reaches its plateau. Considering the biofilm as an elastic medium, the internal pressure within the biofilm increases with its volume growth. This pressure triggers bacterial signaling pathways that promote biofilm dissociation. In addition, detachment is facilitated by fluid shear forces, which help to remove biofilm fragments. This detachment stage is critical because it enables the biofilm to disseminate bacteria through the bloodstream (hematogenous dissemination), potentially leading to local recurrence or infection at distant sites [143]. Once the dispersed bacteria revert to a proliferative state, the biofilm's developmental life cycle is completed, beginning the cycle of attachment and biofilm formation anew.

1.2 Biofilm on medical implants and implant infections

Biofilms play a particularly important role in the context of medical implants, where their formation can lead to serious complications such as infections. Research on biofilms has surged in recent decades, largely due to their critical role in hospital-acquired infections. However, most studies have not fully accounted for the complex interactions between biofilms, medical implants, and the host environment. As a result, findings from laboratory models often fail to translate effectively into clinical practice. Biofilms grown in laboratory settings differ from those found in patients in several key aspects, including phenotypic characteristics and pathogenicity. These differences present significant challenges in bridging the gap between experimental research and real-world medical applications.

Although orthopaedic and other indwelling implants have significantly improved patient quality of life, they also present potential health risks, particularly the risk of infection. Prosthetic joint infections, which occur in 0.5–2% of patients, are the most common complication following orthopaedic implant surgeries [1]. Medical biofilms, which are dense communities of microbial cells with altered phenotypes and a unique architecture, can form on these devices. Various bacterial species are capable of producing biofilms on medical equipment [57]. These biofilms differ substantially from those found in marine or industrial environments due to differences in microbial species, available nutrients, and surface characteristics [62]. Implant-related biofilms have the potential to cause infection and disrupt normal device functioning.

Evidence suggests that biofilms can contaminate human integuments, cardiac valves, pacemakers, orthopaedic implants, catheters, and dental tissues and implants [66, 108]. Biofilms on implants can give rise to three main types of infections: late infections, deep immediate infections, and superficial infections. A late infection refers to an infection that appears in the deep tissue surrounding the implant months or years after surgery. This is caused by proliferative bacteria entering the bloodstream, potentially originating from another biofilm infection elsewhere in the body. Deep immediate infections are associated with bacteria introduced at the surgery site, which may come from the implant, surgical instruments, the surgeon's hands, or the patient's skin. Superficial infections can develop on the surface of the surgical site and are generally caused by skin-resident bacteria. Among these, deep infections, whether immediate or late, pose the greatest health risk, as they are difficult to treat and can spread to critical tissues such as muscle and bone [124]. A detailed list of materials used in medical devices and their associated environments and primary colonisers is provided in Table 1 (pp. 140) of [87]. In addition, a recent systematic review covering nearly all aspects of implant-associated biofilm formation can be found in [29].

1.3 Challenges in treating biofilm

One of the most significant challenges in treating biofilms is their resilience to antibiotics, particularly due to the presence of persister cells. Biofilm resilience refers to the ability of bacteria within biofilms to withstand and recover from environmental stresses, particularly antimicrobial treatments. This resilience is exhibited in two primary forms: resistance and tolerance. Resistance involves the capacity of biofilm-associated bacteria to grow and reproduce despite the presence of antibiotics, driven by genetic adaptations. These adaptations, such as mutations or the acquisition of resistance genes, enable bacteria to neutralise, expel, or evade the antibiotic's effects. A key characteristic of resistance is its heritability; these adaptive traits are passed on to subsequent bacterial generations. In contrast, tolerance refers to the ability of bacteria to survive temporary antibiotic exposure without necessarily replicating. Unlike resistance, tolerance does not stem from genetic changes, but rather from phenotypic adaptations, such as entering a persister state or receiving physical protection from the extracellular matrix of the biofilm. Tolerant bacteria, such as persister cells, are not actively killed by antibiotics but persist through the treatment and can repopulate the biofilm once the antibiotic is removed. This survival is facilitated by multiple factors, including the biofilm's three-dimensional structure, which provides surface bacteria with better access to nutrients than those in deeper layers. Additionally, the EPS matrix creates a microenvironment that supports bacterial communication via quorum sensing and modulates gene expression [89, 131]. Persister cells have emerged as significant contributors to biofilm resilience, conventional antibiotics are less effective against deep biofilm infections than superficial ones [37, 71]. Furthermore, biofilm-associated bacteria can activate additional resistance mechanisms. These include the use of antibiotic efflux pumps, secretion of enzymes that inactivate antibiotics, and the induction of programmed cell death in a subset of the population, enhancing the overall survival strategy of the biofilm.

Exposing cultures to high doses of antibiotics is a common method used to identify persister bacteria. In Pseudomonas aeruginosa planktonic cultures, persister cells typically constitute about 0.1% of the population, but this percentage increases to 1% upon quorum-sensing activation [85]. Biofilms contain substantial subpopulations of persister cells, which exploit the biofilm matrix as a protective environment, allowing them to survive and re-establish after antibiotic treatment [74]. The positive charge of conventional antibiotics, such as aminoglycosides and polymyxins, interacts with negatively charged EPS, thus preventing the penetration of antibiotics [72,73]. The presence of persisters in biofilms leads to biphasic killing, where an initial rapid phase of bacterial death is followed by a slower, more resistant phase, reducing the overall effectiveness of treatment despite high antibiotic concentrations [84]. Primary implant infections remain clinically significant despite the use of aseptic techniques and preventive measures. In many cases, implant exchange surgery is necessary, but this procedure is costly, involves extended immobility, and presents challenges such as removing hardened cement and inadequate bone stock for new implant integration. Minimally invasive implant-retention procedures, such as "debridement, antibiotics, and implant retention" (DAIR), are sometimes preferred in early acute infections. However, the success of such procedures largely depends on the thoroughness of biofilm removal [78, 100]. These factors make the treatment of established bacterial biofilms challenging, emphasising the need for novel treatment strategies that aim to eliminate the EPS matrix and target persister cells within biofilms.

1.4 Key methods of treating implant infection

Given the challenges in treating biofilms, several approaches have been developed to address implant infections. The most common approach to remove established biofilms is extensive debridement, which effectively reduces the number of bacterial colonies. However, this method may be less effective on devices with irregular surfaces, cavities, or micro-structured morphologies [127]. Physically scrubbing contaminated surfaces, such as medical implants, can be difficult due to limited access. Moreover, the natural structure of biofilms has been proven to be resistant to many chemical treatments, and the environmental risks associated with harsh chemicals often limit their use [136]. Recent advances in biofilm treatment research include the use of shockwaves, enzymes, and antibodies. For example, antibiotics are more effective in breaking down biofilms when combined with shock waves, high-energy sound waves that enhance antibiotic action [57]. Enzymes offer another approach by specifically targeting biofilm-structuring mechanisms, leading to the breakdown or hydrolysis of the biofilm's polymeric links [60]. In addition, antibiotics functionalised with nitroxide, a stable radical with antibiofilm properties, show promising results in eradicating biofilms, as seen with ciprofloxacin-nitroxide compounds [133]. Despite the variety of therapeutic strategies available, no single treatment has been universally successful for biofilm-infected implants.

Aseptic techniques and antibiotic prophylaxis are considered the gold standard for preventing biofilm formation. In clinical settings, preventive measures include both systemic antibiotic injections and local antibiotic reservoirs. More advanced prophylactic approaches involve novel biomaterials with inherent antibacterial properties or surface modifications that incorporate antimicrobial agents [144]. Current systemic antibiotic treatments often do not achieve sufficient intracellular bacterial concentrations, contributing to persistent infections [10]. To address the growing issue of antibiotic resilience in biofilms, drug-coated implants have emerged as a common strategy, offering localised and controlled antibiotic delivery to prevent implant infections [25, 35, 70, 106, 123]. The surface characteristics of implants are crucial to inhibiting biofilm growth and ensuring antibiotics are delivered within the therapeutic range, from minimum effective concentration (MEC) to minimum toxic concentration (MTC) [75]. Drug-coated implants, using multilayer polymer coatings, thinner struts, and more biocompatible polymers or metal alloys, are designed to control drug release and reduce tissue damage [65]. However, concerns have been raised about possible allergic reactions and vascular inflammation due to the permanent presence of polymers [88, 132]. To address these concerns, modern implant designs are moving towards biodegradable polymers and polymer-free coatings, classified into macroporous, microporous, nanoporous, and smooth surface designs [80, 107, 111, 129]. These strategies, combined with innovations in drug-coated implants, offer new avenues for preventing and treating biofilm-associated infections.

1.5 Literature review

This literature review focusses primarily on studies that use mathematical modelling to investigate biofilm dynamics, as this approach is fundamental to the analysis presented throughout the rest of this thesis. Mathematical modelling has emerged as a powerful tool for understanding biofilm dynamics and developing treatment strategies. Numerous efforts have been made to translate the conceptual understanding of biofilms into mathematical frameworks, offering valuable insights into the behaviour of these complex systems and their underlying processes. Mathematical modelling can help predict the dynamics of biofilms and enhance our understanding of their biological, physiological, and mechanical properties. Several comprehensive review articles have addressed the various perspectives on biofilms, including biological, physiological, mechanical, and mathematical points of view [30, 36, 94, 138].

Biofilm models vary significantly in their complexity and approach. These range from low-dimensional continuum models [141], which provide simplified representations of biofilm growth and structure, to diffusion-limited aggregation models [54] that focus on spatial processes [125], continuum-discrete models that bridge the gap between macroscopic and microscopic scales [14], and fully coupled biofilm-fluid interaction models [40, 93]. Given the highly nonlinear nature of the governing equations in biofilm dynamics, advanced numerical methods are necessary for solving these models. Custom-built code, as well as scientific software such as MATLAB®, and COMSOL Multiphysics ®, are commonly employed to address these computational challenges.

This interdisciplinary approach is particularly valuable in addressing antibiotic resilience in biofilm-related infections associated with medical implants, with the goal of optimising drug delivery through these devices. By integrating mathematical modelling with biological and physiological insights, researchers aim to develop more targeted and practical solutions to combat biofilm-associated infections. However, significant challenges remain in the field of mathematical biofilm modelling. One of the foremost difficulties lies in integrating the diverse physical, chemical, biological, and ecological processes that occur across multiple time and length scales into a comprehensive mathematical or computational framework. Solving these complex, multiscale problems remains an open and active area of research.

1.5.1 Modelling the biofilm growth

In the early stages of this research area, the groundwork was laid with a one-dimensional (1D) model, which was dependent on the spatial vector in the x-direction and focused solely on nutrient uptake. This model used a biological rate equation encapsulating nutrient uptake within biofilms using Monod kinetics. The Monod term was represented by the expression $\mu = \mu_{\max} \frac{S}{K_s + S}$, where μ, the specific growth rate; S, the nutrient concentration; $\mu_{\max}$, the maximum growth rate, and K_s, the half-saturation constant [11]. This foundational model paved the way for subsequent advancements in understanding biofilm growth.

The relationship between biofilm thickness at steady state and nutrient flux was explored in detail in [104]. In their study, the nutrient flux and biofilm thickness were calculated for a range of bulk nutrient concentrations, denoted as S, where $S > S_{min}$, and S_{min} represents the minimum nutrient concentration necessary for biofilm growth. It was found that below this threshold, nutrient flux would drop to zero, preventing biofilm formation at steady state. This result underscores the critical role of nutrient availability in sustaining biofilm growth.

A multi-species biofilm model later developed in [140] expanded on this concept by predicting the evolution of biofilm thickness, microbial dynamics, and the spatial distribution of species and nutrients. This model accounted for key processes such as biomass degradation due to shear stress and sloughing. It was built upon the continuum description of biofilm material and conservation principles, incorporating foundational mathematical structures from earlier models. This approach has proven to be a powerful tool for quantitatively understanding biofilm processes across a range of applications.

Subsequent advances in biofilm modelling included the development of an extended mixed culture biofilm model, which introduced greater flexibility in describing the transport of dissolved components within the biofilm. This model also considered the diffusive transport of particulate components within the biofilm's solid matrix, which impacts the volume fraction of the liquid phase within the biofilm [141]. This one-dimensional extended model, grounded in experimental data, provides predictions about biofilm growth behaviour over short and long-term periods, enhancing the ability to simulate biofilm dynamics under various environmental conditions.

Models that use Cellular Automaton (CA) [92, 96] and hybrid discrete continuous frameworks [94] have shown the ability to simulate biofilm growth in ways that correspond well to experimental data. These models account for key processes such as bacterial reproduction, cell-to-cell communication, and nutrient diffusion. However, one limitation of these approaches is the inherent randomness in the biomass redistribution phase, which may be viewed as an artefact of the algorithm rather than an accurate representation of the biological growth process. In such cases, a deterministic model may be preferable to reduce algorithmic bias and improve prediction accuracy [6, 28, 45]. A spatiotemporal continuum model with density-dependent diffusivity [45] predicts that, under nutrient-limited conditions, biofilms develop spatially heterogeneous structures, while abundant nutrients result in a more compact and interconnected biofilm structure. Another continuum model examines biofilm expansion into a stationary aqueous medium, treating the biofilm as a homogeneous, viscous, and incompressible liquid, with the biofilm velocity determined by Darcy's law [69]. This model provides insight into the dynamics of biofilm growth and structural changes. In a continuous model describing biofilms as a biological gel composed of water and EPS [28], the primary forces driving movement are exerted on the EPS and the fluid solvent. This mechanism leads to EPS swelling and the redistribution of biomass, offering a detailed understanding of biofilm expansion at the molecular level. Additionally, a hybrid model integrates the EPS matrix via a continuum approach, while microbial cells are represented discretely [5]. This multidimensional hybrid model provides a nuanced perspective on the microscale structures within biofilms, offering a comprehensive understanding of biofilm dynamics across different spatial scales.

Further advancements were made with the formulation of a system of partial differential equations (PDE) to represent biofilm growth dynamics. This system is expressed as $\frac{\partial B_i}{\partial t} + \nabla . J_i^B = G_i(B_i, C_i)$, where J_i^B is the flux and $G_i(B_i, C_i)$ is the rate of nutrient consumption by the biomass B_i in which C_i being the nutrient concentration. By capturing the spatial distribution of biomass and nutrients, this model represents a significant leap towards more realistic biofilm simulations [6].

The field also witnessed significant progress in exploring mass transport and microbial activity within biofilms. This was exemplified by the utilisation of a reaction-diffusion 1D model, expressed as $D\nabla^2 C = r(C, X)$ to describe nutrient diffusion and consumption [17]. Further enrichment of the understanding of biofilm mechanics can be seen by investigating detachment and structural integrity through comprehensive 3D viscoelastic modelling of biofilm's mechanical properties [20, 21, 126].

1.5.2 Modelling the moving boundary

In biofilm modelling, the boundary between the biofilm and the bulk fluid is dynamic, influenced by factors such as attachment and detachment fluxes. In a simplified model, the bacterial density can be assumed to start as a uniform distribution within a well-defined medium. Then, the bacteria search for surfaces to adhere to by using sensing molecules to determine their proximity to the surface [46]. At this initial stage, the extent of the boundary (L) between the biofilm and bulk fluid depends on the attachment and detachment fluxes. We may consider the rate of change of biofilm thickness (L) in the 1D case as [34, 41]

$$\frac{dL}{dt} = u(L(t), t) + \sigma_a(t) - \sigma_d(L(t)), \tag{1.1}$$

where $u(L(t),t)$ is the velocity of biomass at the interface at time t, $\sigma_a(t)$ and $\sigma_d(L(t))$ are the attachment and detachment flux, respectively. Here, $\sigma_d(L(t))$ can be modelled as a first-order process with a detachment rate coefficient α (also called the erosion coefficient) and is proportional to the square of the biofilm thickness as [43, 140]

$$\sigma_d(L(t)) = \alpha L^2(t).$$

Most studies [12, 33, 42, 77, 103, 119], however, concentrate on mature biofilms and the detachment flux.

The understanding of biofilm mechanics is further deepened by modelling the detachment rate as

$$\sigma_d(L(t)) = \alpha L(t)\tau_s,$$

where τ_s represents the hydrodynamic shear rate acting on the biofilm. This 1D approach highlighted the dynamic interaction between biofilm structure and environmental forces [2].

In some studies, individual models or extensions of existing models have been developed to investigate the influence of various factors on biofilm boundaries [4, 77, 90, 119, 120, 134, 137, 146]. For example, constant and nutrient-dependent cell death has been shown to significantly affect the thickness of the steady-state biofilm [137]. Cell death is not only the result of detachment at the biofilm-bulk fluid interface but also occurs in the deeper layers, that is, at the interface between the biofilm and implant. This finding highlights that biofilm thinning occurs both through detachment and internal cell death. As the rate of cell death increases, biofilm thickness correspondingly decreases.

In other studies, the detachment of biofilm is found to be influenced by the flow velocity of the bulk fluid surrounding the biofilm. Higher flow rates reduce the mass transfer boundary layer, which in turn decreases biofilm thickness [77]. Additionally, the biofilm boundary can diminish further and even be eradicated with sufficient antimicrobial doses. High doses of biocide can lead to non-unique steady-state conditions, whereas lower, targeted doses can successfully eliminate the biofilm [119]. These findings underscore the delicate balance between biofilm growth and external forces such as fluid dynamics and chemical treatments.

Temperature and osmotic pressure play crucial roles in influencing the dynamics of biofilm boundaries, as discussed in [4]. Even slight increases in temperature can lead to significant increases in biofilm thickness. As biofilm biomass expands or contracts, internal pressure is generated, which can be modelled using Darcy's law in conjunction with Flory-Huggins theory. In this framework, the biofilm is treated as a polymer network immersed in a solvent. The study [4] revealed that osmotic pressure can enhance biofilm synthesis when first-order reaction kinetics are applied, although this effect was not observed with Monod reaction kinetics. Additionally, temperature impacts are slightly amplified through reaction rates influenced by osmotic pressure, indicating a complex interplay between thermal conditions and biofilm growth mechanisms.

1.5.3 Modelling the porous implant

Bacteria can colonise and grow in natural and engineered porous environments. To accurately model bacterial growth in porous media, it is essential to account for both biofilm biomass and suspended biomass, as well as the processes of detachment and attachment [55]. Biofilm biomass refers to bacteria that have attached to a surface and formed a structured, often resilient, layer. In contrast, suspended biomass consists of bacteria that remain free-floating within the fluid. Suspended biomass is generally more susceptible to removal, such as through fluid flow, compared to biofilm biomass, which is more protected due to its structured layers. In biofilms, the deeper layers often have limited access to nutrients, making them more prone to being washed out by fluid flow.

The behaviour of bacterial density is influenced by different growth rates of biomass. Some models assume a constant growth rate, while others allow growth to depend on the porosity of the environment [15, 91]. For constant growth rates, the bacterial density decreases as porosity increases. However, increasing porosity can also promote bacterial attachment and proliferation, suggesting a complex relationship between bacterial growth and the porosity of the surrounding medium. This interplay indicates that the bacterial growth rate is likely dependent on the porosity of the implant or the surface in question. Consequently, achieving a balance between the action of antimicrobial drugs and bacterial proliferation in porous environments becomes critical for effective treatment.

Traditionally, biofilms in porous media have been modelled as impermeable domains [19,22, 44, 95, 122, 135]. However, later studies have shown that biofilms exhibit a higher permeability than their EPS matrix alone [61, 116]. Recently, microfluidic channels have gained popularity for studying biofilms in porous systems [98, 117], as they provide precise control over fluid flow at scales that are comparable to the dimensions of biofilms in such environments.

Research has shown that the permeability of porous media is highly influenced by the permeability of the biofilm itself [63]. In particular, biofilm porosity becomes an important factor when modelling intermediate to high-density biofilm levels. The impact of biofilm porosity is even more pronounced when the biofilm is considered permeable. Additionally, the study highlights the potential for using simplified biofilm geometries, such as uniform coatings or symmetric contact filling, to more effectively estimate the overall permeability of biofilm-clogged porous media. These simplifications are particularly useful when biofilm density levels are high, making them a practical approach for modelling biofilm behaviour in porous systems.

1.5.4 Impact of surface topology and coating morphology of medical implant

The properties of implants, such as hydrophobicity, roughness, surface chemistry, and surface free energy, play a crucial role in bacterial adhesion and biofilm formation. In general, rough and hydrophobic surfaces tend to promote biofilm growth [39]. Surface free energy refers to the excess energy at the surface of a material compared to its bulk; it affects how liquids, such as bacterial adhesion proteins or other substances, interact with the surface. Surfaces with higher free energy tend to improve bacterial adhesion, making it easier for bacteria to attach and form biofilms [150]. Additionally, biofilm development is often enhanced when surface roughness increases beyond a certain threshold. Polishing the implant surface can reduce roughness, which in turn decreases bacterial attachment [83]. However, polishing can also alter the physicochemical properties of the implant, potentially affecting its overall performance.

Several studies have been conducted to evaluate biofilm growth on medical implants under various conditions. Titanium (Ti) is commonly used as an implant material due to its unique combination of properties, including excellent biocompatibility, high strength, and fatigue resistance [23]. Porous titanium structures or coatings are particularly relevant for orthopaedic implants because they allow bone tissue to grow into the porous structure, creating a strong biological anchor between the implant and the host bone. However, the increased surface roughness inherent to porous structures also raises the risk of bacterial adhesion. Research has shown that hydrophobicity and surface roughness are key factors influencing bacterial adherence. When porosity exceeds 15% or the pore size reaches up to 150 μm, the surface roughness increases significantly, which correlates with enhanced bacterial attachment.

In addition, nano-silver-loaded dopamine coatings have been shown to reduce the risk of infection and promote mineralisation, facilitating better osteointegration of Ti implants [148]. These coatings offer dual benefits by both enhancing antimicrobial properties and supporting bone integration. Similarly, research suggests that the topological and chemical properties of Ti surfaces can differentially affect the growth of colonising bacterial species, potentially influencing the composition of the biofilm over time [52]. For example, calcium-coated Ti surfaces have been found to support lower initial levels of biofilm formation compared to non-calcium-coated surfaces, likely due to differences in surface roughness. Given these findings, along with the well-documented osteointegration properties of calcium coatings [53], such surfaces appear to be promising candidates for dental implants.

In addition, different types of implants have varying requirements, such as porosity levels, which require tailored studies for each application. For example, in vitro studies of Staphylococcus aureus and Staphylococcus epidermidis proliferation have been conducted in uncoated and coated titanium materials with varying roughness, porosity, surface topology and hydrophilicity (surface wettability) for orthopaedic implants [56]. The optimised titanium implant surfaces in these studies demonstrated a total porosity of approximately 0.35 ± 0.10, with interconnecting pore channels averaging $\sim 3.5\ \mu$m in size, and a surface roughness (R_a) between 1.5 and 3.0 μ m. Additionally, surface treatment to form an anatase layer ($\sim 40 \pm 20$ mm thick) was recommended. This combination of surface parameters resulted in a reduction in biofilm formation by 80-90% for flat surfaces compared to untreated, non-optimised plasma-sprayed porous Ti, and by 65-95% for other porous Ti coatings. These findings suggest that optimising surface characteristics plays a crucial role in minimising bacterial colonisation and biofilm formation on orthopaedic implants.

Additionally, these porous surfaces have been shown to enhance cell proliferation and gene expression by 10-50% compared to state-of-the-art vacuum plasma-sprayed porous titanium coatings. This suggests a potential to design implant surfaces with intrinsically reduced infection risks, without the need for additional antibacterial substances. A systematic review emphasised that implant surface morphology significantly influences bacterial adhesion, concluding that nano-patterned surfaces can effectively control focal adhesion [13]. Further research on bacterial adhesion to both coated and uncoated surfaces, as well as biofilm dispersal, supports the strategy of modifying the micro-topology and nano-topology of implant surfaces to disrupt microbial adhesion [10]. These findings underscore the importance of surface engineering in reducing biofilm formation, with a particular focus on leveraging nanoscale modifications to interfere with bacterial colonisation and enhance implant performance.

1.5.5 Modelling the local and controlled antibiotic release kinetics

The controlled release of antibiotics from drug-coated implants has been a growing focus in recent years, with models evolving from simple diffusion-based systems to complex simulations that account for both drug properties and the surrounding biological environment.

The biofilm matrix acts as a protective barrier, making bacterial cells within the biofilm more resistant to antimicrobial agents compared to planktonic cells [38, 58]. This phenomenon can be described using Fick's law of diffusion, which provides a theoretical framework for understanding the limited penetration of antimicrobials into biofilms [112]. In this model, the biofilm is considered as a uniformly thick planar slab of thickness L_f, with one side exposed to the bulk fluid and the other adjacent to an impermeable boundary. Beyond the physical penetration barrier, the presence of persister cells is another important factor contributing to the resilience of biofilms to antimicrobial treatments.

To investigate biofilm responses to antibiotic treatments, a 1D model was developed to describe the interaction between antibiotic concentration (A) and biofilm density (B). This interaction is captured by the equation $\frac{\partial B}{\partial t} = g(B,A) - h(B,A)$, where g and h represent growth and loss terms influenced by antibiotic effects [8,9]. Additionally, a phenotype-switching model [27] accounts for changes in biofilm dynamics, incorporating growth, antibiotic-induced cell death, the transition of susceptible cells into persister cells, and the reverse process where persister cells revert to susceptible cells. This model posits that only the susceptible cells absorb nutrients, and highlights that the efficacy of periodic dosing regimens depends critically on the relative timing of dose administration and withdrawal. As the field expanded and provided an increased understanding of antibiotic resilience and the complexities of biofilms, mathematical models attempted to capture the spatial heterogeneity and intermicrobial interactions [113]. A further advancement involved introducing a 2D model demonstrating how antibiotics affect biofilm growth and death. This was shown by a convection-diffusion-reaction equation of biomass, including terms where the antibiotic affects the metabolic and death rates of biomass [84].

Conventional antibiotic treatments are becoming increasingly ineffective in controlling bacterial infections, largely due to the emergence of antibiotic-resistant pathogens. Bacteria in their biofilm growth mode significantly contribute to the development of drug resistance [37, 71]. Several factors are responsible for the enhanced antibiotic resilience of biofilms, as highlighted in studies [72–74]. One key factor is the differential physiological activity of bacteria within biofilms, often caused by limited nutrient penetration. This results in varying metabolic rates among bacteria, contributing to their ability to withstand antimicrobial agents. Another critical factor is the presence of persister cells, which are dormant variants of regular bacteria. Persister cells exhibit significantly reduced metabolic activity, allowing them to evade the effects of antibiotics, which typically target actively dividing cells. Additionally, enzymes secreted by bacteria embedded within the biofilm can hydrolyse and deactivate antibiotics, further increasing resilience. The EPS also plays a crucial role in antibiotic resistance. Many conventional antibiotics, such as aminoglycosides and polymyxins, carry a positive net charge, which causes them to interact with the negatively charged EPS. This interaction hinders the penetration of antibiotics, reducing their effectiveness in eradicating biofilm-associated bacteria. Other mechanisms contributing to antibiotic resistance in biofilms are discussed in further detail in [59]. Given the increasing antibiotic resilience in biofilms, there is an urgent need for the development of novel treatment strategies to combat these infections [25, 105, 106, 123]. These strategies must address the unique challenges posed by biofilm-associated bacteria, including their protective matrix and phenotypic adaptations.

A mathematical and experimental model of Pseudomonas aeruginosa biofilm formation in the lungs and its management using silver carbene complex (SCC) antibacterials, delivered either in polymeric biodegradable particles or aqueous form, is described in [84]. The study examined two treatment scenarios: (i) a twice-daily dosage using aqueous SCCs and (ii) a single dose of SCC-loaded particles with uniform degradation times. The results indicated that the SCC-polymer-based approach outperformed the aqueous-based treatment. Additionally, the study found that using particles with varying degradation times did not offer any significant advantage over those with uniform degradation times.

To overcome the challenges posed by biofilm persistence in medical implants and rejuvenate antibiotic treatments, controlled local elution of antimicrobials from implantable devices has been a focus in recent decades [26, 48, 49, 97, 115]. The surface topography and coating morphology of implants play crucial roles in both inhibiting biofilm growth and ensuring the controlled release of antimicrobials within a therapeutic range, which must be maintained between the minimum effective concentration (MEC) and the minimum toxic concentration (MTC) [75]. This approach aims to enhance the efficacy of antimicrobial treatments while minimising the risk of toxicity, addressing both biofilm resistance and implant-associated infections.

Due to complications such as allergic reactions and vascular inflammatory responses associated with the presence of durable polymers on medical implants [88], research has increasingly focused on polymer-free drug-eluting implants. In [82], the first model of drug elution from polymer-free drug-eluting stents is presented. This model predicts drug release from various polymer-free systems, including nanoporous, nanotubular, and smooth surfaces. Through analytical solutions, the study identifies key parameters such as porosity, absorption, desorption, tortuosity, and drug layer thickness that can be modified during the manufacturing process to tailor the drug release profile. Nanoporous systems, in particular, are highlighted for their potential to offer highly controlled drug release due to the large number of tunable parameters. By adjusting porosity and tortuosity, specific release profiles can be achieved. The study also explores a two-stage release method to further enhance flexibility in controlling the drug release profile, emphasising the advantages of polymer-free designs in mitigating issues related to polymer coatings. Additionally, it was found that the thickness of the drug layer, the ratio of drug absorption to desorption, and the ratio of drug solubility to initial drug concentration are critical factors that significantly affect the release duration.

In recent years, there has been a growing interest in polymer-free drug-eluting systems in the orthopaedic domain [67]. However, there remains a lack of comprehensive studies that integrate mathematical modelling of antibiotic resilience mechanisms with the efficacy of implant-based drug delivery targeting biofilm development. This thesis aims to address this gap by proposing a generalised mathematical model that describes biofilm structure at the phenotypic level, coupled with controlled drug delivery from a polymer-free drug-coated implant to combat biofilm infections. While mathematical models of biofilm dynamics have garnered considerable attention in recent years, to our knowledge, no previous works have developed a model that addresses drug release from an implant specifically designed to counteract biofilm formation. This area of research is expected to grow significantly, given its commercial, technological, and scientific importance.

1.6 Thesis motivation and objectives

Despite advances in understanding biofilm behaviour, significant research gaps remain that hinder the development of effective treatments for biofilm-associated implant infections. Understanding biofilm behaviour in non-antibiotic environments is essential, yet this area has received limited attention. Much of the current research has focused on biofilm dynamics under antibiotic pressure, leaving a gap in our understanding of how biofilms naturally develop and mature in environments free from external stressors. Without a clear baseline of biofilm behaviour, it becomes difficult to accurately assess the specific impacts that antibiotics have on biofilm structure and growth.

Another significant challenge lies in the insufficient integration of key bacterial phenotypes—proliferative, persister, and dead bacteria, into mathematical models, particularly in terms of how nutrient availability influences their transitions. These phenotypes play crucial roles in biofilm structure and resilience, especially under antibiotic treatment, but most existing models fail to capture the complex interactions between these states. While some models account for these bacterial phenotypes, they often do so without considering the critical role of nutrient availability in driving the transitions between these states. Nutrients directly influence bacterial metabolic activity, affecting the shift between growth, dormancy, and survival under stress conditions. Research, such as that by [7] and [99], has shown that nutrient starvation can trigger persister cell formation, underscoring the importance of incorporating nutrient-driven transitions into models. The presence of persister cells, often shielded within the EPS matrix, contributes significantly to biofilm resilience and survival in medical implant infections. However, current models lack the sophistication needed to simulate nutrient-driven transitions between bacterial phenotypes, particularly in the context of antibiotic treatments, where nutrient limitation can trigger resilience mechanisms such as increased persister cell formation and enhanced EPS production. This gap complicates efforts to fully understand and manage biofilm behaviour.

Furthermore, while biofilm dynamics and controlled drug delivery systems have been studied extensively but separately, there is a notable lack of comprehensive models that integrate these elements into a single framework. This gap is particularly evident when modelling the effectiveness of implant-based drug delivery systems that target biofilm infections. Mathematical models that can simulate the interactions between biofilm growth and controlled drug delivery are essential for optimising implant-based treatments. However, few studies have developed models that rigorously address how drug release from implants can be tailored to overcome biofilm-associated infections.

Finally, despite the growing use of controlled drug delivery systems in clinical settings, there is a lack of generalised models that can optimise these systems in a variety of implant infections and settings. Current models tend to be tailored to specific infection sites or implant types, limiting their applicability to broader clinical scenarios. There is a need for a comprehensive, generalised model that can be adapted to different implant infections and drug delivery strategies, whether through localised implant release or systemic treatments such as oral antibiotics. Such a model would provide valuable insight into how drug delivery can be optimised to improve treatment efficacy for biofilm-related infections in medical implants.

Given these critical gaps, the objectives of this research are designed to directly address these challenges by developing mathematical models that provide a more detailed, integrated understanding of biofilm dynamics in the context of implant-related infections. The objectives aim to bridge the existing knowledge gaps by incorporating bacterial phenotypes, nutrient dynamics, and localised controlled antibiotic delivery into a cohesive modelling framework. By doing so, the study seeks to improve strategies for biofilm management and optimise drug delivery for biofilm-associated infections. The following research objectives are formulated to guide this work:

- Develop mathematical models that simulate biofilm growth in environments without external stressors to establish a clear baseline for evaluating antibiotic interventions.
- Integrate bacterial phenotypes and nutrient dynamics into biofilm models to capture the interactions between proliferative, persister, and dead bacteria, and explore how nutrient availability influences their transitions and develop biofilm resilience.
- Create integrated models that simulate biofilm growth and localised drug delivery from implants.
- Develop a generalised model to optimise drug delivery strategies that are adaptable to various clinical scenarios, and perform an initial optimisation to demonstrate the applicability and effectiveness of the model in improving treatment outcomes.

Outline of the thesis

The remainder of this thesis is dedicated to addressing the research objectives. Chapter 2 presents a hierarchy of one-dimensional biofilm growth models, where the initial complex model is systematically simplified in stages. Instead of reducing the model to a single version, each level of simplification captures different aspects of biofilm dynamics. Chapter 3 extends the discussion by focussing on biofilm development in non-antibiotic environments. It provides a baseline understanding of biofilm behaviour before incorporating antibiotic treatments. Chapter 4 introduces continuous antibiotic administration into the models, exploring its impact on biofilm growth. It models the interactions between proliferative, persister, and dead bacterial populations under antibiotic pressure, offering insights into biofilm resilience mechanisms. The chapter also examines varying nutrient availability, further enhancing the understanding of biofilm behaviour under stress. Chapter 5 integrates controlled antibiotic release from porous implants into the biofilm models, investigating its effects on biofilm composition and bacterial phenotypes in relation to nutrient availability. The chapter also introduces an initial optimisation approach for enhancing antibiotic delivery strategies, demonstrating the potential for tailored drug release to more effectively combat biofilm infections. The thesis concludes by summarising the key findings and suggesting future research directions to further enhance the modelling of biofilm dynamics and optimise implant-based drug delivery systems.

Chapter 2

A hierarchy of 1D biofilm growth models

This chapter presents a generalised model that includes biofilm structure at a phenotypic level, accompanied by controlled antibiotic release from an antibiotic-eluting porous implant aimed at combating biofilm infections. We have formulated a 1D model that captures biofilm growth, focussing on the interactions between various bacterial phenotypes, including proliferative bacteria, persister bacteria, and dead bacteria and the EPS. In this model, the phenotypic shift from proliferative to persister bacteria is depicted as dependent on nutrient levels, thereby examining the problem of antibiotic resilience linked to nutrient scarcity. In addition, we have modelled the impact of administering antibiotics from antibiotic-coated porous implants on biofilm development to allow insight into the interactions of bacteria and antibiotics in a biofilm setting.

The primary aim of this chapter is to present a series of models that explore the key biological mechanisms that drive biofilm growth. Rather than fully simplifying the initial model to a single version, we systematically reduce its complexity in stages, creating a hierarchy of models that capture various aspects of biofilm dynamics. This hierarchical modelling strategy offers a structured framework to isolate the impact of biological phenomena, such as nutrient thresholds, phenotypic transitions, and antibiotic exposure, on biofilm growth, which has not been systematically addressed in previous work. These models are designed to offer flexibility, allowing modelers to select the appropriate level of detail based on the specific characteristics of their real-world system. By introducing assumptions at each step, we present possible simplifications for future modelling efforts, while focussing on a subset of models that are most relevant to the biofilm system under investigation. This approach helps to balance computational efficiency with biological accuracy, ensuring that the essential features of biofilm behaviour are retained throughout the process. The detailed mathematical analyses for the models referred to in this chapter as Models 11 and 8 are discussed in Chapter 3, Models 5 and 3 in Chapter 4, and Models 10 and 2 in Chapter 5.

Outline

This chapter begins with the introduction of a comprehensive mathematical model that details the dynamics of biofilm growth and antibiotic release from a porous implant, focussing on bacterial phenotypes and their environmental interactions. Following a detailed introduction of the model, we list possible simplification strategies through a series of seven specific assumptions. Each simplification step reduces complexity while retaining essential characteristics, isolating specific biological phenomena for focused study. Each simplification or combination of them creates a new biofilm growth model that focusses on particular aspects of biofilm growth. The chapter emphasises understanding the biology behind these simplifications, providing a clear framework for analysing biofilm behaviour.

2.1 Modelling biofilm growth on antibiotic eluting porous implant (Model 1)

In this section, we introduce the comprehensive biofilm growth model that details the controlled antibiotic release from a porous, antibiotic-eluting implant. This initial complex model has been mentioned in later sections as **Model 1**. All variables and parameters explained in this section are detailed in Table 2.1 and Table 2.2.

Variables	Description
C_p	Antibiotic concentration in porous implant
C_b	Bound antibiotic concentration in porous implant
L_1	Position of a moving boundary separating the undissolved and dissolved antibiotic in the porous implant
C	Antibiotic concentration in biofilm
S	Nutrient concentration in biofilm
B	Proliferative bacteria concentration in biofilm
B_p	Persister bacteria concentration in biofilm
B_d	Dead bacteria concentration in biofilm
E	EPS concentration in biofilm
ϕ_{bio}	Water volume fraction in biofilm
v	Advective flow velocity for biomass in biofilm
P	Pressure within biofilm
L	Biofilm thickness
x	Independent space variable
t	Independent time variable

Table 2.1: Summary of the model variables

We assume that the system is one-dimensional (1D), with the spatial variable denoted by x, as illustrated in Figure 2.1. While this approach simplifies the inherently three-dimensional geometry of the system, it remains valid for mathematical analysis and significantly simplifies the analysis [2, 149]. The justification for this dimensional reduction lies in the predominant direction of antibiotic release, which occurs normal to the implant surface. This directional release is due to the minimal thickness of the antibiotic layer relative to its lateral dimensions (e.g., [81]). The time variable is denoted as t.

Fig. 2.1 schematically represents the model configuration, consisting of a porous implant medium occupying the space from $x = -L_d$ to $x = 0$, initially saturated with antibiotic, adjacent to a biofilm medium from $x = 0$ to $x = L(t)$. $L(t)$ refers to the thickness of the biofilm that changes over time. This biofilm medium is comprised of various bacterial phenotypes, EPS, and nutrients, extending into a bulk fluid medium, from $x = L(t)$ to $x = \infty$.

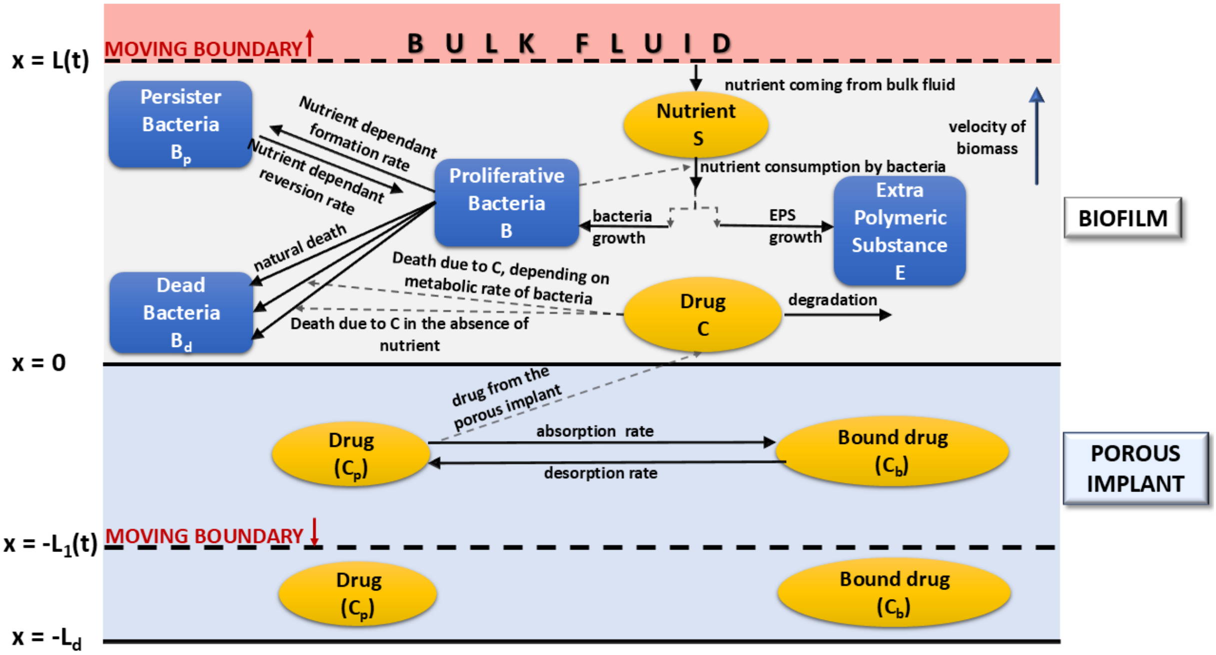

Figure 2.1: This figure represents the 1D model showing the interactions in two media: biofilm and porous implant region. The bulk fluid medium is not included in any of the models. The blue boxes indicate variables contributing to biofilm growth, including proliferative bacteria (B), persister bacteria (B_p), dead bacteria (B_d) and EPS (E). The yellow boxes represent the chemical compound variables within the pores of the respective medium, nutrient (S) and antibiotic (C) in the biofilm and antibiotic (C_p) and bound antibiotic (C_b) in the porous implant. The moving boundaries at $x = L(t)$ and $x = -L_1(t)$ represents the biofilm thickness and the boundary between the undissolved and dissolved antibiotic respectively.

Parameters	**Description**	**Values (SI)**	**References**
D_C	Diffusion coefficient of antibiotic in biofilm medium	10^{-10} m^2/s	[130, 151]
D_S	Diffusion coefficient of nutrient	2.97×10^{-10} m^2/s	[84]

Parameters	**Description**	**Values (SI)**	**References**
D_B	Diffusion coefficient of proliferative bacteria	1.485×10^{-12} m^2/s	[109]
D_{B_p}	Diffusion coefficient of persister bacteria	1.485×10^{-12} m^2/s	[109]
D_{B_d}	Diffusion coefficient of persister bacteria	1.485×10^{-12} m^2/s	[109]
D_E	Diffusion coefficient of EPS	1.485×10^{-12} m^2/s	[109]
ϕ	Porosity of the implant medium	0.6	[82]
ϕ_e	Effective porosity of the implant medium	0.6	[32]
ϕ_b	Volume fraction of the adhered region by bound antibiotic	0.1	[82]
τ	Tortuosity of the implant medium	3	[32]
K	Equilibrium dissociation constant	0.1	[82]
ρ_B	Mass density of bacteria	200 kg/m^3	[145]
ρ_E	Mass density of EPS	33 kg/m^3	[145]
X_∞	Maximum biomass density of the biofilm	10 kg/m^3	[2]
γ_{bio}	Yield coefficient	0.63	[2]
σ	Detachment rate	0.0086806 /m^{-1} s^{-1}	[2]
μ_b	Maximum growth rate	6.9444×10^{-5} s^{-1}	[16]
μ	Maximum nutrient consumption rate	1.1111×10^{-4} s^{-1}	[16]
k_S	Nutrient consumption half saturation constant	6.5×10^{-4} kg/m^3	[16]
k_B	Metabolic rate to biomass production rate conversion factor	0.86625	[16]
k_E	Metabolic rate to EPS production rate conversion factor	k_B	[84]
k_c	Degradation rate of antibiotic	6.4583×10^{-5} s^{-1}	[84]
κ	Antibiotic effectiveness rate	192.92 m^3/kg	[84]
α_1	Stationary antibiotic effectiveness rate	0.011743 m^3/(kg s)	[84]

Parameters	**Description**	**Values (SI)**	**References**
α_2	Stationary antibiotic minimal concentration	$3.7576 \times 10^{-4}\ \mathrm{s}^{-1}$	[84]
b	Proliferative bacteria endogenous death rate	$1.2031 \times 10^{-5}\ \mathrm{s}^{-1}$	[84]
k_F	Rate of persister formation	$7.2188 \times 10^{-7}\mathrm{s}^{-1}$	[84]
k_R	Rate of persister reversion	$2.4063 \times 10^{-5}\mathrm{s}^{-1}$	[84]
C_0	Initial concentration of the antibiotic in implant medium	$0.1\ \mathrm{kg/m}^3$	[82]
C_{in}	Initial concentration of the antibiotic in biofilm medium	$0\ \mathrm{kg/m}^3$	[82]
C_S	Solubility of the antibiotic in the biofilm medium	$0.01\ \mathrm{kg/m}^3$	[82]
L_d	Thickness of the antibiotic layer in the porous implant	$10^{-4}\ \mathrm{m}$	[82]
$L_{1,0}$	Initial thickness of the dissolved antibiotic layer	$10^{-15}\ \mathrm{m}$	
L_0	Initial biofilm thickness	$10^{-5}\ \mathrm{m}$	
B_0	Initial proliferative bacteria concentration	$2.2074 - 6.6221\ \mathrm{kg/m}^3$	
B_{p0}	Initial persister bacteria concentration	$2.2074 - 6.6221\ \mathrm{kg/m}^3$	
B_{d0}	Initial dead bacteria concentration	$2.2074 - 6.6221\ \mathrm{kg/m}^3$	
E_0	Initial EPS concentration	$2.2074 - 6.6221\ \mathrm{kg/m}^3$	
S_1	Nutrient concentration threshold below which all proliferative transforms to persister	$5.2 \times 10^{-4}\ \mathrm{kg/m}^3$	[84]
S_2	Nutrient concentration threshold above which all persister transforms to proliferative	$8.45 \times 10^{-4}\ \mathrm{kg/m}^3$	[84]
S_0	Nutrient concentration initially and at moving boundary	$3.9 - 9.75 \times 10^{-4}\ \mathrm{kg/m}^3$	[84]
ϕ_{bio0}	Initial water volume fraction in the biofilm	$0.7 - 0.9$	[101]

Table 2.2: Description of model parameters and symbols

We will describe the variables in Fig.2.1 from the bottom up, starting at the lower edge of the implant, progressing through the implant and biofilm, and finally into the bulk fluid. Additionally, we will explain the interactions that affect each variable within its respective medium. We define $C_p(x,t)$ and $C(x,t)$ as the concentrations of the antibiotic within the pores of the implant and the biofilm medium, respectively. Antibiotic molecules may adhere to the pore walls, with the concentration of the bound antibiotic represented by $C_b(x,t)$. The porosity of the whole implant is denoted by ϕ, while the volume fraction of the region occupied by C_b is denoted by ϕ_b. This antibiotic delivery modelling follows a similar approach to that described in [82], with the delivery mechanism structured in accordance with the methods detailed in that article.

Initially, the antibiotic is uniformly distributed within the pores at a concentration C_0. Upon exposure to fluid, the antibiotic dissolves and the thickness of the solid antibiotic layer decreases over time, represented by the moving boundary $-L_1(t)$. For simplicity in the simulation, we assume a negligible initial dissolution of the antibiotic. The presence of fluid in the pores facilitates the diffusion process, as it allows the dissolved antibiotic to be carried out by diffusion. The dynamics of the dissolved antibiotic within the pores is governed by an unsteady reaction-diffusion equation, which incorporates both adsorption and desorption kinetics in the reaction term.

The effective diffusivity, D_e, of the antibiotic in the implant encapsulates several factors affecting diffusion within the porous medium. This relationship is mathematically expressed as:

$$D_e = \frac{\phi_e}{\tau} D_c,$$

where D_c denotes the diffusion coefficient of the antibiotic within the biofilm, ϕ_e represents the effective porosity of the medium and τ is the measure of its tortuosity [32]. Both ϕ_e and τ are dimensionless parameters, and their ratio, ϕ_e/τ, plays a crucial role as a microstructural parameter in the diffusion system. The effective porosity, ϕ_e, refers to the fraction of the overall porosity, ϕ, which contributes to the transport of solutes. It is smaller in scenarios where small pores impede access to the solute, a condition termed as constrictivity. For example, $\phi_e < \phi$ might occur if the smaller pores of the medium are inaccessible to the solute. Tortuosity, τ, accounts for the increased path length that particles traverse due to the intricate pathways within the pores [32]. This parameter offers an additional mechanism to modulate the rate of antibiotic release, influencing the diffusion process by varying the effective path length within the medium.

Assuming a rapid equilibrium between the absorption and desorption processes relative to the diffusion rate, we can establish an equilibrium expression linking the concentrations of free and bound antibiotic. Consequently, the concentration of the bound antibiotic, $C_b(x,t)$, is dependent on the free antibiotic concentration, $C_p(x,t)$, as well as the volume fractions of the bound region, ϕ_b, and the porosity, ϕ. This relationship is governed by the equilibrium dissociation constant K, which quantifies the ratio of the desorption rate to the absorption rate. The antibiotic dissolved in the pores diffuses into the biofilm, thereby modulating the release dynamics.

The antibiotic concentration within the biofilm, $C(x,t)$, is governed by time-dependent advection, diffusion, and the reactions it undergoes. The reaction specifically accounts for the degradation of the antibiotic due to environmental interactions. Within the biofilm, soluble species are transported through the fluid-filled spaces between bacterial cells and EPS. Therefore, the transport of C, is dependent on the water volume fraction, ϕ_{bio}, of the biofilm.

We enforce continuity in antibiotic concentration at the interface between the implant and biofilm medium. We have two distinct boundary conditions of C_p at $x = -L_1(t)$ to capture two scenarios. The first scenario occurs when the interface $-L_1(t)$ is moving through the implant. In this case, we impose a boundary condition where C_p equals the solubility of the antibiotic (C_S) in the biofilm medium at the moving boundary $-L_1(t)$, defining the maximum concentration that can dissolve. This scenario holds until a specific time, denoted as $t_{L_1=L_d}$, when the moving boundary reaches the solid boundary, $-L_d$, which represents the boundary of the implant. The second scenario begins at time $t_{L_1=L_d}$, when the entire antibiotic within the implant is dissolved. From this point onward, a zero-flux condition is applied for C_p at $x = -L_1(t) = -L_d$. The moving boundary between the undissolved and dissolved antibiotic layers in the implant is governed by a Stefan condition, which acts as the boundary condition for C_p. Additionally, a continuity of flux condition is specified at $x = 0$. Together, the Stefan condition and the flux condition at $x = 0$ ensure the conservation of the total antibiotic quantity within the system. At the interface between the biofilm and the bulk fluid ($x = L(t)$), an infinite sink condition is applied for the antibiotic. This results in a rapid depletion of the antibiotic at this boundary, reflecting the scenario where the antibiotic quickly diffuses away into the surrounding fluid, effectively preventing any accumulation of antibiotic at the biofilm edge.

Nutrient transport in the biofilm is facilitated by the bulk fluid. In this thesis, the term "nutrient" refers to essential components such as oxygen, glucose, or other substances that support bacterial growth and biofilm development. This definition of nutrient applies consistently throughout the thesis. Within the biofilm, the concentration of nutrients is dictated by time-dependent advection-reaction-diffusion phenomena.The transport of nutrients, like antibiotic transport, is influenced by the water volume fraction within the biofilm, ϕ_{bio}. The nutrient reaction accounts for nutrient consumption by proliferative bacteria for growth. Given the assumption that biofilm growth does not occur within the porous implant, it is also presumed that nutrients do not penetrate the implant's porous structure. Consequently, a zero-flux boundary condition is imposed at $x = 0$. At the other boundary, $x = L(t)$, a constant influx of nutrients is maintained into the biofilm, which is modelled using a Dirichlet boundary condition.

Following [141], we assume that a biofilm's solid matrix initially has a high water volume fraction. As the biofilm matures, this solid matrix becomes more compact. Observations indicate that the water volume fraction, also known as the porosity of the biofilm, decreases from the surface of the biofilm to the substratum [147]. In our model, ϕ_{bio} is governed by time-dependent advection and reaction processes. These processes quantify how biomass production contributes to volume expansion. The advection component captures the influence of ϕ_{bio} on the velocity changes due to biofilm volume variation, while the reaction aspect describes how biomass production directly drives the biofilm's expansion. At the biofilm-bulk fluid interface, a zero-flux condition for ϕ_{bio} is implemented, which implies that there is no net change in water content at the surface, with porosity driven solely by internal biofilm dynamics. At the implant-biofilm interface, ϕ_{bio} is set to the initial value ϕ_{bio0}, reflecting a stable, unchanged porosity near the solid boundary where biofilm growth is constrained.

Within the biofilm, the bacterial population is classified into proliferative bacteria (B), persister bacteria (B_p), and dead bacteria (B_d). We propose that the biomass can migrate within the biofilm via advection and diffusion, although the movement due to diffusion is significantly slower compared to the diffusion of nutrients and antibiotics. Proliferative bacteria actively consume nutrients to produce biomass and EPS (E). Proliferative bacteria that can enter a dormant state, which is known as the persister phenotype, primarily in response to adverse environmental conditions such as fluctuations in nutrient levels, pH, temperature, and the presence of antibiotics or immune cells, which significantly enhance their antibiotic tolerance. Dead bacteria, on the other hand, no longer contribute to biomass production or other active processes but continue to occupy physical space within the biofilm.

The dynamics of the proliferative bacteria subpopulation are governed by time-dependent advection, diffusion and reactions it undergoes. The reaction accounts for biomass production utilising nutrients, bacterial death influenced by antibiotic concentration and metabolic rate, death in the absence of nutrients, natural mortality, formation of persister cells under specific nutrient thresholds, and the conversion of persisters back to proliferative form contingent on a different nutrient threshold. Since the transport of nutrients and antibiotics depends on the available fluid space of the biofilm, the reaction terms representing the interactions between bacteria and nutrients or antibiotics will depend on the variable ϕ_{bio}.

In our model, antibiotics are assumed to cause cellular damage, which results in cell death when the compromised cells are unable to perform necessary functions. This effect is particularly pronounced in metabolically active cells. Accordingly, the first aspect of antibiotic-induced cell death in our model is influenced by the metabolic activity of the bacteria, which is represented by a Monod-based relationship. To address antibiotic effects in low nutrient environments, we introduce a second component, defined as $\max(\alpha_1 \phi_{bio} C - \alpha_2, 0)B$, which accounts for bacterial adaptation under stress conditions such as low nutrient availability and high cell density. This adaptation involves upregulation of damage repair genes, positing that antibiotic-induced cell death occurs only when the antibiotic concentration exceeds a critical threshold $\alpha_2/\phi_{bio}\alpha_1$, overwhelming the bacterial repair mechanisms. After this threshold, the death rate increases linearly with drug concentration. For model validity, we stipulate $\alpha_1 > 0$ and $\alpha_2 > 0$. In nutrient-rich conditions, both model components influence the bactericidal efficacy of the antibiotic. However, in the absence of nutrients, only the latter component is effective, necessitating higher antibiotic concentrations to achieve a bactericidal effect comparable to that under nutrient-rich conditions. Our approach shares conceptual similarities with the framework presented in [84].

We have also incorporated that the formation of persister bacteria is influenced by the nutrient availability within the biofilm. Specifically, we define two nutrient concentration thresholds, S_1 and S_2, with $S_1 < S_2$. We assume that when nutrient concentrations fall below S_1, the environment is considered nutrient-deficient, prompting proliferative bacteria to transition into a persister state for survival, but not vice versa. In contrast, when nutrient levels increase above S_2, the environment is considered nutrient-sufficient, causing persister bacteria to revert to a proliferative state to resume growth, but not vice versa. For nutrient concentrations between S_1 and S_2, both the formation of persister bacteria from proliferative bacteria and the reversion to a proliferative state are possible. This model of nutrient-dependent persister formation allows us to track patterns of antibiotic resistance within the biofilm.

The dynamics of persister bacteria, dead bacteria, and EPS within the biofilm follows the same kind of phenomena as that of proliferative bacteria. The reaction components for these bacterial phenotypes are designed to align with those that govern proliferative bacteria. EPS formation by proliferative bacteria is driven by nutrient availability, with growth being dependent on the available nutrients in a manner similar to the Monod growth dynamics.

Furthermore, the advective velocity of the biomass, which influences transport and spatial distribution within the biofilm, is determined by a balance of forces and the conservation of volume. As biomass grows at a specific location within the biofilm, it causes a local increase in volume, leading to a movement of the biofilm in the positive direction along the x- axis. As a result, the entire biofilm structure shifts and evolves dynamically in response to changes in biomass production and distribution, affecting both the transport and positioning of these components. The progression of the fluid-biofilm interface, denoted as $x = L(t)$, is governed by the biomass velocity at this interface, integrating the mechanical and biological factors that drive biofilm expansion or contraction. The conservation of volume equation is derived in the same way as [141]. In this model, we assume an incompressible system so that the combined volume fraction of all components in the biofilm—including all bacterial phenotypes, EPS, and water, remains constant and is equal to 1.

The governing equations are designed to focus on the principal dynamics within the biofilm and do not account for bacterial attachment or detachment processes at the interface, which we assume to be in equilibrium and thus negligible for the model's purposes. Additionally, the effects of shear forces and viscosity are omitted from consideration. Given the assumption that there is no biofilm growth within the porous implant, we impose a zero-flux condition for all bacterial phenotypes and EPS at both the biofilm implant and the fluid-biofilm interfaces. Correspondingly, the biomass velocity is set to zero at $x = 0$, reflecting a static boundary at the implant interface.

We account for a range of nutrient concentrations coming from the bulk fluid. Based on [84], the average nutrient range is well-defined. However, to thoroughly examine different scenarios, our model considers three nutrient conditions: nutrient-poor, intermediate, and nutrient-rich. The nutrient-poor scenario uses a value lower than the average range described in [84]. The intermediate condition falls within the average range, and the nutrient-rich condition is set at the higher end of the range. This approach allows us to explore the biofilm's behavior under varying nutrient availability.

Additionally, in our biofilm model, we consider a range of initial conditions for ϕ_{bio} between 0.7 and 0.9. The initial conditions for the bacterial phenotypes and EPS are calculated using the volume constraint equation, applying the relevant initial ϕ_{bio} values. We have opted to use identical initial conditions and diffusion coefficients for proliferative, persister, and dead bacteria, as well as EPS. Biologically, this approach can be justified based on the early homogeneity and diffusion dynamics within biofilms. During the initial stages of biofilm formation, the spatial distribution of bacterial cells and EPS tends to be relatively uniform, making it reasonable to assume similar diffusion properties [118]. The EPS matrix, being a highly hydrated and porous gel, facilitates the movement of similarly sized molecules and particles with minimal variability [109]. Additionally, at the onset of biofilm growth, the concentrations of these components are initially low and fairly homogeneous, which supports the assumption of identical initial conditions. Since the biofilm has not yet undergone significant differentiation or structural complexity, this uniformity aligns with early biofilm development stages [31, 110]. This implies that the effective diffusion coefficients of active, persister, and dead bacteria, as well as EPS, are not substantially different in a way that would critically impact the model's accuracy. By adopting this simplification, we ensure numerical stability and computational efficiency without compromising the biological realism of our model. Thus, our model remains robust, biologically justified, and computationally feasible.

2.2 Simplification strategies

In this section, we explore several strategies to simplify our biofilm growth model in Sec. 2.1, highlighting their biological significance and effects on the model's framework. The aim for these simplifications is to make the model easier to handle while preserving the crucial dynamics of biofilm formation and antibiotic release mechanisms. We examine seven particular simplifications, each addressing distinct facets of the model, and analyse how they alter the system to aid in better analysis and interpretation.

2.2.1 Simplification 1: Constant biofilm porosity

The water volume fraction of the biofilm, ϕ_{bio}, is an important parameter that influences the diffusion of nutrients and antimicrobial agents within the biofilm. In Model 1, ϕ_{bio} is treated as a variable to accurately reflect the heterogeneous and dynamic nature of biofilm porosity.

However, to simplify the model, we assume that

$$\phi_{bio} = \text{constant}.$$

This implies that the biofilm's porosity remains uniform throughout its structure and over time. Biologically, this means that the distribution of EPS and bacterial cells is consistent, leading to uniform diffusion rates and mechanical properties across the biofilm. This simplification makes the model more computationally quicker while maintaining a high degree of accuracy. It allows us to focus on the biofilm's overall behaviour without the added complexity of modelling dynamic porosity changes. The equations governing the variable ϕ_{bio} are thus removed. This approach is particularly relevant for studies aimed at understanding the fundamental dynamics of biofilm growth and development without the intricacies of variable porosity.

2.2.2 Simplification 2: Non-porous implant medium

The effective porosity of the implant medium, ϕ_e, influences the diffusion of antibiotics through the implant medium and is important for modelling how antibiotics are delivered from the implant to the biofilm. A higher ϕ_e indicates more porous medium, facilitating greater diffusion of antibiotics into the biofilm. Conversely, a lower ϕ_e restricts this diffusion, impacting the availability of the antibiotic to the biofilm. For this simplification we assume that

$$\phi_e = 0.$$

So we assume that the implant medium is non-porous, preventing the diffusion of antibiotics through it. Consequently, the rate of change of the thickness of the antibiotic layer within the porous implant medium is zero. This simplification eliminates the need to model the porous implant medium, as the diffusion of antibiotics through it is negligible. The model thus focuses solely on the biofilm medium. The equations governing the implant medium and the antibiotic diffusion in the biofilm within it are removed, simplifying the overall system. It is relevant for studies that aim to isolate the dynamics of the biofilm without considering the complexities of antibiotic delivery from the implant.

2.2.3 Simplification 3: Absence of antibiotic supply

C_0 signifies the availability of antibiotics within the implant that can diffuse into the biofilm. It acts as a reservoir from which antibiotics are supplied to the biofilm environment. For this simplification we assume that

$$C_0 = 0.$$

By setting this condition, we assume that there are no antibiotics present in the biofilm, and there is no supply of antibiotics from the implant. This results in the absence of antibiotic effects on proliferative bacteria within the biofilm. It effectively removes all terms related to antibiotic effects on proliferative bacteria from the model. Without C_0, the biofilm model does not need to account for the dynamics of antibiotic diffusion and its impact on bacterial growth and death. This significantly reduces the complexity of the model by focusing solely on the intrinsic growth and interactions of bacteria within the biofilm, without the added layer of antibiotic influence. This condition is particularly important in scenarios where the antibiotic effect is negligible or can be ignored, such as in early stages of biofilm formation before antibiotic treatment is initiated, or in studies aiming to understand the natural growth dynamics of biofilms without external influences. It is also useful in preliminary studies to establish a baseline model of biofilm behavior, which can later be refined by including antibiotic effects. This makes the model more tractable and computationally efficient, providing a clear focus on the natural growth and interactions within the biofilm.

2.2.4 Simplification 4: Constant phenotypic transition rates

In Model 1 described in Sec. 2.1, S_1 and S_2 define critical nutrient levels that influence bacterial state changes. When nutrient concentration is very low (below S_1), bacteria enter a persister state to survive harsh conditions. When nutrient concentration is high (above S_2), persister bacteria revert to a proliferative state to take advantage of the favourable environment. In the intermediate range, both proliferative and persister states coexist, with transitions influenced by the current nutrient levels. For this simplification we assume

$$S_1 \to -\infty,$$

$$S_2 \to \infty.$$

This implies that the nutrient concentration does not affect the state transitions between proliferative and persister bacteria. The transitions occur continuously and uniformly, regardless of the nutrient availability. This simplification is relevant in situations where nutrient concentrations are not key determinants of bacterial state changes, such as in settings with variable or consistently low/high nutrient levels. It is also useful for studies focusing on intrinsic bacterial behavior rather than environmental influences. It provides a baseline model that focuses on the intrinsic rates of state transitions, which can later be refined to include nutrient dependency if needed.

2.2.5 Simplification 5: Negligible persister bacteria population

In Model 1, k_F and k_R are rate constants that describe the formation and transformation of bacterial states. These parameters are crucial for modelling the dynamic transitions between different bacterial states within the biofilm. k_F represents the frequency at which actively growing proliferative bacteria switch to a dormant persister state. Persister cells are a subpopulation of bacteria that are highly tolerant to antibiotics and environmental stresses. k_R, on the other hand, indicates how often these persister cells revert back to a proliferative state. These transitions are important for understanding strategies for bacterial survival and resilience within the biofilm. In this simplification we assume both of these parameters tends to zero.

$$k_F = 0,$$

$$k_R = 0.$$

This means we assume that the rates of transition between persister and proliferative states are zero and can be ignored. This simplification eliminates the equations and terms related to the transitions between persister and proliferative states. The model no longer needs to account for the formation of persister cells from proliferative ones or the reverse process, thereby reducing the number of variables and simplifying the system's overall dynamics. It allows for a more straightforward analysis of biofilm growth and behavior by focusing on the predominant bacterial state without the added complexity of persister-proliferative dynamics. It facilitates quicker computational simulations and provides a clear baseline model that can be later expanded to include state transitions if more detailed analysis is required. It can be applied in studies where the impact of persister cells on the overall system dynamics is minimal or when a preliminary understanding of biofilm behavior is desired without the complexity of state transitions.

2.2.6 Simplification 6: Standardised conversion factors for metabolic rates

In Model 1, k_B and k_E are conversion factors that represent the efficiency of converting metabolic rate into biomass production and EPS production, respectively. These factors are defined as:

$$k_B = 0.21 \times \frac{k_s + S_0}{\mu \times S_0},$$

$$k_E = k_B.$$

Here, k_s is the nutrient consumption half-saturation constant, S_0 is the constant nutrient concentration coming from the bulk fluid, and μ is the maximal nutrient consumption rate. Biologically, k_B indicates how efficiently nutrients are used to produce biomass, while k_E shows how effectively nutrients are used to produce EPS, which is crucial for biofilm structure. The simplification sets both k_B and k_E to 1:

$$k_B = 1,$$

$$k_E = 1.$$

We indicate that the conversion of the metabolic rate to the biomass or EPS production rate is uniform and does not vary with the concentration of nutrients or metabolic rates. This standardisation implies that every unit of metabolic activity results in an equivalent and constant amount of biomass or EPS, simplifying the relationship. This simplification of k_B and k_E reduces the complexity of the model, making it easier to solve analytically or numerically. It is crucial in scenarios where detailed nutrient dynamics are not the primary focus. It is useful for preliminary studies, where understanding the general behaviour of the system is more critical than capturing every detail. In addition, it facilitates faster computational analysis, allowing researchers to gain insight without the computational burden of more complex models. This simplification provides a baseline model that can be refined later with more detailed parameters if necessary.

2.2.7 Simplification 7: Insufficient antibiotic concentration

In Model 1, $\max(\alpha_1 C - \alpha_2, 0)$ represents the death rate of proliferative bacteria due to the antibiotic. the term $\alpha_1 C$ represents the rate at which the antibiotic is effective in killing the bacteria, and α_2 is the threshold concentration below which the antibiotic has no effect. When α_2 is very large, the death term $\max(\alpha_1 C - \alpha_2, 0)$ is zero, indicating that the antibiotic concentration is not sufficient to cause bacterial death. This mechanism is crucial for modelling how bacteria survive under low antibiotic concentrations, leveraging stress response mechanisms. This simplification sets

$$\alpha_2 \to \infty.$$

Under these circumstances, the antibiotic-induced death term for proliferative bacteria $\max(\alpha_1 C - \alpha_2, 0)$ is removed. This implies that the concentration of antibiotics within the biofilm is not high enough to kill bacteria. This mirrors a situation where bacteria can survive the presence of antibiotics by up-regulating genes responsible for damage repair and other stress response mechanisms, thus preventing lethal damage. It eliminates the antibiotic-related death term for low-nutrient environment from the equations that govern the dynamics of proliferative bacteria. As a result, the model emphasises bacterial growth and survival without accounting for the deadly effects of antibiotics at low concentrations. It reflects the antibiotic's effects on metabolic processes driven by nutrient consumption. This simplifies the model by eliminating the need to determine the antibiotic-induced death rate under these conditions. This is particularly appropriate in scenarios where the antibiotic and nutrient concentration is anticipated to be low, such as during the initial phases of treatment or in contexts where antibiotics diffuse slowly into the biofilm. It is also significant in research aimed at understanding bacterial survival strategies under sub-lethal antibiotic conditions in low nutrient environment.

2.3 Transformation of models based on the simplifications

In this section, we explain how each simplification step transforms Model 1 into various simplified models. This progressive simplification will ultimately lead to the simplest model, which retains essential characteristics while being more manageable and computationally efficient. Fig. 2.2 shows the sequential application of the simplifications, leading to different models. We will describe each simplified model and elaborate on the biological relevance and practical importance.

Model 2: Cosidering constant biofilm porosity

By applying Simplification 1 to Model 1, we solve the comprehensive model using a constant ϕ_{bio}. This model solves for the same variables as Model 1, except for ϕ_{bio}. The study with constant water volume fraction has been validated in various studies [84, 140]. We have conducted comparisons between models with variable and constant ϕ_{bio}. Our results indicate that key biofilm characteristics, such as biofilm thickness, biomass velocity, and temporal and spatial changes of proliferative bacteria, exhibit similar qualitative behaviour in both models. Additionally, our analysis shows that ϕ_{bio} remains nearly constant over time and space in the variable ϕ_{bio} model. Therefore, we can reasonably adopt this simplification without significant loss of accuracy. Detailed comparisons supporting this conclusion can be found in Appendix. A.

Model 3: Removing implant medium

Applying Simplification 2, which is setting the effective porosity of the implant as zero in Model 2, we only solve the model applicable in the biofilm medium. According to Sec. 2.2.2, this simplification lets us presume that the implant medium is solid, rendering the antibiotic diffusion within the implant insignificant, and thus eliminating the need to model the implant's porous medium. The resulting model variables are B, B_p, B_d, E, S, C, v and L. Despite the lack of antibiotic diffusion from the implant, we aim to observe the antibiotic's impact on biofilm growth and behavior. Therefore, we assume a constant antibiotic flux with concentration C_0 at the implant-biofilm interface. This is represented by a Dirichlet boundary condition for C at $x = 0$. This model studies the effects of antibiotic without considering the complexities of the implant medium.

Model 4: Eliminating antibiotic concentration

Now we apply Simplification 3 in Model 3, assuming there are no antibiotics present in the biofilm and no continuous supply of antibiotics from the implant. We end up with a model that

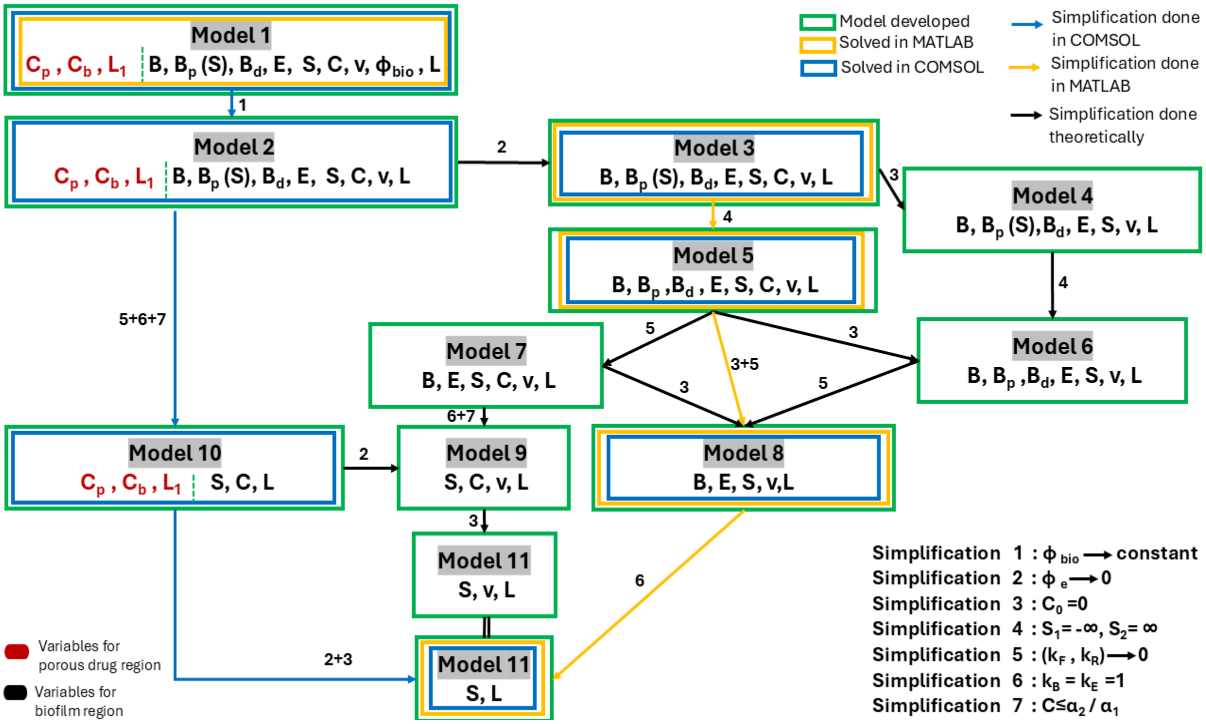

Figure 2.2: Overview of simplification strategies for the mathematical models. This figure depicts the different simplification strategies (1 through 7) applied to Model 1, which includes variables for both the porous antibiotic region (in red) and the biofilm region (in black). The flow of simplifications is represented by arrows: COMSOL implementations in blue arrows, MATLAB implementations in yellow arrows, and theoretical simplifications in black arrows. Each box outlines the variables retained after each simplification step. The diagram also differentiates between the model developed (green boxes), simulations done in MATLAB (yellow highlighted), and those in COMSOL (blue highlighted).

does not account for any effect that arises from antibiotics. Hence we can ignore the antibiotic equation and the antibiotic effectiveness terms from the proliferative bacteria equation. This model with variables B, B_p, B_d, E, S, v and L focuses solely on the biofilm dynamics excluding the influence of the antibiotic.

Model 5: Making the phenotype transitions nutrient-independent

From Model 3, we can develop another simplified model by applying the Simplification 4. This assumption enables the phenotypic transition between proliferative and persister states to be independent of nutrient levels. This model will account for the same variables as Model 2, excluding the parameters S_1 and S_2. This model lets us study biofilm behavior and antibiotic effects with a constant antibiotic supply, without focusing on resistance due to lack of nutrients. The use of a similar model in [84] indicates that this approach aligns with established methodologies in the field, reinforcing the validity of our simplification.

Model 6: Eliminating environmental stresses

This model studies the fundamental biofilm characteristics without considering any antibiotic or nutrient effects. We developed this model by applying Simplification 3 in Model 5 or Simplification 4 in Model 4. In this model, we assume a non-antibiotic environment for the biofilm, where the rates of phenotypic changes remain constant. We solve for the same variables as in Model 4, focusing primarily on biofilm growth and incorporating key microbial characteristics such as nutrient consumption, natural death, and EPS production.

Model 7: Removing phenotypic transitions

Now we apply Simplification 5 in Model 5 and set the rates of the phenotypic transition between proliferative and persister as zero. This develops a model with variables B, E, S, C, v, and L. The main focus of this model is to understand how antibiotic is affecting the proliferative bacteria hence affecting the biofilm growth. It is important to mention that this simplification gets rid of the persister equation. Additionally, we omit the dead bacteria equation for simplicity, but we still account for the terms in the proliferative bacteria equation that lead to dead bacteria within the v equation, which is derived from the continuity of volume.

Model 8: Simplest model considering bacteria and EPS formation

It is clear that the next step would be to remove effects of antibiotic from Model 7. This model only solves for B, E, S, v and L, and focuses solely on biofilm growth, while still considering the phenomena of bacteria growth and EPS formation. This model can be developed by applying Simplification 3 in Model 7 or Simplification 5 in Model 6.

Model 9: Standardising metabolic rates and antibiotic effects

Using Simplifications 6 and 7 in Model 7, we standardise the conversion factors for the metabolic rate to the production rate and eliminate the antibiotic-induced death term in low nutrient conditions. This model considers the biomass formation using nutrient concentration with a simple Monod term. The antibiotics are assumed to cause cellular damage, which results in cell death when the compromised cells are unable to perform necessary functions. This effect is only seen in metabolically active cells, assuming that cells in low nutrient environments are immune to antibiotic effects. This model only solves for S, C, v, and L. The biomass growth and death are considered in the L equation, which makes it possible to eliminate the extra equations for bacteria and EPS. This model provides a bird's-eye view of the effects of antibiotics on biofilm growth in a simplified environment, capturing only the essential characteristics of the biofilm.

Model 10: Simplest biofilm growth model considering both biofilm and implant media

This model has a similar implant model as Model 2 while having a similar biofilm model as Model 9. We can develop this model by applying the following adjustments to Model 2: setting phenotypic transition rates to zero using Simplification 5, standardising metabolic rates using Simplification 6, and removing antibiotic-induced death in low nutrient environments using Simplification 7. By setting the implant medium as solid using Simplification 2, we can revert to Model 9. This model solves for the variables C_p, C_b, L_1, S, C, v and L. This model primarily aims to understand the effects of antibiotics on biofilm growth in a realistic scenario, while considering a simplified biofilm environment.

Model 11: Simplest biofilm growth model without antibiotic

The simplest model for understanding biofilm growth considers only the Monod term for biomass production and the diffusion term for transport of nutrient. This model can be achieved by either eliminating antibiotic concentration from Model 9 using simplification 3, standardising metabolic rates in Model 8 with simplification 6, or setting the implant medium as solid and assuming a no-antibiotic environment in Model 10 through simplifications 2 and 3. This model, with variables S and L, focuses solely on the essential interactions driving biofilm growth. It offers a highly tractable and computationally efficient framework, serving as a baseline for more detailed studies. This model has been used and validated in [2], confirming its practicality.

2.4 Summary

In this chapter, we systematically simplified an 1D biofilm growth model to make it more manageable while retaining its essential characteristics. Starting with a detailed model that includes antibiotic diffusion, bacterial growth, EPS production, and state transitions within bacterial phenotypes, we applied a series of simplifications to progressively streamline the model. We first established the complex model, capturing the dynamics and interactions of various bacterial phenotypes, nutrient conditions and antibiotic release from a polymer-free porous implant. Through each subsequent simplification, we reduced the complexity of the model by making key assumptions and removing less critical components. This process allowed us to isolate the fundamental behaviors of biofilm growth and antibiotic resistance while simplifying computational requirements. The transformations were guided by specific simplifications such as constant biofilm porosity, negligible antibiotic diffusion through the implant, the absence of antibiotics, constant rates of phenotypic transitions, and standardising metabolic rate conversion factors. Each step in the simplification process was carefully detailed, emphasising the biological reasoning and the implications for the model. A key contribution of this chapter is the formulation of the modular framework that connects mechanistic biofilm features to a hierarchy of reduced models, enabling targeted analysis of specific biological processes. By reducing the complexity of the initial model, we could concentrate on the key interactions between bacteria and nutrients in the biofilm using the most basic biofilm growth model. These models provided valuable insights into biofilm dynamics and antibiotic effectiveness, showing the balance between retaining essential features and ensuring computational efficiency.

Chapter 3

Biofilm growth models in a non-antibiotic environment

In the previous chapter, we considered various simplifications of a complex biofilm model while retaining key elements necessary to accurately represent biofilm dynamics. Building on that, this chapter focusses on two one-dimensional biofilm growth models, Models 11 and 8 from Chapter 2, studied in non-antibiotic environments. These models provide a baseline for understanding biofilm growth on medical implants before, in subsequent chapters, we consider antibiotic effects. They address nutrient transport, biomass growth, and biofilm detachment, providing a framework for studying biofilm development in a controlled setting. This foundation is essential for future investigations that involve antibiotic interactions.

The first simplified model in this chapter, Model 11, focusses on the diffusion of nutrients, the accumulation of biomass, and detachment, to understand how these factors influence the growth rate and thickness of biofilms. The second model, Model 8, introduces bacterial proliferation and EPS production, allowing us to study both biofilm structure and composition. These models are crucial in investigating different aspects of biofilm growth. They are capable of producing spatial and temporal behaviour of biofilm growth and composition, allowing us to analyse key factors that drive biofilm development. Model 11 helps us understand how the consumption of nutrients affects overall biofilm growth, while Model 8 offers information on the internal structure and composition of the biofilm, such as the distribution of bacteria and EPS. The main novelty of this chapter is the focused sensitivity analysis of these simplified models under antibiotic-free conditions, which reveals how nutrient availability, death and detachment rates, and EPS dynamics independently shape biofilm growth and structure—without the confounding influence of antibiotics. This detailed baseline characterisation not only clarifies the independent roles of biological mechanisms but also creates a reference framework against which the effects of antibiotics can later be isolated and interpreted. By studying these two models, we obtain a foundational understanding of both biofilm expansion and composition, which is essential for future complex modelling to optimise interventions such as antibiotic delivery.

Outline

The chapter begins with the simplest biofilm growth model, Model 11, describing growth under non-antibiotic conditions with a focus on nutrient diffusion and biomass accumulation. The model equations, boundary conditions, and initial conditions are presented. The model is non-dimensionalised with numerical solutions obtained using MATLAB®version:23.2.0 (R2023b) (MATLAB). It is also linearised to obtain analytical solutions. The sensitivity analysis from the numerical solution explores how variations in key parameters, such as bacterial death rate, detachment rate, nutrient concentration, and initial biofilm thickness, affect biofilm growth. A comparison between the numerical and analytical solutions is also conducted. The second model, Model 8, is then introduced, building on Model 11 by incorporating EPS formation and unsteady bacterial growth. This model also includes advection within the biofilm, driven by changes in the volume fractions of bacterial and EPS. The sensitivity to nutrient diffusion coefficients and consumption rates is examined to assess their impact on biofilm growth and structure. The methodology for obtaining solutions for both models is described in detail.

3.1 Simplest biofilm growth model (Model 11)

This section examines a fundamental biofilm growth model, focussing on nutrient consumption and biomass production, referred to as Model 11. The governing equations are non-dimensionalised, and solved numerically. The model is also linearised and is solved analytically. The numerical solutions of the model and the analytical solutions of the linearised model are compared, and sensitivity analysis is performed to explore how key parameters, such as the bacterial death rate, detachment rate, nutrient concentration, and initial biofilm thickness, influence biofilm growth.

3.1.1 Model development

This model focusses on the transport of nutrients within the biofilm and their uptake from the bulk fluid at the biofilm-fluid interface. Nutrient transport is modelled using Fickian diffusion. The consumption of nutrients by biomass is governed by Monod kinetics, where the resulting biomass production contributes to an increase in biofilm thickness [2]. This Monod term is also multiplied by a ratio of the maximum biomass density to the yield coefficient. The maximum biomass density represents the upper limit of biomass that can be sustained within the biofilm, reflecting the real-world constraints of physical space, nutrient availability, and waste accumulation that prevent indefinite growth. This parameter ensures that the model accurately captures the biofilm's carrying capacity. Similarly, the yield coefficient is essential to represent the efficiency of the conversion of nutrients into biomass, recognising that not all nutrients consumed directly contribute to growth, as some are used for maintenance and cellular processes. Together, these parameters ensure that the model realistically depicts the balance between nutrient availability, biomass production, and environmental limitations. A commonly employed time-scale argument in biofilm modelling [68, 139] enables us to assume that the nutrient equation is in a quasi-steady state in this model.

Assuming that biofilm growth does not occur within the porous implant and that nutrients do not penetrate the porous structure of the implant, a no-flux boundary condition is imposed at $x = 0$. This assumption is reasonable, as the nutrient supply is quickly consumed by the bacteria, leaving little nutrient available at the biofilm-bulk fluid boundary. Moreover this approach aligns with that of [2], who implemented similar boundary conditions in their work. However, we acknowledge that this may not fully represent all implant-biofilm interactions in reality. For the purposes of this study, this assumption provides a tractable model. At the biofilm-bulk fluid interface $x = L(t)$, a constant influx of nutrients is maintained, modelled using a Dirichlet boundary condition, assuming that external mass transfer resistance is negligible, as outlined in [2]. This assumption reflects a scenario where nutrients are readily available at the interface, which makes it a realistic representation for systems where nutrient supply is abundant and is not limited by external transport constraints. This boundary condition enables us to focus on internal nutrient dynamics within the biofilm. This concept of nutrient boundary conditions is maintained throughout the thesis.

The growth of biomass within the biofilm is implicitly modelled through the nutrient consumption dynamics described above. There are no separate equations specifically governing biomass growth; instead, changes in biomass are captured by the evolution of biomass velocity, which is driven by nutrient uptake according to Monod kinetics. The increase in biofilm thickness occurs as a result of this nutrient-driven biomass production, while biomass loss is accounted for through detachment in the biofilm-bulk fluid interface and natural death processes.

The detachment rate increases proportionally with the thickness of the biofilm. This approach has become widely accepted as the standard for modelling detachment processes. Originally proposed by [128], it has been widely applied in various studies, including [24, 139, 140]. By incorporating these elements into the biomass velocity equation, the model accounts for the dynamic balance between nutrient consumption, biomass growth, natural death, and detachment. The interaction between these factors ultimately determines the evolution of the thickness of the biofilm.

3.1.2 Governing equations

Now, we will introduce and derive the key equations that form the foundation of the model's dynamics. We begin by focussing on the transport of nutrients within the biofilm medium and then progress to describe the biofilm growth dynamics. Each equation is accompanied by relevant boundary conditions to comprehensively define the system.

Throughout this thesis, the notation involving a variable or function followed by a subscript using the independent variables, refers to partial derivatives. Specifically, if a variable is followed by a subscript and x (e.g., S_x), it represents the first partial derivative with respect to x, i.e., $\frac{\partial S}{\partial x}$. Similarly, when a variable is followed by an subscript and xx (e.g., S_{xx}), it denotes the second partial derivative with respect to x, i.e., $\frac{\partial^2 S}{\partial x^2}$. Furthermore, a variable followed by a subscript and t (e.g., S_t) represents the partial derivative with respect to time, i.e., $\frac{\partial S}{\partial t}$. These conventions are applied consistently throughout the thesis for clarity in the mathematical formulation.

In this model, the nutrient dynamics within the biofilm is modelled using an equation that balances diffusion and reaction terms, which captures the changes in nutrient concentration as a result of both diffusion and consumption by biomass [2]. The governing equation for nutrient dynamics is expressed as:

$$D_S S_{xx} = \frac{X_\infty}{\gamma_{bio}} \mu_b \left(\frac{S}{k_S + S} \right), \quad 0 < x < L(t),\ t > 0. \tag{3.1}$$

Here D_S is the nutrient diffusion coefficient. The right-hand side of the equation represents nutrient consumption by the biomass. Here, X_∞ is the maximum biomass density, and γ_{bio} is the yield coefficient that relates biomass growth to nutrient consumption. The Monod term $\mu_b \frac{S}{k_S+S}$ models the growth of the biomass, where μ_b is the maximum specific growth rate of the bacteria, and k_S is the half-saturation constant. Upon consumption of the nutrient by the biomass, the biofilm grows and the biofilm boundary, at $L(t)$, moves with a velocity that is determined by integrating the nutrient-dependent biomass growth rate minus the death rate, b, over the extent of the biofilm

$$v = \int_0^L \left[\mu_b \left(\frac{S}{k_S + S} \right) - b \right] dx.$$

Thus, the expansion of biofilm by taking into account the growth, death and detachment process may be written as

$$\frac{dL}{dt} = \int_0^L \left[\mu_b \left(\frac{S}{k_S + S} \right) - b \right] dx - \sigma L^2, \quad t > 0, \tag{3.2}$$

where σL^2 represents a quadratic detachment term, modelling the detachment of biofilm as a function of its thickness.

Initial and boundary conditions

The initial biofilm thickness is

$$L(0) = L_0. \tag{3.3}$$

At the implant-biofilm interface ($x = 0$), the zero-flux condition is imposed and at the biofilm-bulk fluid interface ($x = L(t)$) a Dirichlet's boundary condition is assumed:

$$-D_S S_x = 0, \quad \text{at}\, x = 0,\, t > 0, \tag{3.4}$$

$$S = S_0, \quad \text{at}\, x = L(t),\, t > 0. \tag{3.5}$$

The description and values of the parameters are given in Table 2.2 and the description of the variables are given in Table 2.1.

3.1.3 Non-dimensionalisation

Non-dimensionalisation is a common technique in mathematical modelling that simplifies the governing equations by reducing the number of parameters. For complex systems like biofilm model, non-dimensionalisation is particularly valuable as it helps to isolate the dominant processes, like for this model the interactions between nutrient transport, growth, death, and detachment without the complications of unit-specific parameters. Non-dimensionalisation is applied to every model discussed in this thesis. We employ the following non-dimensionlisation for Model 11:

$$\overline{S} = \frac{S}{k_S}, \quad \overline{x} = \frac{x}{M}, \quad \overline{L} = \frac{L}{M}, \quad \overline{t} = \mu_b t,$$

where $M = \sqrt{\frac{D_S \gamma_{bio} k_S}{\mu_b X_\infty}}$. The parameter M serves as a characteristic length scale for the biofilm system, combining several factors of the biofilm. It provides a measure of the spatial extent over which nutrient dynamics and biofilm growth are balanced. This particular non-dimensionalisation was selected to reduce the number of parameters in the governing equations. Additionally, it highlights important non-dimensional parameters, which represent the ratios of key biological and physical processes, such as bacterial death relative to growth and bacterial detachment relative to growth.

Using the above non-dimensionalisation, equations (3.1) and (3.2) take the following non-dimensional forms

$$\overline{S}_{\overline{x}\overline{x}} = \frac{\overline{S}}{1+\overline{S}}, \quad 0 < \overline{x} < \overline{L}(\overline{t}),\, \overline{t} > 0, \tag{3.6}$$

$$\frac{d\overline{L}}{d\overline{t}} = \int_0^{\overline{L}} \left(\frac{\overline{S}}{1+\overline{S}} - \varepsilon_1 \right) d\overline{x} - \varepsilon_2 \overline{L}^2, \quad \overline{t} > 0, \tag{3.7}$$

where $\varepsilon_1 = \frac{b}{\mu_b}$ and $\varepsilon_2 = \frac{\sigma M}{\mu_b}$. After non-dimensionalisation, these two parameters are the only parameters appearing in the governing equations, significantly simplifying the system. The parameter ε_1 represents the ratio of the bacterial death rate to the bacterial growth rate and the parameter ε_2 represents the ratio of the bacterial detachment rate to the growth rate.

Using equation (3.6), equation (3.7) can be written as

$$\frac{d\overline{L}}{d\overline{t}} = \left[\frac{\partial \overline{S}}{\partial \overline{x}}\right]_0^{\overline{L}} - \varepsilon_1 \overline{L} - \varepsilon_2 \overline{L}^2, \quad t > 0. \tag{3.8}$$

The non-dimensional initial condition for biofilm thickness is

$$\overline{L}(0) \;=\; \varepsilon_3, \tag{3.9}$$

where $\varepsilon_3 = \frac{L_0}{M}$. This parameter represents the initial biofilm thickness normalised by the characteristic length scale M, indicating the relative size of the initial biofilm compared to the typical length scale of the system.

The boundary conditions (3.4)-(3.5) have their respective dimensionless forms as

$$\overline{S}_{\overline{x}} \;=\; 0, \quad \text{at } \; \overline{x} = 0, \, \overline{t} > 0, \tag{3.10}$$

$$\overline{S} \;=\; \overline{S}_0, \quad \text{at } \; \overline{x} = \overline{L}(\overline{t}), \, \overline{t} > 0, \tag{3.11}$$

where $\overline{S}_0 = \frac{S_0}{k_S}$.

3.1.4 Linearisation of the model

In this section, we explore the linearisation of the model under two distinct scenarios defined by the concentration of nutrients within the biofilm: when the dimensionless nutrient concentration $\overline{S}$ is much smaller than 1 ($\overline{S} \ll 1$) and when $\overline{S}$ is much greater than 1 ($\overline{S} \gg 1$). Linearisation allows us to simplify the model equations and make analytical solutions more tractable.

Case I: $\overline{S} \ll 1$

In the first case, we consider the situation where the dimensionless nutrient concentration $\overline{S}$ is much smaller than 1. This condition implies that the concentration of nutrients within the biofilm is significantly lower than the half-saturation constant k_S. Under these circumstances, we can assume that $\overline{S}_0$, is also much smaller than 1.

By applying the Taylor series expansion we get

$$\frac{\overline{S}}{1+\overline{S}} \sim \overline{S}.$$

This leads to a reduction in the complexity of the original equation (3.6), which now becomes

$$\frac{\partial^2 \overline{S}}{\partial \overline{x}^2} \sim \overline{S}. \tag{3.12}$$

To solve this equation, we apply the relevant boundary conditions (3.10) - (3.11), leading to the expression for the nutrient concentration in the biofilm

$$\overline{S} = A(e^{\overline{x}} + e^{-\overline{x}}), \tag{3.13}$$

where $A = \left(\frac{\overline{S}_0 e^{\overline{L}}}{e^{2\overline{L}}+1}\right)$.

Next, we substitute the linearised expression for $\overline{S}$ in the equation governing the thickness of the biofilm (3.8). The resulting equation is

$$\frac{d\overline{L}}{d\overline{t}} = \int_0^{\overline{L}} A(e^{\overline{x}} + e^{-\overline{x}})d\overline{x} - \varepsilon_1\overline{L} - \varepsilon_2\overline{L}^2.$$

After integrating and simplifying, this equation takes the form

$$\frac{d\overline{L}}{d\overline{t}} = \overline{S}_0 \frac{e^{2\overline{L}}-1}{e^{2\overline{L}}+1} - \overline{L}\left(\varepsilon_1 + \varepsilon_2\overline{L}\right). \tag{3.14}$$

This ordinary differential equation is non-linear and does not have a straightforward analytical solution, necessitating numerical methods to solve it.

To further simplify the analysis, we linearise this equation under the assumption that $\overline{L} \ll 1$ (i.e., $L < M$). Applying a series expansion in this regime, we obtain

$$\frac{d\overline{L}}{d\overline{t}} \approx \overline{L}\left(\overline{S}_0 - \varepsilon_1 - \varepsilon_2\overline{L}\right). \tag{3.15}$$

The solution to the above differential equation is

$$\overline{L} = \frac{(\overline{S}_0 - \varepsilon_1)\varepsilon_3}{(\overline{S}_0 - \varepsilon_1 - \varepsilon_2\varepsilon_3)e^{-(\overline{S}_0-\varepsilon_1)\varepsilon_2\overline{t}} + \varepsilon_2\varepsilon_3}. \tag{3.16}$$

This solution describes the evolution of biofilm thickness over time in the regime where the biofilm is thin. For $\overline{L} \ll 1$, it is crucial that ε_3 is also much smaller than 1.

We also consider the opposite scenario within Case I, where the biofilm thickness is much larger than M ($\overline{L} \gg 1$). Here, we simplify the equation by considering the asymptotic behaviour of the first term on the right-hand side of equation (3.14) for large L. This simplification is performed to reduce the equation into a more analytically tractable form. In this regime, the differential equation simplifies to

$$\frac{d\overline{L}}{d\overline{t}} = \overline{S}_0 - \overline{L}\left(\varepsilon_1 + \varepsilon_2\overline{L}\right). \tag{3.17}$$

The solution in this case is

$$\overline{L} = \frac{r_1 - \left(\frac{r_1-\varepsilon_3}{r_2-\varepsilon_3}\right) r_2 e^{-\varepsilon_2(r_1-r_2)\overline{t}}}{1 - \left(\frac{r_1-\varepsilon_3}{r_2-\varepsilon_3}\right) e^{-\varepsilon_2(r_1-r_2)\overline{t}}}, \tag{3.18}$$

where the constants r_1 and r_2 are defined as $r_{1,2} = \frac{-\varepsilon_1 \pm \sqrt{\varepsilon_1^2 + 4\varepsilon_2 \overline{S}_0}}{2\varepsilon_2}$. This equation remains positive for all values of $\bar{t}$, given our set of parameters, and provides information on the growth dynamics of a thick biofilm.

For $\overline{L}$ to exist and remain positive and large in the thick biofilm scenario, the time $\bar{t}$ must satisfy the condition $\bar{t} > \frac{1}{\varepsilon_2(r_1 - r_2)} \ln\left(\frac{r_1(r_2 - \varepsilon_3)}{r_2(r_1 - \varepsilon_3)}\right)$. In our specific case, this simplifies to $\bar{t} > 0.00687$, which can be practically approximated as $\bar{t} > 0$.

Case II: $\overline{S} \gg 1$

The second case examines the scenario where the dimensionless nutrient concentration $\overline{S}$ is much greater than 1, indicating that the nutrient concentration within the biofilm is significantly higher than the half-saturation constant k_S. In this high-nutrient regime, using the asymptotic limit $\overline{S} \to \infty$, we have

$$\frac{\overline{S}}{1 + \overline{S}} \sim 1.$$

Consequently, equation (3.6) simplifies to

$$\frac{\partial^2 \overline{S}}{\partial \bar{x}^2} \sim 1. \tag{3.19}$$

Upon solving this equation and applying the boundary conditions (3.10) - (3.11), we arrive at the expression for the nutrient concentration profile

$$\overline{S} = \frac{1}{2}(\bar{x}^2 - \overline{L}^2) + \overline{S}_0. \tag{3.20}$$

This solution reflects the parabolic distribution of nutrients within the biofilm, with the constant $\overline{S}_0$ shifting the profile.

Subsequently, the equation governing biofilm growth, when linearised under these conditions, transforms into

$$\frac{d\overline{L}}{d\bar{t}} = \int_0^{\overline{L}} (1 - \varepsilon_1)\, d\bar{x} - \varepsilon_2 \overline{L}^2. \tag{3.21}$$

Solving this yields

$$\overline{L} = \frac{(1 - \varepsilon_1)\frac{\varepsilon_3}{(1-\varepsilon_1) - \varepsilon_2\varepsilon_3}}{e^{(\varepsilon_1 - 1)\bar{t}} + \frac{\varepsilon_2\varepsilon_3}{(1-\varepsilon_1) - \varepsilon_2\varepsilon_3}}. \tag{3.22}$$

In this case, when $\varepsilon_1 - 1 < 0$, or equivalently $b < \mu_b$, the death rate of the bacteria is less than the growth rate. As time progresses ($\bar{t} \to \infty$), the biofilm thickness asymptotically approaches $\overline{L}_{\max} = \frac{(1-\varepsilon_1)}{\varepsilon_2}$, indicating a maximum sustainable thickness for the biofilm.

Conversely, if $\varepsilon_1 - 1 > 0$, meaning $b > \mu_b$, the bacterial death rate exceeds the growth rate, leading to a scenario in which, as $\bar{t} \to \infty$, the biofilm thickness $\overline{L}$ tends towards zero, ultimately resulting in the disappearance of the biofilm. For the parameter set under consideration, the solution to equation (3.22) remains positive for any value of $\bar{t}$, ensuring the physical validity of the model.

3.1.5 Numerical solution methodology

The model equations (3.6) and (3.7), along with the initial and boundary conditions (3.9)-(3.11), are solved using the Forward Euler method. At each time step, the biofilm thickness and the nutrient concentration are updated sequentially based on their values from the previous time step. This process is iterated until the solution converges within a specified tolerance. For quantitative analysis, the model is solved using MATLAB. The equation governing biofilm thickness is solved using the explicit Euler method. This method was chosen primarily for its simplicity and ease of implementation, given the straightforward nature of the model. We tested its accuracy and stability and found that it gave reliable results for the cases we considered. Since the method worked well, there was no need to use more complicated approaches. The boundary value problem for nutrient transport within the biofilm is solved numerically using MATLAB's `bvp4c` routine. This solver is specifically designed for the numerical solution of boundary value problems and is based on a collocation method. More precisely, `bvp4c` implements the 3-stage Lobatto IIIa formula, a collocation scheme that yields a fourth-order accurate, continuously differentiable (C^1-continuous) solution over the entire integration interval [79]. The collocation technique discretises the domain by introducing a mesh of points, dividing the interval into subintervals. On each subinterval, the method constructs a polynomial approximation that satisfies both the differential equation and the boundary conditions. The resulting global system of algebraic equations, derived from collocation and boundary constraints, is solved to obtain the numerical solution. The solver estimates the residual (error) of the continuous solution and uses this estimate to adaptively refine the mesh if the local error exceeds the specified tolerance. This adaptive mesh refinement, along with built-in error control, enhances the stability and accuracy of the solution. To initiate the procedure, the user must supply an initial guess for the solution and an initial mesh. `bvp4c` then iteratively refines both until the solution meets the desired accuracy.

3.1.6 Results and discussions

The values (rounded to 3 d.p.) of the dimensionless parameters are: $\varepsilon_1 = \frac{b}{\mu_b} = 0.173$, $\varepsilon_2 = \frac{\sigma M}{\mu_b} = 0.001$, $\varepsilon_3 = \frac{L_0}{M} = 0.007$ and $\overline{S}_0 = \frac{S_0}{K_{bio}} = 1.1$. The values of the non-dimensional parameters are calculated from the baseline values stated in Table 2.2. In order to understand the growth and characteristics of the biofilm, we performed a sensitivity analysis based on the numerical solution to examine how variations in the parameters ε_1, ε_2, ε_3, and $\overline{S}_0$ affect the behaviour of the system. From this point onwards, we have omitted the overlines for non-dimensionalised parameters in the figures to enhance the clarity. All the plots are for 10 days, which corresponds to a non-dimensional time of 60.

Sensitivity analysis

Fig. 3.1 illustrates the evolution of biofilm thickness and nutrient concentration against time for various ratios of bacterial death to growth rates (ε_1). In Fig. 3.1(a), it is evident that lower ε_1 values lead to thicker biofilms over time, as the bacterial growth rate outpaces the death rate. Fig. 3.1(b) shows nutrient concentration as a function of x, throughout the biofilm at the final time. It reveals that nutrient concentration within the biofilm increases towards the biofilm-bulk fluid interface, located on the right side of the x-axis, but at different rates depending on ε_1. For thicker biofilms (lower ε_1), the nutrient concentration remains closer to zero throughout most of the biofilm thickness, indicating more extensive nutrient consumption by the bacterial population. In contrast, for thinner biofilms (higher ε_1), nutrient concentration is higher across a larger portion of the biofilm, reflecting less nutrient consumption. This pattern suggests the emergence of a "tip" near the biofilm-bulk fluid interface, where nutrients are abundant,

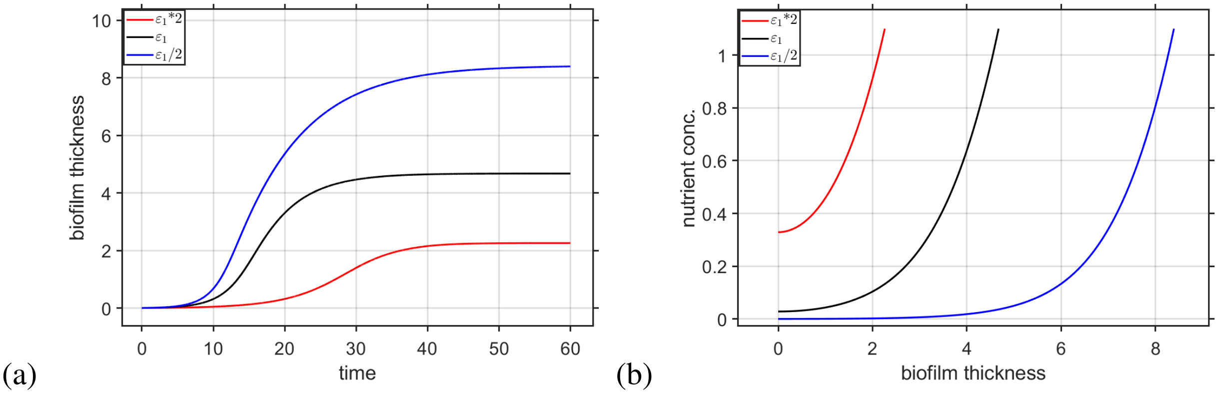

Figure 3.1: Effect of varying ε_1 on (a) temporal variation of biofilm thickness, (b) spatial variation of nutrient concentration at final time.

Fig. 3.2 examines the impact of the parameter ε_2, defined as the ratio of biofilm detachment rate to bacterial growth rate (considering M is constant), on biofilm thickness and nutrient concentration. As expected, in Fig. 3.2(a), we can see that lower ε_2 values correspond to slower detachment relative to growth, resulting in thicker biofilms over time, whereas higher ε_2 values lead to thinner biofilms due to faster detachment. Fig. 3.2 (b) shows the nutrient concentration throughout the biofilm at the final time. It reveals that the nutrient concentration profile varies with ε_2. For higher values of ε_2, which correspond to thinner biofilms (with higher detachment rates), nutrient concentration remains higher across more of the biofilm, suggesting less nutrient consumption by the bacteria. In contrast, for lower values of ε_2 (thicker biofilms), the nutri-

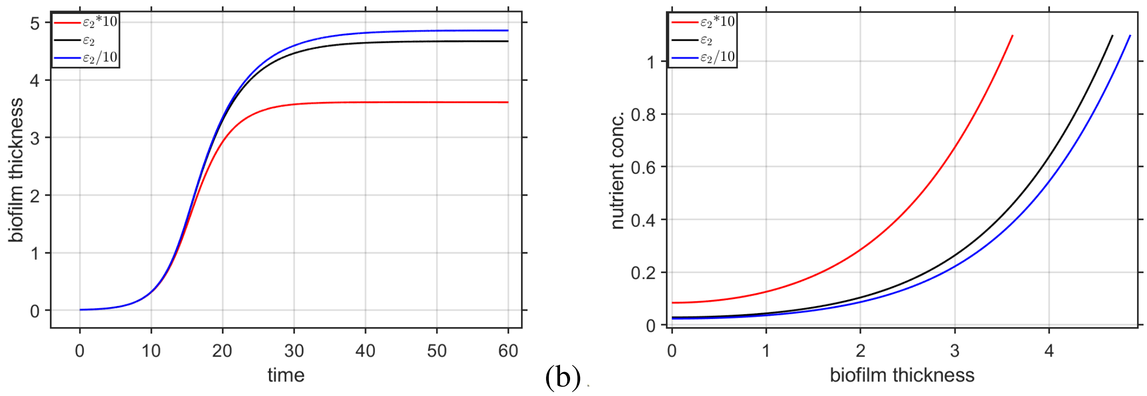

(a) (b)

Figure 3.2: Effect of varying ε_2 on (a) temporal variation of biofilm thickness, (b) spatial variation of nutrient concentration at final time.

ent concentration is closer to zero in a larger portion of the biofilm, reflecting more extensive nutrient consumption due to increased bacterial growth.

Fig. 3.3 illustrates the impact of ε_3, which represents the non-dimensional initial biofilm thickness, on the development of biofilm thickness and nutrient concentration. In Fig. 3.3(a), we observe that a higher initial biofilm thickness leads to a more rapid increase and quicker achievement of steady state compared to a smaller initial thickness, where biofilm thickness reaches steady state much later. However, it is important to note that, in all cases, the final biofilm thickness converges to the same value. Fig. 3.3(b) illustrates that for any ε_3 value, the nutrient concentration within the biofilm remains unchanged since the final biofilm thickness is identical across all scenarios.

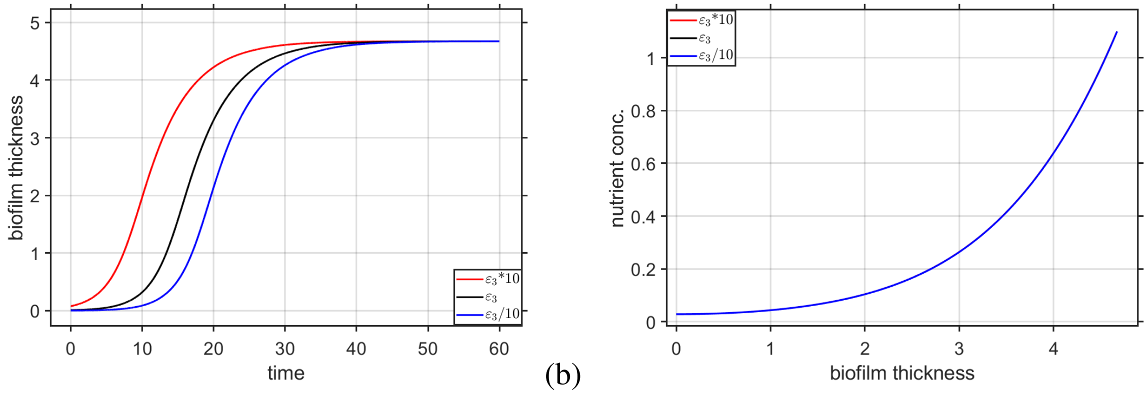

(a) (b)

Figure 3.3: Effect of varying ε_3 on (a) temporal variation of biofilm thickness, (b) spatial variation of nutrient concentration at final time.

Fig. 3.4 illustrates the effects of varying $\overline{S}_0$ on biofilm thickness and nutrient concentration. The parameter $\overline{S}_0$ influences the nutrient concentration at the moving boundary. In particular, with higher $\overline{S}_0$, the thickness of the biofilm increases more rapidly, reaching a steady state earlier due to the abundance of nutrients (see Fig. 3.4 (a)). As expected, Fig. 3.4(b) illustrates how nutrient concentration varies throughout the biofilm for different values of $\overline{S}_0$, For lower values of

$\overline{S}_0$, the biofilm reaches a steady state with a thinner structure. At the final time, when the biofilm is no longer growing, the nutrient concentration is higher throughout most of the biofilm. This is because the steady-state biofilm consumes fewer nutrients overall due to the limited bacterial growth, allowing nutrients to accumulate within the biofilm. Although the nutrient level at the biofilm-bulk fluid interface is lower, the reduced consumption within the biofilm results in higher nutrient concentrations across the biofilm compared to other cases. In contrast, for higher values of $\overline{S}_0$, the biofilm is thicker, indicating more substantial bacterial growth and nutrient consumption. Even though more nutrients are supplied from the bulk fluid due to the higher $\overline{S}_0$, the increased growth rate of the bacteria causes the nutrient levels to be nearly depleted throughout the biofilm at the final time. The higher nutrient availability at the biofilm-bulk fluid interface drives rapid bacterial growth, leading to extensive nutrient uptake within the biofilm. As a result, the nutrient concentration remains close to zero across most of the biofilm, demonstrating that higher nutrient supply can sustain a thicker biofilm but also results in greater nutrient depletion due to the higher metabolic activity.

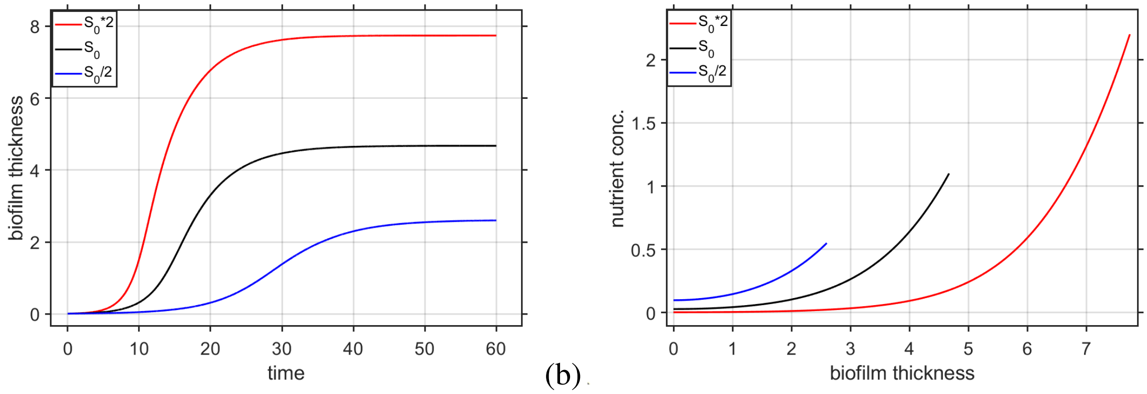

(a) (b)

Figure 3.4: Effect of varying S_0 on (a) temporal variation of biofilm thickness, (b) spatial variation of nutrient concentration at final time.

Comparison of solutions of the baseline model and the linearised models for early time

Fig. 3.5 compare the evolution of biofilm thickness over a non-dimensionalised time of 1, between the numerical solutions derived from the original baseline model (Section.3.1.3) and the solutions obtained from the linearised model (Section.3.1.4). The parameters of the baseline model, $\overline{S}_0$ (initial substrate concentration) and ε_3 (initial biofilm thickness), were carefully adjusted for each scenario to match the conditions used in the corresponding linearised model, enabling a meaningful comparison. Specifically, solving the baseline model for each case, we chose values of $\overline{S}_0$ and ε_3 to reflect the specific assumptions or parameter ranges inherent in the linearised approach. Then, while solving the linearised model, we modified the parameter values accordingly to match these conditions, ensuring that the same $\overline{S}_0$ and ε_3 values were used in both the linearised model and its parallel baseline model. This approach ensures a direct and fair comparison between the solutions from the linearised model and the numerical solutions from the baseline, non-linear model, under identical parameter settings for each respective case. For better visual clarity in the comparison, the legend of Fig. 3.5 displays the non-dimensional versions of these parameters. The black lines in all figures represent the baseline numerical solutions, while the coloured lines illustrate the solutions corresponding to various linearised solutions.

In Fig. 3.5(a), the linearised solution shows a higher rate of biofilm growth compared to the baseline solution. The linearised model tends to overestimate the biofilm thickness over time, indicating that the assumptions used in the linearisation result in an approximate solution that deviates from the baseline model. The discrepancy arises due to the original model capturing more complex non-linear dynamics, such as substrate consumption through Monod kinetics, that are not fully addressed in the linearised form. In the baseline model, even when setting S_0 to a low value, nutrient concentration does not remain small due to the dynamic nutrient influx in the biofilm. However, in the linearised model, nutrient concentration remains lower throughout, as it lacks this feedback. To achieve closer overlap between the baseline and linearised models, nutrient diffusion into the biofilm would need to be significantly reduced so that nutrient concentrations stay low across the simulation duration. However, this approach is not entirely realistic in biofilm modelling, as it does not accurately reflect the natural dynamics of nutrient transport. For this scenario, we considered $\overline{S}_0 = 0.2$ which is smaller than 1.

In Fig.3.5(b), the comparison between the baseline model and the linearised model solutions shows excellent agreement, with only a slight deviation at later times. This close correspondence suggests that the linearised model is well suited to describe the system's dynamics when both nutrient concentration and the biofilm thickness is small. The results justify the use of linearisation for analytical simplicity in this regime, as the system behaves in a nearly linear manner when both S_0 and L_0 are small. For this scenario, we considered $\overline{S}_0 = 0.2$ and $\varepsilon_3 = 7.55 \times 10^{-5}$, both are less than 1.

In Fig.3.5(c), the baseline model shows a slower growth rate compared to the linearised model. The more significant deviation between the two solutions indicates that for larger biofilm thicknesses and smaller nutrient concentrations, nonlinear effects become more pronounced. The linearised model does not fully account for the effects, resulting in an overprediction of the growth rate. This suggests that linearisation may not be suitable for cases with a large biofilm thickness, as the simplifying assumptions do not capture the more complex growth-limiting factors that arise under these conditions. In the baseline model, even when setting S_0 to a very low value and ε_3 to a very high value, the nutrient concentration and biofilm thickness do not remain constant over time due to the non-linear nature of the model. In contrast, the linearised model maintains smaller nutrient concentration and higher biofilm thickness throughout the simulation. To achieve closer overlap between the baseline and linearised models, nutrient flow into the biofilm would need to be restricted by lowering the nutrient diffusion coefficient, so that nutrient concentration remains low across the entire simulation. Additionally, biofilm growth could be increased by adjusting relevant parameters or even removing detachment to maintain a higher biofilm thickness throughout. However, this approach is not entirely realistic in biofilm modelling. For this scenario, we considered $\overline{S}_0 = 0.2$ and $\varepsilon_3 = 1.25$.

In Fig.3.5(d), the linearised solution closely follows the baseline solution, especially at early times, with minor deviations as time progresses. This indicates that under conditions of abundant nutrient, the growth dynamics are less sensitive to the non-linear factors that differentiate the baseline model from the linearised version. The linearised model can effectively approximate the baseline behaviour. The slight deviation observed at later times could be due to arising nonlinearity in nutrient consumption as the biofilm thickens. For this scenario, we considered $\overline{S}_0 = 20$, which is much higher than 1.

These results provide insights into the applicability of linearisation techniques for modelling biofilm growth. They emphasise the importance of considering parameter regimes when choosing between linearised and non-linear models for accurate predictions. The findings underscore the necessity for using the original, non-linear model in cases with large biofilm thickness or when accounting for complex nutrient limitations, while linearisation remains a useful analytical tool under more constrained conditions.

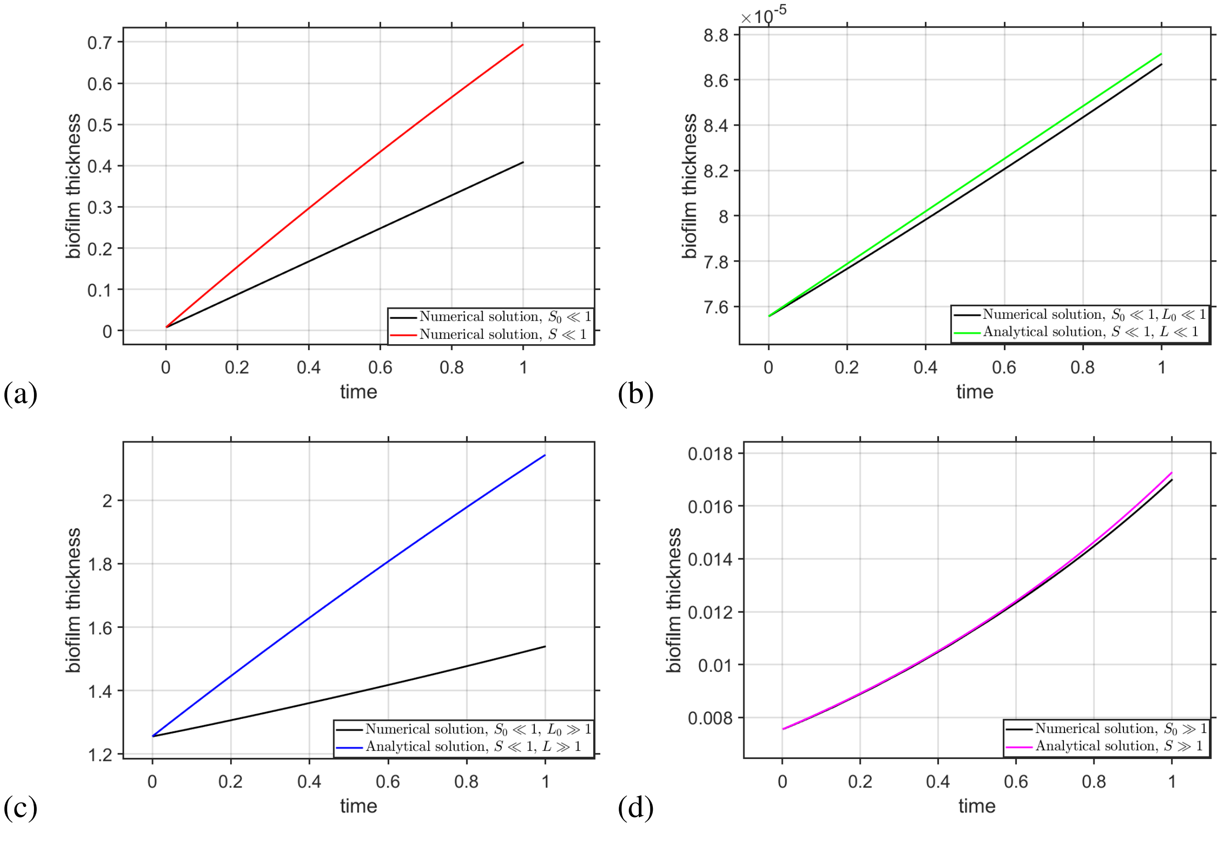

Figure 3.5: Temporal variation of biofilm thickness for the baseline model (black line) and linearised solutions (coloured lines) over a total non-dimensionalised time of 1. The parameters S_0 and L_0 in the baseline model are adjusted to match the corresponding conditions in the following linearised cases: (a) $S \ll 1$, (b) $S \ll 1, L \ll 1$, (c) $S \ll 1, L \gg 1$, and (d) $S \gg 1$.

3.2 Introducing bacteria and EPS (Model 8)

The model considered in this section is an extension of the model outlined in Section 3.1 with additional consideration of the time-dependent growth of the proliferative bacteria population (B), and the time-dependent formation of EPS (E). This model also integrates additional complexities, including velocity of the growing biomas at each point in the biofilm and water volume fraction, alongside the previously considered dynamics of nutrient and biofilm thickness. We refer to this model as Model 8, consistent with the nomenclature used in Chapter 2. The governing equations are first non-dimensionalised and then solved in MATLAB. The influences of the diffusivity of the nutrient (D_s) and the nutrient consumption rate (μ) on the development and structure of the biofilm are discussed in detail.

3.2.1 Model development

This extended model was developed to capture the microbial structure of the biofilm, with a focus on the interactions between EPS and proliferative bacteria. Although it builds on Model 11, it closely aligns with the concepts described in Section 2.1. Nutrient transport is modelled using a quasi-steady advection-diffusion-reaction equation, where nutrient consumption by biomass follows Monod kinetics [84]. The resulting biomass production contributes to an increase in biofilm thickness. The transport of nutrients is influenced by the water volume fraction (ϕ_{bio}) within the biofilm, and a zero-flux boundary condition is imposed at $x = 0$. At the opposite boundary, $x = L(t)$, a constant influx of nutrients is maintained, modelled using a Dirichlet boundary condition.

In this model, the Monod term used to represent nutrient consumption is driven by the maximal nutrient consumption rate, rather than the maximum bacterial growth rate as in Section 3.1. This is because the equations governing proliferative bacteria and EPS include the Monod term to quantify the nutrient consumption by bacteria for growth, which is then multiplied by a conversion factor representing the metabolic rate to production rate for both bacteria and EPS. This adjustment reflects the fact that not all the nutrients consumed contribute directly to biomass growth. Although the application differs, using a conversion factor in the bacteria equation here, as opposed to the maximum biomass density and yield coefficient in the nutrient equation in Model 11, the fundamental concept remains consistent with Model 11 in Section 3.1 that not all of the nutrient consumed contributes directly to growth.

The dynamics of proliferative bacteria and EPS are governed by an unsteady advection-diffusion-reaction equation. The reaction terms for both bacteria and EPS account for biomass production via nutrient utilisation, with an additional term for natural bacterial death in the proliferative bacteria equation. Since nutrient transport is influenced by the available fluid space within the biofilm, the reaction terms depend on ϕ_{bio}. The advective velocity of the biomass, which affects its transport and spatial distribution within the biofilm, is determined by a force balance equation and conservation of volume.

The progression of the biofilm-bulk fluid interface, at $x = L(t)$, is governed by the biomass velocity at this interface, integrating the biological factors that contribute to biofilm expansion. In this model, we have excluded the detachment term to focus solely on biofilm growth driven by bacteria and EPS. We assume an incompressible system so that the combined volume fraction of all components in the biofilm, including all bacterial phenotypes, EPS, and water, remains constant and is equal to 1. This implies that there are no air gaps within the biofilm, which is a valid assumption for a fully diffused biofilm, such as those found in the body. The nutrients are dissolved in the water and do not contribute to the volume as a separate component. Nutrient molecules are small compared to the biofilm components so their presence does not significantly affect the volume of the water. Therefore, nutrients are not included separately in the volume constraint. Here, 'water' refers to plasma and any small blood constituents that do not significantly affect the fluid properties, allowing it to be modelled as a simple fluid. For simplicity, ϕ_{bio} is assumed to have a constant value following the simplification strategy 1 in Section 2.2. We take the average value of 0.8 from Table 2.2. This is also assumed for the next models in Chapter 4 and 5. Additionally, given the assumption that there is no biofilm growth within the porous implant, a zero-flux condition is imposed for bacteria and EPS at both the implant-biofilm interface and the biofilm-bulk fluid interface. The biomass velocity is set to zero at $x = 0$, reflecting a static boundary at the implant interface.

3.2.2 Governing equations

As described in the previous section, the growth of proliferative bacteria and the formation of EPS within the biofilm are governed by the following partial differential equations [84]

$$\begin{aligned} B_t + (vB)_x &= D_B B_{xx} + k_B \frac{\mu \phi_{bio} S}{k_S + \phi_{bio} S} B - bB, \quad 0 < x < L(t),\ t > 0, && (3.23) \\ E_t + (vE)_x &= D_E E_{xx} + k_E \frac{\mu \phi_{bio} S}{k_S + \phi_{bio} S} B, \quad 0 < x < L(t),\ t > 0. && (3.24) \end{aligned}$$

The advective velocity v governs the movement of biomass within the biofilm with the terms $(vB)_x$ and $(vE)_x$ representing the advective transport of bacteria and EPS, respectively. The Monod term $\frac{\mu \phi_{bio} S}{k_S + \phi_{bio} S}$ represents the rate of nutrient consumption by the bacteria, which drives both bacterial growth and EPS production. ϕ_{bio} represents the water volume fraction within the biofilm, which modulates the effective transport and availability of nutrients. Here, b denotes the natural death rate of the bacteria. The variables D_B and D_E represent the diffusivities of the bacteria and EPS, respectively.

Nutrient transport within the biofilm is described by:

$$\phi_{bio}(vS)_x = \phi_{bio} D_S S_{xx} - \frac{\mu \phi_{bio} S}{k_S + \phi_{bio} S} B, \quad 0 < x < L(t),\ t > 0, \qquad (3.25)$$

where D_S is the diffusivity of the nutrient. The relationship between ϕ_{bio}, bacterial concentration B, and EPS concentration E is given by

$$1 = \phi_{bio} + \frac{B}{\rho_B} + \frac{E}{\rho_E}, \tag{3.26}$$

where ρ_B and ρ_E are the densities of bacteria and EPS, respectively. This equation ensures that the total volume fraction within the biofilm, consisting of water, bacteria, and EPS, remains constant.

The advective velocity v of the biofilm constituents, which influences their transport and distribution, is determined by the following equations:

$$v = -\lambda P_x, \quad 0 < x < L(t), \tag{3.27}$$

$$v_x = \frac{1}{1-\phi_{bio}}\left(\left(\frac{k_B}{\rho_B} + \frac{k_E}{\rho_E}\right)\frac{\mu\phi_{bio}S}{k_S + \phi_{bio}S}B - \frac{bB}{\rho_B}\right), \quad 0 < x < L(t),\ t > 0. \tag{3.28}$$

Here, we assume that the densities ρ_B and ρ_E remain constant to simplify the analysis. Under this assumption, the advective transport of biofilm constituents is described by equation (3.28). Here, P_x represents the pressure gradient within the biofilm, and λ is a proportionality constant related to the biofilm's mechanical properties. The first equation approximates the force balance within the biofilm, while the second equation represents the conservation of volume, accounting for the growth and movement of biomass within the biofilm. To derive this equation, we first sum equation (3.23), divided by ρ_B, and equation (3.24), divided by ρ_E. The resulting expression is then substituted into equation (3.26). In this study, the force balance equation is deemed redundant and will not be used in the analysis, as it is only needed if the pressure P is required, which is not essential for solving the remaining equations. Furthermore, we have ignored the diffusion terms in the conservation of volume equation (3.28), because they are significantly smaller compared to the reaction terms, allowing us to simplify the calculations without compromising the accuracy of the model.

The evolution of the biofilm-fluid interface, denoted by $L(t)$, is governed by the following equation

$$\frac{dL}{dt} = v(L), \quad t > 0, \tag{3.29}$$

which describes the rate at which the biofilm expands over time and is simply the velocity of the biomass at the point $x = L$.

Initial and Boundary Conditions

The initial conditions assume that:

$$\begin{aligned} B(x,0) &= B_0 e^{\frac{v(x,0)}{D_B}x}, \quad 0<x<L(0), && (3.30)\\ E(x,0) &= E_0 e^{\frac{v(x,0)}{D_E}x}, \quad 0<x<L(0), && (3.31)\\ L(0) &= L_0. && (3.32) \end{aligned}$$

The initial condition of bacteria and EPS is spatially dependent, ensuring consistency with the boundary conditions.

At the implant-biofilm interface ($x=0$), a zero-flux condition is imposed on the nutrient, bacteria, and EPS concentrations to reflect the lack of nutrient and biomass transport through this boundary and the velocity is set to zero:

$$\begin{aligned} -D_S S_x = -D_B B_x = -D_E E_x &= 0, \quad \text{at } x=0,\ t>0, && (3.33)\\ v &= 0, \quad \text{at } x=0,\ t>0. && (3.34) \end{aligned}$$

At the biofilm-bulk fluid interface ($x=L(t)$), a Dirichlet boundary condition is applied for the nutrient concentration S. Meanwhile, a zero-flux condition is applied for the bacteria and EPS concentrations to prevent their transport through the interface:

$$\begin{aligned} S &= S_0, \quad \text{at } x=L(t),\ t>0, && (3.35)\\ -D_B B_x + vB = -D_E E_x + vE &= 0, \quad \text{at } x=L(t),\ t>0. && (3.36) \end{aligned}$$

These boundary conditions ensure that the biofilm dynamics are appropriately constrained by the physical and biological interactions at the biofilm's interfaces.

The parameters involved in the equations (3.23)-(3.36) are detailed in Table 2.2 and the variables are detailed in Table 2.1.

3.2.3 Non-dimensionalisation

To simplify the analysis and make the model equations dimensionless, we introduce the following non-dimensional variables:

$$\overline{B} = \frac{B}{k_S}, \quad \overline{E} = \frac{E}{k_S}, \quad \overline{S} = \frac{S}{k_S}, \quad \bar{t} = bt, \quad \overline{v} = \frac{v}{bL_0}, \quad \overline{x} = \frac{x}{L_0}.$$

Using these non-dimensional variables, we rewrite the governing equations (3.23)–(3.29) and the initial and boundary conditions (3.30)–(3.36) in their non-dimensional forms:

$$
\begin{aligned}
\overline{B}_{\overline{t}}+(\overline{v}\overline{B})_{\overline{x}} &= \overline{D}_B\overline{B}_{\overline{x}\overline{x}}+G_1\frac{\phi_{bio}\overline{S}}{1+\phi_{bio}\overline{S}}\overline{B}-\overline{B}, \quad 0<\overline{x}<\overline{L}(\overline{t}),\ \overline{t}>0, && (3.37)\\
\overline{E}_{\overline{t}}+(\overline{v}\overline{E})_{\overline{x}} &= \overline{D}_E\overline{E}_{\overline{x}\overline{x}}+G_2\frac{\phi_{bio}\overline{S}}{1+\phi_{bio}\overline{S}}\overline{B}, \quad 0<\overline{x}<\overline{L}(\overline{t}),\ \overline{t}>0, && (3.38)\\
\phi_{bio}(\overline{v}\overline{S})_{\overline{x}} &= \phi_{bio}\overline{D}_S\overline{S}_{\overline{x}\overline{x}}-G_3\frac{\phi_{bio}\overline{S}}{1+\phi_{bio}\overline{S}}\overline{B}, \quad 0<\overline{x}<\overline{L}(\overline{t}),\ \overline{t}>0, && (3.39)\\
1 &= \phi_{bio}+\frac{\overline{B}}{\overline{\rho}_B}+\frac{\overline{E}}{\overline{\rho}_E}, && (3.40)\\
\overline{v}_{\overline{x}} &= \frac{1}{1-\phi}\left(\left(\frac{k_B}{\overline{\rho}_B}+\frac{k_E}{\overline{\rho}_E}\right)G_3\frac{\phi_{bio}\overline{S}}{1+\phi_{bio}\overline{S}}\overline{B}-\frac{\overline{B}}{\overline{\rho_B}}\right), \quad 0<\overline{x}<\overline{L}(\overline{t}),\ \overline{t}>0, && (3.41)\\
\frac{d\overline{L}}{d\overline{t}} &= \overline{v}(\overline{L}), \quad \overline{t}>0. && (3.42)
\end{aligned}
$$

The initial conditions in non-dimensional form are

$$
\begin{aligned}
\overline{B}(\overline{x},0) &= \overline{B}_0 e^{\frac{\overline{v}(\overline{x},0)}{\overline{D}_B}\overline{x}}, \quad 0<\overline{x}<\overline{L}(0), && (3.43)\\
\overline{E}(\overline{x},0) &= \overline{E}_0 e^{\frac{\overline{v}(\overline{x},0)}{\overline{D}_E}\overline{x}}, \quad 0<\overline{x}<\overline{L}(0), && (3.44)\\
\overline{L}(0) &= \overline{L}_0. && (3.45)
\end{aligned}
$$

The boundary conditions (3.33)–(3.36) also transform into their non-dimensional forms as follows

$$
\begin{aligned}
-\overline{D}_S\overline{S}_{\overline{x}}=-\overline{D}_B\overline{B}_{\overline{x}}=-\overline{D}_E\overline{E}_{\overline{x}} &= 0, \quad \text{at} \quad \overline{x}=0,\ \overline{t}>0, && (3.46)\\
\overline{v} &= 0 \quad \text{at} \quad \overline{x}=0,\ \overline{t}>0, && (3.47)\\
\overline{S} &= \overline{S}_0 \quad \text{at} \quad \overline{x}=\overline{L}(\overline{t}),\ \overline{t}>0, && (3.48)\\
-\overline{D}_B\overline{B}_{\overline{x}}+\overline{v}\overline{B}=-\overline{D}_E\overline{E}_{\overline{x}}+\overline{v}\overline{E} &= 0 \quad \text{at} \quad \overline{x}=\overline{L}(\overline{t}),\ \overline{t}>0. && (3.49)
\end{aligned}
$$

The non-dimensional parameters introduced in the equations above are defined as

$$
G_1=\frac{k_B\mu}{b}, \quad G_2=\frac{k_E\mu}{b}, \quad G_3=\frac{\mu}{b}, \quad \overline{D}_s=\frac{D_s}{bL_0{}^2}, \quad \overline{D}_B=\frac{D_B}{bL_0^2}, \quad \overline{D}_E=\frac{D_E}{bL_0^2},
$$

$$
\overline{B}_0=\frac{B_0}{k_S}, \quad \overline{E}_0=\frac{E_0}{k_S}, \quad \overline{L}_0=\frac{L_0}{L_0}=1, \quad \overline{S}_0=\frac{S_0}{k_S}, \quad \overline{\rho}_B=\frac{\rho_B}{k_S}, \quad \overline{\rho}_E=\frac{\rho_E}{k_S}.
$$

3.2.4 Solution methodology

The computational procedure for solving this model is very similar to the methodology described in Section 3.1.5. First, using the initial values of $\overline{B}$ and $\overline{S}$, we solve equation (3.41) to obtain the advective velocity v. Next, the thickness of the biofilm in the subsequent time step is determined by solving equation (3.42) using the computed velocity v and the initial value of L. We then update $\overline{B}$, $\overline{E}$, and $\overline{S}$ for the next time step by solving equations (3.37), (3.38), and (3.39), respectively. The newly obtained values of $\overline{B}$, $\overline{E}$, and $\overline{S}$ replace the initial values $\overline{B}_0$, $\overline{E}_0$, and $\overline{S}_0$ in preparation for the next iteration. This process is repeated from the first step until the solution converges within a specified tolerance. For quantitative analysis, the governing equations (3.37)-(3.42), along with the prescribed boundary and initial conditions (equations (3.43)–(3.49)), are solved using MATLAB. The unsteady equations governing bacteria, EPS, and biofilm thickness are solved using the explicit Euler method, using MATLAB, while the boundary value problem for nutrient transport within the biofilm is solved numerically using MATLAB's 'bvp4c' function. This function is specifically designed to handle boundary value problems by automatically satisfying boundary conditions at both ends, providing higher accuracy and stability through a fourth-order collocation method with adaptive mesh refinement and error control.

3.2.5 Results and discussions

It is important to note that all results are presented in non-dimensional form, although the overline notation is omitted in the figures for clarity. In addition, a sensitivity analysis was conducted to investigate the effects of varying parameters such as nutrient diffusivity and the maximal nutrient consumption rate on biofilm growth and structure. For each species (e.g. B), a key quantity of interest is the total concentration, defined as the integral of the concentration of that species over the 1D spatial domain. For example, a total concentration of proliferative bacteria would be calculated as $\int_0^{L(t)} B(x,t)dx$. This quantity is equal to mass per unit area, an areal concentration, but the term 'total concentration' is used throughout the thesis for consistency with other measures of the system. All plots are for a final time of 20 days. This time was chosen because, although the biofilm had not yet reached a steady state, it exhibited prominent behaviours and structures by this point. Unlike Model 11, which used a 10-day final time, this model incorporates both bacterial and EPS dynamics, leading to more complex growth behaviours that take longer to develop.

Effect of diffusion coefficient (D_S) of nutrient

Fig. 3.6(a) presents the total bacterial concentration over time for three different diffusion scenarios: $D_S \times 10$ (red curve), D_S (black curve), and $D_S/10$ (blue curve), where D_S is the non-dimensionalised value based on the parameter's base value listed in Table 2.2. With increased nutrient diffusion, there is a rapid increase in bacterial concentration, particularly evident in higher diffusion case, reflecting the increased availability of nutrients. This surge peaks sharply before declining, indicating that while higher diffusion initially promotes rapid bacterial growth, it is not sustainable over time due to factors such as nutrient depletion or bacterial death. In contrast, the lower diffusion scenario shows a more gradual increase in bacterial concentration, suggesting slower growth due to limited nutrient availability. Fig. 3.6(b) depicts the corresponding total EPS concentration under the same conditions, revealing a continuous increase in EPS production that correlates with nutrient diffusion rates. The red curve, representing the highest diffusion rate, shows the fastest and most substantial EPS production, which continues to rise even after bacterial growth declines. EPS production allows the biofilm to stabilise and maintain its structure, even as the bacterial population decreases. However, the rate of growth of EPS slows down from the time the bacteria concentration starts decreasing.

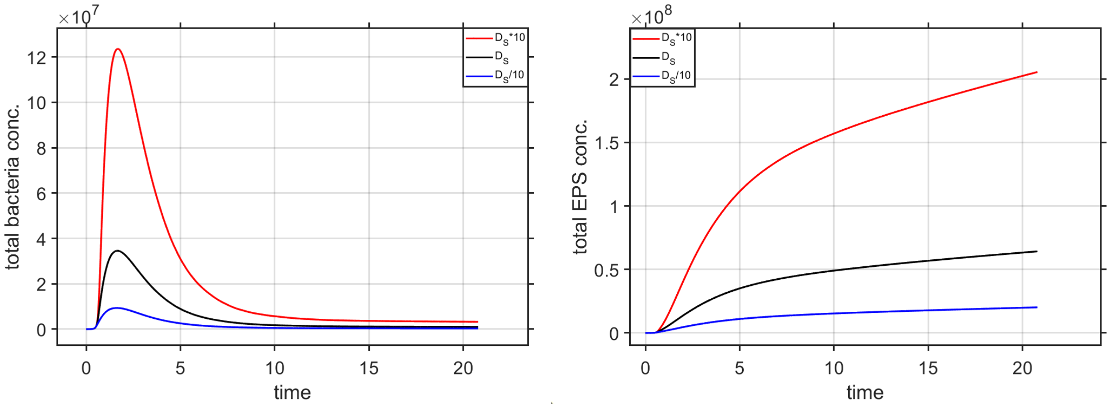

(a)

Figure 3.6: Effect of varying nutrient diffusivity (D_S) on (a) temporal variation of total bacteria concentration, (b) temporal variation of total EPS concentration.

Fig. 3.7(a) illustrates that from the implant-biofilm interface the bacteria concentration increases as you move towards the biofilm-bulk fluid interface. It is particularly noticeable under the highest nutrient diffusion condition, where the concentration peaks near the biofilm-bulk fluid interface, due to the abundant nutrient supply, which enters the biofilm from the bulk fluid interface. However, as we move deeper into the biofilm, which is towards the implant-biofilm interface $(x = 0)$, the bacterial concentration decreases, especially for the highest diffusion coefficient. This counterintuitive result can be attributed to the scarcity of nutrients in the deeper layers, as shown in Fig. 3.7(c), where nutrient concentration diminishes rapidly away from the biofilm-bulk fluid interface. Moreover, in these deeper layers, the higher diffusion condition leads to an increase in EPS production (as seen in Fig. 3.7(b)), which might further restrict bacterial growth by consuming resources that could otherwise be used for bacterial proliferation.

Fig. 3.7(b) shows the distribution of EPS concentration across the biofilm thickness, revealing that EPS is highest in the deeper layers of the biofilm, particularly under conditions of higher nutrient diffusion. In nutrient-deprived conditions found deeper in the biofilm, bacteria may shift their metabolic focus from growth to EPS production for stability. EPS plays a critical role in protecting the biofilm's structural integrity and shielding bacteria from environmental stresses. As nutrients become more abundant near the interface with the bulk fluid, the need for EPS production decreases, while the drive for biofilm growth intensifies, resulting in a gradual decline in EPS concentration.

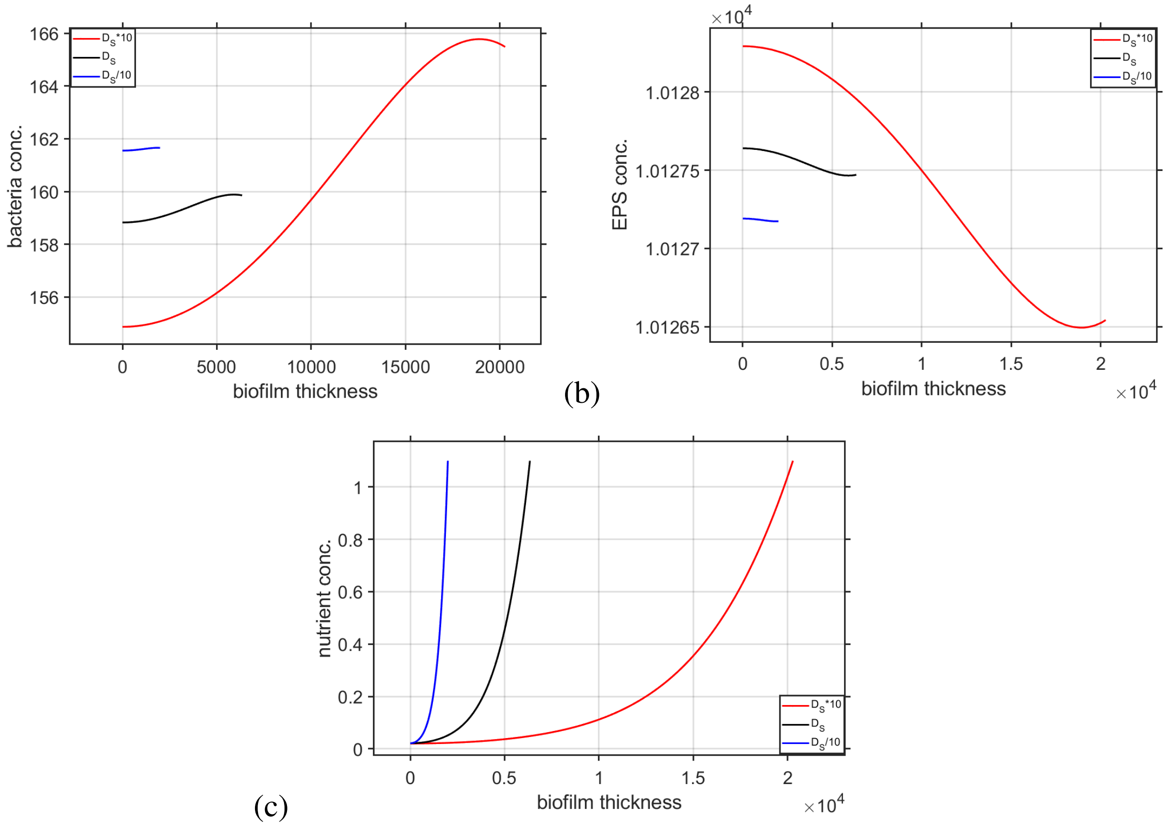

(a) (b) (c)

Figure 3.7: Effect of varying nutrient diffusivity (D_S) on (a) spatial variation of bacteria concentration at final time, (b) spatial variation of EPS concentration at final time, (c) spatial variation of nutrient concentration at final time.

Fig. 3.7(c) reinforces these observations by depicting the nutrient concentration across the biofilm. The nutrient concentration is highest at the biofilm-bulk fluid interface as a result of the direct nutrient influx from the bulk fluid. As nutrients diffuse deeper into the biofilm, their concentration decreases significantly, especially under higher diffusion conditions, where the nutrients are quickly consumed by the actively growing bacterial population near the interface. This rapid consumption leads to nutrient scarcity in the deeper layers, which is consistent with the observed decrease in bacterial concentration in Fig. 3.7(a) [114]. The lower nutrient availability, combined with higher EPS production in these regions, further limits bacterial growth, creating a stratified biofilm structure where the outer layers near the interface are dominated by active bacterial growth, while the deeper layers focus on EPS synthesis for biofilm stability.

Fig. 3.8(a) illustrates the growth of biofilm thickness over time for three different nutrient diffusion scenarios. As the biofilm develops, the thickness increases in all scenarios, but the rate and extent of this growth are heavily dependent on the nutrient diffusion coefficient. In the scenario with the highest diffusion, the biofilm expands rapidly, achieving significantly greater thickness compared to the other conditions. This rapid expansion is driven by the abundant nutrient supply available throughout the biofilm, particularly near the biofilm-bulk fluid interface, where bacterial growth is most active. The higher diffusion allows nutrients to penetrate deeper into the biofilm, supporting sustained growth and resulting in a thicker biofilm over time. In contrast, in the lower diffusion scenarios, the thickness of the biofilm increases more slowly, reflecting the limited availability of nutrients that constrains bacterial proliferation and biofilm expansion. This slower growth under lower diffusion conditions highlights how nutrient scarcity can limit the biofilm's ability to develop fully.

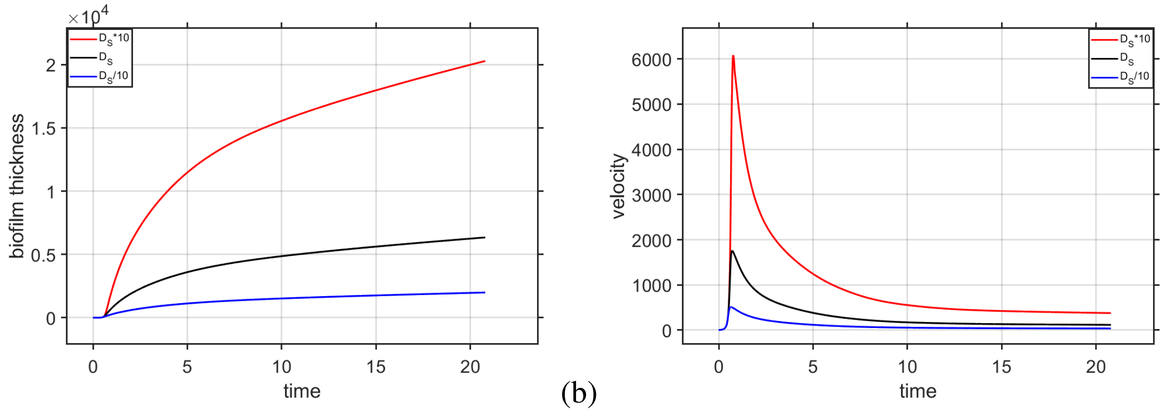

(a) (b)

Figure 3.8: Effect of varying nutrient diffusivity (D_S) on (a) temporal variation of biofilm thickness, (b) temporal variation of velocity at the biofilm-bulk fluid interface.

Fig. 3.8(b) shows the velocity of biomass at the biofilm-bulk-fluid interface over time, representing the rate at which the biofilm's outer boundary is advancing. The velocity is highest for the scenario with the highest nutrient diffusion, where the ample nutrient availability fuels a rapid expansion of the biofilm. This high initial velocity corresponds to the early and rapid increase in biofilm thickness observed in Fig. 3.8(a). However, over time, the velocity decreases, with a more rapid decline observed in the high-diffusion scenario, eventually stabilising at a low value. This decline in velocity suggests that, as the biofilm thickens, the nutrient supply becomes more limited within the biofilm, slowing the rate of expansion at the boundary. In the high diffusion scenario, the initial rapid consumption of nutrients leads to faster depletion, causing a reduction in the biofilm's growth rate over time. The lower diffusion scenarios exhibit a similar trend, but with lower initial velocities and a more gradual decline, consistent with the slower increase in biofilm thickness. This slower velocity and biofilm growth under low diffusion conditions further emphasise the critical role of nutrient diffusion in biofilm development, where limited nutrient availability can restrict both the growth rate and the ultimate thickness of the biofilm.

Effect of maximal nutrient consumption rate (μ)

Fig. 3.9(a) shows the total bacterial concentration as a function of time for three different scenarios: μ increased by 20% (red curve), the baseline μ (black curve), and μ decreased by 20% (blue curve),where μ is the parameter value listed in Table 2.2. Initially, all scenarios exhibit a rapid increase in bacterial concentration, which have slightly delayed peaks and with different magnitudes, as μ decreases. The highest peak is observed when μ increases by 20%, indicating that higher nutrient consumption rates lead to faster and more substantial bacterial growth. Conversely, the scenario with a 20% decrease in μ results in a lower peak, reflecting slower bacterial growth due to reduced nutrient uptake. After reaching these peaks, the bacterial concentration declines sharply in all scenarios, eventually stabilising at a lower level. This suggests that increased nutrient consumption supports more bacterial activity, even as the biofilm matures and resources become limited.

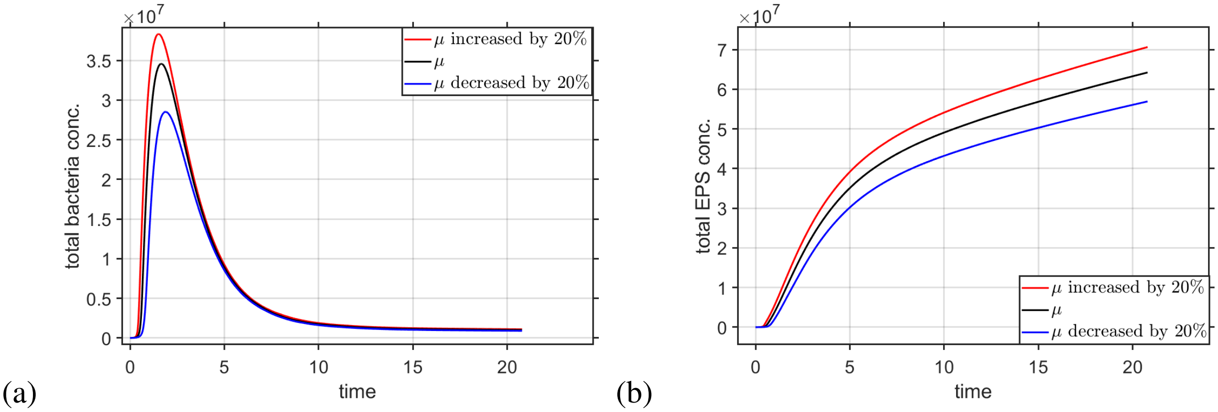

Figure 3.9: Effect of varying maximal nutrient consumption rate (μ) on (a) temporal variation of total bacteria concentration, (b) temporal variation of total EPS concentration.

Fig. 3.9(b) illustrates the total EPS concentration over time for the same three scenarios. Unlike the bacterial concentration, the EPS concentration steadily increases throughout the time period, with the rate of increase directly correlated to μ. The scenario with a 20% increase in μ shows the highest EPS production, followed by the baseline and then the 20% decrease in μ. This trend indicates that higher nutrient consumption rates not only accelerate bacterial growth but also enhance EPS production. As the bacteria consume more nutrients, they produce more EPS to maintain the biofilm structure, particularly as the biofilm matures and nutrient availability begins to diminish. Although the total EPS concentration increases with time, the growth rate slows once the total bacterial population begins to decline [50].

Fig. 3.10(a) shows the bacterial concentration across the biofilm thickness under different μ conditions. Bacterial concentration generally increases towards the biofilm-bulk fluid interface, where nutrients are the most abundant. This interface is the main source of nutrients, leading to the highest bacterial growth in this region. However, across the biofilm thickness, bacterial concentration is lowest when μ is highest, despite the initial nutrient influx. This occurs because a higher μ accelerates nutrient consumption, leading to rapid depletion near the interface and, consequently, limiting bacterial growth in the deeper biofilm layers. In contrast, when μ is decreased by 20%, nutrient consumption is slower and more evenly distributed, allowing for a more sustained bacterial presence throughout the biofilm.

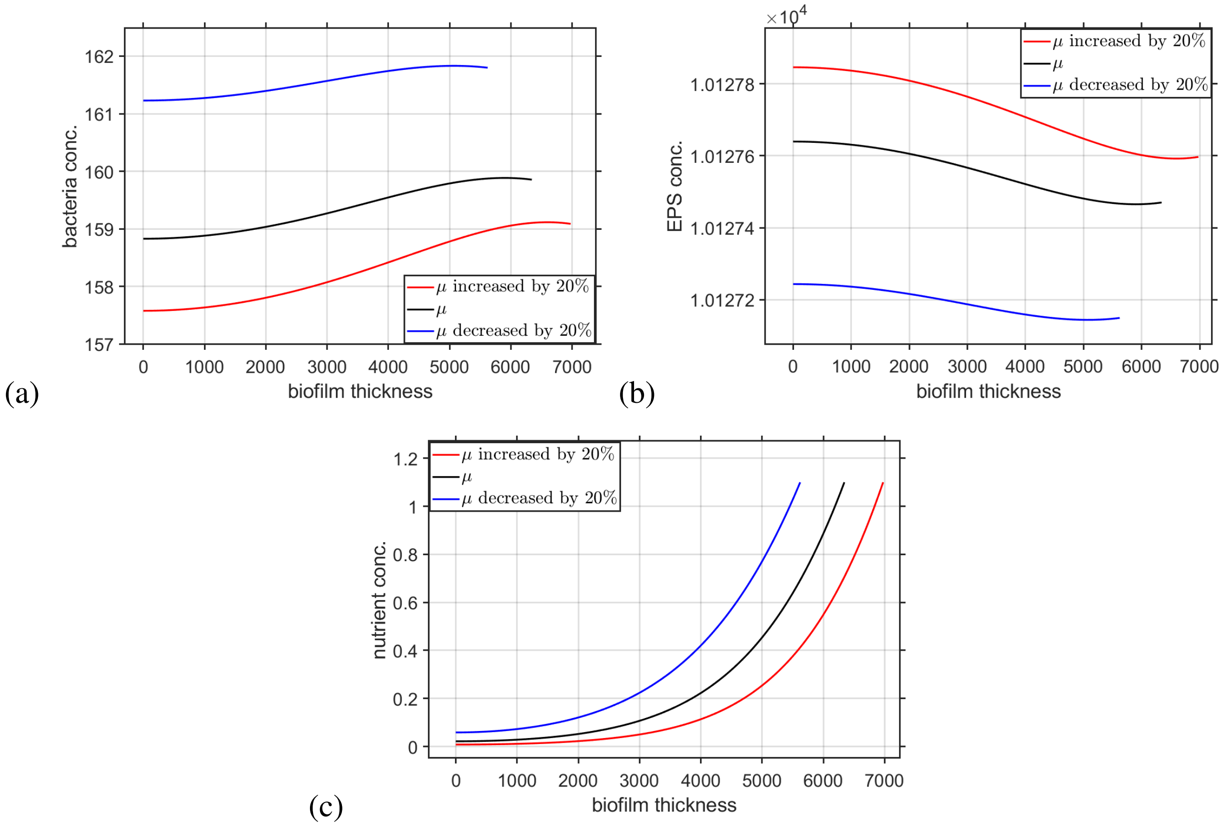

Figure 3.10: Effect of varying maximal nutrient consumption rate (μ) on (a) spatial variation of bacteria concentration at final time, (b) spatial variation of EPS concentration at final time, (c) spatial variation of nutrient concentration at final time.

Fig. 3.10(b), which depicts EPS concentration across the biofilm thickness, complements these findings. The EPS concentration is highest when μ is increased by 20%, despite the lower bacterial concentrations observed in Fig. 3.10(a). This relationship can be attributed to the fact that a higher μ results in faster nutrient consumption, leading to rapid bacterial growth, which subsequently stimulates EPS production. Consequently, this case exhibits a lower bacterial concentration throughout the biofilm. As nutrients become scarce, particularly at the deeper levels of the biofilm, bacteria shift their metabolic focus towards producing EPS to stabilise the biofilm structure and facilitate the transition to a mature biofilm state. The increased EPS concentration at these deeper levels is a clear indication of the need of the biofilm to maintain structural integrity. This contrasts with the scenario where μ is decreased by 20%, where nutrient consumption is slower, leading to higher bacterial concentrations but lower EPS production, as the bacteria prioritise growth.

Fig. 3.10(c) illustrates nutrient concentration across the biofilm thickness, providing insights into the underlying causes of the patterns observed in Fig. 3.10(a) and (b). Nutrient concentration is highest when μ is decreased by 20%, particularly in the thicker regions of the biofilm. This higher availability of nutrients supports the sustained bacterial growth observed in Fig. 3.10(a) and corresponds to a lower production of EPS, as seen in Fig. 3.10(b). Alternatively, when μ is increased by 20%, nutrient concentration is significantly lower, especially in the deeper layers of the biofilm. This scarcity of nutrients explains the reduced growth of bacteria and the increase in EPS production. A higher μ accelerates nutrient consumption, causing a faster depletion of resources and rapid initial bacterial growth, which results in a higher EPS concentration at the final time. A lower μ promotes more uniform bacterial growth across the biofilm with less emphasis on EPS production. These findings underscore the critical role of nutrient dynamics in determining the spatial and functional characteristics of biofilms, with the maximal nutrient consumption rate being a key factor that influences the biofilm's maturation and stability.

Fig. 3.11(a) shows the evolution of biofilm thickness over time under three different scenarios. When μ is increased by 20%, the biofilm thickens more rapidly, reaching a greater final thickness compared to the baseline and decreased μ conditions. This accelerated growth is due to the higher rate of nutrient consumption, which drives faster bacterial proliferation, leading to a faster accumulation of biomass. However, when μ is decreased by 20%, the growth rate is slower, resulting in a thinner biofilm. The slower growth in this scenario reflects reduced nutrient uptake, which limits bacterial activity and biomass accumulation.

In Fig. 3.11(b) the velocity of biomass, defined as the rate of change of biofilm thickness, changes over time at the biofilm-bulk fluid interface. The velocity represents how quickly the biofilm thickness is changed. Initially, the velocity is highest in the scenario where μ is increased by 20%, corresponding to the rapid initial growth in biofilm thickness observed in Fig. 3.11(a). This high velocity occurs because the increased nutrient consumption rate fuels fast biomass growth, pushing the biofilm boundary outward quickly. However, as time progresses, the velocity decreases sharply and stabilises at a lower level. In the high μ scenario, where the initial rapid consumption of nutrients leads to depletion, the expansion of the biofilm slows as resources become scarce. The baseline and decreased μ scenarios exhibit similar trends but with lower initial velocities and more gradual declines, consistent with the slower increase in biofilm thickness seen in Fig. 3.11(a). These findings highlight the importance of nutrient dynamics in biofilm development, with the maximal nutrient consumption rate being a key determinant of both the speed and sustainability of biofilm growth.

3.3 Summary

This chapter explored the development and analysis of one-dimensional biofilm growth models in antibiotic-free environments, focussing on biofilm formation on medical implants. The main goal was to gain a clear understanding of the core mechanisms underlying biofilm development before introducing the added complexity of antibiotic interactions. By examining these baseline conditions, we laid the groundwork for future studies on how antibiotics influence biofilm

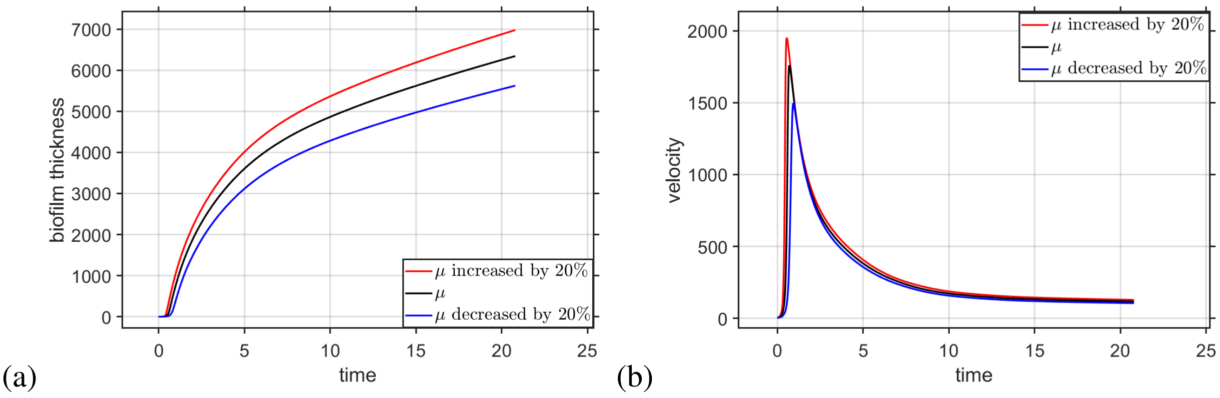

Figure 3.11: Effect of varying maximal nutrient consumption rate (μ) on (a) temporal variation of biofilm thickness, (b) temporal variation of velocity at the biofilm-bulk fluid interface.

dynamics. A central contribution of this work is the characterisation of nutrient-driven structural and compositional changes in biofilms, offering a modular and interpretable framework to support later investigations involving antibiotic effects.

In the first part of the chapter, we introduced a simplified biofilm growth model based on the model in [2]. However, our work differs significantly as we analysed different aspects of biofilm study. This model concentrated on the essential processes of nutrient diffusion, biomass accumulation, and biofilm detachment. This model was designed to capture the basic dynamics of biofilm growth, emphasising the interactions between these processes and their collective impact on biofilm development over time. By non-dimensionalising and linearising the model equations, we made the system more manageable. MATLAB code was developed to carry out the numerical simulations, allowing for a detailed sensitivity analysis of key parameters, such as bacterial death and growth rates, detachment rate, nutrient concentrations, and initial biofilm thickness. Building on the insights from the first model, the second part of the chapter introduced an extended model that incorporated additional complexities, including the unsteady growth of proliferative bacteria and the formation of EPS. This model also accounted for the advective processes within the biofilm, driven by changes in the volume fractions of bacteria and EPS.

In the first model, a sensitivity analysis was conducted to examine the effects of key parameters on biofilm thickness and nutrient distribution. The analysis revealed that lower ratios of bacterial death to growth rates resulted in thicker biofilms over time, as bacterial growth outpaced death. In contrast, higher values, where death rates were more pronounced, led to thinner biofilms. This highlighted the crucial balance between bacterial proliferation and mortality in determining the biofilm structure. Furthermore, the detachment rate relative to bacterial growth was shown to play a significant role. Lower values led to thicker biofilms as a result of slower detachment, while higher values caused more rapid thinning. The availability of nutrients at the boundary was also a key factor, with higher concentrations accelerating biofilm growth and thickness. The initial thickness of the biofilm mainly influenced the growth trajectory, where larger initial thicknesses led to a faster achievement of steady-state thickness, although all scenarios eventually converged to the same final thickness. The comparison between the baseline and linearised models demonstrates that linearisation provides a reasonable approximation under conditions of low nutrient concentration and small biofilm thickness, as well as when nutrients are abundant. However, it deviates significantly when biofilm thickness is large or nutrient availability is limited, emphasising the importance of accounting for non-linear effects in these regimes.

In the second model, which studied the effects of nutrient diffusion and maximal nutrient consumption rates, the findings further enriched our understanding of biofilm dynamics. Higher nutrient diffusion coefficients were found to drive rapid initial increases in bacterial concentration and biofilm thickness, but this was followed by faster nutrient depletion. This led to a decline in bacterial concentration in the deeper layers and a shift towards increased EPS production. The maximal nutrient consumption rate also played a crucial role. Higher values resulted in a more pronounced peak in bacterial concentration, followed by a sharper decline as nutrients were quickly exhausted. This was accompanied by an increase in the rate of EPS production, particularly in the deeper layers of the biofilm, because bacteria focused on maintaining structural integrity. In contrast, lower values supported more uniform bacterial growth throughout the biofilm, with less emphasis on EPS production. These findings highlight the dynamic nature of biofilm development, where different processes dominate depending on the environmental context.

These findings align with the theoretical understanding of biofilm dynamics. However, the analysis provided a more nuanced understanding of how biofilm growth and structure are influenced by different factors, especially when the dynamics of EPS and bacteria are incorporated simultaneously. These results will be crucial for understanding the more complex models that incorporate antibiotic interactions because the baseline behaviours observed here, such as nutrient distribution, biofilm growth patterns, and the role of EPS, help define how biofilms respond to their environment under normal conditions. When antibiotics are introduced into future models, these baseline dynamics will provide a reference point, allowing us to identify how antibiotics alter nutrient consumption, bacterial growth, and EPS production, and how these shifts impact biofilm structure.

This model is limited due to the lack of antibiotic exposure and the exclusion of different bacterial phenotypes and their influence on biofilm composition. In reality, the presence of antibiotics and varying bacterial phenotypes, such as persister and dead bacteria, significantly impacts biofilm dynamics. These limitations will be addressed in the following chapter, where the influence of antibiotics on biofilm behaviour and the interactions between different bacterial phenotypes, such as proliferative, persister, and dead bacteria, will be explored, building on the insights gained in this chapter. In conclusion, this chapter has provided a detailed examination of biofilm growth in non-antibiotic environments, offering a thorough understanding of the underlying mechanisms and setting the stage for more advanced studies.

Chapter 4

Biofilm growth models with continuous antibiotic administration

In the previous chapter, we explored simplified biofilm growth models in a non-antibiotic environment, focussing on understanding the basic structure and dynamics of biofilm growth. Model 8 in Section 3.2 considered proliferative bacteria and EPS, laying the groundwork for a deeper investigation of biofilm behaviour. The chapter concluded with a discussion of potential future directions, specifically the incorporation of additional bacterial phenotypes such as persister and dead cells, which are known to play critical roles in biofilm resilience. As discussed in Section 1.3, biofilm resilience refers to the ability of bacteria within biofilms to withstand antimicrobial treatments through two mechanisms: resistance and tolerance. Resistance involves genetic adaptations, such as mutations or the acquisition of resistance genes, allowing bacteria to grow despite antibiotics. These traits are heritable. Tolerance, on the other hand, is a phenotypic adaptation where bacteria survive temporary antibiotic exposure without replicating, often by entering a persister state or receiving protection from the biofilm's extracellular matrix. Unlike resistance, tolerance is not genetically driven but allows bacteria to endure treatment and any adverse conditions and repopulate after antibiotics are removed or the environment is good enough to proliferate again [89, 131]. These additional complexities were suggested as the next logical step in refining our understanding of biofilm dynamics, particularly in environments where biofilms are subjected to external stressors such as antibiotics. Building on these ideas, this chapter introduces these additional complexities into the biofilm growth models. This chapter focusses on two simplified one-dimensional biofilm growth models, referred to as Models 5 and 3 of Chapter 2. We focus on the interactions between proliferative, persister, and dead bacteria under antibiotic pressure and nutrient availability, aiming to isolate the antibiotic effects on biofilm dynamics. Specifically, our models examine the impact of a constant influx of antibiotics from an implant on biofilm growth and structure, without the added complexity of modelling the implant itself. Both models are analysed to understand the dynamics of biofilm growth and the detailed microbial structure in the presence of antibiotics, providing insights into the potential mechanisms that drive biofilm resilience. The novelty of this chapter lies in the incorporation of nutrient-regulated persister formation and reversion, enabling the investigation of how nutrient availability modulates persister dynamics and influences the overall biofilm structure and resilience under antibiotic stress. This physiologically realistic feature, absent from the models in previous studies, offers a new framework for capturing adaptive biofilm behaviour in nutrient-limited and antibiotic-exposed environments.

The primary goal of this chapter is to develop and analyse two biofilm growth models to obtain a deeper understanding of biofilm composition under antibiotic influence and its dependence on nutrient availability. In the first model of this chapter, Model 5, the focus is on understanding how a constant antibiotic concentration influences the biofilm growth and the interactions between proliferative, persister, and dead bacteria. The second model, Model 3, builds on Model 5 by introducing nutrient-dependent formation and reversion rates of persister bacteria. This addition allows the model to simulate how nutrient availability influences the resilience mechanism of the biofilm. The goal here is to explore how different levels of nutrient availability, ranging from sufficient to insufficient, affect biofilm resilience and structure in an antibiotic-laden environment. Through these models, we aim to elucidate how antibiotics and nutrient conditions shape biofilm growth and structure, providing a detailed analysis of the mechanisms that enable biofilms to persist even under continuous antibiotic exposure.

Outline

In this chapter, we build on the biofilm growth model introduced in Section 3.2 by extending it to include additional bacterial phenotypes, specifically persister and dead bacteria. The equations for Model 5 are presented in detail, along with the initial and boundary conditions applied. We then proceed to non-dimensionalise the model and perturb it around the initial condition. We then solve the model using MATLAB. A sensitivity analysis is conducted by varying the concentration of antibiotics delivered from the implant to assess its effects on bacterial phenotypes and overall biofilm growth. Additionally, we explore how changes in the formation and reversion rates of persister bacteria influence these dynamics. The study concludes by comparing the perturbed solution with the numerical solution.

Model 3 in Section 4.2 further develops the biofilm model by incorporating nutrient-dependent formation and reversion rates for persister bacteria. After nondimensionalising and solving it using MATLAB, we vary the constant influx of antibiotics and compare the outcomes with Model 5 to examine how nutrient dependency alters various factors such as bacterial concentration, EPS concentration, and biofilm thickness. Furthermore, we investigate the impact of varying nutrient availability from the bulk fluid, ranging from insufficient to intermediate to sufficient levels. This variation helps us gain deeper insights into antibiotic resilience and reveals how different levels of nutrient availability affect biofilm characteristics.

4.1 Biofilm model incorporating antibiotics and bacterial phenotypes (Model 5)

The model described in this section builds on Model 8 from Section 3.2, with key enhancements to include different bacterial phenotypes, such as persister and dead bacteria. We examine the effects of a constant antibiotic presence on biofilm structure, simplifying the scenario by excluding a more complex time-dependent antibiotic release from porous implant. Referred to as Model 5, in line with the nomenclature of Chapter 2, this model explores the impact of varying antibiotic concentrations and persistence formation and reversion rates on biofilm growth and composition. Additionally, we compare the numerical solutions with perturbed solutions over shorter time intervals to assess the model's accuracy and behaviour in early stages.

4.1.1 Model development

The model aims to capture the intricate microbial architecture of the biofilm, with particular emphasis on the dynamic interactions among proliferative, persister, and dead bacterial cells, along with the EPS. The antibiotic concentration, denoted as $C(x,t)$, is described by an unsteady advection-diffusion-reaction equation. This equation includes a reaction term that specifically addresses the degradation of the antibiotic due to its interactions within the environment. Transport of soluble species, including the antibiotic, occurs through the fluid-filled spaces that exist between the bacterial cells and EPS, making it dependent on the biofilm's water volume fraction, ϕ_{bio}.

At the boundary where the biofilm meets the implant, a constant influx of the antibiotic is enforced via a Dirichlet boundary condition. This boundary condition is simplified, as the primary goal is to study the effects of antibiotics in the most straightforward setting. However, this will be refined in the next chapter with the introduction of controlled antibiotic delivery from a porous implant, allowing for a more accurate representation of antibiotic distribution. Conversely, at the interface between the biofilm and the bulk fluid, an infinite sink condition is applied. This results in a rapid depletion of the antibiotic at this boundary, reflecting the scenario where the antibiotic quickly diffuses away into the surrounding fluid.

Nutrient transport within the biofilm is similarly governed by an unsteady advection-diffusion-reaction equation. The consumption of nutrients by the biomass is modelled using Monod kinetics, and the resulting biomass growth leads to an increase in the thickness of the biofilm. The water volume fraction continues to influence nutrient transport within the biofilm. A zero-flux boundary condition is imposed at $x = 0$, while at the boundary $x = L(t)$, nutrient influx is maintained through a Dirichlet boundary condition. This approach is similar to the one used for Model 8 in Section 3.2.

The characteristics of the microbial community, including bacterial phenotypes and EPS, and the evolution of the biofilm-fluid interface are modelled consistently with the approach detailed in Section 2.1.

In this model, we assume an incompressible system where the combined volume fraction of all components in the biofilm, including bacterial phenotypes, EPS, and water, remains constant and equals 1, following the same explanation as Model 8 in Section 3.2.1. The water volume fraction is set to a constant value of 0.8. As this follows similar dynamics to Model 8, the detailed explanation provided for these assumptions in Section 3.2.1 applies to this model as well.

4.1.2 Governing equations

The bacterial phenotypes considered in this model include proliferative bacteria, persister bacteria, and dead bacteria, in addition to the EPS. The behaviour of these components is captured by a set of partial differential equations, very similar to the equations presented in [84]. Fig. 2.1 illustrates the interactions between the different species and the concentrations within the biofilm, providing a visual representation of the processes modelled here. A thorough explanation of the physical interpretation of each term in the following equations is provided in Section 2.1, under the discussion of Model 1. The equation governing the dynamics of proliferative bacteria is given by:

$$\begin{aligned} B_t + (vB)_x &= D_B B_{xx} + (k_B - \kappa\phi_{bio}C)\frac{\mu\phi_{bio}S}{k_S + \phi_{bio}S}B - \max(\alpha_1\phi_{bio}C - \alpha_2, 0)B \\ &\quad - bB - k_F B + k_R B_p, \quad 0 < x < L(t),\ t > 0. \end{aligned} \tag{4.1}$$

The term, $D_B B_{xx}$, represents the diffusion of proliferative bacteria, accounting for the spreading of bacteria within the biofilm. The advective velocity v governs the movement of biomass within the biofilm ϕ_{bio} represents the water volume fraction within the biofilm, which modulates the effective transport and availability of nutrients. The growth of proliferative bacteria is modelled by the term $(k_B - \kappa\phi_{bio}C)\frac{\mu\phi_{bio}S}{k_S+\phi_{bio}S}B$, which depends on the availability of nutrients and is inhibited by the presence of antibiotics. Furthermore, the term $\max(\alpha_1\phi_{bio}C - \alpha_2, 0)B$ captures the death of bacteria due to antibiotic activity under low nutrient conditions. Cell death occurs when antibiotic concentration exceeds a critical threshold $\alpha_2/\phi_{bio}\alpha_1$, after which the death rate increases linearly with concentration. This approach is conceptually similar to [84]. See Fig. 4.1 for a clear visual representation of the max function. The term bB account for natural bacterial death, whereas $k_F B$ and $k_R B_p$ represent the transition between proliferative and persister states.

The dynamics of persister and dead bacteria are governed by the following equations:

$$(B_p)_t + (vB_p)_x = D_{B_p}(B_p)_{xx} + k_F B - k_R B_p, \quad 0 < x < L(t),\ t > 0, \tag{4.2}$$

$$\begin{aligned} (B_d)_t + (vB_d)_x &= D_{B_d}(B_d)_{xx} + \kappa\phi_{bio}C\frac{\mu\phi_{bio}S}{k_S + \phi_{bio}S}B \\ &\quad + \max(\alpha_1\phi_{bio}C - \alpha_2, 0)B + bB, \quad 0 < x < L(t),\ t > 0. \end{aligned} \tag{4.3}$$

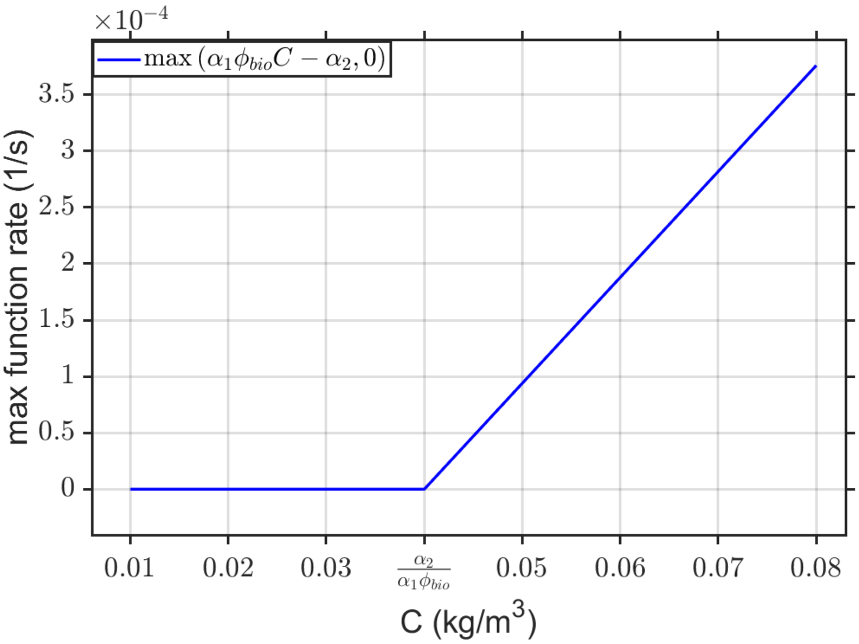

Figure 4.1: Plot of the antibiotic-induced death rate as a function of C. The parameter values considered for are from Table. 2.2. C is considered in the range $[0.01, 0.08]$ kg/m^3.

In the persister bacteria equation (4.2), the diffusion term $D_{B_p}(B_p)_{xx}$ captures the spatial spread of persister bacteria, while the terms $k_F B$ and $k_R B_p$ represent the transition between proliferative and persister states, complementing the corresponding terms in the proliferative bacteria equation. We have not considered growth of persister bacteria and the effects of antibiotic on them due to their dormant nature. In the dead bacteria equation (4.3), the diffusion term $D_{B_d}(B_d)_{xx}$ governs the spread of dead cells, and the terms $\kappa\phi_{bio}C\frac{\mu\phi_{bio}S}{k_S+\phi_{bio}S}B$ and $\max(\alpha_1\phi_{bio}C - \alpha_2, 0)B$ reflect bacteria killed by antibiotics, while bB represents natural death. These terms mirror those in the proliferative bacteria equation, showing how dead cells arise from the proliferative population due to both antibiotic effects and natural death.

The dynamic of the EPS is described by

$$E_t + (vE)_x = D_E E_{xx} + k_E \frac{\mu\phi_{bio}S}{k_S + \phi_{bio}S} B, \quad 0 < x < L(t),\ t > 0, \tag{4.4}$$

where the term $k_E \frac{\mu\phi_{bio}S}{k_S+\phi_{bio}S} B$ models the production of EPS from the proliferative bacteria, which is influenced by the availability of nutrients. The diffusion of EPS within the biofilm matrix is also considered. While EPS typically forms a relatively stationary matrix, including diffusion is not entirely inaccurate, as small-scale movement of EPS molecules can occur due to local reorganization or detachment processes within the biofilm [51].

The transport of nutrients and antibiotics within the biofilm is modelled by the following equations.

$$\begin{aligned} \phi_{bio}S_t+\phi_{bio}(vS)_x &= \phi_{bio}D_SS_{xx}-\frac{\mu\phi_{bio}S}{k_S+\phi_{bio}S}B, \quad 0<x<L(t),\ t>0, && (4.5)\\ \phi_{bio}C_t+\phi_{bio}(vC)_x &= \phi_{bio}D_CC_{xx}-k_c\phi_{bio}C, \quad 0<x<L(t),\ t>0. && (4.6)\end{aligned}$$

The equation of nutrients includes diffusion and advection, as well as the consumption of nutrients by bacteria, modelled by the term $\frac{\mu\phi_{bio}S}{k_S+\phi_{bio}S}B$. The equation of antibiotic transport also includes diffusion and advection. The degradation term $k_c\phi_{bio}C$ denotes deactivation of the antibiotic due to interaction with the environment.

The volume constraint is expressed by the equation:

$$1 = \phi_{bio}+\frac{B+B_p+B_d}{\rho_B}+\frac{E}{\rho_E}. \tag{4.7}$$

The advective velocity v of the biofilm constituents, which influences their transport and distribution, is determined by the following relationship.

$$v_x = \frac{1}{1-\phi}\left(\frac{k_B}{\rho_B}+\frac{k_E}{\rho_E}\right)\frac{\mu S}{k_S+S}B, \quad 0<x<L(t),\ t>0. \tag{4.8}$$

Equation (4.8) has been derived in the same manner as equation (3.28) for Model 8.

The evolution of biofilm thickness $L(t)$ over time is governed by the advective velocity at the biofilm-bulk fluid interface, thus controlling the expansion of the biofilm.

$$\frac{dL}{dt} = v(L), \quad t>0. \tag{4.9}$$

This represents the rate of biofilm expansion over time, determined by the velocity of the biomass at $x=L$.

Initial and boundary conditions

The initial conditions are given by

$$\begin{aligned} C(x,0) &= C_{in}, \quad 0<x<L(0), && (4.10)\\ S(x,0) &= S_0, \quad 0<x<L(0), && (4.11)\\ B(x,0) &= B_0e^{\frac{v(x,0)}{D_B}x}, \quad 0<x<L(0), && (4.12)\\ B_p(x,0) &= B_{p0}e^{\frac{v(x,0)}{D_{B_p}}x}, \quad 0<x<L(0), && (4.13)\\ B_d(x,0) &= B_{d0}e^{\frac{v(x,0)}{D_{B_d}}x}, \quad 0<x<L(0), && (4.14)\\ E(x,0) &= E_0e^{\frac{v(x,0)}{D_E}x}, \quad 0<x<L(0), && (4.15)\\ L(0) &= L_0. && (4.16)\end{aligned}$$

The initial condition of bacterial phenotypes and EPS is spatially dependent, ensuring consistency with the boundary conditions.

At the implant-biofilm interface ($x = 0$), zero-flux boundary conditions are imposed on the concentrations of nutrients and biomass constituents

$$-D_S S_x = -D_B B_x = -D_{B_p}(B_p)_x = -D_{B_d}(B_d)_x = -D_E E_x = 0, \text{ at } x = 0,\ t > 0. \tag{4.17}$$

In addition, the advective velocity at this boundary is assumed to be zero and antibiotic is assumed to have a Dirichlet boundary condition to represent the constant presence of antibiotic.

$$\begin{aligned} v &= 0, \quad \text{at } x = 0,\ t > 0, && (4.18)\\ C &= C_0, \quad \text{at } x = 0,\ t > 0. && (4.19) \end{aligned}$$

At the biofilm-bulk fluid interface ($x = L(t)$), the biomass constituents follow a zero-flux condition, while the nutrient concentration is governed by a Dirichlet boundary condition

$$\begin{aligned} S &= S_0, \quad \text{at } x = L(t),\ t > 0, && (4.20)\\ -D_B B_x + vB = -D_{B_p}(B_p)_x + vB_p &= -D_{B_d}(B_d)_x + vB_d \\ &= -D_E E_x + vE = 0, \quad \text{at } x = L(t),\ t > 0. && (4.21) \end{aligned}$$

All parameters used in the above equations are defined in detail in Table 2.2 and the variables in Table 2.1.

4.1.3 Non-dimensionalisation

To simplify the model and reduce the number of parameters, we introduce the following non-dimensional variables. This method of non-dimensionalisation is a relatively standard approach, as it highlights key dimensionless groups that govern the system's behaviour and simplifies the analysis. While not identical, similar non-dimensionalisations have been used in some studies [121, 142], making this a reasonable choice for analysing biofilm behaviour.

$$\overline{B} = \frac{B}{k_S}, \quad \overline{B}_p = \frac{B_p}{k_S}, \quad \overline{B}_d = \frac{B_d}{k_S}, \quad \overline{E} = \frac{E}{k_S}, \quad \overline{S} = \frac{S}{k_S}, \quad \overline{C} = \frac{\alpha_1 C}{\alpha_2},$$

$$\bar{t} = bt, \quad \bar{v} = \frac{v}{bL_0}, \quad \bar{x} = \frac{x}{L_0}.$$

Using these non-dimensional variables, the governing equations (4.1)–(4.9) are transformed into

$$\overline{B}_{\bar{t}} + (\bar{v}\overline{B})_{\bar{x}} = \overline{D}_B \overline{B}_{\bar{x}\bar{x}} + \left(G_1 - G_4 \phi_{bio}\overline{C}\right) \frac{\phi_{bio}\overline{S}}{1 + \phi_{bio}\overline{S}} \overline{B} - \max\left(\beta_1(\phi_{bio}\overline{C} - 1), 0\right) \overline{B}$$

$$
\begin{aligned}
& \quad -\overline{B}-\beta_2\overline{B}+\beta_3\overline{B}_p, \quad 0<\overline{x}<\overline{L}(\overline{t}),\ \overline{t}>0, && (4.22)\\
(\overline{B}_p)_{\overline{t}}+(\overline{v}\overline{B}_p)_{\overline{x}} &= \overline{D}_{B_p}(\overline{B}_p)_{\overline{x}\overline{x}}+\beta_2\overline{B}-\beta_3\overline{B}_p, \quad 0<\overline{x}<\overline{L}(\overline{t}),\ \overline{t}>0, && (4.23)\\
(\overline{B}_d)_{\overline{t}}+(\overline{v}\overline{B}_d)_{\overline{x}} &= \overline{D}_{B_d}(\overline{B}_d)_{\overline{x}\overline{x}}+G_4\phi_{bio}\overline{C}\frac{\phi_{bio}\overline{S}}{1+\phi_{bio}\overline{S}}\overline{B} \\
&\quad +\max\big(\beta_1(\phi_{bio}\overline{C}-1),0\big)\,\overline{B}+\overline{B}, \quad 0<\overline{x}<\overline{L}(\overline{t}),\ \overline{t}>0, && (4.24)\\
\overline{E}_{\overline{t}}+(\overline{v}\overline{E})_{\overline{x}} &= \overline{D}_E\overline{E}_{\overline{x}\overline{x}}+G_2\frac{\phi_{bio}\overline{S}}{1+\phi_{bio}\overline{S}}\overline{B}, \quad 0<\overline{x}<\overline{L}(\overline{t}),\ \overline{t}>0, && (4.25)\\
\phi_{bio}\overline{S}_{\overline{t}}+\phi_{bio}(\overline{v}\overline{S})_{\overline{x}} &= \phi_{bio}\overline{D}_S\overline{S}_{\overline{x}\overline{x}}-G_3\frac{\phi_{bio}\overline{S}}{1+\phi_{bio}\overline{S}}\overline{B}, \quad 0<\overline{x}<\overline{L}(\overline{t}),\ \overline{t}>0, && (4.26)\\
\phi_{bio}\overline{C}_{\overline{t}}+\phi_{bio}(\overline{v}\overline{C})_{\overline{x}} &= \phi_{bio}\overline{D}_C\overline{C}_{\overline{x}\overline{x}}-\beta_4\phi_{bio}\overline{C}, \quad 0<\overline{x}<\overline{L}(\overline{t}),\ \overline{t}>0, && (4.27)\\
1 &= \phi_{bio}+\frac{\overline{B}+\overline{B}_p+\overline{B}_d}{\overline{\rho}_B}+\frac{\overline{E}}{\overline{\rho}_E}, && (4.28)\\
\overline{v}_{\overline{x}} &= \frac{1}{1-\phi_{bio}}\left(\frac{k_B}{\overline{\rho}_B}+\frac{k_E}{\overline{\rho}_E}\right)G_3\frac{\phi_{bio}\overline{S}}{1+\phi_{bio}\overline{S}}\overline{B}, \quad 0<\overline{x}<\overline{L}(\overline{t}),\ \overline{t}>0, && (4.29)\\
\frac{d\overline{L}}{d\overline{t}} &= \overline{v}(\overline{L}), \quad \overline{t}>0. && (4.30)
\end{aligned}
$$

The non-dimensional initial conditions are given by

$$
\begin{aligned}
\overline{C}(\overline{x},0) &= \overline{C}_{in}, \quad 0<\overline{x}<\overline{L}(0), && (4.31)\\
\overline{S}(\overline{x},0) &= \overline{S}_0, \quad 0<\overline{x}<\overline{L}(0), && (4.32)\\
\overline{B}(\overline{x},0) &= \overline{B}_0 e^{\frac{\overline{v}(\overline{x},0)}{\overline{D}_B}\overline{x}}, \quad 0<\overline{x}<\overline{L}(0), && (4.33)\\
\overline{B}_p(\overline{x},0) &= \overline{B}_{p0} e^{\frac{\overline{v}(\overline{x},0)}{\overline{D}_{B_p}}\overline{x}}, \quad 0<\overline{x}<\overline{L}(0), && (4.34)\\
\overline{B}_d(\overline{x},0) &= \overline{B}_{d0} e^{\frac{\overline{v}(\overline{x},0)}{\overline{D}_{B_d}}\overline{x}}, \quad 0<\overline{x}<\overline{L}(0), && (4.35)\\
\overline{E}(\overline{x},0) &= \overline{E}_0 e^{\frac{\overline{v}(\overline{x},0)}{\overline{D}_E}\overline{x}}, \quad 0<\overline{x}<\overline{L}(0), && (4.36)\\
\overline{L}(0) &= \overline{L}_0. && (4.37)
\end{aligned}
$$

The boundary conditions (4.17)–(4.21) are similarly transformed into their non-dimensional forms as follows

$$
\begin{aligned}
-\overline{D}_S\overline{S}_{\overline{x}}=-\overline{D}_B\overline{B}_{\overline{x}}=-\overline{D}_{B_p}(\overline{B}_p)_{\overline{x}} &= -\overline{D}_{B_d}(\overline{B}_d)_{\overline{x}} \\
&= -\overline{D}_E\overline{E}_{\overline{x}}=0, \quad \text{at } \overline{x}=0,\ \overline{t}>0, && (4.38)\\
\overline{v} &= 0, \quad \text{at } \overline{x}=0,\ \overline{t}>0, && (4.39)\\
\overline{C} &= \overline{C}_0, \quad \text{at } \overline{x}=0,\ \overline{t}>0, && (4.40)\\
\overline{S} &= \overline{S}_0, \quad \text{at } \overline{x}=\overline{L}(\overline{t}),\ \overline{t}>0, && (4.41)\\
-\overline{D}_B\overline{B}_{\overline{x}}+\overline{v}\overline{B}=-\overline{D}_{B_p}(\overline{B}_p)_{\overline{x}}+\overline{v}\overline{B}_p &= -\overline{D}_{B_d}(\overline{B}_d)_{\overline{x}}+\overline{v}\overline{B}_d \\
&= -\overline{D}_E\overline{E}_{\overline{x}}+\overline{v}\overline{E}=0, \quad \text{at } \overline{x}=\overline{L}(\overline{t}),\ \overline{t}>0. && (4.42)
\end{aligned}
$$

The dimensionless parameters for the above model are defined as

$$\overline{D}_B = \frac{D_B}{bL_0^2}, \quad \overline{D}_{B_p} = \frac{D_{B_p}}{bL_0^2}, \quad \overline{D}_{B_d} = \frac{D_{B_d}}{bL_0^2}, \quad \overline{D}_E = \frac{D_E}{bL_0^2}, \quad \overline{D}_S = \frac{D_S}{bL_0^2}, \quad \overline{D}_C = \frac{D_C}{bL_0^2},$$

$$G_1 = \frac{k_B\mu}{b}, \quad G_2 = \frac{k_E\mu}{b}, \quad G_3 = \frac{\mu}{b}, \quad G_4 = \kappa\frac{\alpha_2\mu}{\alpha_1 b}, \quad \beta_1 = \frac{\alpha_2}{b}, \quad \beta_2 = \frac{k_F}{b}, \quad \beta_3 = \frac{k_R}{b}, \quad \beta_4 = \frac{k_C}{b},$$

$$\overline{\rho}_B = \frac{\rho_B}{k_S}, \quad \overline{\rho}_E = \frac{\rho_E}{k_S}, \quad \overline{B}_0 = \frac{B_0}{k_S}, \quad \overline{B}_{p0} = \frac{B_{p0}}{k_S}, \quad \overline{B}_{d0} = \frac{B_{d0}}{k_S}, \quad \overline{E}_0 = \frac{E_0}{k_S}, \quad \overline{S}_0 = \frac{S_0}{k_S},$$

$$\overline{C}_{in} = \frac{\alpha_1 C_{in}}{\alpha_2}, \quad \overline{C}_0 = \frac{\alpha_1 C_0}{\alpha_2}, \quad \overline{L}_0 = \frac{L_0}{L_0} = 1.$$

4.1.4 Perturbation of the model

To gain insight into the behaviour of the system for early time, we introduce perturbations to the variables around their initial values. This approach allows us to explore how small deviations from the initial state evolve over time. For simplicity in calculation and notation, we now omit the bars on the non-dimensionalised variables.

The perturbed variables are defined as follows:

$$B(x,t) = B_0 + B_1(x,t), \tag{4.43}$$

$$B_p(x,t) = B_{p0} + B_{p1}(x,t), \tag{4.44}$$

$$B_d(x,t) = B_{d0} + B_{d1}(x,t), \tag{4.45}$$

$$E(x,t) = E_0 + E_1(x,t), \tag{4.46}$$

$$S(x,t) = S_0 + S_1(x,t), \tag{4.47}$$

$$C(x,t) = C_{in} + C_1(x,t), \tag{4.48}$$

$$v(x,t) = v_0 + v_1(x,t), \tag{4.49}$$

where $B_1, B_{p1}, B_{d1}, E_1, S_1, C_1, v_0, v_1$ are the unknown small perturbation functions that will be determined.

To determine the leading order term v_0, we substitute the initial values B_0, S_0 into equation (4.29), yielding:

$$v_0 = k\frac{\phi_{bio}S_0}{1+\phi_{bio}S_0}B_0 x, \tag{4.50}$$

where $k = \frac{1}{1-\phi_{bio}}\left(\frac{k_B}{\rho_B} + \frac{k_E}{\rho_E}\right)$.

Next, by substituting the perturbed variables from equations (4.43)–(4.49) into the proliferative bacteria equations (4.22) we obtain the following expressions:

$$\begin{aligned}(B_0+B_1)_t+[(v_0+v_1)(B_0+B_1)]_x &= (G_1-G_4\phi_{bio}(C_{in}+C_1))\frac{\phi_{bio}(S_0+S_1)}{1+\phi_{bio}(S_0+S_1)}(B_0+B_1)\\ &\quad -\max(\beta_1(\phi_{bio}(C_{in}+C_1)-1),0)(B_0+B_1)\\ &\quad -(\beta_2+1)(B_0+B_1)+\beta_3(B_{p0}+B_{p1}).\end{aligned}$$

Keeping only terms up to first order in perturbations, substituing the expression for v_0 (4.50) and using the fact that B_0, C_{in}, and S_0 are constants, the expression simplifies to:

$$\begin{aligned}(B_1)_t &= (G_1-G_4\phi_{bio}C_{in})\frac{\phi_{bio}S_0}{1+\phi_{bio}S_0}B_0+\beta_3B_{p0}-(\beta_2+1)B_0\\ &\quad -\max(\beta_1(\phi_{bio}C_{in}-1),0)B_0-k\frac{\phi_{bio}S_0}{1+\phi_{bio}S_0}B_0^2.\end{aligned}$$

Integrating in time gives:

$$\begin{aligned}B_1(t) &= t\Bigg[(G_1-G_4\phi_{bio}C_{in})\frac{\phi_{bio}S_0}{1+\phi_{bio}S_0}B_0+\beta_3B_{p0}-(\beta_2+1)B_0\\ &\quad -\max(\beta_1(\phi_{bio}C_{in}-1),0)B_0-k\frac{\phi_{bio}S_0}{1+\phi_{bio}S_0}B_0^2\Bigg].\end{aligned} \tag{4.51}$$

Following the same procedure as for B_1, we obtain:

$$B_{p1} = t\left[\beta_2B_0-\beta_3B_{p0}-k\frac{\phi_{bio}S_0}{1+\phi_{bio}S_0}B_0B_{p0}\right], \tag{4.52}$$

$$B_{d1} = t\left[G_4\frac{\phi_{bio}C_{in}\phi_{bio}S_0}{1+\phi_{bio}S_0}B_0-B_0-\max(\beta_1(\phi_{bio}C_{in}-1),0)-k\frac{\phi_{bio}S_0}{1+\phi_{bio}S_0}B_0B_{d0}\right], \tag{4.53}$$

$$E_1 = t\left[G_2\frac{\phi_{bio}S_0}{1+\phi_{bio}S_0}B_0-k\frac{\phi_{bio}S_0}{1+\phi_{bio}S_0}B_0E_0\right], \tag{4.54}$$

$$S_1 = -t\left[G_3\frac{\phi_{bio}S_0}{1+\phi_{bio}S_0}B_0+k\frac{\phi_{bio}S_0}{1+\phi_{bio}S_0}B_0S_0\right], \tag{4.55}$$

$$C_1 = -t\left[\beta_4\phi_{bio}C_{in}+k\frac{\phi_{bio}S_0}{1+\phi_{bio}S_0}B_0C_{in}\right], \tag{4.56}$$

$$L_1 = t\left[k\frac{\phi_{bio}S_0}{1+\phi_{bio}S_0}B_0L_0\right]. \tag{4.57}$$

The first-order velocity perturbation v_1 is then found to be:

$$v_1 = k\phi_{bio}\left[\frac{B_1S_0}{1+\phi_{bio}S_0}+\frac{B_0S_1}{1+\phi_{bio}S_0}-\frac{B_0S_0\phi_{bio}S_1}{(1+\phi_{bio}S_0)^2}\right]x. \tag{4.58}$$

The perturbed solutions are then computed using the expressions for the perturbed variables $B_1, B_{p1}, B_{d1}, E_1, S_1, C_1, v_0, v_1$ derived above, allowing us to approximate the system's response to small deviations from the initial state.

4.1.5 Results and discussions

Following the computational procedure outlined in Section 3.2.4, we solve the non-dimensional equations (4.22)-(4.30) under the initial and boundary conditions specified in equations (4.31)-(4.42) using MATLAB. It is important to emphasise that all results presented pertain to non-dimensionalised variables, although we have omitted the overline notation in the figures for clarity. Additionally, we performed a sensitivity analysis to examine the effects of varying key parameters, such as antibiotic concentration. The analysis also explored scenarios where the formation rate of persister bacteria exceeds the reversion rate, as well as cases where the formation rate is lower than the reversion rate. The total concentration of any biofilm constituent at a given time refers to the concentration integrated across the spatial domain at that moment, effectively representing mass per unit area, an areal concentration. Furthermore, we compared the numerical solutions to perturbed solutions. Unless stated otherwise, all plots correspond to a final simulation time of 4 days. This time was selected because it showed significant behaviours and structures by that time. Unlike Model 8 in Section 3.2.5, which used a 20-day final time, this model involves continuous antibiotic exposure, causing the biofilm to mature more rapidly.

Effect of varying antitbiotic concentration (C_0)

Fig. 4.2(a) illustrates the temporal dynamics of proliferative bacterial concentrations under three distinct antibiotic conditions: $C_0 \times 5$ (red curve), baseline C_0 (black curve) and $C_0/5$ (blue curve), where C_0 is the non-dimensionalised value based on the base value of the parameter listed in Table 2.2. The results show that proliferative bacteria, which are directly susceptible to antibiotic action, exhibit a rapid decline in their population as the antibiotic concentration increases. In the case of the highest antibiotic concentration ($C_0 \times 5$), there is a swift decrease in the number of proliferative bacteria, reflecting an elevated rate of antibiotic-induced cell death. Conversely, under the lowest antibiotic concentration ($C_0/5$), the decline in proliferative bacteria is more gradual, as the reduced antibiotic stress allows these cells to persist for a longer period.

Persister cells, known for their antibiotic tolerance, are derived from proliferative cells. Fig. 4.2(b) illustrates that as the concentration of proliferative bacteria diminishes, the formation of persister cells correspondingly decreases. This pattern is consistent across all antibiotic conditions, with the most significant reduction in persisters observed under the highest antibiotic concentration. In this scenario, the rapid decline in proliferative cells results in fewer cells available to transition into persisters. In contrast, the lowest antibiotic concentration sustains a more gradual decrease in persister cells, as the slower reduction in proliferative bacteria permits continued, though declining, persister formation over time.

Fig. 4.2(c) highlights the accumulation of dead bacteria over time. Initially, higher antibiotic

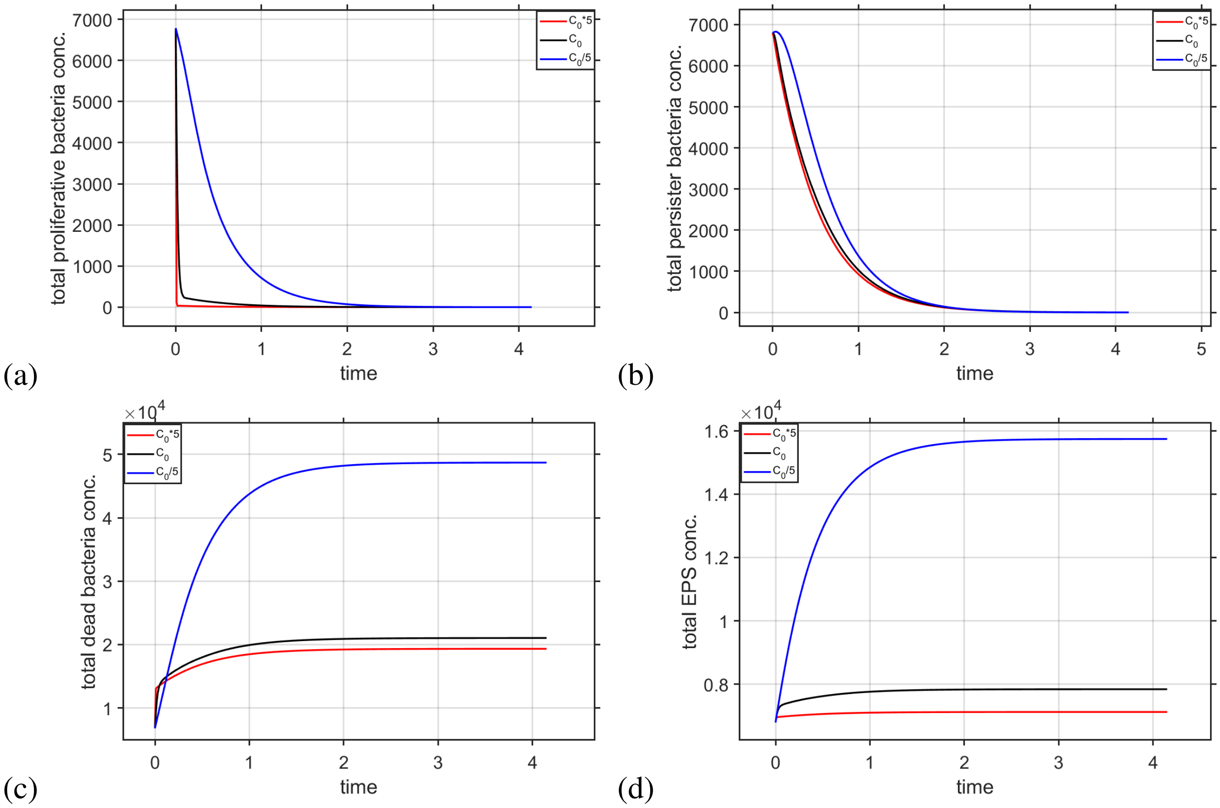

Figure 4.2: Effect of varying antibiotic concentration (C_0) on (a) temporal variation of total proliferative bacteria concentration, (b) temporal variation of total persister bacteria concentration, (c) temporal variation of total dead bacteria concentration, (d) temporal variation of total EPS concentration.

concentrations lead to a rapid increase in dead bacteria, as proliferative cells are quickly killed. However, as the population of proliferative bacteria decreases, the rate of accumulation of dead bacteria slows down, eventually reaching a plateau. In contrast, under the lowest antibiotic concentration, there is a sustained increase in dead bacteria over time, due to the larger population of proliferative cells over time that are gradually killed off. Interestingly, this result, where lower antibiotic concentrations lead to a higher total concentration of dead bacteria at later time points, is somewhat counterintuitive. One would expect higher antibiotic doses to lead to more dead cells, but in this case, the prolonged presence of proliferative cells in the low-antibiotic scenario allows for a continuous killing process over time, resulting in a higher accumulation of dead cells.

Fig. 4.2(d) reveals that lower antibiotic concentrations lead to a higher number of surviving proliferative cells, which in turn results in greater EPS production. In contrast, higher antibiotic concentrations rapidly reduce the number of viable proliferative cells, thereby limiting EPS production and leading to a lower overall EPS concentration over time.

In summary, higher antibiotic concentrations induce rapid proliferative cell death, reducing both the formation of persisters and EPS production due to the swift depletion of viable cells.

This initially leads to a high accumulation of dead cells, which stabilises as the number of proliferative bacteria decreases. On the other hand, lower antibiotic concentrations allow for sustained bacterial survival, resulting in a larger persister population, a greater accumulation of dead bacteria over time, and increased EPS production. The overall trend observed across all scenarios is a gradual decline in proliferative bacteria, which in turn limits the formation of persister cells as fewer proliferative bacteria remain to transition into this state.

The biofilm thickness over time is also affected by the concentration of antibiotics. In Fig. 4.3(a), the highest antibiotic concentration leads to the lowest biofilm thickness. This occurs because the antibiotic is highly effective at killing proliferative bacteria, which are the primary contributors to biofilm growth. As a result, there is less accumulation of proliferative cells, leading to fewer persister cells and dead bacteria. Consequently, the production of EPS is also limited, resulting in a thinner biofilm. In contrast, when the antibiotic concentration is low, the biofilm thickness is the highest. The insufficient antibiotic stress allows more proliferative bacteria to survive and multiply, contributing directly to biofilm growth. Additionally, the higher number of proliferative bacteria leads to the formation of more persister cells and eventually more dead cells as these proliferative cells are exposed to stress over time. The accumulation of dead cells and the continuous production of EPS further add to the biofilm thickness, resulting in a more substantial biofilm structure. For the intermediate antibiotic concentration, the biofilm thickness shows a moderate increase. This reflects a balance where the antibiotic is effective enough to kill a significant portion of proliferative bacteria, but not so much that it completely suppresses biofilm growth. The moderate levels of persister cells, dead bacteria, and EPS production contribute to a balanced biofilm thickness.

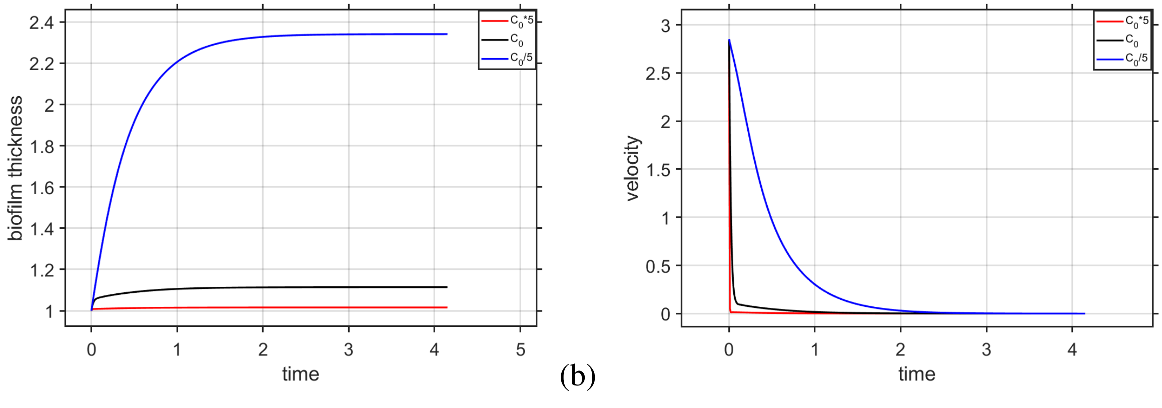

(a) (b)

Figure 4.3: Effect of varying antibiotic concentratin (C_0) on (a) temporal variation of biofilm thickness, (b) temporal variation of velocity at the biofilm-bulk fluid interface.

The velocity of the biofilm-bulk fluid interface reflects the rate at which the biofilm thickness changes, indicating how rapidly the biofilm is growing. Although the initial velocities appear to be the same across all antibiotic concentrations (see Fig. 4.3(b)), the differences in growth rates become apparent shortly after the initial time. The velocity decreases for all antibiotic concentrations over time, but at different rates. For the lowest antibiotic concentration, the velocity remains high in the early stages, suggesting rapid early growth of the biofilm. This is due to the high number of proliferative bacteria that are not effectively controlled by the antibiotic, leading to quick accumulation of biomass. As the antibiotic concentration increases, the velocity decreases more quickly after the initial time. For the highest antibiotic concentration, the velocity quickly approaches zero, as the antibiotic effectively kills the proliferative bacteria early on, preventing significant growth. The reduced formation of persister cells and dead bacteria, coupled with limited EPS production, results in a slower rate of biofilm expansion. Over time, the velocities in all cases converge towards zero as the biofilm reaches a steady state. This steady state results from the balance between bacterial proliferation, transition, cell death, and EPS production. For high antibiotic concentrations, this steady state is reached with a thinner biofilm, while for low concentrations, the biofilm is thicker due to the greater accumulation of all contributing factors, leading to a delayed stabilisation as seen from the blue curve in Fig. 4.3(b).

Now we examine the spatial profiles of different bacterial concentrations and EPS across the biofilm at final time, which refers to the last time point simulated in this study, under varying levels of antibiotic concentration. In Fig. 4.4(a), the proliferative bacteria concentration is lowest for the highest antibiotic concentration and highest for the intermediate antibiotic concentration. When the antibiotic is the highest, the intense antibiotic stress leads to more cell death, resulting in the lowest proliferative concentration. At the intermediate antibiotic concentration, there is a balance between bacterial growth and antibiotic-induced death, allowing the proliferative population to have the highest concentration at final time among the three scenarios. Interestingly, at the lowest antibiotic concentration, the proliferative concentration is not the highest, as one might expect, because more cells are alive initially, leading to a more gradual death over time, which results to intermediate proliferative bacteria concentration at final time. This results in a slightly lower proliferative concentration compared to the intermediate case, as some of the proliferative cells eventually die off.

In Fig. 4.4(b), the persister bacteria concentration is highest for the intermediate antibiotic concentration and lowest for the lowest antibiotic concentration. The intermediate antibiotic level creates the perfect environment for a balanced transformation between proliferative and persister cells. This results in the highest persister concentration, which is expected given the elevated proliferative concentration at this antibiotic level. When the antibiotic concentration is low, there is less stress on the proliferative bacteria, so they have a higher metabolic rate than persister formation rate. This leads to a higher proliferative population and eventually a higher death rate, but fewer persisters are formed. At the highest antibiotic concentration, fewer proliferative cells are present due to antibiotic-induced death. However, the increased antibiotic stress leads to greater persister formation, as the growth rate is suppressed, resulting in a moderate persister concentration.

In Fig. 4.4(c), the dead bacteria concentration is highest for the lowest antibiotic concentra-

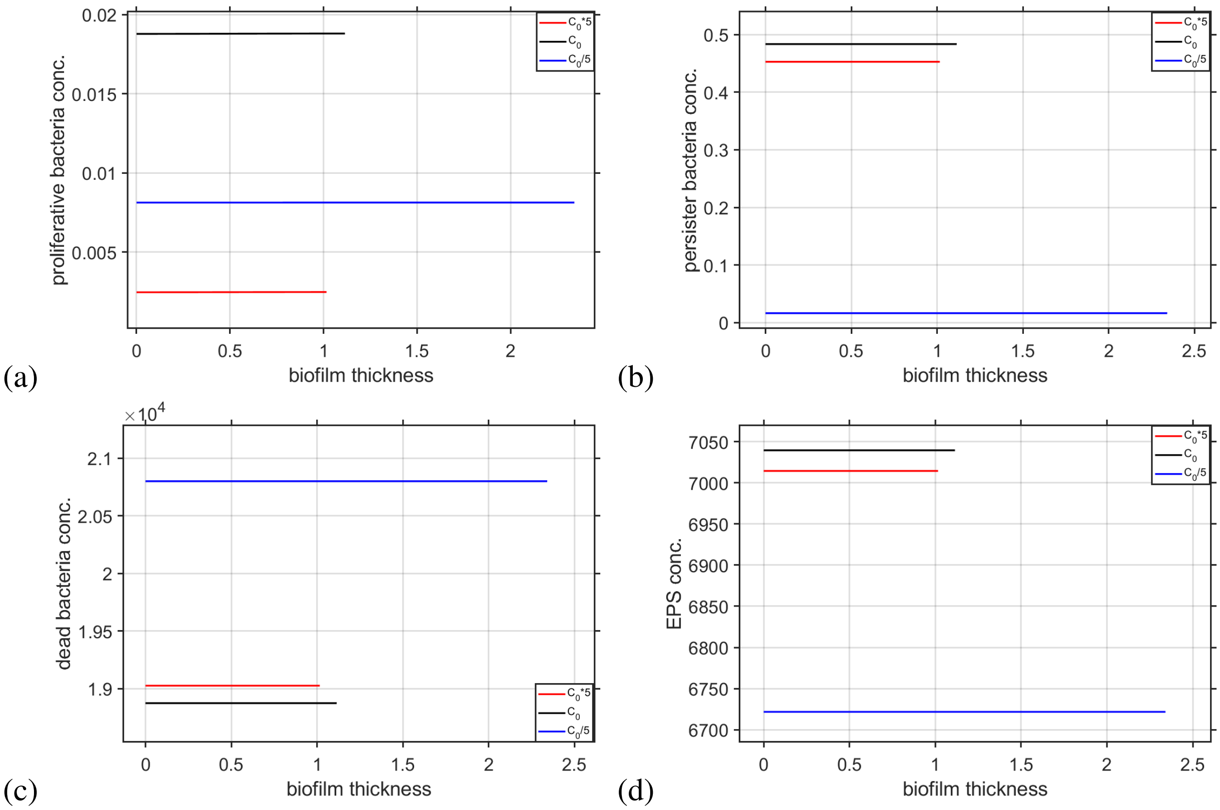

(a) (b) (c) (d)

Figure 4.4: Effect of varying antibiotic concentration (C_0) on (a) spatial variation of proliferative bacteria concentration at final time, (b) spatial variation of persister bacteria concentration at final time, (c) spatial variation of dead bacteria concentration at final time, (d) spatial variation of EPS concentration at final time.

tion and lowest for the intermediate antibiotic concentration. With the lowest antibiotic concentration, more proliferative bacteria survive initially, but over time, they gradually die off, leading to the highest concentration of dead bacteria at the final time. The intermediate antibiotic concentration strikes a balance between bacterial growth, death, and phenotypic transformations, resulting in the lowest dead bacteria concentration, as we see highest persister (Fig. 4.4(b)) and EPS (Fig. 4.4(d)) concentration in this case. For the highest antibiotic concentration, although the antibiotic is more potent, leading to more cell death initially, the overall number of proliferative bacteria is lower, so the final dead bacteria concentration is moderate.

In Fig. 4.4(d), the EPS concentration is highest for the intermediate antibiotic concentration and lowest for the lowest antibiotic concentration at final time. At the intermediate antibiotic level, a balance is maintained between the biomass constituents. This results in the highest EPS concentration, which is expected given the elevated proliferative concentration at this antibiotic level. When the antibiotic concentration is low, the bacteria focus more on growth since the metabolic rate will be higher and hence overtime more death bacteria will be produced, rather than on producing protective EPS, leading to the lowest EPS concentration. For the highest concentration of antibiotics, the stress on the proliferative cells causes them to produce more

EPS, since the growth of proliferative cells is suppressed. However, since these proliferative cells die off over time, the final EPS concentration is higher than in the low antibiotic case but lower than in the intermediate case.

At the highest antibiotic concentration, the proliferative population is minimised due to high cell death, but a significant portion of the surviving cells transitions to persisters, leading to moderate persister and EPS levels. This outcome highlights a potential risk in treatment strategies. If antibiotic treatment were stopped or nutrient conditions improved, these persisters could revert to proliferative states, allowing the biofilm to regrow, potentially leading to a resurgence of infection. At the intermediate antibiotic concentration, the balance between growth, death, and phenotypic transformations results in the highest proliferative, persister and EPS concentrations, with a corresponding lower death rate. When the antibiotic concentration is at its lowest, the focus shifts towards bacterial proliferation, eventually leading to the highest dead cell concentration but the lowest EPS and persister bacteria concentration as the biofilm matures. This suggests that while lower antibiotic doses may result in high initial bacterial survival, over time, more bacteria will die, but without sufficient persister or EPS formation, the biofilm may be less resilient overall. It is important to note that the temporal plots of the total concentrations (Fig. 4.2) refer to the cumulative amount of each biofilm constituent across the entire biofilm thickness at any given time. Therefore, even if the local concentration of a species is lower at a specific point, a larger biofilm thickness can result in a higher total concentration. This explains why a thicker biofilm, such as in the case of low antibiotic concentration, can have higher total concentrations of bacterial cells, even though the local concentrations are lower for some biomass constituents like persister and EPS (Fig. 4.4). This difference between local and total concentrations is important when considering treatment strategies, as targeting biofilm thickness alone might not fully address the underlying composition, particularly if persisters remain embedded within the biofilm matrix. Treatment approaches that consider both the biofilm's overall structure and its internal bacterial composition may be more effective in ensuring long-term biofilm eradication.

Fig. 4.5 show the spatial structure of the different biomass constituents (proliferative bacteria, persister bacteria, dead bacteria, and EPS) across the biofilm at the final time for various antibiotic concentrations (C_0). In previous analyses in Fig. 4.4, we explored how C_0 affected the concentration levels across the biofilm at the final time, where the concentrations appeared constant. However, the aim of these figures is to reveal the spatial structure more clearly. For this, the concentrations at each spatial point are normalised by the concentration at $x = 0$, which is the implant-biofilm boundary. This normalisation allows us to reveal potential spatial trends or patterns within the biofilm.

In Fig. 4.5(a), we observe a consistent spatial structure across all cases of C_0, for proliferative bacteria. In each case, the concentration is lowest at the implant-biofilm boundary, where the antibiotic concentration is highest, suppressing growth. As we move towards the biofilm-bulk fluid boundary, the normalised concentration of proliferative bacteria increases. This reflects the bacteria's reliance on nutrients, which are more available towards that boundary. The gradient seen in all three cases highlights the spatial advantage for proliferative bacteria in nutrient-rich regions far from the direct antibiotic influence.

The spatial structure of persister bacteria (Fig. 4.5(b)) is also consistent across different cases of antibiotic . In all cases, the persister concentration is highest at the implant-biofilm boundary, where the stress from the antibiotic induces cells to transition from a proliferative state into a persister state for survival, due to comparatively higher transition rate than supressed growth rate of proliferative bacteria. As we move towards the biofilm-bulk fluid boundary, where nutrients are more available and antibiotic pressure decreases, the persister concentration gradually decreases. This decline is in line with the reduced transition rate to persisters as the growth rate of proliferative gets higher. Despite differences in the levels of persister concentrations for different C_0 , the overall spatial distribution follows a similar trend for all antibiotic levels.

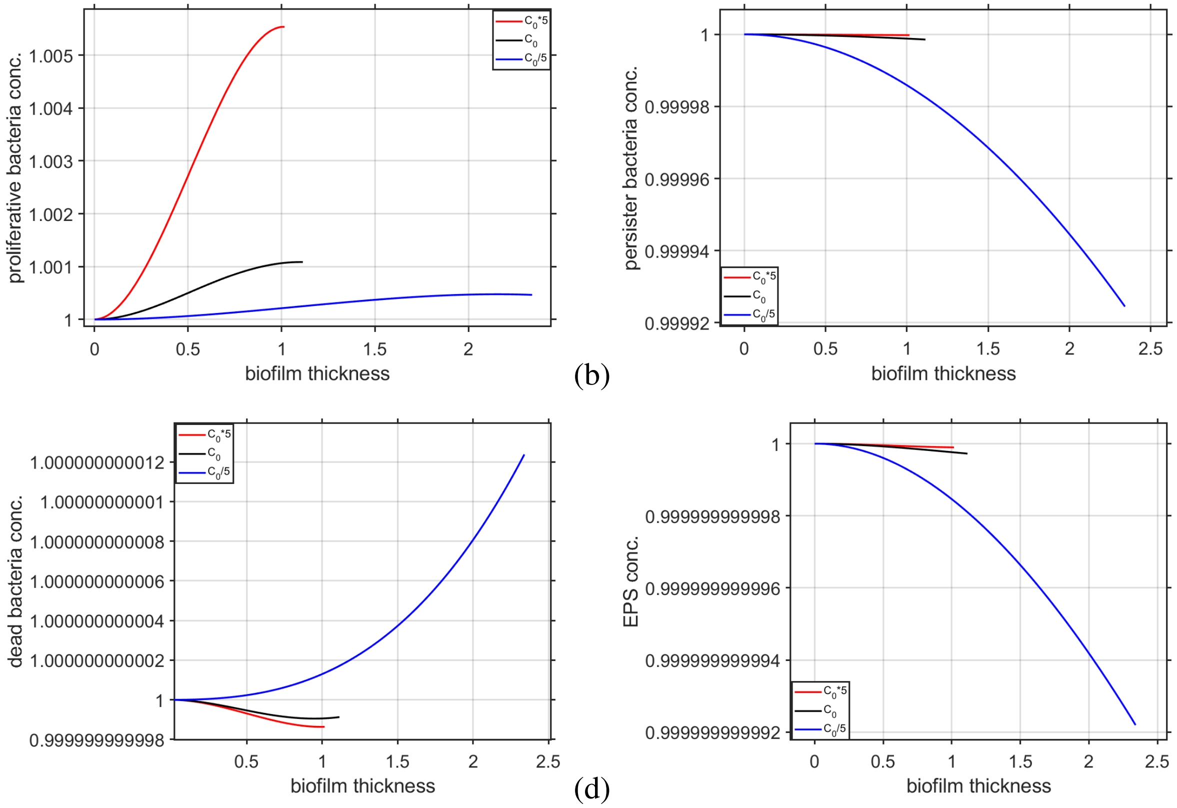

(a) (b) (c) (d)

Figure 4.5: Spatial variation of (a) proliferative bacteria, (b) persister bacteria, (c) dead bacteria, and (d) EPS at the final time, shown for varying antibiotic concentrations (C_0). In each plot, the concentrations are scaled by dividing the value at each spatial point by the concentration at $x = 0$.

In Fig. 4.5(c) the spatial structure of dead bacteria shows more variability compared to the other constituents, especially between different C_0 values. For lower antibiotic concentrations, we observe a significant increase in dead bacteria concentration as we move towards the biofilm-bulk fluid boundary. This pattern reflects the higher concentration of proliferative bacteria near the nutrient source, which leads to more cell death due to nutrient exhaustion and natural death over time. The dead bacteria accumulate in regions where proliferative activity was initially high. For intermediate and higher antibiotic concentrations, the spatial structure of dead bacteria exhibits a different pattern. In these cases, the concentration of dead bacteria decreases gradually from the implant boundary towards the biofilm-bulk fluid boundary, then shows a slight dip followed by an increase again near the biofilm-bulk fluid boundary. This structure arises because, under higher antibiotic pressure, more proliferative cells die near the implant boundary. However, towards the biofilm-bulk fluid boundary, there is less antibiotic concentration due to diffusion restrictions. As a result, the death rate is lower, leading to a dip. However, near the boundary with the bulk fluid, where there is still some proliferation occurring due to nutrient access, the dead bacteria concentration increases again as the remaining proliferative cells die.

The spatial distribution of EPS in Fig. 4.5(d) mirrors the pattern seen for persister cells. In all cases, EPS concentration is highest at the implant-biofilm boundary, where cells experience stress from the antibiotic and the EPS production rate gets much higher than the supressed growth rate. As we move towards the biofilm-bulk fluid boundary, the concentration of EPS decreases, with a more pronounced decline for lower antibiotic concentrations. This pattern is consistent with the tendency of cells near the implant boundary to produce EPS, while in nutrient-rich regions with fewer stressors, EPS production is minimised as the growth rate increases. The overall trend of EPS decreasing from the implant boundary towards the bulk fluid boundary is consistent across all antbiotic concentration scenarios.

In all subfigures of Fig. 4.5, the spatial structures are shaped by the competing effects of antibiotic stress from the implant-biofilm boundary and nutrient availability from the biofilm-bulk fluid boundary. The structures of the biomass constituents show very little variation across the biofilm, with very close values along the x-axis. Proliferative bacteria concentrate near the nutrient source, increasing towards the biofilm-bulk fluid boundary. In contrast, persister bacteria and EPS are concentrated near the implant boundary due to supressed growth rate of proliferative induced by antibiotic, with decreasing concentrations toward nutrient-rich regions. Dead bacteria show more variability: under lower antibiotic conditions, they accumulate near the biofilm-bulk fluid boundary, while higher antibiotic levels result in a more complex distribution, with a dip followed by an increase near the biofilm-bulk fluid boundary. These spatial patterns highlight how each biomass constituent responds to antibiotic and nutrient gradients across the biofilm.

Impact of persister formation and reversion rates

For the intermediate antibiotic scenario, Figs. 4.6 to 4.7 depict the temporal dynamics of bacterial populations, EPS concentration and biofilm thickness for a total of 100 days which refers to a non-dimensional time of 103.95. We consider two conditions: where the persister formation rate (k_F) is greater than the reversion rate (k_R) and vice versa. The baseline values for these parameters, as shown in Table 2.2, indicate that $k_R > k_F$. For the reversed case where $k_F > k_R$, we simply flipped the values, using the value of k_R in Table 2.2 as the value for k_F, and the value of k_F as the value for k_R.

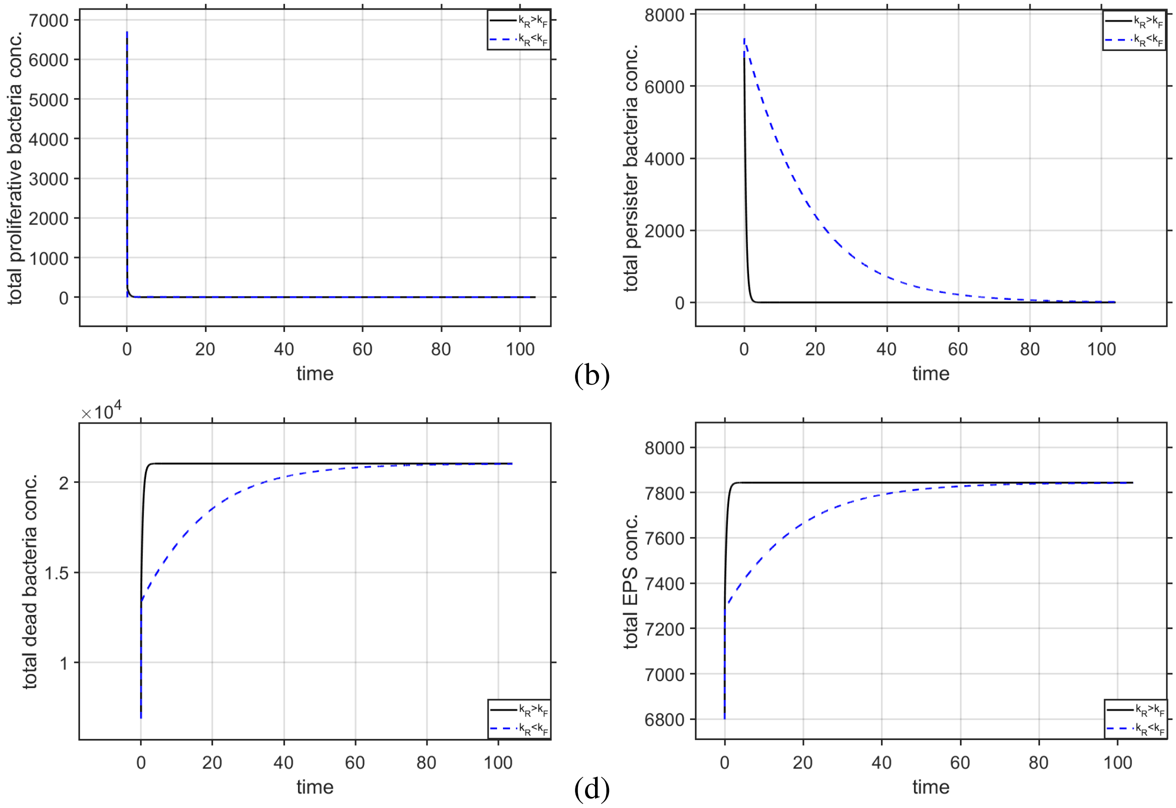

(a) (b) (c) (d)

Figure 4.6: Effect of reversed formation (k_F) and reversion (k_R) rate of persister bacteria on (a) temporal variation of total proliferative bacteria concentration, (b) temporal variation of total persister bacteria concentration, (c) temporal variation of total dead bacteria concentration, (d) temporal variation of total EPS concentration.

Fig. 4.6(a) illustrates that the total proliferative bacteria concentration remains nearly identical in both scenarios. This observation is logical because the antibiotic targets proliferative bacteria exclusively, leading to their rapid decline. When $k_R > k_F$, more proliferative bacteria revert from persisters, but these quickly succumb to the antibiotic, resulting in their death. Conversely, when $k_F > k_R$, proliferative cells are more frequently converted to persisters, reducing their numbers. This reduction in proliferative bacteria due to conversion and antibiotic action explains why the proliferative count does not differ significantly between the two cases.

Fig. 4.6(b) shows the behaviour of persister bacteria over time. When $k_F > k_R$, a higher persister population is sustained because more proliferative bacteria are converted to persisters, which are unaffected by the antibiotic. In contrast, when $k_R > k_F$, persister bacteria revert back to the proliferative state, making them susceptible to the antibiotic, leading to a quicker decline in their numbers. Despite this, both scenarios eventually converge to the same persister concentration because the system reaches an equilibrium where the formation and reversion rates balance out, leading to a steady state.

Fig. 4.6(c) displays the total dead bacteria concentration. Initially, the dead bacteria increase rapidly due to the initial antibiotic impact on proliferative bacteria. Over time, whether $k_F > k_R$ or $k_R > k_F$, the dead bacteria concentration converges to the same value. This occurs because, in both scenarios, the rate of cell death eventually stabilises as the populations of proliferative and persister bacteria decline, leading to fewer new deaths. However, the rate at which this equilibrium is reached differs. When $k_R > k_F$, the reversion to proliferative bacteria (and subsequent death) occurs faster, leading to a rapid initial increase in dead bacteria. In contrast, when $k_F > k_R$, the conversion of proliferative to persisters slows down the increase in dead bacteria, but the eventual accumulation reaches the same level.

Fig. 4.6(d) illustrates the total EPS concentration. This follows almost the same logic as the total dead bacteria. $k_R > k_F$ results in a rapid initial rise in EPS production. Conversely, when $k_F > k_R$, the conversion from proliferative to persister cells slows down the increase in EPS; however, the eventual accumulation ultimately reaches the same level.

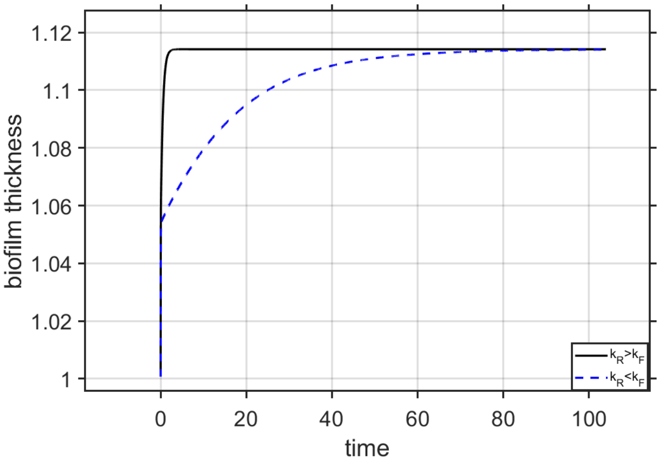

Figure 4.7: Effect of reversed formation (k_F) and reversion (k_R) rate of persister bacteria on temporal variation of biofilm thickness.

Initially, biofilm thickness increases rapidly in both cases, reflecting the rapid growth of the biofilm due to bacterial proliferation and EPS production (see Fig. 4.7). However, the dynamics of this growth differ depending on the relative rates of persister formation and reversion. When $k_R > k_F$, the biofilm thickness stabilises more quickly. This is because a higher reversion rate leads to more persister bacteria converting back to the proliferative state, which are then targeted by the antibiotic. As a result, the proliferative bacteria die, contributing to the initial increase in dead bacteria and EPS, which stabilises the biofilm structure early on. On the other hand, when $k_F > k_R$, the biofilm thickness increases more gradually and takes longer to stabilise. This is due to the higher rate of persister formation, which protects a portion of the bacterial population from the antibiotic. These persisters contribute to the slow and steady growth of the biofilm over a longer period. Eventually, however, both scenarios converge to the same biofilm thickness as the populations of proliferative, persister, and dead bacteria, along with EPS, reach equilibrium.

In the beginning, the different rates of bacterial transformation (formation and reversion) lead to distinct growth patterns, but as time progresses, the overall contributions of the proliferative, persister, and dead bacteria, along with EPS production, balance out. This equilibrium ensures that, despite the different initial growth rates, the biofilm thickness stabilises at the same level in both scenarios. This transition between proliferative and persister states will be explored further in a later section in this chapter and the following chapter, where a more sophisticated approach to modelling these transitions is introduced.

Comparison of numerical and perturbed solutions for early-time

Finally, we compare our numerical results with those of the perturbed solution for smaller times. Fig. 4.8 shows the comparison between the numerical solutions and the solution achieved analytically by perturbing the variables around the initial values. The maximum non-dimensional time considered here is 0.1. Initially, the biofilm thickness predicted by both the numerical and perturbed solutions is identical, as reflected by the overlapping curves. This initial agreement is expected because, at the very beginning of the simulation, the influence of the perturbation is minimal, making the system's response predominantly governed by the initial condition. As time progresses, however, the perturbed solution begins to diverge slightly from the numerical solution. This divergence occurs because the perturbation, though small, introduces a gradual deviation in the system's dynamics. Over time, the term $L_1(t)$ becomes more influential, causing the perturbed solution to predict a slightly larger biofilm thickness compared to the unperturbed numerical solution. This divergence, albeit small within the observed time frame, underscores the sensitivity of the biofilm growth model to initial conditions. It suggests that even minor perturbations can lead to noticeable differences in the predicted outcomes, especially as time increases.

Performing a perturbation around the initial time is useful because it provides a simplified analytical framework to approximate the system's behavior near the initial conditions, making it computationally less intensive and easier to solve. This approach helps validate the numerical model by ensuring that early-stage dynamics predicted by the full model align with those obtained through analytical approximations. In addition, it offers information on the sensitivity of the system, as small deviations from the initial condition can propagate over time, influencing the growth of the biofilm.

In this comparison, we have focussed on the temporal variation of biofilm thickness, as it is a key indicator of the overall system dynamics. The reason we did not show other plots, like those seen in previous studies (such as different bacterial phenotypes), is that the biofilm thickness provides the most direct and observable measure of the biofilm's macroscopic growth. It

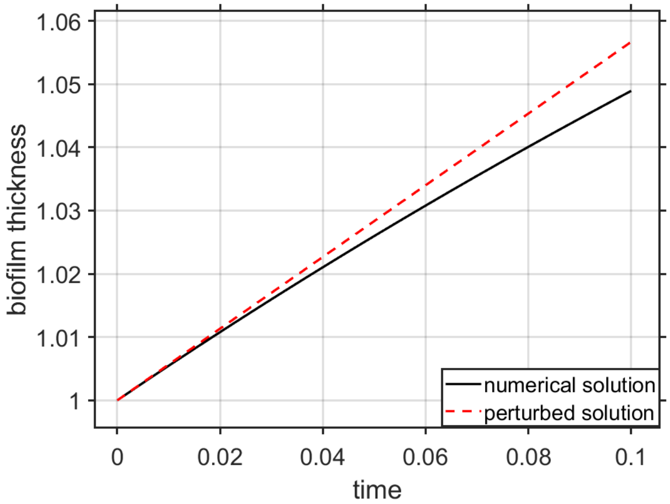

Figure 4.8: Temporal variation of biofilm thickness for numerical and perturbed solution for total time of 0.1 days.

encapsulates the cumulative effect of multiple factors, such as nutrient availability, bacterial proliferation, and EPS production, which are affected by the perturbation. Although other quantities such as bacterial concentration could be analysed in a similar manner, biofilm thickness gives a straightforward and representative comparison between the numerical and perturbed solutions in this early-stage validation.

4.2 Introducing nutrient-dependent formation and reversion rate of persister bacteria (Model 3)

In this section, we develop a biofilm model that accounts for the dynamic response of bacterial phenotypes to varying nutrient conditions within the biofilm. Unlike Model 5 in Section 4.1, which assumed constant rates for the formation and reversion of persister cells, this model introduces a more realistic nutrient-dependent mechanism. Specifically, the model captures how bacteria switch between proliferative and persister states in response to nutrient availability, incorporating critical nutrient thresholds that dictate these transitions. This approach is motivated by experimental and theoretical studies that demonstrate the strong influence of nutrient conditions on bacterial state transitions. For example, [7] showed that nutrient starvation triggers persister formation, while [99] highlighted the importance of metabolic cues in persister dynamics. This model offers a more detailed representation of biofilm behaviour under nutrient-limited conditions. The core characteristics of the model remain consistent with those described in Section 4.1. We refer to this model as Model 3, consistent with the nomenclature used in Chapter 2. The governing equations are solved numerically using MATLAB. We also examine the impact of varying antibiotic concentrations at the implant-biofilm boundary and nutrient concentrations at the biofilm-bulk fluid boundary.

4.2.1 Model development

This model builds upon the foundational structure of the model in Section 4.1 by introducing a critical aspect of biofilm dynamics: the nutrient-dependent transitions between proliferative and persister bacterial phenotypes. The primary objective of this model is to elucidate how varying nutrient concentrations within the biofilm influence the formation and reversion of persister cells, thereby impacting the overall biofilm structure and resilience. The approach taken for these nutrient-dependent transition rates follows the same conceptual framework as described in Section 2.1. Aside from the nutrient-dependent formation and reversion rates, all other characteristics of the model are consistent with those of the model described in Section 4.1.

The model incorporates two key nutrient thresholds, S_1 and S_2, which govern the transition rates between the proliferative and persister states, thereby dictating the biofilm's structural and functional responses to changes in nutrient availability.

When the nutrient concentration within the biofilm falls below the lower threshold S_1, the environment is deemed insufficient for sustaining active bacterial proliferation. In this scenario, the model assumes that proliferative bacteria transition into the persister state as a survival strategy. The persister state is characterised by reduced metabolic activity, which allows bacteria to withstand harsh conditions, including nutrient deprivation and antibiotic exposure. In this nutrient-insufficient environment, the formation rate of persisters is maximised to ensure a rapid shift from the proliferative to the persister state. Concurrently, the reversion rate from the persister to the proliferative state is effectively set to zero, reflecting the unsuitability of the environment for bacterial growth.

In contrast, when the nutrient concentration exceeds the upper threshold S_2, the environment is rich enough to support bacterial growth and division. Under these conditions, the model assumes that persister cells revert to the proliferative state to take advantage of the abundant nutrients. This transition is driven by maximising the reversion rate, allowing persister cells to re-enter the cell cycle and proliferate. The formation rate for the persister bacteria is set to zero, as the environmental conditions do not necessitate the formation of persister cells. This dynamic allows the bacterial population to exploit the favourable nutrient conditions to expand the biofilm structure.

In the intermediate nutrient range, where the concentration of nutrient is in between S_1 and S_2, the model captures a more complex behaviour. Here, both the formation and reversion of persister bacteria from proliferative bacteria occur simultaneously. Neither of the rates are zero, meaning that both processes are active, but to varying extents depending on the nutrient concentration. As the nutrient concentration increases from S_1 to S_2, the rate of persister formation gradually decreases, while the rate of reversion to the proliferative state increases. This balance reflects the bacterial community's adaptive response to moderate nutrient levels, where some bacteria remain in the persister state as a precautionary measure, while others revert to proliferation to exploit the available resources. This interpolation between the two rates provides a realistic representation of biofilm dynamics, capturing the gradual adaptation of the bacterial population to the changing nutrient environment at every space and time point.

Nutrient transport within the biofilm is governed by an unsteady advection-diffusion-reaction equation, as in Model 5. The consumption of nutrients by the biomass follows Monod kinetics, and the resulting growth of biomass contributes to the expansion of the biofilm. The water volume fraction remains a critical parameter, as it influences the porosity of the biofilm matrix, which in turn affects the diffusion and advection of nutrients and other soluble species within the biofilm.

Boundary conditions are applied to reflect the interaction between the biofilm and its surrounding environment. At the implant-biofilm interface, a zero-flux boundary condition is imposed stating that nutrient cannot travel to the implant medium. At the biofilm-fluid interface, a Dirichlet boundary condition is applied to maintain a constant influx of nutrients, simulating a steady supply.

In addition to nutrient transport, the antibiotic concentration within the biofilm is also described by an unsteady advection-diffusion-reaction equation. This equation incorporates a reaction term specifically addressing the degradation of the antibiotic due to its interactions within the biofilm environment. The transport of soluble species, including the antibiotic, occurs through the fluid-filled spaces that exist between the bacterial cells and the EPS, making it dependent on the biofilm's water volume fraction. At the boundary where the biofilm meets the implant, a constant presence of the antibiotic is enforced via a Dirichlet boundary condition. Conversely, at the interface between the biofilm and the bulk fluid, an infinite sink condition is applied. This results in a rapid depletion of the antibiotic at this boundary, reflecting the scenario in which the antibiotic quickly diffuses into the surrounding fluid.

The microbial community within the biofilm, including proliferative bacteria, persister cells, dead bacteria, and EPS, is modelled consistently with the approach used in Model 5 in Section 4.1 of this chapter. However, the introduction of nutrient-dependent transition rates adds a significant layer of complexity to the model. The assumption of an incompressible system is is retained, making the sum of the volume fractions of biomass constituents and water equal to 1, similar to Model 8 and Model 5. The water volume fraction fixed at 0.8, following the same explanation in Section. 3.2.1.

4.2.2 Governing equations

The dynamics of the biofilm, including interactions among different bacterial phenotypes, EPS, nutrients, and antibiotics, are governed by a series of equations. This section particularly emphasises the nutrient-dependent formation and reversion rates of persister bacteria, while other aspects of the model mirror those described in Section 4.1.2. A thorough explanation of the physical interpretation of each term in the following equations is provided in Section 2.1, under the discussion of Model 1. These equations, in combination with the initial and boundary conditions, establish a thorough mathematical framework for simulating biofilm behaviour. To avoid redundancy, only the equations for proliferative and persister bacteria are mentioned here, as they differ from Model 5. All other equations remain the same as in Model 5 and are explained in detail in Section 4.1.2.

In this model, the bacterial phenotypes under consideration include proliferative bacteria, persister bacteria, and dead bacteria, as well as the EPS. The proliferative bacteria dynamics are described by a partial differential equation that accounts for various factors: diffusion, advection, and reaction terms influenced by nutrient availability and antibiotic presence. The new equation is given as

$$\begin{aligned} B_t + (vB)_x &= D_B B_{xx} + (k_B - \kappa\phi_{bio}C)\frac{\mu\phi_{bio}S}{k_S + \phi_{bio}S}B - \max(\alpha_1\phi_{bio}C - \alpha_2, 0)B - bB \\ &\quad - \max\left(k_F\frac{S_2 - S}{S_2 - S_1}, 0\right)B \\ &\quad + \max\left(k_R\frac{S - S_1}{S_2 - S_1}, 0\right)B_p, \quad 0 < x < L(t),\ t > 0. \end{aligned} \tag{4.59}$$

The advective velocity v governs the movement of biomass within the biofilm ϕ_{bio} represents the water volume fraction within the biofilm, which modulates the effective transport and availability of nutrients. In this equation, the growth of proliferative bacteria is modulated by nutrient concentration and antibiotic concentration, with growth described by the term $(k_B - \kappa\phi_{bio}C)\frac{\mu\phi_{bio}S}{k_S+\phi_{bio}S}B$. Antibiotic-induced bacterial death under low nutrient conditions is captured by $\max(\alpha_1\phi_{bio}C - \alpha_2, 0)B$, while bB represents natural bacterial death. Transitions between proliferative and persister states, driven by nutrient concentration, are modelled by the terms $\max\left(k_F\frac{S_2-S}{S_2-S_1}, 0\right)B$ and $\max\left(k_R\frac{S-S_1}{S_2-S_1}, 0\right)B_p$. When $S \le S_1$, the term representing reversion from persister bacteria to proliferative bacteria, $\max\left(k_R\frac{S-S_1}{S_2-S_1}, 0\right)B_p$, is zero. When $S \ge S_2$, the term representing formation of persister bacteria from proliferative bacteria, $\max\left(k_F\frac{S_2-S}{S_2-S_1}, 0\right)B$, is zero. When $S_1 < S < S_2$, both the terms are non-zero. See Fig. 4.9 for a clear visual representation of the max functions.

The dynamics of persister is governed similarly by partial differential equations. For persister bacteria, the governing equation includes advection, diffusion and nutrient-driven transition terms, as expressed by

$$\begin{aligned} (B_p)_t + (vB_p)_x &= D_{B_p}(B_p)_{xx} + \max\left(k_F\frac{S_2 - S}{S_2 - S_1}, 0\right)B \\ &\quad - \max\left(k_R\frac{S - S_1}{S_2 - S_1}, 0\right)B_p, \quad 0 < x < L(t),\ t > 0. \end{aligned} \tag{4.60}$$

All other governing equations, those for dead bacteria, EPS, nutrients, antibiotics, vol-

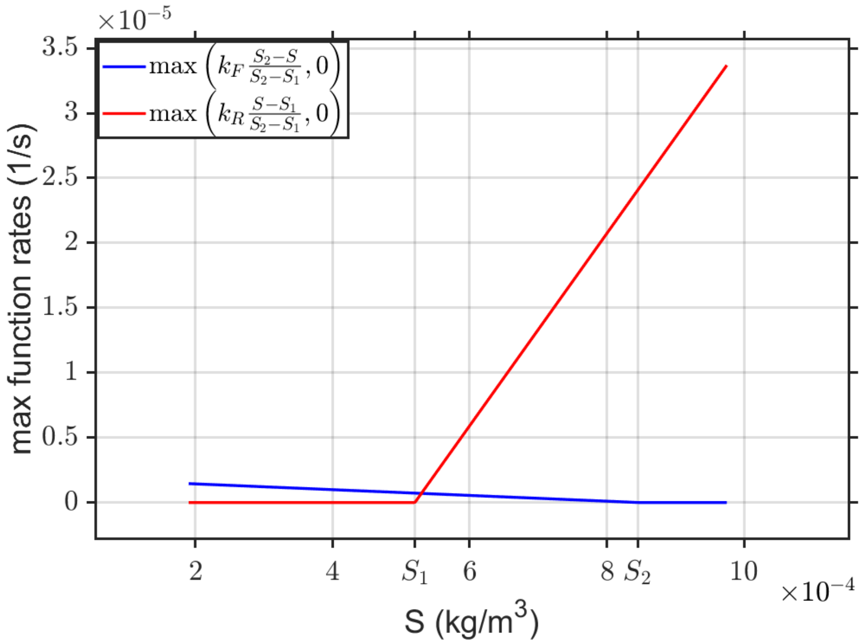

Figure 4.9: Plot of the formation and reversion rate of persister bacteria as a function of S. The parameter values considered for are from Table. 2.2. The functions are plotted over the range $1.9\times10^{-4}\,\text{kg/m}^3 \leq S \leq 9.75\times10^{-4}\,\text{kg/m}^3$.

ume conservation constraint, velocity of biomass and biofilm thickness remain unchanged from Model 5 (Section 4.1.2).

Initial and boundary conditions

The initial and boundary conditions for this model remain unchanged from Model 5. For a detailed description of the initial and boundary conditions, refer to Section 4.1.2.

4.2.3 Non-dimensionalisation

The non-dimensionalisation process follows the same approach as used for Model 5 in Section 4.1.3. Only the modified equations for proliferative bacteria (equation 4.59) and persister bacteria (equation 4.60) have been non-dimensionalised here.

$$\begin{aligned}
\overline{B}_{\overline{t}} + (\overline{v}\overline{B})_{\overline{x}} &= \overline{D}_B\overline{B}_{\overline{x}\overline{x}} + \left(G_1 - G_4\phi_{bio}\overline{C}\right)\frac{\phi_{bio}\overline{S}}{1+\phi_{bio}\overline{S}}\overline{B} - \max\left(\beta_1(\phi_{bio}\overline{C}-1),0\right)\overline{B} \\
&\quad -\overline{B} - \max\left(\beta_2\frac{\overline{S}_2-\overline{S}}{\overline{S}_2-\overline{S}_1},0\right)\overline{B} \\
&\quad +\max\left(\beta_3\frac{\overline{S}-\overline{S}_1}{\overline{S}_2-\overline{S}_1},0\right)\overline{B}_p, \quad 0<\overline{x}<\overline{L}(\overline{t}),\ \overline{t}>0, \qquad (4.61) \\
(\overline{B}_p)_{\overline{t}} + (\overline{v}\overline{B}_p)_{\overline{x}} &= \overline{D}_{B_p}(\overline{B}_p)_{\overline{x}\overline{x}} + \max\left(\beta_2\frac{\overline{S}_2-\overline{S}}{\overline{S}_2-\overline{S}_1},0\right)\overline{B}
\end{aligned}$$

$$-\max\left(\beta_3\frac{\overline{S}-\overline{S}_1}{\overline{S}_2-\overline{S}_1},0\right)\overline{B}_p, \quad 0<\bar{x}<\overline{L}(\bar{t}),\ \bar{t}>0 \tag{4.62}$$

New dimensionless parameters that appear in the above transformed equations are defined as follows

$$\overline{S}_1=\frac{S_1}{k_S}, \quad \overline{S}_2=\frac{S_2}{k_S}$$

For all other non-dimensionalised equations, initial and boundary conditions, and dimensionless parameters, refer to the non-dimensionalisation for Model 5 in Section 4.1.3.

4.2.4 Results and discussions

Following the computational approach described in Section 3.2.4, we solve the non-dimensional model using MATLAB. It is important to note that all results are based on non-dimensionalised variables, with the overline notation omitted in the figures for clarity. Additionally, we conducted a sensitivity analysis to explore the impact of key parameters, such as varying antibiotic concentrations at the implant-biofilm boundary, and compared the outcomes with those discussed in Section 4.1.5. We also varied nutrient concentrations at the biofilm-bulk fluid boundary to investigate how these changes influence the nutrient-dependent formation and reversion rates of persisters. The total concentration of a biofilm constituent at a given time refers to the spatial integral of its concentration over the biofilm thickness, effectively representing its mass per unit area. Unless otherwise specified, all plots correspond to a final simulation time of 4 days, same as Model 5.

Effect of varying antitbiotic concentration (C_0)

Figs. 4.10-4.12 explore the dynamics of bacterial populations and EPS concentrations in response to varying antibiotic concentrations. For all cases depicted in the figures, the nutrient concentration available from the bulk fluid is maintained between S_1 and S_2. The analysis for Fig. 4.10 and 4.11 is based on two different models. The solid lines represent the results from the current model, Model 3, which incorporates nutrient-dependent rates for the formation of persister bacteria from proliferative bacteria and their reversion back to proliferative states. In contrast, the dashed lines correspond to the solutions for Model 5 (Section 4.1), where these rates are constant and independent of nutrient concentration. We will refer to this as Model 5, consistent with the terminology used in Chapter 2, throughout this discussion.

Fig. 4.10(a) illustrates the dynamics of total proliferative bacteria concentration over time under different antibiotic concentrations, comparing Model 3 with Model 5. For the highest antibiotic concentration, the proliferative bacteria shows a rapid and sharp decline in the proliferative bacteria population. This is because the combination of strong antibiotic stress forces the killing of a significant portion of the bacteria. Also for Model 3, the rapid reduction is exacerbated by the fact that, as nutrient levels drop below S_2, proliferative bacteria also starts transitioning to a persister state. At the lowest antibiotic concentration, the decline in proliferative bacteria is much more gradual in both models. However, the decline is slower in Model 3 because the nutrient-driven transitions allow more proliferative bacteria to temporarily survive by shifting to persister states. The solid blue line indicates that lower antibiotic pressure allows proliferative bacteria to survive longer and transition to persisters and other biomass constituents more slowly, as the growth rate will be higher due to less antibiotic, maintaining a higher overall concentration for an extended period. The dashed blue line is consistently lower than the solid blue line, reflecting the fact that without the nutrient-driven transition to persisters, the proliferative bacteria are reduced at a higher rate. This lower decline across all antibiotic levels in Model 5 results from the lack of nutrient-dependent shifts that would otherwise temporarily sustain higher concentrations of proliferative bacteria.

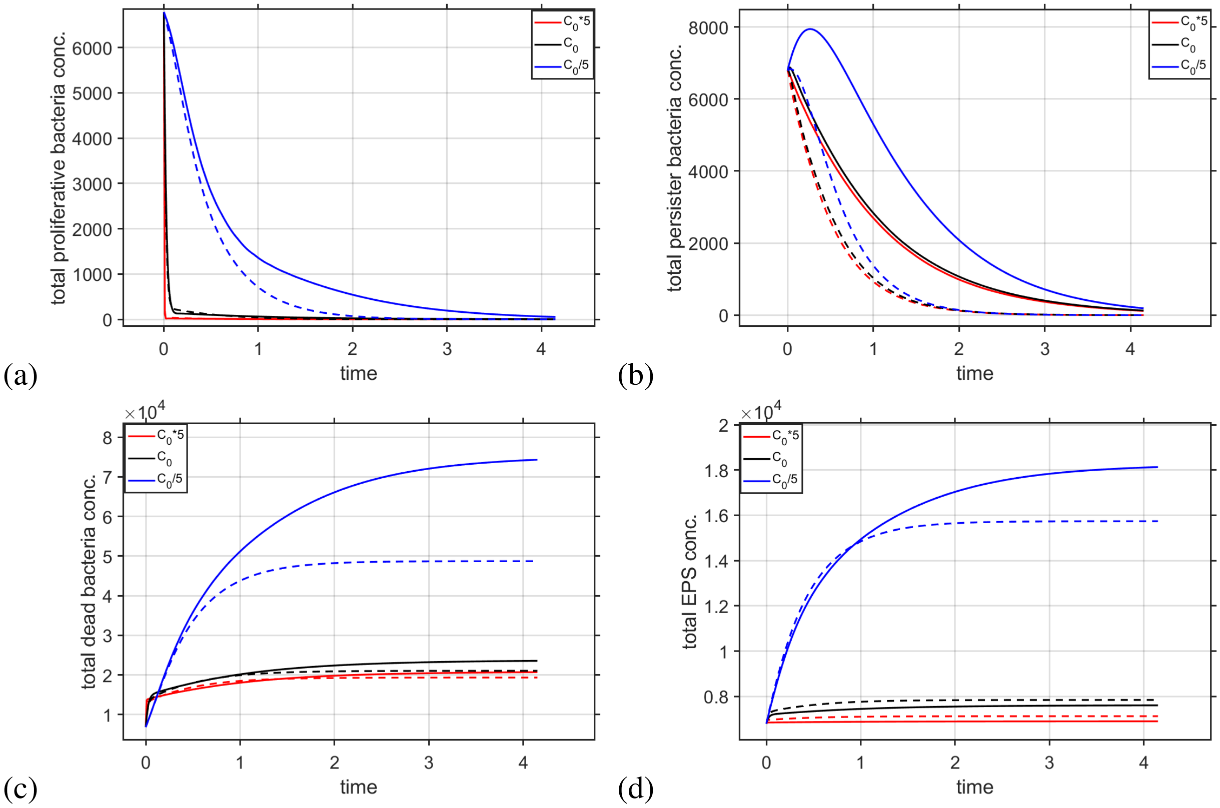

(a) (b) (c) (d)

Figure 4.10: Effect of varying antibiotic concentration (C_0) on (a) temporal variation of total proliferative bacteria concentration, (b) temporal variation of total persister bacteria concentration, (c) temporal variation of total dead bacteria concentration, (d) temporal variation of total EPS concentration.The solid lines refers to the Model 3, whereas the dashed lines refer to Model 5.

The consistent observation across all antibiotic concentrations is that Model 3 results in higher concentrations of proliferative bacteria compared to Model 5. This is because the nutrient-dependent transitions in the current model allow proliferative bacteria to transition back and forth from persister state, depending on nutrient availability, before being fully eliminated by the antibiotic. In Model 5, the constant rate of transition does not offer this dynamic survival strategy, resulting in an overall lower concentration of proliferative bacteria.

Fig. 4.10(b) presents the total concentration of persister bacteria over time. The solid blue line, representing the lowest antibiotic concentration ($C_0/5$) for Model 3, shows the highest peak in persister concentration, but then gradually decreases. This peak is unique compared to the other curves, which do not exhibit such a clear maximum. This peak is due to the lower antibiotic pressure that allows more proliferative bacteria to survive longer which leads to elevated persister population. The dashed blue line, although following a similar trend, has consistently lower values than the solid blue line. This difference is because in Model 5, the constant rate of transition does not allow for accumulation of persisters in response to nutrient levels, resulting in a slower and lower accumulation of persisters. For the highest antibiotic concentration, the persister population declines more quickly. The strong antibiotic stress rapidly kills proliferative bacteria, leading to a lower persister population. As nutrients become available, some persisters revert to proliferative states, leading to a faster decline in the persister population. The dashed red line, representing Model 5, again shows a sharper decline in persister concentration. The constant transition rate in Model 5 does not allow for the rapid response to environmental changes, resulting in less concentration overall and a sharper decline.

Across all antibiotic concentrations, the persister concentrations in the current model are higher than in Model 5. The nutrient-dependent transitions in Model 3 allow for a more dynamic and responsive shift between bacterial states, particularly in environments with lower antibiotic pressure, where the peak in persister concentration is most evident. In Model 5, the lack of nutrient dependency leads to a more subdued response, resulting in lower persister concentrations overall.

Fig. 4.10(c) depicts the total concentration of dead bacteria over time, reflecting the direct impact of antibiotic treatment on the bacterial population. The dead bacteria population is primarily composed of proliferative bacteria that have been killed by the antibiotic or naturally. The trend across all antibiotic concentrations scenario is that the lowest antibiotic concentration leads to the highest concentration of dead bacteria, followed by the intermediate concentration, and then the highest concentration of antibiotic. In Model 3, the concentration of dead bacteria increases rapidly, especially under the highest antibiotic concentration. This initial rapid accumulation of dead bacteria is a direct consequence of the high antibiotic pressure effectively killing a large number of proliferative bacteria in a short period. The quick transition of proliferative bacteria to the dead state, combined with nutrient-dependent shifts, leads to a substantial and early peak in dead bacteria concentration for higher antibiotic concentration. At the lowest antibiotic concentration, the increase in dead bacteria is more gradual and reaches a higher concentration overtime. This is because the larger population of proliferative cells over time allows for a slower accumulation of dead cells. The slower killing rate is consistent with the longer survival of proliferative bacteria and the gradual conversion to persisters, which are less susceptible to antibiotics. The dashed lines, representing Model 5, consistently show lower concentrations of dead bacteria across all antibiotic levels compared to the solid lines. This is because, in Model 5, the constant transition rates mean that proliferative bacteria are not killed as quickly or in as large numbers as in Model 3. The lack of a dynamic response to nutrient availability results in a more gradual and less intense accumulation of dead bacteria, leading to consistently lower values across the board.

Fig. 4.10(d) focusses on the total concentration of EPS over time, which is crucial for biofilm formation and stability. The EPS production is directly tied to the presence of proliferative bacteria, which are responsible for synthesising EPS as part of the biofilm matrix. In Model 3, the total EPS concentration increases over time, with the highest values observed at the lowest antibiotic concentration. This is because the lower antibiotic pressure allows more proliferative bacteria to survive and continue producing EPS. As a result, the biofilm matrix becomes more robust over time, with EPS levels peaking as bacterial activity persists. At the highest antibiotic concentration, EPS production is significantly lower. The rapid killing of proliferative bacteria due to the high antibiotic pressure means that fewer bacteria remain to contribute to EPS synthesis, leading to a lower overall concentration. This decrease in EPS production reflects the reduced biomass and the inability of the bacterial community to maintain a strong biofilm under intense antibiotic treatment. Model 5 shows lower EPS concentrations compared to Model 3 at all antibiotic levels. This lower EPS production is due to the less dynamic response of bacteria in Model 5, where constant transition rates result in fewer proliferative bacteria surviving to produce EPS. Without the nutrient-dependent survival strategies seen in Model 3, the bacterial population in Model 5 is less capable of sustaining high EPS production, leading to consistently lower values.

Fig. 4.10 collectively illustrate the complex interactions between proliferative bacteria, persister bacteria, dead bacteria, and EPS concentrations in response to antibiotic treatment. Proliferative bacteria are the key contributors to all other bacterial states and EPS production. Antibiotic treatment primarily targets proliferative bacteria, and their reduction directly influences the formation of persister bacteria, the accumulation of dead bacteria, and the level of EPS production. In Model 3, nutrient-dependent transition rates allow proliferative bacteria to dynamically adapt to environmental changes, leading to higher concentrations of bacterial phenotypes and EPS compared to Model 5. With constant transition rates, it results in a less responsive bacterial population, leading to lower concentrations across all scenarios. A key observation is that as the antibiotic concentration decreases, the difference between the two models becomes more pronounced. The consistent trend observed is that lower antibiotic concentrations result in the highest values for proliferative, persister, dead bacteria, and EPS. This is because lower antibiotic pressure allows more bacteria to survive longer, maintain higher activity levels, and produce more EPS. The intermediate antibiotic concentration results in moderate values, while the highest antibiotic concentration leads to the lowest values, reflecting the greater efficacy of the antibiotic in reducing bacterial populations and their byproducts.

Fig. 4.11(a) illustrates the biofilm thickness over time under different antibiotic concentrations. In Model 3, the biofilm thickness increases over time, and the greatest thickness observed at the lowest antibiotic concentration. This trend is consistent with previous observations where lower antibiotic pressure allows more proliferative bacteria to survive, leading to increased persister bacteria, dead bacteria and EPS production and, consequently, greater biofilm growth. The biofilm continues to grow as bacteria persist in the nutrient environment, with thickness stabilising as the biofilm reaches a equilibrium state. In contrast, the dashed blue line, representing Model 5 at the same low antibiotic concentration, shows a similar trend but with lower overall biofilm thickness. This reduced thickness is due to the less dynamic response of bacteria in Model 5, where constant transition rates limit the extent to which the biofilm can grow. Without the nutrient-driven shifts seen in Model 3, the bacteria are less capable of sustaining the same level of biomass production production and structural growth, leading to a thinner biofilm. For the highest antibiotic concentration, both the models indicate minimal biofilm growth. It shows a slight increase in thickness that quickly stabilises, reflecting the rapid killing of proliferative bacteria and the corresponding lack of bacteria and EPS production necessary for substantial biofilm growth.

Across all antibiotic concentrations, Model 3 consistently results in higher biofilm thickness compared to Model 5. This difference is due to the nutrient-dependent transition rates in Model 3, which allow for more robust bacterial activity and EPS production, facilitating greater biofilm growth. The observed trend, where lower antibiotic concentrations result in greater biofilm thickness, followed by intermediate, then high antibiotic concentrations, reinforces the idea that antibiotic pressure directly inhibits biofilm development by reducing bacterial viability and EPS production capacity.

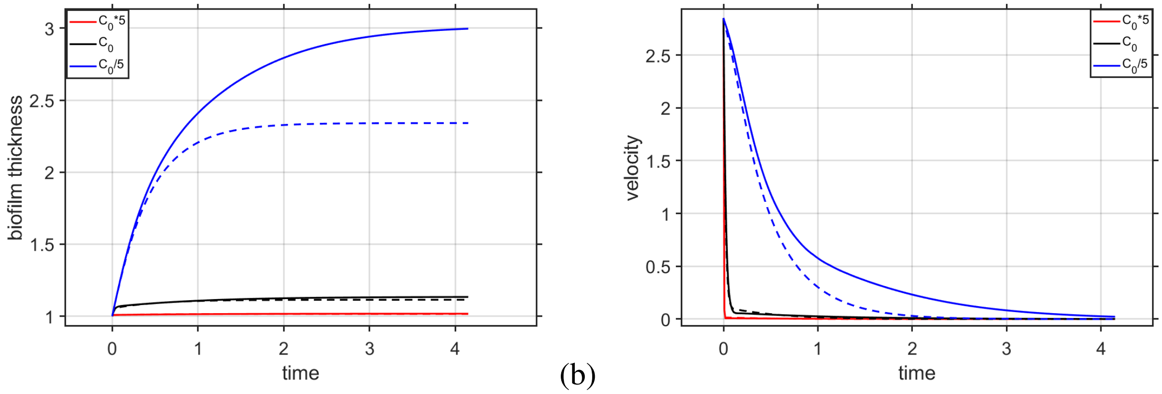

(a) (b)

Figure 4.11: Effect of varying antibiotic concentratin (C_0) on (a) temporal variation of biofilm thickness, (b) temporal variation of velocity at the biofilm-bulk fluid interface. The solid lines refers to Model 3, whereas the dashed lines refer to Model 5.

Fig. 4.11(b) depicts the velocity at the biofilm-bulk fluid interface over time under different antibiotic concentrations. This velocity represents the rate of change of biofilm thickness, indicating how quickly the biofilm is expanding in response to the presence of antibiotics. In Model 3, the velocity decreases rapidly, particularly at higher antibiotic concentrations. This rapid decrease is due to the rapid reduction in biofilm growth, as proliferative bacteria are quickly killed by the antibiotic, leading to a sharp decline in the rate at which the biofilm thickness changes. As the bacterial population decreases and the growth of the biofilm slows down, the velocity stabilises at a low level, indicating that the biofilm is no longer expanding significantly. At the lowest antibiotic concentration , the initial velocity is higher and decreases more gradually compared to the high antibiotic case. This slower decline reflects sustained biofilm growth as more proliferative bacteria survive and continue to contribute to the biofilm's expansion. The gradual reduction in velocity is consistent with the continued increase in biofilm thickness observed in Fig. 4.11(a) under low antibiotic conditions. The dashed lines, representing Model 5, show consistently lower velocities compared to the solid lines across all antibiotic concentrations. This lower velocity is a consequence of the less dynamic bacterial response in Model 5, where constant transition rates lead to a more gradual reduction in biofilm expansion. Without nutrient-dependent transitions, the bacterial population is less able to maintain rapid biofilm growth, resulting in a more pronounced decrease in the velocity of the biofilm-bulk fluid interface.

The thickness of the biofilm is determined primarily by biomass production, while the velocity reflects the rate at which the biofilm expands in response to antibiotic treatment. In Model 3, nutrient-dependent transition rates enable bacteria to dynamically adapt to their environment, resulting in greater biofilm growth and sustained expansion rates under lower antibiotic pressures. Model 5, with its constant transition rates, leads to thinner biofilms and lower velocities across all antibiotic concentrations, reflecting a less responsive bacterial population.

Fig. 4.12 shows the spatial variation of bacterial phenotypes and EPS at final time, which refers to the last time point simulated in this study. Fig. 4.12(a) presents the concentration of proliferative bacteria across biofilm at the final time under different antibiotic concentrations. Proliferative bacteria are directly impacted by the antibiotic. In this nutrient-dependent model, the highest antibiotic concentration results in the lowest concentration of proliferative bacteria across the biofilm thickness. This is because high antibiotic pressure effectively reduces the population of proliferative bacteria by killing them. High antibiotic pressure also means supressed growth of proliferative bacteria, hence higher transition rate to persister and EPS. Therefore, it minimises the active proliferative population within the biofilm. At the lowest antibiotic concentration, the concentration of proliferative bacteria is highest. Here, reduced antibiotic pressure allows for a greater number of proliferative bacteria to survive, leading to a higher biofilm thickness as more bacterial biomass accumulates. The nutrient dependency in this model allows the bacteria to remain in the proliferative state longer when antibiotics are less aggressive and nutrient levels are favourable, promoting biofilm growth. The intermediate antibiotic concentration shows an intermediate level of proliferative bacteria, indicating that as the antibiotic concentration increases, there is a gradual shift from proliferation to transition to persister and EPS production. This gradient reflects how the balance between nutrient availability and antibiotic pressure governs the fate of proliferative bacteria within the biofilm.

Fig. 4.12(b) depicts the concentration of persister bacteria across the biofilm at the final time under different antibiotic concentrations. At the highest antibiotic concentration, the persister concentration is the highest. The high antibiotic pressure forces a large number of proliferative bacteria to transition into the persister state as the transition rate would be higher than the supressed growth rate. This shows antibiotic resilience in the biofilm. Conversely, at the lowest antibiotic concentration, the persister concentration is the lowest at final time, despite the thickest biofilm. This occurs because the lower antibiotic pressure allows more bacteria to remain in the proliferative state, reducing the need for bacteria to transition into persisters, since in this case proliferation rate would be higher. The biofilm in this case grows primarily through the activity of proliferative bacteria. The intermediate antibiotic concentration results in a moderate concentration of persisters. This reflects a balanced scenario where some proliferative bacteria are killed or converted to persisters, but a significant proportion continues to proliferate, sustaining the biofilm growth.

Fig. 4.12(c) shows the concentration of dead bacteria across the biofilm at the final time under different antibiotic concentrations. Dead bacteria result from antibiotic-induced death of proliferative bacteria or natural cell death within the biofilm. Interestingly, the highest concentration of dead bacteria is observed at the lowest antibiotic concentration. This occurs because the biofilm under low antibiotic pressure contains a higher population of proliferative bacteria. Over time, these bacteria either die naturally or due to the residual antibiotic effect, leading to a high concentration of dead cells even though the killing rate is lower compared to higher antibiotic concentrations. At the highest antibiotic concentration, the concentration of dead bacteria is the lowest. This is because the antibiotic quickly reduces the population of proliferative bacteria, leaving fewer cells to die and accumulate as dead biomass within the biofilm. The rapid and effective killing reduces the opportunity for a large accumulation of dead bacteria over time. The intermediate antibiotic concentration produces a moderate concentration of dead bacteria. This reflects the balance between the number of proliferative bacteria that survive long enough to die naturally or from antibiotic effects and the effectiveness of the antibiotic in reducing the bacterial population.

Fig. 4.12(d) represents the concentration of EPS across the biofilm at the final time. EPS is produced by proliferative bacteria and is essential for biofilm structure and defense against environmental stresses, including antibiotic treatment. The highest EPS concentration at final time is found at the highest antibiotic concentration. Under severe antibiotic pressure, the biofilm compensates by producing large amounts of EPS, since the Eps production rate would be higher than the supressed proliferation rate. This helps protect the remaining bacterial cells by rein-

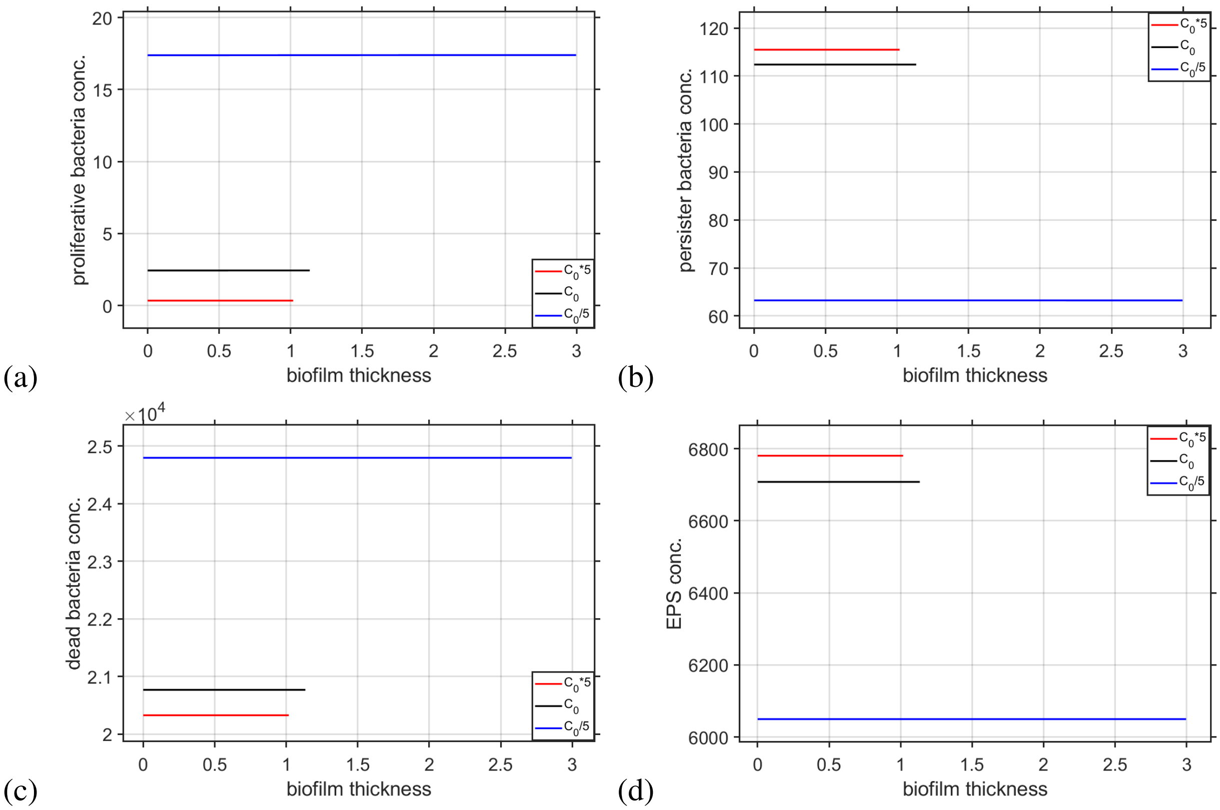

(a) (b) (c) (d)

Figure 4.12: Effect of varying antibiotic concentration (C_0) on (a) spatial variation of proliferative bacteria concentration at final time, (b) spatial variation of persister bacteria concentration at final time, (c) spatial variation of dead bacteria concentration at final time, (d) spatial variation of EPS concentration at final time.

forcing the biofilm's structural integrity. This is a survival mechanism where the biofilm, though reduced in bacterial numbers, maintains its protective matrix through increased EPS production. Although this survival mechanism is not explicitly modelled, it is clearly evident from the results. The lowest antibiotic concentration shows the lowest concentration of EPS, despite the thickest biofilm. In this scenario, the biofilm's growth is driven by the high concentration of proliferative bacteria, which are less stressed and therefore produce less EPS. This happens due to higher growth rate in low antibiotic scenario. The bacteria focus on expansion rather than defense, leading to a biofilm that is thicker but less fortified with EPS. The intermediate antibiotic concentration results in a moderate level of EPS production. This reflects a situation where the biofilm is under moderate stress, leading to the production of enough EPS to maintain structural integrity without the extreme protective measures seen at the highest antibiotic concentration.

In Model 3, the antibiotic directly affects proliferative bacteria, leading to their death. Persisters, in turn, can revert to proliferative bacteria if conditions become favourable, while dead bacteria accumulate as a result of antibiotic-induced killing or natural death. EPS, produced by proliferative bacteria, plays a crucial role in maintaining the biofilm's structural integrity, especially under high antibiotic pressure. At low antibiotic concentrations, the biofilm is characterised by a high concentration of proliferative bacteria, leading to thick biofilm formation with low persister and EPS concentrations. Although the spatial concentrations of persisters and EPS are low, the total concentrations can still be substantial due to the larger biofilm thickness. A thicker biofilm results in a higher total concentration of species, even if the spatial concentration at any time is low. So, under milder antibiotic conditions, the biofilm prioritises growth and expansion rather than persister or EPS production. In contrast, at high antibiotic concentrations, the biofilm becomes thinner, with a higher concentration of persisters and EPS, indicating a shift towards high transition rates than growth rate which leads to survival and protection. The biofilm reduces its active proliferative population and reinforces its structure through increased EPS production, which is essential for defending against the harsh antibiotic environment. The intermediate antibiotic concentration results in a balanced biofilm, where both growth and survival mechanisms are at play. The biofilm maintains a moderate level of proliferative bacteria, persisters, dead cells, and EPS, reflecting a dynamic response to the antibiotic stress while still allowing for biofilm expansion.

Fig. 4.13 show the spatial structure of the different biomass constituents (proliferative bacteria, persister bacteria, dead bacteria, and EPS) across the biofilm at the final time for various antibiotic concentrations (C_0). In previous analyses in Fig. 4.12, we explored how C_0 affected the concentration levels across the biofilm at the final time, where the concentrations appeared constant. However, the aim of these figures is to reveal the spatial structure more clearly. For this, the concentrations at each spatial point are normalised by the concentration at $x = 0$, which is the implant-biofilm boundary. This normalisation allows us to reveal potential spatial trends or patterns within the biofilm. It is important to note that the spatial structures observed in this figure are almost similar to those in Fig. 4.5 of Model 5. So we will not go into detailed explanations of each figure again.

The patterns are nearly constant across the biofilm, as indicated by the close-values along the x-axis. Proliferative bacteria (see Fig. 4.13(a)) continue to be concentrated near the biofilm-bulk fluid boundary, where nutrients are more abundant, while persister cells and EPS (see Fig. 4.13(b) and (d)) are concentrated near the implant-biofilm boundary, where antibiotic stress is higher. The distribution of dead bacteria (see Fig. 4.13(c)) shows some variability, following similar explanation as Fig. 4.5.

Effect of varying nutrient concentration (S_0)

In Figs. 4.14-4.16, we explore how the nutrient concentration coming from the biofilm-bulk fluid interface (S_0), influences the dynamics of bacterial populations and EPS production within the biofilm. The scenarios are represented by three distinct cases: **nutrient-rich environment** ($S_1 < S_2 < S_0$, red line), where the nutrient concentration at the biofilm-bulk fluid interface is above S_2; **intermediate nutrient environment** ($S_1 < S_0 < S_2$, black line), where the nutrient concentration lies between S_1 and S_2; and **nutrient-poor environment** ($S_0 < S_1 < S_2$, blue line), where the

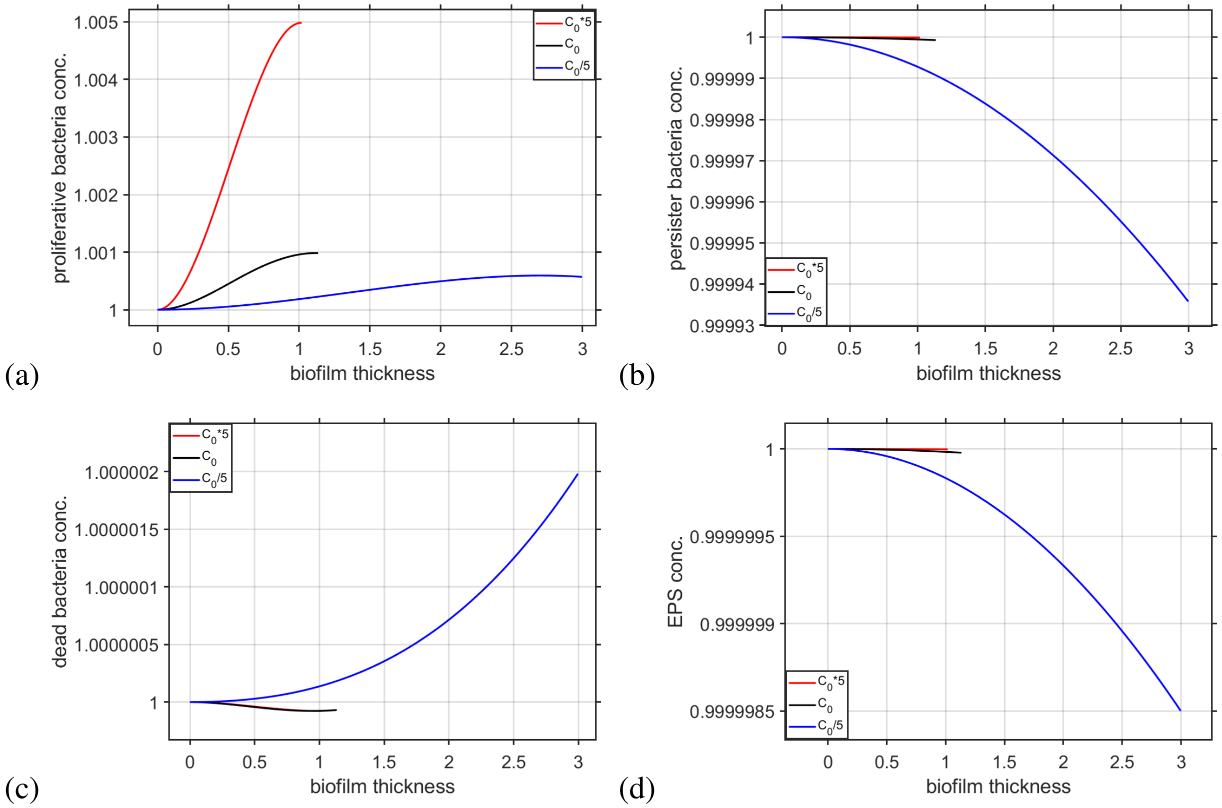

Figure 4.13: Spatial variation of (a) proliferative bacteria, (b) persister bacteria, (c) dead bacteria, and (d) EPS at the final time, shown for varying antibiotic concentrations (C_0). In each plot, the concentrations are scaled by dividing the value at each spatial point by the concentration at $x = 0$.

nutrient concentration is below S_1. These nutrient conditions dictate the transitions between proliferative and persister bacterial states, ultimately affecting the overall biofilm structure and resilience. For all cases, the antibiotic concentration available from the implant-biofilm interface is maintained at the baseline value ($0.1 kg/m^3$) from Table: 2.2.

Fig. 4.14(a) illustrates the total concentration of proliferative bacteria over time under these three nutrient scenarios. Across all cases, the total proliferative bacteria concentration sharply declines during the initial phase, showing little to no variation between the different nutrient conditions. Although we would expect a nutrient-rich environment to support a higher concentration of proliferative bacteria, the figure shows that this effect is minimal. This can be explained by the fact that the antibiotic condition used here is such that it never depletes, meaning the growth of proliferative bacteria is continuously suppressed by the antibiotic. Also a higher initial concentration of proliferative bacteria leads to greater production of EPS and a higher rate of antibiotic-induced death, as indicated by the EPS and dead bacteria plots in Fig. 4.14(c) and (d). Consequently, the proliferative population declines similarly across all nutrient scenarios, stabilising at low levels, very close to zero, regardless of the nutrient availability.

Fig. 4.14(b) examines the total concentration of persister bacteria over time under the same three nutrient scenarios. The trends here are more distinct across the different nutrient conditions. In the very initial phase, there is a slight buildup of persister bacteria across all scenarios as proliferative bacteria transition to the persister state. As time progresses, distinct differences arise between the nutrient conditions. In the nutrient-rich environment, there is a rapid decline in persister concentration over time. This rapid decline is because the high nutrient availability continuously converts persisters back into proliferative bacteria. In the intermediate nutrient scenario, the persister concentration declines more gradually, reflecting a balance where some bacteria remain in the persister state while others revert to being proliferative. Interestingly, in the nutrient-poor environment, persisters continue to accumulate even in the later phases of biofilm development. This increase is due to the lack of sufficient nutrients, which forces more bacteria into the persister state as a survival strategy, maintaining a high persister population that is less susceptible to antibiotic effects. This clearly reflects the resilience produced in biofilm due to nutrient-scarce environment.

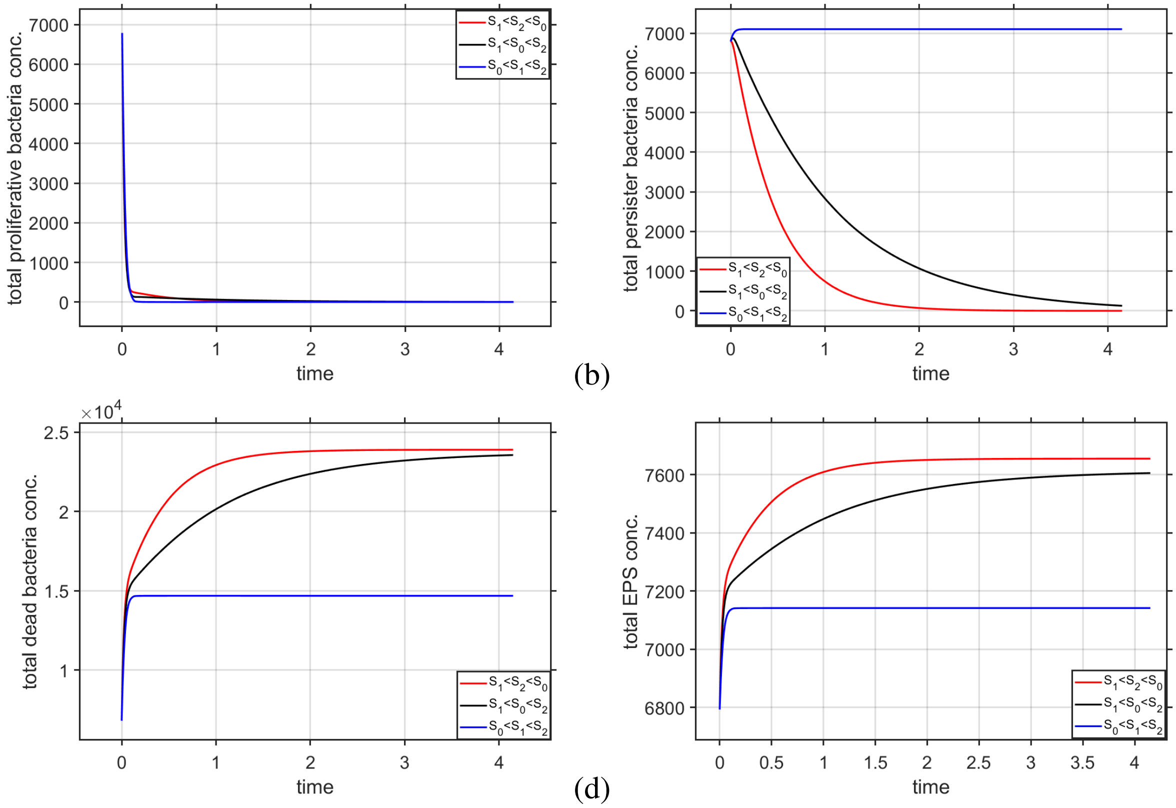

(a) (b) (c) (d)

Figure 4.14: Effect of varying nutrient concentration (S_0) on (a) temporal variation of total proliferative bacteria concentration, (b) temporal variation of total persister bacteria concentration, (c) temporal variation of total dead bacteria concentration, (d) temporal variation of total EPS concentration.

Fig. 4.14(c) shows the total concentration of dead bacteria over time, which arises primarily from the death of proliferative bacteria due to antibiotic action or natural cell death. The dead bacteria concentration increases sharply during the initial phase as the antibiotic quickly targets proliferative bacteria, resulting in a rapid increase in dead cells across all nutrient conditions. However, the rate and extent of this increase vary significantly in the next stage of biofilm development. In the nutrient-rich environment, the dead bacteria concentration is the highest. This is because the nutrient abundance initially supports a larger population of proliferative bacteria, which are then more heavily targeted and killed by the antibiotic or naturally. This leads to a high dead bacteria concentration over time. The intermediate nutrient scenario results in a slightly lower concentration of dead bacteria, consistent with the moderate level of bacterial proliferation and subsequent death. In the nutrient-poor environment, the dead bacteria concentration is the lowest. This lower concentration reflects the initially smaller proliferation of bacteria and transition to persister due to nutrient scarcity, leading to fewer bacteria available for antibiotic-induced or natural killing.

Fig. 4.14(d) represents the total concentration of EPS over time. EPS, produced by proliferative bacteria, is critical for biofilm structure and protection against environmental stresses, including antibiotics. The trends in EPS concentration closely mirror those observed in the dead bacteria concentration. EPS concentration increases rapidly in the early phase for all nutrient conditions. In the nutrient-rich environment, the EPS concentration is the highest, driven by the higher activity of proliferative bacteria that are supported by the abundant nutrients. In the intermediate nutrient scenario, the EPS concentration is slightly lower but still significant, reflecting the moderate level of bacterial activity and EPS production. In the nutrient-poor environment, the EPS concentration is the lowest. This is because the lack of nutrients severely limits the activity of proliferative bacteria, leading to higher persister population and minimal EPS production.

Fig. 4.14 collectively reveals the complex interplay between nutrient availability, bacterial states, and biofilm components. Proliferative bacteria, which rely on nutrients for growth and EPS production, are directly affected by the nutrient concentration available from the biofilm-bulk fluid interface. When nutrient levels are high, the biofilm thrives initially, with a higher concentration of proliferative bacteria and increased EPS production. However, this also leads to greater susceptibility to antibiotics, resulting in a higher concentration of dead bacteria. Despite the expected effects of nutrient richness on proliferative activity, the interplay with EPS production and bacterial death results in similar levels of proliferative bacteria across different nutrient scenarios, highlighting the complex, interconnected nature of biofilm dynamics. It is important to note that the antibiotic condition in this scenario ensures that it never depletes, which continuously inhibits proliferative bacterial growth. This is in contrast to what will be explored in the next chapter, where a more realistic model of controlled antibiotic delivery will be introduced. Persisters are more prominent in nutrient-poor environments, where they enter a dormant state to survive the harsh conditions. In such environments, the biofilm composition shifts towards survival rather than growth, with fewer proliferative bacteria, lower EPS production, and reduced susceptibility to antibiotics, as evidenced by the lower concentration of dead bacteria. The intermediate nutrient scenario presents a balanced biofilm state, where both proliferative and persister bacteria coexist, resulting in moderate levels of EPS production and dead bacteria. This reflects a biofilm that is simultaneously growing and maintaining resilience to environmental stressors. The nutrient-dependent transitions between proliferative and persister states allow the biofilm to dynamically adapt to changing environmental conditions, balancing growth, survival, and structural integrity to maintain its overall resilience. The two-phase behaviour of the biomass constituents, with an initial phase marked by rapid changes and a subsequent stabilisation phase, sets the stage for the more detailed study of biofilm growth phases in the next chapter. There, the introduction of controlled antibiotic delivery will allow us to investigate how these phases evolve under more realistic treatment scenarios.

Fig. 4.15(a) shows the biofilm thickness over time under the three nutrient scenarios. Initially, the biofilm thickness grows quickly in all scenarios; however, the degree of growth differs depending on nutrient availability. In the nutrient-rich environment, the biofilm thickness reaches the highest value. This outcome is expected as the abundant nutrients support robust bacterial growth, particularly dead bacteria and EPS growth (see Fig. 4.14(c), (d)). This leads to the expansion of the biofilm structure. The intermediate nutrient scenario results in a moderately thick biofilm. Here, the nutrient availability is sufficient to support some growth, but not as extensively as in the nutrient-rich case. In contrast, the nutrient-poor environment produces the least biofilm growth, with the thickness stabilising quickly at a much lower value. The lack of sufficient nutrients restricts bacterial activity and biofilm expansion, leading to a thinner biofilm.

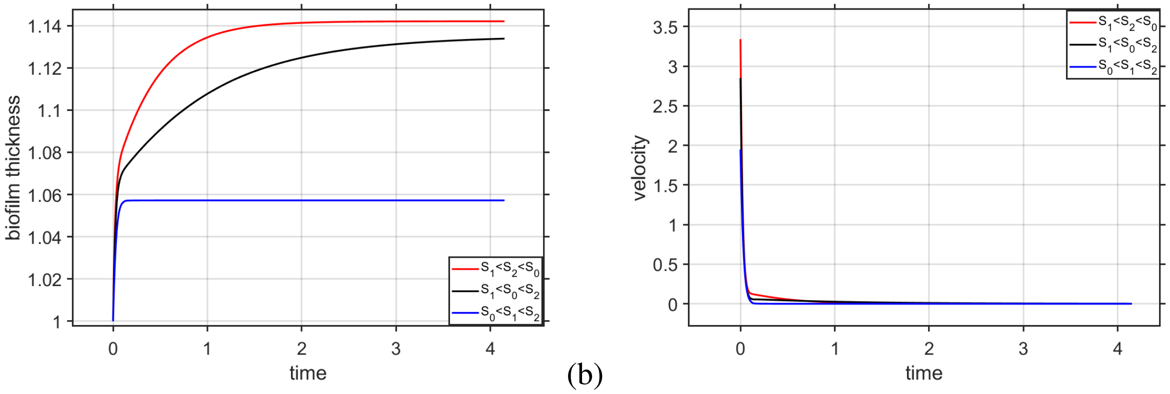

(a) (b)

Figure 4.15: Effect of varying nutrient concentration (S_0) on (a) temporal variation of biofilm thickness, (b) temporal variation of velocity at the biofilm-bulk fluid interface.

Fig. 4.15(b) illustrates the velocity of the biofilm-bulk fluid interface, which represents the rate of change of biofilm thickness over time, under the same nutrient scenarios. The velocity decreases over time for all cases, but it starts from different initial values based on the nutrient conditions. In the nutrient-rich environment, the velocity starts from the highest value, reflecting the initial growth of the biofilm due to the ample nutrient supply. In the intermediate nutrient scenario, the velocity starts from an intermediate value, corresponding to a moderate initial rate of biofilm expansion. In the nutrient-poor environment, the velocity starts from the lowest value, indicating a slower initial growth rate due to limited nutrient availability. Despite these differences in initial velocity, the velocity for all nutrient conditions eventually approaches zero, indicating that the biofilm growth slows down and stabilises over time, regardless of the initial nutrient availability.

In a nutrient-rich environment, the biofilm exhibits the greatest thickness and the highest initial velocity of growth. The availability of abundant nutrients supports increase in dead bacteria and EPS, leading to the swift expansion of the biofilm's structure. As the nutrients are consumed and the biofilm reaches its maximum thickness, the velocity decreases and eventually approaches zero, indicating a stabilisation of the biofilm's growth. In the intermediate nutrient scenario, the biofilm grows at a moderate rate, leading to a moderately thick biofilm. The corresponding initial velocity is lower than in the nutrient-rich environment, reflecting the more limited nutrient supply. However, as in the nutrient-rich case, the velocity decreases over time and approaches zero, indicating that the biofilm growth also stabilises as the system reaches equilibrium. The nutrient-poor environment results in the thinnest biofilm and the lowest initial velocity of growth. The limited nutrient availability restricts bacterial activity and biofilm expansion, leading to a quick stabilisation at a low thickness. The initial velocity is the lowest among the three cases, and it decreases over time to approach zero, reflecting the minimal growth potential under nutrient-limited conditions.

The rate of biofilm expansion, as indicated by the velocity of the biofilm-bulk fluid interface, is initially dependent on the availability of nutrients. However, regardless of the initial growth rate, all scenarios show that the velocity decreases and approaches zero over time, indicating that the biofilm eventually stabilises, with little to no further growth. This suggests that while nutrient availability influences the initial growth phase, the long-term behaviour of the biofilm is characterised by a stabilisation in thickness, regardless of the nutrient conditions.

Fig. 4.16 shows the spatial variation of bacterial phenotypes and EPS at final time. Fig. 4.16 (a) shows the concentration of proliferative bacteria throughout biofilm at the final time, which refers to the last time point simulated in this study. In the nutrient-rich environment, the concentration of proliferative bacteria is notably low across the biofilm . This might seem unexpected at first because abundant nutrients should theoretically support a larger proliferative population. However, the high availability of nutrients leads to a transition of proliferative bacteria into dead bacteria over time due to antibiotic susceptibility or natural death. This indirectly limits the proliferative population. In the intermediate nutrient scenario, the concentration of proliferative bacteria is the highest across the biofilm. This scenario reflects a balance where nutrient availability supports some proliferation, but this is counterbalanced by the conversion of some proliferative bacteria into persisters or their death. The stable profile suggests that proliferation and depletion processes are at equilibrium. In the nutrient-poor environment, the proliferative bacteria concentration is almost zero and overlaps with the nutrient-rich case. This indicates that under nutrient-limited conditions, the biofilm's capacity to maintain an active, growing population is severely restricted, as most bacteria transition into the persister state to survive.

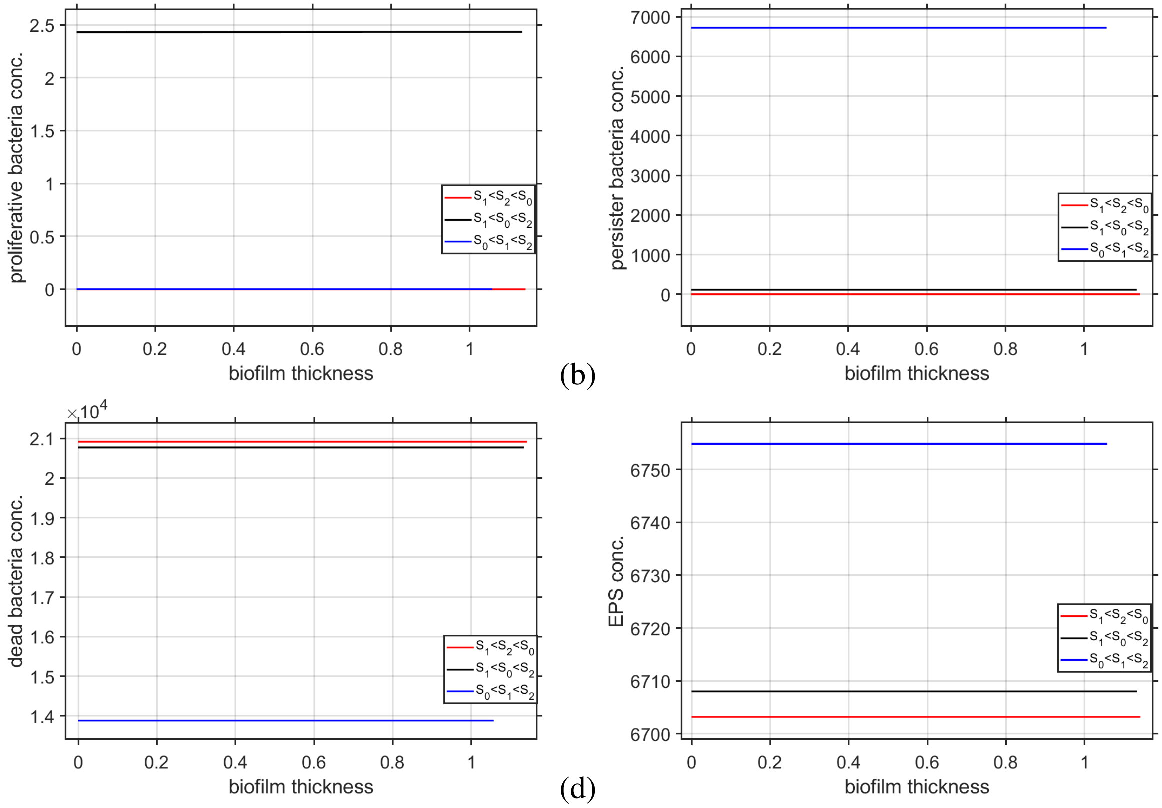

(a) (b) (c) (d)

Figure 4.16: Effect of varying nutrient concentration (S_0) on (a) spatial variation of proliferative bacteria concentration at final time, (b) spatial variation of persister bacteria concentration at final time, (c) spatial variation of dead bacteria concentration at final time, (d) spatial variation of EPS concentration at final time.

Fig. 4.16(b) examines the concentration of persister bacteria throughout the biofilm at the final time. The results in this figure clearly show the inverse relationship between nutrient availability and persister concentration. In the nutrient-poor environment, the concentration of persister bacteria is highest across the entire biofilm. This distribution highlights how the lack of nutrients across the biofilm drives the entire population to adopt the persister state as a survival strategy. In the intermediate nutrient scenario, the persister concentration is lower but still significant. This suggests that the bacteria are exposed to moderate stress, which induces some of the population to become persisters while allowing others to remain or revert to the proliferative state. In the nutrient-rich environment, the persister concentration is very low. The abundance of nutrients encourages the bacteria to maintain or revert to the proliferative state, reducing the need for a dormant, persister state. This scenario represents a biofilm where growth is favoured over survival, reflected by the low persister numbers.

Fig. 4.16(c) shows the concentration of dead bacteria across the biofilm at the final time. In the nutrient-rich environment, the dead bacteria concentration is the highest across the biofilm thickness. This is consistent with the earlier observations of low proliferative and persister concentrations in this scenario. The initial high proliferative activity under nutrient-rich conditions makes these bacteria more susceptible to antibiotic-induced or natural death over time, leading to a higher accumulation of dead cells at final time. In the intermediate nutrient scenario, the dead bacteria concentration is slightly lower. This reflects a more balanced situation where some bacteria survive by converting to persisters, while others die due to antibiotic exposure. In the nutrient-poor environment, the dead bacteria concentration is the lowest. This suggests that with fewer proliferative bacteria initially present, there are fewer cells to die, leading to a reduced accumulation of dead cells within the biofilm.

Fig. 4.16(d) illustrates the concentration of EPS across biofilm at the final time. In the nutrient-rich environment, the EPS concentration is relatively low, despite high initial proliferative activity. This is likely because the rapid conversion of proliferative bacteria to dead cells limits the sustained production of EPS. The lower than expected EPS concentration suggests that while initial growth is high, the biofilm's structural development might be less robust than anticipated due to the quick depletion of proliferative bacteria. In the intermediate nutrient scenario, the EPS concentration is slightly higher across the biofilm. This indicates a more stable production of EPS due to the sustained, though moderate, proliferative activity. The biofilm in this scenario is likely more structurally sound, with a balanced bacterial composition supporting steady EPS production. In the nutrient-poor environment, the EPS concentration is the highest, even though the proliferative bacteria are nearly absent. This suggests that the few proliferative bacteria in this scenario prioritise EPS production, as its production rate remains higher and is not affected by antibiotics like the proliferation rate. This strategy helps maintain the biofilm's integrity under harsh conditions, resulting in a biofilm structure that is highly resilient but growth-limited.

In nutrient-rich environments, although abundant nutrients are available, the proliferative bacteria population at final time remains low due to death from antibiotic exposure or naturally. The total concentration of proliferative bacteria is high in this case (Fig. 4.14(a)), even though spatial concentrations might be lower than the other scenarios, because the biofilm is thicker overall. A larger biofilm thickness results in higher total concentrations, even if the spatial concentrations are low. This nutrient-rich scenario highlights the delicate balance between growth and survival within the biofilm. The high concentration of dead bacteria and relatively low EPS production reflect the biofilm's struggle to maintain structural integrity while coping with high death rates. In nutrient-poor environments, the biofilm adopts a survival-first strategy, with most bacteria transitioning into the persister state. The high persister concentration across the biofilm indicates the biofilm's resilience in harsh conditions, prioritising long-term survival over short-term growth. Despite the limited number of proliferative bacteria, the biofilm manages to produce a substantial amount of EPS, ensuring structural stability even as bacterial activity is minimised. The intermediate nutrient scenario represents a balanced state where both growth and survival are moderated. The biofilm in this scenario maintains a moderate level of proliferative bacteria, sufficient to support steady EPS production, while also ensuring that a fraction of the population remains in the persister state to safeguard against environmental stresses. The consistent levels of dead bacteria and EPS across the biofilm thickness suggest that this scenario supports a structurally stable biofilm capable of both growth and resilience.

Fig. 4.17 shows the spatial structure of the different biomass constituents (proliferative bacteria, persister bacteria, dead bacteria, and EPS) across the biofilm at the final time for various nutrient concentrations (S_0). In previous analyses in Fig. 4.16, we explored how S_0 affected concentration levels across the biofilm, where the concentrations appeared constant. However, the aim of these figures is to reveal the spatial structure more clearly. To achieve this, the concentrations at each spatial point are normalised by the concentration at $x = 0$, the implant-biofilm boundary, allowing for the identification of potential spatial trends or patterns within the biofilm. Notably, the spatial structures observed in this figure are similar to those in Fig. 4.5 of Model 5 and Fig. 4.13 of Model 3. The analysis of these spatial structures reveals key patterns for the various biomass constituents, demonstrating how proliferative bacteria, persister bacteria, dead bacteria, and EPS are distributed across the biofilm thickness, from the implant-biofilm boundary (left side) to the biofilm-bulk fluid boundary (right side).

In Fig. 4.17(a), the proliferative bacteria exhibit an increasing trend from the implant-biofilm boundary towards the biofilm-bulk fluid boundary. This trend is consistent across all nutrient conditions, where the concentration of proliferative bacteria increases toward the bulk fluid boundary. This growth reflects the nutrient and antibiotic gradient, as nutrients from the bulk fluid allow proliferative bacteria to thrive, while antibiotic from the implant-biofilm boundary induce bacterial death. The different nutrient conditions do not significantly alter the spatial structure, but they slightly affect the magnitude of the increase, with higher nutrient concentrations leading to more pronounced growth near the biofilm-bulk fluid boundary.

In Fig. 4.17(b), the spatial structure is somewhat inverse to that of the proliferative bacteria. Persister bacteria are more concentrated near the implant boundary, where nutrients are lower, and their concentration decreases toward the bulk fluid boundary, where there is abundant nutrient. This makes sense, as persisters are favoured in low-nutrient environments to survive harsh conditions. In cases where the nutrient concentration is high, the persister concentration drops faster across the biofilm thickness, indicating a transition back to proliferative bacteria due to favourable nutrient conditions. In the lowest nutrient case, persisters maintain a higher concentration across the biofilm as also evidenced in Fig. 4.16(b).

In Fig. 4.17(c), for intermediate nutrient concentrations, the concentration of dead bacteria decreases gradually from the implant boundary toward the biofilm-bulk fluid boundary, with a slight dip followed by an increase near the bulk fluid interface. This pattern arises because higher antibiotic pressure near the implant boundary leads to more proliferative cell death. However,

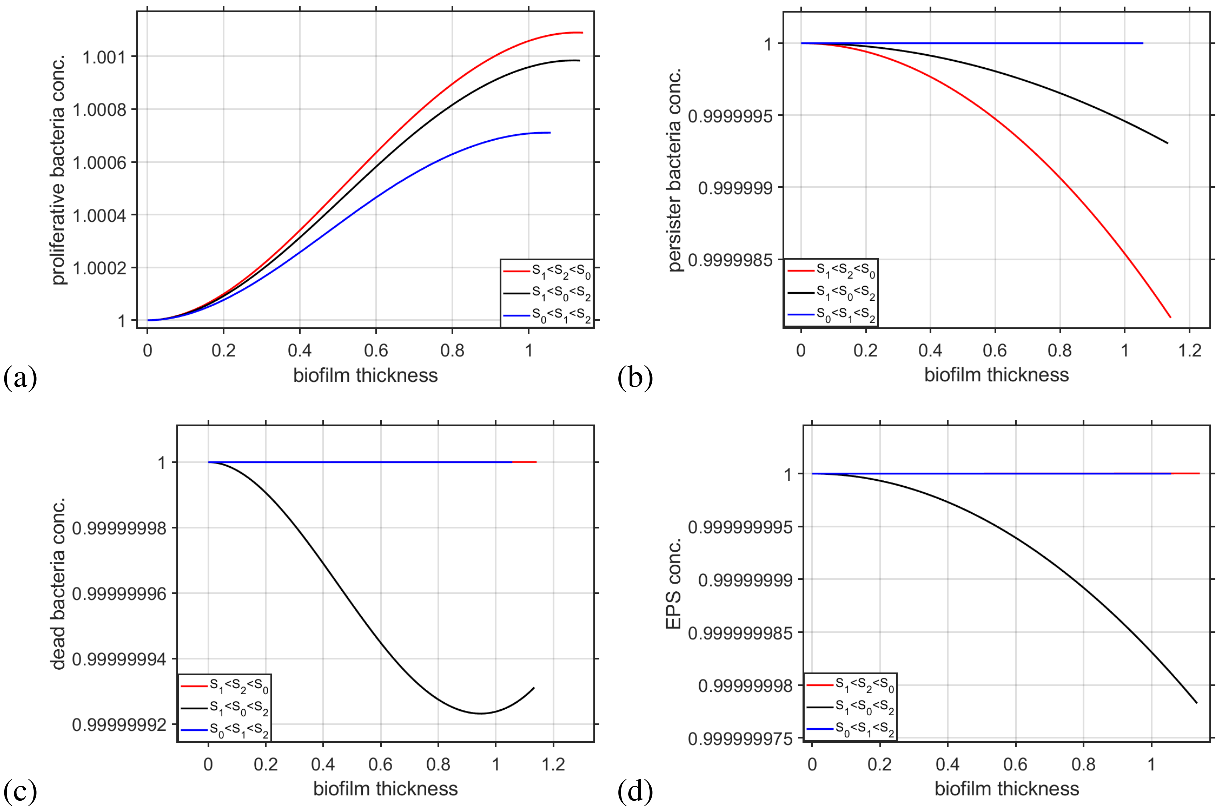

Figure 4.17: Spatial variation of (a) proliferative bacteria, (b) persister bacteria, (c) dead bacteria, and (d) EPS at the final time, shown for varying nutrient concentrations (S_0). In each plot, the concentrations are scaled by dividing the value at each spatial point by the concentration at $x = 0$.

as the antibiotic concentration diminishes with distance due to diffusion limitations, the death rate decreases, resulting in a dip. Near the biofilm-bulk fluid boundary, where nutrients support continued proliferation, the dead bacteria concentration rises again as proliferative cells die. Interestingly, we observe a close overlap in dead bacteria distribution between nutrient-poor and nutrient-rich environments, indicating minimal structural variation in these cases. After normalisation, the distribution remains almost constant. This phenomenon may be attributed to higher levels of proliferative bacteria across the biofilm in the intermediate nutrient condition compared to other nutrient scenarios (Fig. 4.16), leading to greater variation in dead bacteria distribution for the intermediate nutrient scenario.

For the spatial distribution of EPS in Fig. 4.17(d), the highest EPS concentration occurs at the implant-biofilm boundary, where cells experience stress from antibiotics, leading to a comparatively higher EPS production rate than the suppressed bacterial growth rate. Moving toward the biofilm-bulk fluid boundary, the EPS concentration decreases, with a more pronounced decline at intermediate nutrient concentrations. This pattern reflects the tendency of cells near the implant-biofilm boundary to produce more EPS under stress, while in nutrient-rich regions, EPS production is minimised as bacterial growth increases. The overall trend of decreasing EPS concentration from the implant-biofilm boundary toward the bulk fluid boundary is consistent across all antibiotic concentration levels. Interestingly, there is a close overlap in EPS distribution between nutrient-poor and nutrient-rich environments, indicating minimal structural variation in these cases. This suggests that, even after normalisation, the EPS levels remain nearly constant. This phenomenon can be attributed to higher levels of proliferative bacteria across the biofilm in the intermediate nutrient condition than that of other nutrient scenarios (Fig. 4.16), which results in greater variation in EPS production throughout the biofilm for the intermediate nutrient scenario.

In summary, the spatial structures of proliferative bacteria, persister bacteria, dead bacteria, and EPS concentrations highlight the dynamic interplay between nutrient availability, antibiotic effects, and bacterial responses within the biofilm. The structures of the biomass constituents show very little variation across the biofilm, with very close values along the x-axis. Proliferative bacteria flourish in nutrient-rich areas near the biofilm-bulk fluid boundary, while persister bacteria dominate in nutrient-poor regions near the implant boundary. EPS concentrations decrease from the implant boundary to the bulk fluid boundary, reflecting the influence of antibiotics and nutrient-driven bacterial transitions. Dead bacteria show greater variability, accumulating near the biofilm-bulk fluid boundary at intermediate nutrient levels. In nutrient-poor and nutrient-rich cases dead bacteria and EPS result in overlapping, relatively constant spatial distributions. These patterns illustrate how each biomass constituent responds to the gradients of antibiotics and nutrients throughout the biofilm.

4.3 Summary

This chapter explored biofilm growth dynamics under continuous antibiotic administration, building on the models from the previous chapter. The focus was on how a constant antibiotic influx affects biofilm structure, particularly the interactions between proliferative, persister, dead bacteria and EPS. Two models were developed: one with fixed transition rates between bacterial states, and another with nutrient-dependent rates, providing a more detailed understanding of biofilm behaviour under different nutrient conditions.

In Model 5, the constant antibiotic concentration was observed to significantly affect the biofilm's microbial architecture. As expected, higher antibiotic concentrations led to a rapid decline in proliferative bacteria, with a notable increase in the concentration of dead cells. The results demonstrated that as antibiotic concentration increased, the biofilm's reliance on persister cells intensified, thereby enhancing its overall resilience to the treatment. Although this antibiotic-dependent resilience is not directly modelled, we observe this behavior due to the antibiotic's impact on growth and death rates, while it does not affect other transition rates, such as those to persister cells or EPS production. This model also revealed that the production of EPS, which plays a crucial role in biofilm structural integrity and protection, was inversely related to antibiotic concentration. Lower antibiotic concentrations allowed for more substantial EPS production, which contributed to thicker and more robust biofilms, indicating that biofilm structure is heavily influenced by the balance between antibiotic concentration and the biofilm's ability to maintain EPS production. This general behaviour aligns with existing biofilm studies that emphasise the role of persister cells in maintaining biofilm resilience under antibiotic pressure (e.g., [72]). However, the inverse relationship between EPS production and antibiotic concentration offers a new insight that is important for understanding biofilm structural integrity under treatment. It will be interesting to investigate whether this effect persists in more complex models that incorporate nutrient dynamics and controlled antibiotic delivery.

Model 3 introduced a more complexity by incorporating nutrient-dependent formation and reversion rates for persister bacteria. This model aimed to simulate more realistic biofilm behaviour by considering how nutrient availability within the biofilm environment affects bacterial state transitions and, consequently, biofilm resilience. The results were particularly insightful, showing that nutrient availability plays a pivotal role in determining the biofilm's response to antibiotic treatment. In nutrient-rich environments, the biofilm initially exhibited a rapid proliferation of bacteria; however, this also made the biofilm more susceptible to antibiotic-induced or natural cell death, leading to a higher concentration of dead bacteria over time. This reveals a two-phase behaviour, where an initial period of rapid change is followed by a slower, stabilising phase as bacterial transitions and EPS production adjust to the nutrient and antibiotic conditions. Conversely, in nutrient-poor environments, the biofilm shifted towards a survival strategy, characterised by a higher concentration of persister cells and reduced proliferative activity. This shift was accompanied by an increase in the level of EPS production, even in the absence of significant bacterial growth, underscoring the adaptive mechanisms of the biofilm to maintain structural integrity under stress. The interaction between nutrient conditions and persister formation in the presence of antibiotics highlighted the biofilm's capacity to adapt by modulating persister and EPS levels dynamically, depending on external stressors. The two-phase behaviour observed, with an initial phase marked by rapid changes in biomass constituents followed by a stabilising phase, sets the stage for the more detailed investigation of biofilm growth phases in the next chapter. The contribution of this model lies in its ability to capture the dynamic coupling between nutrient levels and persister behaviour, revealing how nutrient availability can regulate phenotypic switching and ultimately shape biofilm resilience and structure in the presence of antibiotics. This mechanistic insight is not accounted for in fixed-transition models and marks a key conceptual advancement in modelling biofilm resilience.

Comparing the results of the two models highlighted the critical influence of nutrient conditions on biofilm dynamics. Model 5, with its fixed transition rates, provided a more static view of biofilm development, where the balance between proliferative, persister, and dead bacteria was primarily driven by antibiotic concentration. This model showed that under constant antibiotic stress, the biofilm could maintain resilience through the formation of persister cells, but this came at the cost of reduced EPS production and overall biofilm thickness. In contrast, Model 3, with nutrient-dependent transition rates, revealed a more dynamic and adaptable biofilm structure. This model demonstrated that nutrient availability not only influenced the balance between bacterial phenotypes but also significantly impacted the biofilm's structural properties. In nutrient-rich environments, the biofilm was more prone to rapid growth and subsequent death, while in nutrient-poor environments, the biofilm adopted a defensive stance, increasing persister cell prevalence and EPS production to withstand external stressors. The comparison between the two models underscored the importance of considering environmental factors, such as nutrient levels, in biofilm modelling to accurately predict biofilm behaviour and resilience under antibiotic treatment. While most of these results align with theoretical expectations, the role of nutrient concentration and its impact on biofilm resilience and persister formation, provides a fresh perspective that may influence future biofilm control strategies. These findings provide new evidence for the regulatory role of nutrient availability in coordinating survival strategies in biofilms exposed to antibiotics, a feature that may be essential for understanding chronic infections.

This model is limited by its assumption of constant antibiotic exposure; however, in reality, antibiotics would be delivered over a finite time. To address this limitation, the next chapter will focus on incorporating more realistic and clinically relevant scenarios, particularly focussing on the impact of controlled antibiotic release on biofilm structure and growth. A key direction for future work is the development of implant models that simulate antibiotic release from porous implants. This approach would involve modelling the diffusion of antibiotics through the porous structure of the implant and its subsequent release into the surrounding biofilm. By integrating these dynamics into the biofilm growth models, we can gain a deeper understanding of how controlled antibiotic release affects the distribution of antibiotics within the biofilm and how this influences the transition between bacterial phenotypes, EPS production, and overall biofilm growth. Moreover, the effects of controlled antibiotic release should be studied within the context of the second model from this chapter, which incorporates nutrient-dependent persister formation and reversion. This would involve investigating how nutrient gradients within the biofilm, combined with controlled antibiotic release, affect the distribution and behaviour of persister cells, EPS production, and the overall structure of the biofilm. These aspects are addressed in the following chapter, where models are developed to study the interplay between controlled antibiotic release, bacterial phenotypes, and nutrient availability, offering a deeper understanding of biofilm behaviour. In conclusion, the models developed in this chapter offer a strong foundation for understanding the intricate relationships between bacterial phenotypes, nutrient availability, and antibiotic pressure in biofilm growth, setting the stage for more refined models simulating controlled antibiotic release and implant interactions to improve strategies for managing biofilm-associated infections.

Chapter 5

Biofilm growth models with controlled antibiotic release

In the previous chapter, we explored biofilm growth models under continuous antibiotic administration, focussing on the dynamics of biofilm development in response to sustained antibiotic exposure. The findings highlighted the need for more advanced models to simulate scenarios where antibiotics are delivered through controlled release mechanisms. There are various ways in which antibiotic could be delivered from an implant in a controlled manner. One such way is through incorporation of solid antibiotic in a porous structure. This approach involves modelling the diffusion of antibiotics through the porous structure of the implant and their subsequent release into the surrounding biofilm. These complexities were identified as the next critical step in advancing our understanding of biofilm dynamics. This novel modelling framework explicitly couples a porous implant medium with a biofilm that includes proliferative, persister, and dead bacterial phenotypes, as well as nutrient - dependent persister formation and reversion. To the best of our knowledge, such a combined implant–biofilm system with this level of biological complexity has not been studied in prior literature. We focus on two one-dimensional models, referred to as Models 10 and 2 from Chapter 2, to investigate the effects of controlled antibiotic delivery on biofilm growth.

The primary goal of this chapter is to investigate how biofilms behave in terms of growth and microstructural dynamics under controlled antibiotic release from porous implants. This chapter presents a generalised framework to optimise antibiotic delivery strategies that are adaptable to various clinical scenarios. In Model 10, the focus is on understanding how antibiotic delivery from a porous implant influences overall biofilm growth. This model aims to determine how key parameters related to the porous implant and antibiotic delivery affect biofilm expansion. Model 2 introduces a more complex microbial structure by incorporating all the bacterial phenotypes discussed in previous chapters, as well as EPS formation. This model also includes the nutrient-dependent formation and reversion rates of persister bacteria, providing a more detailed understanding of how nutrient availability, coupled with controlled antibiotic release, impacts biofilm composition and growth. In addition, a third model is introduced to explore initial strategies for optimising antibiotic delivery from the porous implant. This approach has not been previously considered in biofilm modelling studies to the best of our knowledge.

Outline

This chapter introduces several new aspects in the field of biofilm modelling. First, we create integrated models that simulate biofilm growth and localised antibiotic delivery from porous implants. In this chapter, we build upon the simplest biofilm growth model, Model 11, from Section 3.1, by introducing an antibiotic delivery mechanism from a porous implant. This antibiotic delivery mechanism has been modelled using the approach outlined in [82]. The equations governing Model 10 are presented in detail, along with the initial and boundary conditions. The model is then non-dimensionalised and boundary immobilised to solve the dimensionless form within a fixed domain. Using COMSOL Multiphysics version 6.2®(COMSOL), a finite element analysis, solver, and simulation software, we solve Model 10 and compare the results with those from Model 11 to assess the impact of antibiotic delivery on biofilm growth. Additionally, sensitivity analyses are performed by varying the antibiotic effectiveness rate and the ratio of the initial antibiotic concentration to the solubility of the antibiotic in the biofilm, highlighting the influence of these parameters on biofilm dynamics.

Second, by integrating bacterial phenotypes and nutrient dynamics into biofilm models, we capture the interactions between proliferative, persister, and dead bacteria, and explore how nutrient availability influences their transitions, thereby developing biofilm resilience. In Section 5.2, Model 2 expands the biofilm model further by incorporating these characteristics. This work builds on foundational models in the literature, such as [84] for the primary concept of biofilm modelling, and key studies like [7] and [99] that highlight the importance of nutrient availability in biofilm dynamics. After non-dimensionalising and immobilising the model's domain, we solve it using COMSOL, while varying the nutrient concentration supplied from the bulk fluid. These nutrient levels, ranging from insufficient to intermediate to sufficient, help us explore how different nutrient availability, coupled with controlled antibiotic delivery, affects biofilm growth, composition, and resilience. In this analysis, we have identified five distinct phases of biofilm dynamics that remained consistent across all parameter sets. Sensitivity analyses are conducted, varying both nutrient availability and the solid antibiotic concentration loaded in the implant to examine the effects on these dynamic phases.

Finally, the chapter explores an initial and simplified approach to optimising antibiotic delivery by introducing a spatially dependent solid antibiotic concentration within the implant. This spatial variation represents a first step towards optimising the delivery of the antibiotic to the biofilm. A sensitivity analysis is performed to examine how different distributions of antibiotics across the implant influence the dynamic phases of the biofilm, providing information on potential strategies for more effective and targeted antibiotic delivery.

5.1 Introducing controlled antibiotic release to the simplest biofilm growth model (Model 10)

In this section, we present a mathematical model that captures both biofilm growth and controlled antibiotic release from a porous implant. The biofilm environment is modelled following the methodology outlined in Model 11 in Section 3.1, with the added consideration of antibiotic effects on biofilm development. The implant medium is modelled according to the framework described in Section 2.1. We refer to this model as Model 10, consistent with the nomenclature used in Chapter 2. To deepen our analysis, we compare these solutions with those derived from Model 11. Finally, we perform sensitivity analyses to evaluate the impact of antibiotic on the overall biofilm growth.

5.1.1 Model development

We denote the antibiotic concentration within the pores of the implant as $C_p(x,t)$ and within the biofilm medium as $C(x,t)$. Furthermore, $C_b(x,t)$ represents the concentration of the bound antibiotic that adheres to the walls of the pores, with ϕ_b indicating the volume fraction of this bound region and ϕ the porosity of the implant. This antibiotic delivery modelling follows the same approach to that outlined by [82], with the delivery mechanism structured in alignment with the methods detailed in that paper.

Fig. 2.1 schematically represents the model configuration for Model 1, consisting of a porous implant medium occupying the space from $x = -L_d$ to $x = 0$, initially saturated with antibiotic, adjacent to a biofilm medium from $x = 0$ to $x = L(t)$. $L(t)$ refers to the thickness of the biofilm that changes over time. While the biofilm model differs from Model 1 in the current case, the implant modeling remains the same. This figure can be referred to for a clear visualization of the implant model.

At the initial stage, the antibiotic is uniformly distributed in the pores with a concentration C_0. As the fluid interacts with the implant, the antibiotic begins to dissolve, leading to a reduction in the thickness of the solid antibiotic layer over time, described by the moving boundary $-L_1(t)$. For simplicity in the simulation, we assume a negligible initial dissolution of the antibiotic through considering a small initial value of $L_1(t)$. The presence of fluid in the pores facilitates the diffusion process, as it allows the dissolved antibiotic to be carried out by diffusion. The diffusion of the dissolved antibiotic within the pores is governed by an unsteady reaction-diffusion equation that includes both adsorption and desorption kinetics.

The effective diffusivity D_e of the antibiotic in the implant encapsulates several factors affecting diffusion within the porous medium. It is defined by the relationship

$$D_e = \frac{\phi_e}{\tau} D_c,$$

where D_c is the diffusion coefficient of the antibiotic in the biofilm, ϕ_e represents the effective porosity, and τ denotes tortuosity. Both ϕ_e and τ are dimensionless and their ratio, $\frac{\phi_e}{\tau}$, is a key microstructural parameter that influences the diffusion process. The effective porosity ϕ_e is the fraction of the overall porosity ϕ that actively contributes to solute transport. In cases where smaller pores restrict solute access, a condition known as constrictivity, ϕ_e becomes less than ϕ. Tortuosity τ, on the other hand, accounts for the increased travel path of the particles caused by the complex geometry of the pores. This parameter is instrumental in adjusting the antibiotic release rate by modifying the effective diffusion path within the medium.

Assuming that the adsorption and desorption processes reach equilibrium quickly compared to diffusion, we can express a relationship between the free antibiotic concentration $C_p(x,t)$ and the bound antibiotic concentration $C_b(x,t)$. This equilibrium is characterised by the dissociation constant K, which reflects the ratio of the desorption to the absorption rates. The concentration of the bound antibiotic $C_b(x,t)$ is therefore dependent on $C_p(x,t)$, ϕ_b, and ϕ. As the antibiotic diffuses from the pores into the biofilm, these interactions modulate the overall release dynamics. This assumption is commonly used in antibiotic release modelling, as seen in studies like [82], where equilibrium between adsorption and desorption is assumed to occur rapidly compared to diffusion, simplifying the system. While this is a reasonable approximation for many systems, future models could explore more detailed kinetics.

Within the biofilm, antibiotic concentration $C(x,t)$ is governed by an unsteady advection-diffusion-reaction equation, where the reaction term accounts for antibiotic degradation due to environmental interactions. We maintain continuity in the antibiotic concentration at the interface between the implant and the biofilm medium. For this, we define two distinct boundary conditions for C_p at $x = -L_1(t)$ to account for two different scenarios. The first scenario occurs when the interface $-L_1(t)$ is advancing through the implant. In this case, the boundary condition requires that C_p equals the solubility limit (C_S) of the antibiotic in the biofilm medium at the moving boundary $-L_1(t)$, representing the maximum dissolvable concentration. This scenario holds until a specific time, denoted as $t_{L_1=L_d}$, when the moving boundary reaches the solid boundary, $-L_d$, which represents the boundary of the implant. The second scenario begins at time $t_{L_1=L_d}$, when the entire antibiotic within the implant is dissolved. From this point onward, a zero-flux condition is applied for C_p at $x = -L_1(t) = -L_d$. The movement of the boundary between the undissolved and dissolved antibiotic layers within the implant is described by a Stefan condition, which serves as a boundary condition for C_p. Additionally, a continuity of flux condition is enforced at $x = 0$. These two conditions, the Stefan condition and the flux condition at $x = 0$, work together to ensure the conservation of the total antibiotic amount in the system. At the interface between the biofilm and the bulk fluid ($x = L(t)$), an infinite sink condition is applied for the antibiotic. This results in a rapid depletion of the antibiotic at this boundary, reflecting the scenario where the antibiotic quickly diffuses away into the surrounding fluid, effectively preventing any accumulation of antibiotic at the biofilm edge. Fig. 5.1 illustrates how the antibiotic is stored in the implant, released into the dissolved state, and diffuses into the biofilm.

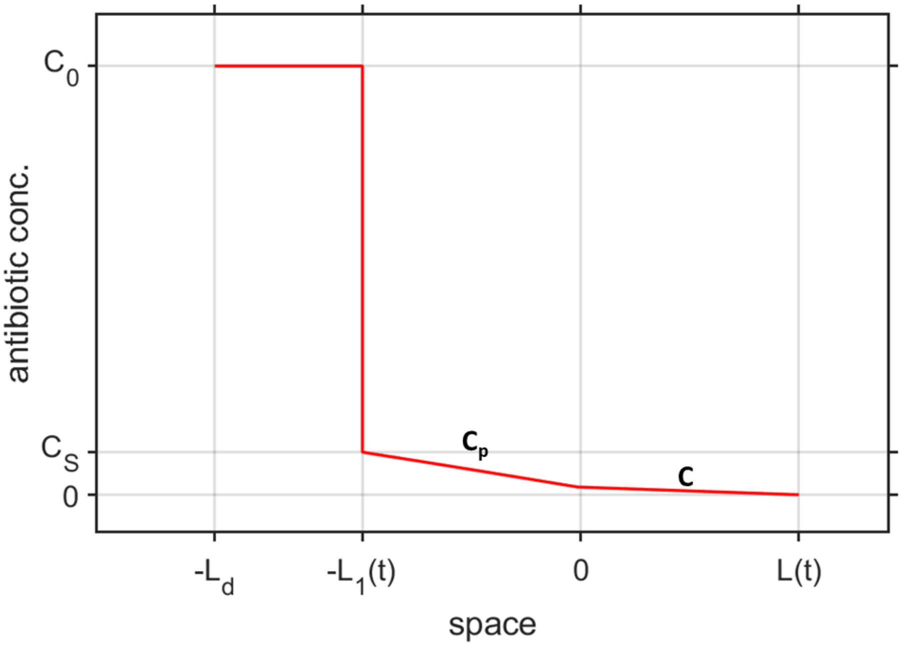

Figure 5.1: Schematic representation of antibiotic concentration profile along the implant and biofilm. The region from $-L_d$ to $-L_1(t)$ represents the solid antibiotic stored in the implant, where the concentration is C_0. Between $-L_1(t)$ and 0, the antibiotic is dissolved, with a concentration C_p, limited by the solubility of the antibiotic (C_s). The region from 0 to $L(t)$ corresponds to the biofilm, where the antibiotic concentration is C. This profile illustrates the transition of the antibiotic from the solid form in the implant to its dissolved state and subsequent diffusion into the biofilm.

As in previous models, here nutrient transport is modelled using Fickian diffusion. Biomass consumes nutrients according to Monod kinetics, leading to increased biofilm thickness as nutrients are converted into biomass. The Monod term is multiplied by the ratio of maximum biomass density to the yield coefficient. The maximum biomass density represents the upper limit of biomass that can be sustained within the biofilm, accounting for physical space and nutrient availability that limit growth. This parameter ensures the model accurately reflects the biofilm's carrying capacity. The yield coefficient, on the other hand, captures the efficiency of nutrient conversion into biomass, acknowledging that not all consumed nutrients contribute directly to growth; some are utilised for maintenance and cellular processes. These parameters together ensure that the model realistically depicts the balance between nutrient availability, biomass production, and environmental constraints. By employing a time-scale argument commonly used in biofilm modelling [68, 139], we assume the nutrient equation to be in a quasi-steady state in this model..

Assuming that biofilm growth does not occur inside the porous implant and that nutrients do not penetrate its porous structure, a no-flux boundary condition is applied at $x = 0$. This assumption is reasonable, as the nutrient supply is quickly consumed by the bacteria, leaving little nutrient available at the biofilm-bulk fluid boundary. Moreover this approach aligns with that of [2], who implemented similar boundary conditions in their work. We acknowledge that this assumption may not capture every aspect of implant-biofilm interactions in reality, but for the purpose of this study, it offers a manageable and useful framework. At the biofilm-bulk fluid interface, $x = L(t)$, we assume a constant influx of nutrients, represented by a Dirichlet boundary condition, with negligible external mass transfer resistance, as discussed in [2]. This reflects a scenario where nutrients are abundantly available at the interface, making it a reasonable representation for systems with ample nutrient supply and minimal external transport limitations. This boundary condition allows us to focus on nutrient dynamics within the biofilm, and this concept is consistently applied throughout the thesis.

The growth of biomass in the biofilm is implicitly modelled through the dynamics of nutrient consumption. Instead of using explicit equations for biomass growth, changes in biomass are captured by the evolution of biomass velocity, driven by nutrient uptake based on Monod kinetics. The biofilm's thickness increases as a result of this nutrient-driven biomass production, while biomass loss occurs through detachment at the biofilm-bulk fluid interface and natural death processes.

The detachment rate grows proportionally with the biofilm's thickness. This method, originally proposed by [128], has become the standard for modelling detachment and has been widely adopted in studies such as [24], [139], and [140]. By incorporating these factors into the biomass velocity equation, the model captures the dynamic interaction between nutrient consumption, biomass growth, natural death, and detachment. These processes together determine the evolution of biofilm thickness.

5.1.2 Governing equations

We begin by introducing and deriving the key equations that govern the system dynamics, starting with antibiotic diffusion in the porous implant and biofilm, followed by nutrient transport and biofilm growth. Each equation is accompanied by the relevant boundary conditions, ensuring a comprehensive definition of the system. The mathematical framework governing antibiotic diffusion in implant medium is similar to that used in [82], while the biofilm medium has characteristics similar to those of [2] with the addition of antibiotic effects on biofilm growth.

The solid antibiotic concentration within the implant is defined by the following relation, although this expression is not used directly in solving the model

$$C_p(x,t) \quad = \quad C_0, \quad -L_d < x < -L_1(t),\ t > 0. \tag{5.1}$$

The transport of antibiotic within the porous structure of the implant is described by an advection-free diffusion-reaction equation. Specifically, the concentration of freely diffusing antibiotic in the pore space, denoted by $C_p(x,t)$, evolves according to the following equation:

$$\phi(C_p)_t = D_e(C_p)_{xx} - \phi k_a C_p + \phi_b k_d C_b, \quad -L_1(t) < x < 0,\ t > 0, \tag{5.2}$$

Here, D_e represents the effective diffusion coefficient for the antibiotic within the porous medium. The constants k_a and k_d denote the absorption (binding) and desorption (unbinding) rate constants, respectively [82]. The porosity of the implant, i.e., the volume fraction, is denoted by ϕ, while ϕ_b denotes the volume fraction associated with the bound antibiotic sites.

The effective diffusivity D_e incorporates structural characteristics of the porous material, including its geometry and connectivity. If D_c denotes the intrinsic diffusion coefficient of the antibiotic in the biofilm, then the effective diffusivity is given by:

$$D_e = \frac{\phi_e}{\tau} D_c, \tag{5.3}$$

where ϕ_e is the effective porosity (accounting for only connected pores), and τ is the tortuosity of the medium [32].

The concentration of bound antibiotic in the porous phase, denoted $C_b(x,t)$, evolves according to:

$$\phi_b(C_b)_t = \phi k_a C_p - \phi_b k_d C_b, \quad -L_1(t) < x < 0,\ t > 0, \tag{5.4}$$

By adding equations (5.2) and (5.4), we obtain an equation for the evolution of the total antibiotic concentration (free and bound) within the implant medium:

$$\phi(C_p)_t + \phi_b(C_b)_t = D_e(C_p)_{xx}, \quad -L_1(t) < x < 0,\ t > 0, \tag{5.5}$$

Assuming that the kinetics of absorption and desorption are fast relative to diffusion, the system rapidly reaches local equilibrium. Under this quasi-steady assumption, the absorption-desorption system satisfies:

$$\begin{aligned} \phi k_a C_p &= \phi_b k_d C_b, \\ \Rightarrow C_b &= \frac{\phi C_p}{\phi_b K}, \end{aligned} \tag{5.6}$$

where $K = \frac{k_d}{k_a}$ is the equilibrium dissociation constant. Substituting the equilibrium condition (5.6) into the total concentration equation (5.5) yields a simplified diffusion equation for C_p:

$$(C_p)_t = D_a(C_p)_{xx}, \quad -L_1(t) < x < 0,\ t > 0, \tag{5.7}$$

This describes diffusion and dissolution behaviour of the antibiotic within the porous implant medium, spanning the region $(-L_1(t), 0)$. Here, D_a represents the apparent diffusion coefficient, defined as

$$D_a = \frac{1}{\phi(1+\frac{1}{K})} D_e = \frac{1}{\tau(1+\frac{1}{K})} \frac{\phi_e}{\phi} D_c, \tag{5.8}$$

Here, D_e is the effective diffusion coefficient, D_c is the intrinsic diffusivity of the antibiotic in the biofilm, τ is the tortuosity, and ϕ_e is the effective porosity. The dissociation constant K summarises the interplay between absorption and desorption dynamics, porosity, and microstructural characteristics of the medium. In our model, D_a is treated as spatially and temporally constant.

For the biofilm medium, the antibiotic concentration dynamics are governed by the advection-diffusion-reaction equation

$$C_t + (vC)_x \quad = \quad D_C C_{xx} - k_c C, \quad 0 < x < L(t),\ t > 0, \tag{5.9}$$

where k_c is the antibiotic degradation rate within the biofilm, D_c is the diffusion coefficient of the antibiotic, and v denotes the advective velocity.

In this model, the nutrient dynamic within the biofilm is modelled using an equation that balances diffusion and reaction terms, which captures the changes in nutrient concentration as a result of both diffusion and consumption by biomass [2]. The governing equation for nutrient dynamics is expressed as:

$$D_S S_{xx} = \frac{X_\infty}{\gamma_{bio}} \mu_b \left(\frac{S}{k_S + S} \right), \quad 0 < x < L(t),\ t > 0. \tag{5.10}$$

Here D_S is the nutrient diffusion coefficient. The right-hand side of the equation represents nutrient consumption by the biomass. Here, X_∞ is the maximum biomass density, and γ_{bio} is the yield coefficient that relates biomass growth to nutrient consumption. The Monod term $\mu_b \frac{S}{k_S+S}$ models the growth of the biomass, where μ_b is the maximum specific growth rate of the bacteria, and k_S is the half-saturation constant. Upon consumption of the nutrient by the biomass, the biofilm grows and the biofilm boundary, at $L(t)$, moves with a velocity that is determined by integrating the nutrient-dependent biomass growth rate minus the death rate, b, over the extent of the biofilm

$$v = \int_0^L \left[(1 - \kappa C)\mu_b \left(\frac{S}{k_S + S} \right) - b \right] dx, \quad t > 0. \tag{5.11}$$

Here the term $(1 - \kappa C)\mu_b \left(\frac{S}{k_S+S} \right)$ represents the growth of the biomass which is inhibited by the effects of antibiotic. Thus, the expansion of the biofilm, considering the detachment process, is expressed as

$$\frac{dL}{dt} = \int_0^L \left[(1 - \kappa C)\mu_b \left(\frac{S}{k_S + S} \right) - b \right] dx - \sigma L^2, \quad t > 0, \tag{5.12}$$

where σL^2 represents a quadratic detachment term, modelling the detachment of biofilm as a function of its thickness.

Initial and boundary conditions

For the implant medium, the initial conditions are specified as

$$C_p(x,0) = C_{in} + (C_S - C_{in})\frac{x^2}{L_{1,0}^2}, \quad \text{for} \quad -L_1(0) < x < 0, \tag{5.13}$$

$$C_b(x,0) = \frac{\phi C_p(x,0)}{\phi_b K}, \quad \text{for} \quad -L_1(0) < x < 0, \tag{5.14}$$

$$L_1(0) = L_{1,0}. \tag{5.15}$$

The spatially dependent initial condition for C_p in the domain $(L_1(t) < x < 0)$ aligns with the boundary conditions, ensuring a well-posed model. Typically, this initial condition would be constant. This alignment is crucial for achieving an efficient numerical solution of the equations. $L_{1,0}$ is a small initial value for $L_1(t)$.

For the biofilm medium, the initial conditions for antibiotic concentration and biofilm thickness are

$$C(x,0) = C_{in}, \quad \text{for} \quad 0 < x < L(0), \tag{5.16}$$

$$L(0) = L_0. \tag{5.17}$$

The boundary condition for C_p ensures continuity of antibiotic concentration at the implant-biofilm interface. The solubility condition at the moving boundary of the antibiotic for the first scenario, and the zero-flux condition for the second scenario, are specified as

$$C_p(-L_1(t),t) = C_s, \quad \text{when} \quad t < t_{L_1=L_d}, \tag{5.18}$$

$$C_p(0,t) = C(0,t) \quad t > 0. \tag{5.19}$$

The boundary flux conditions for the antibiotic concentration at $x = 0$ and $x = -L_1(t)$ are derived under the assumption of total mass conservation within the system, which is the methodology outlined in [82] for similar flux conditions. These conditions capture the interaction between the dissolving implant interface and the biofilm domain.

At the moving boundary $x = -L_1(t)$, the rate of implant dissolution influences the local antibiotic flux, resulting in a Stefan-type condition given by:

$$-D_a(C_p)_x = -\frac{dL_1}{dt}(C_s - C_0), \quad \text{at} \quad x = -L_1(t),\ t < t_{L_1=L_d}, \tag{5.20}$$

where C_s denotes the solubility limit of the antibiotic and C_0 is the concentration at the implant interface. This condition governs the evolution of the boundary $L_1(t)$ as the implant dissolves over time.

Once the implant is fully dissolved ($L_1(t) = L_d$), a zero-flux condition is applied at the now-fixed boundary:

$$(C_p)_x \quad = \quad 0, \quad \text{at} \quad x = -L_1(t) = -L_d,\ t \geq t_{L_1 = L_d}. \tag{5.21}$$

At the interface between the implant and biofilm domains ($x = 0$), continuity of diffusive flux is imposed to ensure consistent transport across the two regions:

$$-D_e(C_p)_x \quad = \quad -D_C C_x, \quad \text{at } x = 0,\ t > 0. \tag{5.22}$$

Equation (5.20) thus acts as a moving boundary condition governing $L_1(t)$, while equation (5.22) provides the coupling condition for antibiotic flux at the implant-biofilm interface.

At the implant-biofilm interface, nutrient concentration is subject to a zero-flux boundary condition and the advective velocity is set to zero,

$$-D_S S_x \quad = \quad 0, \quad \text{at } x = 0,\ t > 0, \tag{5.23}$$

$$v \quad = \quad 0, \quad \text{at } x = 0,\ t > 0. \tag{5.24}$$

Additionally, an infinite sink condition is applied to C at $x = L(t)$,

$$C = 0, \quad \text{at } x = L(t),\ t > 0. \tag{5.25}$$

This boundary condition reflects the rapid depletion of antibiotic at the biofilm edge, where the antibiotic quickly diffuses away into the surrounding fluid, effectively preventing any accumulation at this interface.

Finally, the nutrient concentration at the biofilm-bulk fluid interface is governed by a Dirichlet boundary condition,

$$S \quad = \quad S_0, \quad \text{at } x = L(t),\ t > 0. \tag{5.26}$$

The description and values of the parameters are given in Table 2.2 and the description of the variables are given in Table 2.1.

5.1.3 Non-dimensionalisation

To simplify the model and reduce the number of parameters, we introduce the following non-dimensional variables.

$$\overline{C}_p = \frac{C_p}{C_S}, \quad \overline{C}_b = \frac{C_b}{C_S}, \quad \overline{S} = \frac{S}{k_S}, \quad \overline{C} = \frac{C}{C_S}, \quad \overline{x} = \frac{x}{M}, \quad \overline{L}(t) = \frac{L(t)}{M}, \quad \overline{L}_1(t) = \frac{L_1(t)}{M},$$

$$\bar{t} = \mu_b t, \quad \bar{v} = \frac{v}{\mu_b M},$$

where $M = \sqrt{\frac{D_s \gamma_{bio} k_S}{\mu X_\infty}}$. The non-dimensioanlisation of nutrient, space, length and time is the same as Model 11 in Section 3.1.3.

After applying the above transformations, the equations (5.6) and (5.12) take the following non-dimensional forms

$$(\overline{C}_p)_{\bar{t}} = \overline{D}_a(\overline{C}_p)_{\bar{x}\bar{x}}, \quad -\overline{L}_1(\bar{t}) < \bar{x} < 0,\ \bar{t} > 0, \tag{5.27}$$

$$\overline{C}_b = \frac{\phi \overline{C}_p}{\phi_b K}, \tag{5.28}$$

$$\overline{C}_{\bar{t}} + (\bar{v}\overline{C})_{\bar{x}} = \overline{D}_C(\overline{C})_{\bar{x}\bar{x}} - \beta_4 \overline{C}, \quad 0 < \bar{x} < \overline{L}(\bar{t}),\ \bar{t} > 0, \tag{5.29}$$

$$\overline{S}_{\bar{x}\bar{x}} = \frac{\overline{S}}{1+\overline{S}}, \quad 0 < \bar{x} < \overline{L}(\bar{t}),\ \bar{t} > 0, \tag{5.30}$$

$$\bar{v} = \int_0^{\overline{L}} \left[(1 - G_4 \overline{C}) \left(\frac{\overline{S}}{1+\overline{S}} \right) - \varepsilon_1 \right] d\bar{x}, \quad \bar{t} > 0, \tag{5.31}$$

$$\frac{d\overline{L}}{d\bar{t}} = \int_0^{\overline{L}} \left[(1 - G_4 \overline{C}) \frac{\overline{S}}{1+\overline{S}} - \varepsilon_1 \right] d\bar{x} - \varepsilon_2 \overline{L}^2, \quad \bar{t} > 0. \tag{5.32}$$

The non-dimensional initial conditions are

$$\overline{C}_p(\bar{x},0) = \overline{C}_{in} + \frac{\overline{L}_0^2}{\overline{L}_{1,0}^2}(1 - \overline{C}_{in})\bar{x}^2, \quad \text{for } -\overline{L}_1(0) < \bar{x} < 0, \tag{5.33}$$

$$\overline{C}_b(\bar{x},0) = \frac{\phi \overline{C}_p(\bar{x},0)}{\phi_b K}, \quad \text{for } -\overline{L}_1(0) < \bar{x} < 0, \tag{5.34}$$

$$\overline{L}_1(0) = \overline{L}_{1,0}, \tag{5.35}$$

$$\overline{C}(\bar{x},0) = \overline{C}_{in}, \quad \text{for } 0 < \bar{x} < \overline{L}(0), \tag{5.36}$$

$$\overline{L}(0) = \varepsilon_3. \tag{5.37}$$

The boundary conditions (5.18)-(5.26) have their respective dimensionless forms as

$$\overline{C}_p(-\overline{L}_1(\bar{t}),\bar{t}) = 1, \quad \text{when } \bar{t} < \bar{t}_{L_1 = L_d}, \tag{5.38}$$

$$\overline{C}_p(0,\bar{t}) = \overline{C}(0,\bar{t}), \quad \bar{t} > 0, \tag{5.39}$$

$$-\overline{D}_a(\overline{C}_p)_{\bar{x}} = -\frac{d\overline{L}_1}{d\bar{t}}(1 - Q), \quad \text{at } \bar{x} = -\overline{L}_1(\bar{t}), \text{ for } \bar{t} < \bar{t}_{L_1 = L_d}, \tag{5.40}$$

$$(\overline{C}_p)_{\bar{x}} = 0, \quad \text{at } \bar{x} = -\overline{L}_1(\bar{t}) = -\overline{L}_d, \text{ for } \bar{t} \geq \bar{t}_{L_1 = L_d}, \tag{5.41}$$

$$-\overline{D}_e(\overline{C}_p)_{\bar{x}} = -\overline{D}_C \overline{C}_{\bar{x}}, \quad \text{at } \bar{x} = 0,\ \bar{t} > 0, \tag{5.42}$$

$$-\overline{D}_S \overline{S}_{\bar{x}} = 0, \quad \text{at } \bar{x} = 0,\ \bar{t} > 0, \tag{5.43}$$

$$\bar{v} = 0, \quad \text{at } \bar{x} = 0,\ \bar{t} > 0, \tag{5.44}$$

$$\overline{C} = 0, \quad \text{at } \bar{x} = \overline{L}(\bar{t}),\ \bar{t} > 0, \tag{5.45}$$

$$\overline{S} = \overline{S}_0, \quad \text{at } \bar{x} = \overline{L}(\bar{t}),\, \bar{t} > 0. \tag{5.46}$$

The dimensionless parameters for the above model are defined as

$$\overline{D}_a = \frac{D_a}{\mu_b M^2}, \quad \overline{D}_C = \frac{D_C}{\mu_b M^2}, \quad \overline{D}_e = \frac{D_e}{\mu_b M^2}, \quad \beta_4 = \frac{k_C}{\mu_b}, \quad G_4 = \kappa C_s, \quad \varepsilon_1 = \frac{b}{\mu_b}, \quad \varepsilon_2 = \frac{\sigma M}{\mu_b},$$

$$\overline{C}_{in} = \frac{C_{in}}{C_S}, \quad \overline{L}_{1,0} = \frac{L_{1,0}}{M}, \quad \varepsilon_3 = \frac{L_0}{M}, \quad Q = \frac{C_0}{C_S}, \quad \overline{S}_0 = \frac{S_0}{k_S}.$$

Most of them are the same non-dimensional parameters used in Model 11, as described in Section 3.1.3, with the addition of new dimensionless parameters such as β_4, G_4, $\overline{C}_{in}$, $\overline{L}_{1,0}$, and Q.

5.1.4 Boundary immobilisation

The solvable domain for the non-dimensionalised model is $[-\overline{L}_1(\bar{t}), \overline{L}(\bar{t})]$, with variables dependent on the non-dimensional coordinates $\bar{x}$ and $\bar{t}$. To better understand the reasoning behind the boundary immobilisation transformation, we take the example of antibiotic concentration within this domain.

To calculate the change in $\overline{C}$, the antibiotic concentration, at a specific point $\bar{x}$ in the domain, we need to consider several factors. First, we evaluate the rate of change of $\overline{C}$ with respect to time at that particular point. This gives us an understanding of how the concentration evolves purely over time, independent of other effects. However, because the domain itself is expanding due to the growth of the biofilm, we must account for this spatial expansion and its impact on the concentration at $\bar{x}$. The movement of the domain introduces a shift in the position of the biomass, which, in turn, affects the local concentration of the antibiotic. As the biofilm grows, the velocity of this biomass growth influences the distribution of $\overline{C}$, meaning that the antibiotic concentration at a fixed point $\bar{x}$ is altered not only by time but also by the expansion of the domain. Lastly, we incorporate the reaction terms that govern the behaviour of $\overline{C}$, including factors such as degradation, consumption, or any other interactions between the antibiotic and the biofilm, which contribute to the overall change in concentration.

The challenge of handling moving boundaries, which dynamically evolve over time due to biofilm growth and antibiotic diffusion, can be simplified through a boundary immobilisation transformation. This approach maps the original non-dimensionalised domain $[-\overline{L}_1(\bar{t}), \overline{L}(\bar{t})]$ onto a fixed domain $[-1, 1]$, thereby eliminating the complexities of having to track the movement of the boundaries explicitly. Figure 5.2 illustrates this transformation, where the variable $\bar{x}$ in the original domain is converted into a new coordinate ξ, which remains fixed despite the moving boundaries in the original coordinate system.

To perform this transformation, we define two separate mappings. For the region $0 < \bar{x} <$

$\overline{L}(\bar{t})$, the transformation is given by:

$$\xi = \frac{\bar{x}}{\overline{L}(\bar{t})},$$

and for the region $-\overline{L}_1(\bar{t}) < \bar{x} < 0$, the transformation is:

$$\xi = \frac{\bar{x}}{\overline{L}_1(\bar{t})}.$$

In both cases, the non-dimensional variables are denoted with bars. Through these transformations, the boundaries originally moving at $\bar{x} = -\overline{L}_1(\bar{t})$ and $\bar{x} = \overline{L}(\bar{t})$ are mapped to the fixed points $\xi = -1$ and $\xi = 1$, respectively, making the new solvable domain $[-1, 1]$. This transformation not only fixes the boundaries but also facilitates the numerical solution of the model, as it removes the need to explicitly handle the moving boundaries in the computation.

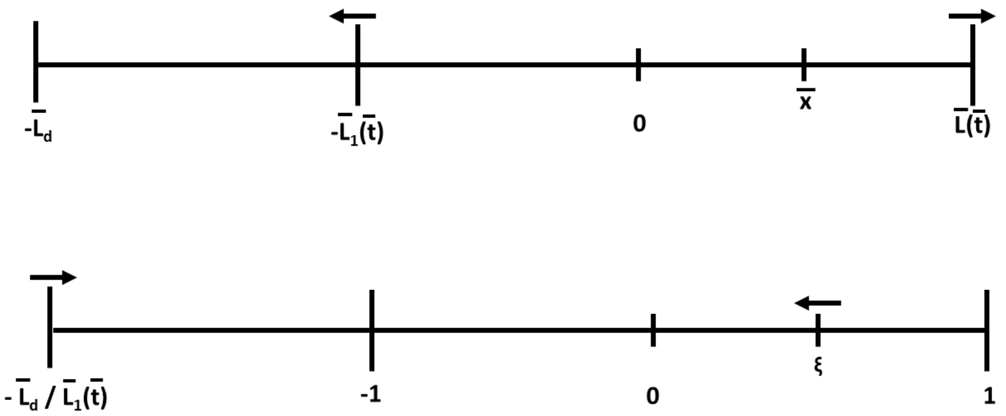

Figure 5.2: Transformation of the domain from the non-dimensionalised coordinates $[-\overline{L}_1(\bar{t}), \overline{L}(\bar{t})]$ (top) to a fixed domain $[-1, 1]$ (bottom) through boundary immobilisation. The variable $\bar{x}$ is mapped to a new coordinate ξ, which accounts for the moving boundaries in the original domain. In the top figure, the arrow above $\overline{L}(\bar{t})$ illustrates the outward movement of the right boundary, representing biofilm growth. The arrow above $\overline{L}_1(\bar{t})$ shows that this boundary moves toward $\overline{L}_d$. In the bottom figure, after boundary immobilisation, the arrow above ξ represents the shifting of the coordinate ξ to the left as $\overline{L}(\bar{t})$ increases. Similarly, the arrow above the boundary $-\overline{L}_d/\overline{L}_1(\bar{t})$ shows its movement toward the positive ξ-direction as $\overline{L}_1(\bar{t})$ increases.

In this transformed coordinate system, $\overline{C}$ becomes a function of ξ and $\bar{t}$. Although the boundaries are now stationary, the points within the domain are not static. The position $\bar{x}$ corresponding to a particular value of ξ still depends on the evolving boundary positions, which change over time as $\bar{t}$ progresses. This means that while the coordinate system ξ is fixed, the physical locations within the biofilm or implant corresponding to any given ξ will shift over time as the biofilm grows. As a result, when calculating the change in $\overline{C}$ at a point ξ, we must account for the additional effect of this shifting coordinate. This introduces an extra advective term in the time derivative, which represents the change in concentration due to the motion of the boundary relative to the fixed ξ coordinate.

Although the transformation fixes the boundaries at $\xi = -1$ and $\xi = 1$, there remains a moving boundary at $\xi = -\overline{L}_d/\overline{L}_1(\overline{t})$. However, this does not pose an issue because we do not need to solve for anything in the region $[-\overline{L}_d/\overline{L}_1(\overline{t}), -1)$, as this region represents the undissolved antibiotic. Thus, the moving boundary at $\xi = -\overline{L}_d/\overline{L}_1(\overline{t})$ can be disregarded in the computational process.

The new time derivative of $\overline{C}$ in the biofilm region $[0,1]$ in the transformed coordinate system can be written as

$$\left(\frac{\partial \overline{C}}{\partial \overline{t}}\right)_{\text{new}} = \left(\frac{\partial \overline{C}}{\partial \overline{t}}\right)_{\text{old}} + \frac{\partial \xi}{\partial \overline{t}} \frac{\partial \overline{C}}{\partial \xi},$$

which simplifies to

$$\left(\frac{\partial \overline{C}}{\partial \overline{t}}\right)_{\text{new}} = \left(\frac{\partial \overline{C}}{\partial \overline{t}}\right)_{\text{old}} - \frac{\xi}{\overline{L}} \frac{d\overline{L}}{d\overline{t}} \frac{\partial \overline{C}}{\partial \xi}.$$

Here, $()_{\text{new}}$ denotes the modified time derivative after boundary immobilisation, while $()_{\text{old}}$ denotes the original non-dimensionalised time derivative. This additional advective term accounts for the change in the position of the boundary and the resulting shift in the location of $\overline{C}$ within the fixed domain. The space derivatives will change as follows

$$\frac{\partial \overline{C}}{\partial \overline{x}} = \frac{1}{\overline{L}} \frac{\partial \overline{C}}{\partial \xi}$$

$$\frac{\partial^2 \overline{C}}{\partial \overline{x}^2} = \frac{1}{\overline{L}^2} \frac{\partial^2 \overline{C}}{\partial \xi^2}$$

By normalising the spatial variables in this way, we significantly simplify the numerical analysis of the model.

Now for the implant region $[-1,0]$, the new time derivative of $\overline{C}_p$ in the transformed coordinate system can be written as

$$\left(\frac{\partial \overline{C}_p}{\partial \overline{t}}\right)_{\text{new}} = \left(\frac{\partial \overline{C}_p}{\partial \overline{t}}\right)_{\text{old}} + \frac{\partial \xi}{\partial \overline{t}} \frac{\partial \overline{C}_p}{\partial \xi},$$

which simplifies to

$$\left(\frac{\partial \overline{C}_p}{\partial \overline{t}}\right)_{\text{new}} = \left(\frac{\partial \overline{C}_p}{\partial \overline{t}}\right)_{\text{old}} - \frac{\xi}{\overline{L}_1} \frac{d\overline{L}_1}{d\overline{t}} \frac{\partial \overline{C}_p}{\partial \xi}.$$

The expressions for the spatial derivatives are updated as follows

$$\frac{\partial \overline{C}_p}{\partial \overline{x}} = \frac{1}{\overline{L}_1} \frac{\partial \overline{C}_p}{\partial \xi}$$

$$\frac{\partial^2 \overline{C}_p}{\partial \bar{x}^2} = \frac{1}{\overline{L}_1^2}\frac{\partial^2 \overline{C}_p}{\partial \xi^2}$$

The transformation allows us to handle the moving boundaries of the biofilm and antibiotic layer more efficiently, as the dynamic nature of the problem is now captured through the transformed coordinates rather than directly in the equations.

Applying these transformations to the dimensionless model in Section 5.1.3, we get,

$$\begin{aligned}
(\overline{C}_p)_{\bar t} - \frac{\xi}{\overline{L}_1}\frac{d\overline{L}_1}{dt}\left(\overline{C}_p\right)_\xi &= \frac{\overline{D}_a}{\overline{L}_1^2}(\overline{C}_p)_{\xi\xi}, \quad -1<\xi<0,\ \bar t>0, && (5.47)\\
\overline{C}_b &= \frac{\phi \overline{C}_p}{\phi_b K}, && (5.48)\\
\overline{C}_{\bar t} + \frac{(\bar v\overline{C})_\xi}{\overline{L}} - \frac{\xi}{\overline{L}}\frac{d\overline{L}}{dt}\overline{C}_\xi &= \frac{\overline{D}_C}{\overline{L}^2}\overline{C}_{\xi\xi} - \beta_4\overline{C}, \quad 0<\xi<1,\ \bar t>0, && (5.49)\\
\frac{1}{\overline{L}^2}\overline{S}_{\xi\xi} &= \frac{\overline{S}}{1+\overline{S}}, \quad 0<\xi<1,\ \bar t>0, && (5.50)\\
\bar v &= \overline{L}\int_0^1 \left[(1-G_4\overline{C})\left(\frac{\overline{S}}{1+\overline{S}}\right) - \varepsilon_1\right] d\xi, \quad \bar t>0, && (5.51)\\
\frac{d\overline{L}}{d\bar t} &= \overline{L}\int_0^1 \left((1-G_4\overline{C})\frac{\overline{S}}{1+\overline{S}} - \varepsilon_1\right) d\xi - \varepsilon_2\overline{L}^2(t), \quad \bar t>0. && (5.52)
\end{aligned}$$

The boundary-immobilised initial conditions are

$$\begin{aligned}
\overline{C}_p(\xi,0) &= \overline{C}_{in} + (1-\overline{C}_{in})\xi^2, \quad \text{for } -1<\xi<0, && (5.53)\\
\overline{C}_b(\xi,0) &= \frac{\phi\overline{C}_p(\xi,0)}{\phi_b K}, \quad \text{for } -1<\xi<0, && (5.54)\\
\overline{L}_1(0) &= \overline{L}_{1,0}, && (5.55)\\
\overline{C}(\xi,0) &= \overline{C}_{in}, \quad \text{for } 0<\xi<1, && (5.56)\\
\overline{L}(0) &= \overline{L}_0. && (5.57)
\end{aligned}$$

Applying the same transformations to the boundary conditions (5.38)-(5.46) we get,

$$\begin{aligned}
\overline{C}_p(-1,\bar t) &= 1, \quad \text{when } \bar t < \bar t_{L_1=L_d}, && (5.58)\\
\overline{C}_p(0,\bar t) &= \overline{C}(0,\bar t), \quad \bar t>0, && (5.59)\\
-\overline{D}_a(\overline{C}_p)_\xi &= -\overline{L}_1\frac{d\overline{L}_1}{d\bar t}(1-Q), \quad \text{at } \xi=-1, \text{ for } \bar t < \bar t_{L_1=L_d}, && (5.60)\\
(\overline{C}_p)_\xi &= 0, \quad \text{at } \xi=-1, \text{ for } \bar t \geq \bar t_{L_1=L_d}, && (5.61)\\
-\frac{\overline{D}_e}{\overline{L}_1}(\overline{C}_p)_\xi &= -\frac{\overline{D}_C}{\overline{L}}\overline{C}_\xi, \quad \text{at } \xi=0,\ \bar t>0, && (5.62)\\
-\overline{D}_S\overline{S}_\xi &= 0, \quad \text{at } \xi=0,\ \bar t>0, && (5.63)\\
\bar v &= 0, \quad \text{at } \xi=0,\ \bar t>0, && (5.64)
\end{aligned}$$

$$\overline{C} = 0, \quad \text{at } \xi = 1, \, \bar{t} > 0, \tag{5.65}$$

$$\overline{S} = \overline{S}_0, \quad \text{at } \xi = 1, \, \bar{t} > 0. \tag{5.66}$$

5.1.5 Solution methodology

Below is an overview of the solution to the equations (5.47)-(5.52), using initial and boundary conditions (5.53)-(5.66). A key challenge in our modelling approach was the management of two moving boundaries. To address this, we applied the boundary immobilisation technique, transforming our solvable domain into $[-1,1]$ (see Section 5.1.4). The boundary immobilised problem was then solved using the following approach.

To effectively handle these complexities, we transitioned from MATLAB to COMSOL for this phase of modelling. COMSOL was chosen for several key reasons: First, the two moving boundaries in our model demanded a high level of control and adaptability, which COMSOL's adaptive time-stepping algorithm provides. This feature is particularly advantageous for complex modelling, allowing the software to dynamically adjust time steps based on solution changes, which ensures stability and efficiency even as boundaries change. Additionally, COMSOL is particularly well-suited for models involving multiple interacting species across different domains, as seen here with antibiotic, nutrient, and bacterial concentrations. The software's modular approach to solving coupled partial differential equations (PDEs) and its user-friendly graphical interface allow for easier integration and management of each species, as well as their respective boundary conditions.

We conducted two studies corresponding to the two scenarios described in Section 5.1.1, utilising COMSOL. The first study focused on the dissolution of the antibiotic within the porous implant in the domain $[-1,0]$, starting from the solid antibiotic region. In this case, the boundary condition (5.58) was imposed for $\overline{C}_p$ at $\xi = -1$. The second study imposed the boundary condition (5.61).

The fixed domain model was solved in COMSOL. The 'Transport of Diluted Species' module was employed to solve the transformed equation for C_p (equation (5.47)). The 'General form PDE' module was used to solve the equations for S, C, and v (equations (5.50), (5.49), and (5.64), respectively). For handling the two moving boundaries, we utilised the 'Domain ODEs and PDEs' module to solve the modified equation for L (equation (5.52)) and the 'Boundary ODEs and PDEs' module to implement the Stefan boundary condition for C_p (equation (5.60)).

Default solver settings were used with a custom relative tolerance set to 0.05 to balance speed and precision. The mesh was customised with a 'Maximum element size' of 0.01, a 'Maximum element growth rate' of 1.1, and a 'Resolution of narrow region' set to 1. Based on initial mesh testing, these settings provided an optimal balance between computational speed and accuracy, yielding more reliable results than the built-in COMSOL mesh settings. However, a detailed mesh sensitivity analysis was not conducted.

To enhance analysis and perform sensitivity studies, we used 'LiveLink$^{\text{TM}}$ for MATLAB$^{®}$'

[86] to analyse results directly with MATLAB. This allowed us to carry out in-depth analyses and sensitivity testing within MATLAB's environment, adding flexibility to the modelling process.

5.1.6 Results and discussions

It is important to note that all results are presented in non-dimensional form. We compared the solutions to the solution of Model 11 described in Section. 3.1. Model 11 focussed on the corresponding biofilm model without incorporating any antibiotic effects. In addition, sensitivity analyses were conducted to investigate the effects of antibiotics through two different parameters- antibiotic effectiveness rate, κ and the ratio of the antibiotic concentration loaded in the implant initially to the solubility of the antibiotic in the biofilm, Q. All parameter values are given in Table 2.2. All plots are generated for a final time of 10 days, consistent with the final time used for Model 11 in Section 3.1.6.

Comparison between models with and without antibiotic eluting porous implant

Fig. 5.3 provides a detailed comparison of biofilm growth dynamics for two models, The current model (Model 10) , which incorporates the effect of an antibiotic delivered through the implant, and Model 11 described in Section 3.1, which serves as a baseline model accounting only for nutrient consumption and biofilm growth.

Fig. 5.3(a) illustrates the temporal evolution of biofilm thickness for the two models. Both models exhibit a characteristic sigmoidal growth pattern, where biofilm thickness increases gradually in the early stages, followed by a rapid growth phase, and eventually levels off as the biofilm reaches its maximum thickness. Model 11, represented by the dashed line, serves as the baseline model, accounting for biofilm growth driven solely by nutrient consumption. In this model, as the biofilm matures, it consumes nutrients more efficiently, which facilitates a rapid increase in thickness until the system reaches a nutrient-limited or otherwise constrained steady state.

In contrast, Model 10, represented by the solid line, extends the baseline model by incorporating the effect of an antibiotic delivered through an antibiotic-eluting porous implant. The inclusion of this antibiotic introduces an additional term in the biofilm growth equation, specifically accounting for the antibiotic's effectiveness in slowing down biofilm development. During the early stages of growth, the antibiotic has a slight impact on the biofilm, as evidenced by the slower increase in biofilm thickness compared to Model 11. This initial divergence between the two models underscores the antibiotic's ability to inhibit biofilm growth by reducing the rate at which the biofilm can expand.

However, the antibiotic's impact is short-lived. The antibiotic diffuses rapidly throughout the biofilm and is subsequently cleared from the system, modelled by an infinite sink condition at the biofilm-bulk fluid boundary. As a result, the concentration of the antibiotic within the biofilm quickly diminishes to near zero. Once the antibiotic is depleted, the biofilm in Model 10 resumes its growth at a rate similar to that in Model 11. This convergence is particularly evident as the growth curves of both models eventually align, leading to the same final biofilm thickness in both scenarios. This behaviour suggests that the antibiotic's influence is confined to the period during which it is present within the biofilm. Once it is no longer available, the biofilm grows unchecked, ultimately reaching the same maximum thickness as in the baseline model.

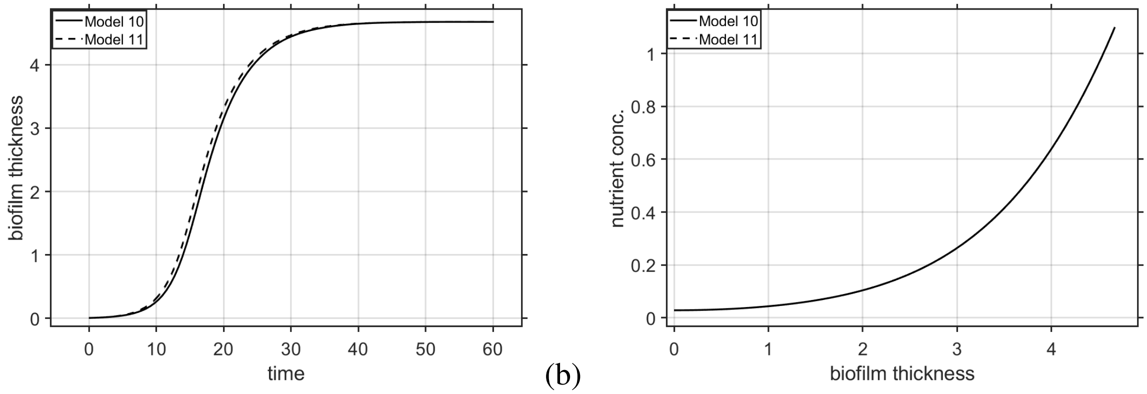

(a) (b)

Figure 5.3: (a)Temporal variation of biofilm thickness (b) spatial variation of nutrient concentration at final time, comparing Model 10 (with antibiotic delivery) and Model 11 (without antibiotic delivery).

Fig. 5.3(b) examines the nutrient concentration across the biofilm at the final time point for both models. The plot shows a strong positive correlation between nutrient concentration and biofilm thickness, which is consistent across both models. This is because nutrients enter from the biofilm's bulk-fluid interface, where they are most concentrated, and gradually decrease as they penetrate deeper into the biofilm, which is towards the implant-biofilm interface, $(x = 0)$, being consumed for biomass growth. However, due to the rapid diffusion and subsequent depletion of the antibiotic within the biofilm, the nutrient dynamics in Model 10 converge with those in Model 11. By the final time point, the nutrient concentration profiles of the two models are nearly identical. This indicates that the antibiotic's transient presence had a minimal long-term effect on nutrient dynamics within the biofilm. Essentially, once the antibiotic concentration drops to near zero, the biofilm regains its ability to utilise nutrients efficiently, leading to nutrient concentration profiles that are indistinguishable from the control model.

Impact of antibiotic effectiveness rate

Fig. 5.4 provides insights into the impact of antibiotic effectiveness on biofilm growth and nutrient dynamics. This analysis was conducted for three different antibiotic effectiveness rates: 100 times higher than the baseline (red line), at the baseline value (black line), and 100 times lower

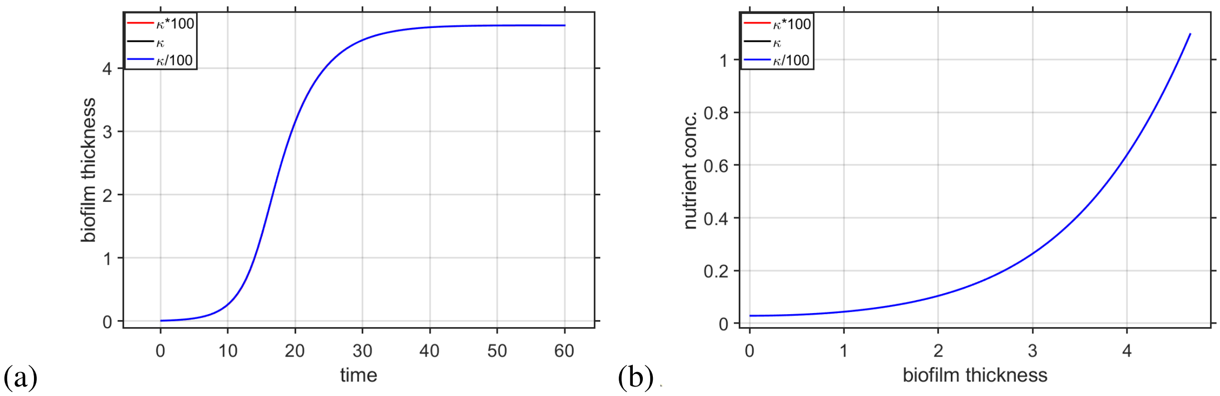

Figure 5.4: Effect of varying antibiotic effectiveness rate, κ on (a) temporal variation of biofilm thickness, (b) spatial variation of nutrient concentration at final time. The plots overlap for different κ values.

than the baseline (blue line).

In all scenarios, the biofilm thickness initially increases, then rapidly during an exponential growth phase, before finally plateauing as the biofilm reaches its maximum thickness (see Fig. 5.4(a)). Fig. 5.4(b) depicts the the nutrient concentration across the biofilm at the final time point for the different κ values. The nutrient is delivered from the biofilm-bulk fluid interface, which corresponds to the right side of the plot. It shows a higher nutrient concentration near that interface and gradually decreases as it goes deeper in the biofilm or nearer the implant-biofilm interface. This figure show that κ has minimal impact on both of them. This seemingly counterintuitive result can be explained by the rapid diffusion of the antibiotic within the biofilm and its subsequent removal to the bulk fluid, which is modelled by an infinite sink condition at the biofilm boundary. This rapid diffusion means that the antibiotic is only present within the biofilm for a very short period after it is introduced. Regardless of the effectiveness rate, the antibiotic quickly exits the biofilm environment, leading to a rapid decrease in its local concentration. Consequently, the nutrient concentration profiles for different κ values look almost identical at the final time point, reflecting the minimal long-term impact of the antibiotic. Once the antibiotic is depleted, the biofilm grows at a rate that quickly negates any initial differences caused by varying antibiotic effectiveness rate, leading to similar outcomes in both biofilm thickness and nutrient concentration across different scenarios.

Impact of the ratio Q

Fig. 5.5 provides insights into the impact of the ratio of the initial antibiotic loaded in the implant to the solubility of the antibiotic in the biofilm on biofilm growth and nutrient dynamics. This analysis was conducted for three different values of Q: 10 times higher than the baseline (red line), at the baseline value (black line), and 5 times lower than the baseline (blue line).

Fig. 5.5(a) shows the time evolution of biofilm thickness for three different values of Q. In

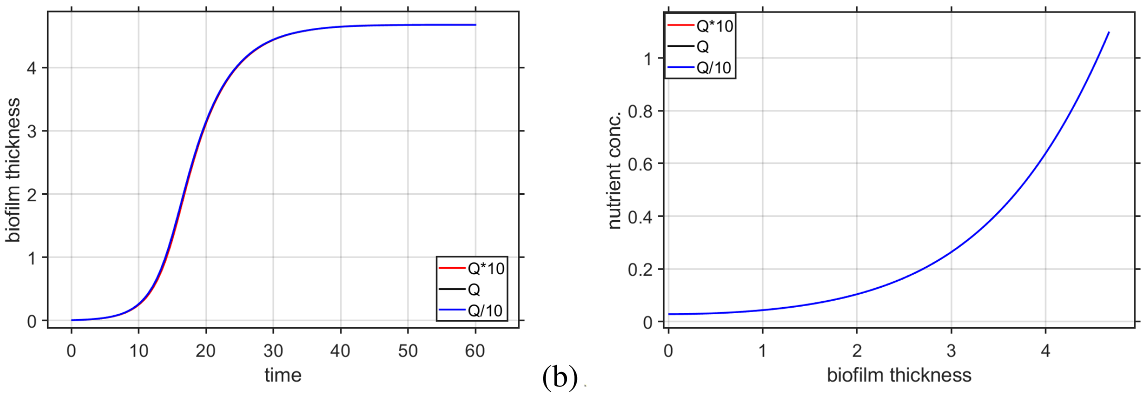

(a) (b)

Figure 5.5: Effect of varying Q on (a) temporal variation of biofilm thickness, (b) spatial variation of nutrient concentration at final time. The plots overlap for different Q values.

this case, the antibiotic initially present in the implant diffuses into the biofilm and affects the growth dynamics of the biofilm. A higher value of Q indicates more antibiotic loaded into the system relative to the biofilm's solubility, theoretically providing a larger reservoir of antibiotic and extending the release time, which helps inhibit biofilm growth. Another case could be if the solubility is lower than the base value, this would similarly result in a prolonged antibiotic release time. In both the cases, the antibiotic should be present in the biofilm for longer time. However, all three curves follow a nearly identical pattern, converging early in the time domain. This indicates that changes in the initial antibiotic to solubility ratio have minimal impact on biofilm growth. The black curve represents the baseline case, while the blue curve represents the lowest Q scenario. The initial slight lead of the blue curve, where it surpasses the other two, indicates that a lower antibiotic-to-solubility ratio might temporarily accelerate biofilm growth. However, this effect diminishes over time and is not sustained. All three scenarios converge and plateau at the same final biofilm thickness, indicating that the biofilm eventually reaches its maximum size once the antibiotic is depleted.

Fig. 5.5(b) shows the nutrient concentration across the biofilm at the final time for the same three Q values. Nutrient is delivered from the biofilm-bulk fluid interface, so we see the highest concentration at that interface. In this figure, all three curves overlap completely. This is because, as shown in Fig. 5.5(a), the biofilm thickness profiles for all Q values are nearly identical for all times, meaning that the biofilm grows at a similar rate regardless of the initial antibiotic to solubility ratio. Since the biofilm thickness remains nearly the same across all cases, and especially at final time, the nutrient consumption, which is directly tied to biofilm growth, also remains the same at final time. Thus, at the final time point, there is no observable difference in nutrient concentration profiles across the different values of Q.

In conclusion, while the initial antibiotic loading ratio (Q) may have a small transient effect on biofilm growth, its long-term impact is negligible. Once the antibiotic is depleted, the biofilm resumes its normal growth, driven by nutrient availability, leading to similar outcomes in both biofilm thickness and nutrient consumption regardless of the initial antibiotic loading.

Since we did not observe significant changes in biofilm dynamics when varying the antibiotic effectiveness parameter or the ratio of the initial antibiotic loading to the solubility, we now consider a case where the ratio Q is increased to ten times the base value. This higher Q implies that the initial antibiotic loading is much higher than the base value, or the solubility of the antibiotic in the biofilm is reduced. As a result, the antibiotic will remain present in the biofilm for a longer period. Under these conditions, we will modify the antibiotic effectiveness rate (κ) to investigate its impact on biofilm thickness and nutrient concentrations, as the prolonged presence of the antibiotic should make any changes in effectiveness more noticeable. This analysis was conducted for three different values of κ: 100 times higher than the baseline (red line), at the baseline value (black line), and 100 times lower than the baseline (blue line).

Fig. 5.6(a) presents the time evolution of biofilm thickness for different antibiotic effectiveness rates. The red curve results in the slowest biofilm growth, with the biofilm thickness increasing more gradually over time compared to the other two cases. The antibiotic's higher effectiveness combined with the higher value of Q leads to a more prolonged suppression of biofilm growth during the early phases. For the baseline value of κ, the biofilm grows more quickly than in the $\kappa \times 100$ case but more slowly than in the lowest effectiveness rate scenario. The antibiotic inhibits biofilm growth, but its effect is less pronounced than in the red curve. For the case represented by the blue curve, the antibiotic has the least impact on biofilm growth, allowing the biofilm to grow faster than in the other scenarios. Interestingly, the blue and black lines almost overlap, with the blue line being slightly higher than the black line. This indicates that despite the differences in antibiotic effectiveness, the lower κ value does not cause a significant increase in biofilm thickness compared to the baseline case, though the blue line reflects slightly faster biofilm growth. All three curves converge and plateau at the same biofilm thickness. This is because, as time progresses, the antibiotic concentration within the biofilm diminishes and eventually becomes negligible, allowing the biofilm to grow uninhibited to its maximum thickness. This convergence indicates that the antibiotic's impact is limited to the early phase, and once the antibiotic is depleted, the biofilm growth is primarily driven by nutrient availability, leading to convergence in biofilm thickness.

Fig. 5.6(b) shows the nutrient concentration across the biofilm at the final time for the same scenarios as Fig. 5.6(a). In this figure, the nutrient concentration profiles for all three cases overlap completely. This is because the biofilm thickness has reached similar values across all scenarios by the final time, as seen in Fig. 5.6(b). Since the biofilm thickness is nearly identical in all cases by the final time, we can conclude that the consumption of nutrients has also been the same across all scenarios. As biofilm growth is driven by nutrient consumption, the similar biofilm thickness at the final stage leads to the same nutrient concentration profile for all the cases. This further highlights that any early differences in biofilm growth have no long-term impact on nutrient dynamics once the biofilm thickness converges.

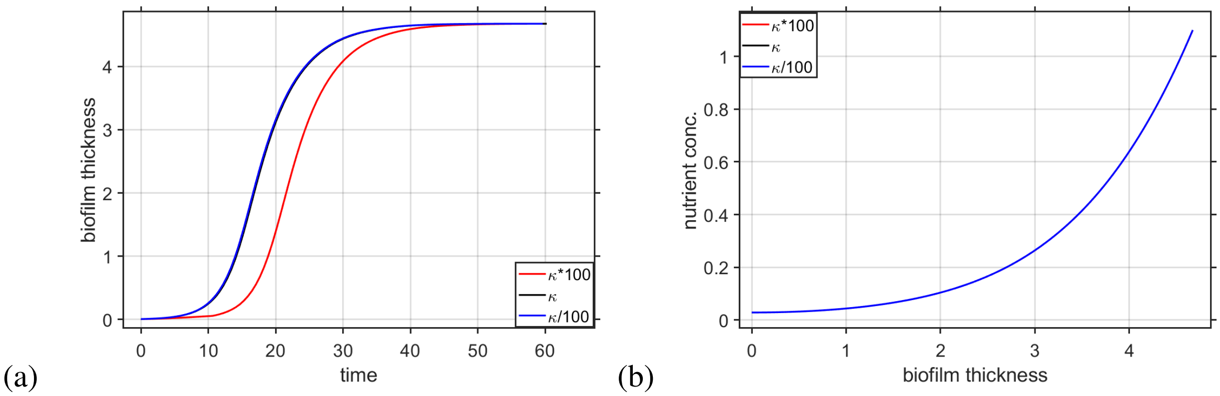
(a) (b)

Figure 5.6: Effect of varying antibiotic effectiveness rate, κ, with a higher Q on (a) temporal variation of biofilm thickness, (b) spatial variation of nutrient concentration at final time.

Changing the κ for higher Q values effectively suppressed biofilm growth, highlighting the significant role of antibiotic presence within the biofilm. The key takeaway from these sensitivity analyses is that the combined adjustment of κ and Q parameters had the desired effect on biofilm suppression. While altering these parameters individually did not yield noticeable changes, modifying them together demonstrated the intended impact, underscoring the importance of optimising both antibiotic loading and effectiveness for successful biofilm control.

5.2 Including bacterial phenotypes and EPS (Model 2)

The model presented in this section builds on the framework described in Section 5.1, with key enhancements to include different bacterial phenotypes, such as proliferative, persister, and dead bacteria, as well as EPS. This model examines how controlled antibiotic release from a porous implant affects the structure of the biofilm. It also captures how bacteria switch between proliferative and persister states based on nutrient availability, using critical nutrient thresholds to determine these changes, similar to the approach in Section 4.2. The model provides a detailed view of the biofilm's microbial structure and studies the effects of antibiotics on the biofilm. We refer to this model as Model 2, consistent with the nomenclature used in Chapter 2. The governing equations are solved numerically using COMSOL. We also explore how varying nutrient concentrations at the biofilm-bulk fluid boundary impacts biofilm dynamics. Additionally, the model identifies different phases of biofilm behaviour, which are consistent across various parameter sets. We examine the effects of different parameters on the timeline associated with these phases.

5.2.1 Model development

While this model builds upon the foundational structure outlined in Section 5.1, it closely mirrors Model 1 described in Section 2.1, with one key simplification. Unlike Model 1, this model assumes a constant water volume fraction, ϕ_{bio}, which is fixed at 0.8. This is an average value from Table 2.2. This simplification effectively aligns this model with Model 2 as discussed in Section 2.3. The rationale behind using a constant water volume fraction to mimic conditions of variable biofilm porosity is thoroughly discussed in Appendix A. Since all other aspects of this model are consistent with the concepts presented in Section 2.1, we will avoid redundancy and proceed directly to the governing equations for this model.

5.2.2 Governing equations

This section aims to encapsulate our model into a structured mathematical framework. While some of the equations and descriptions presented here are repetitions of those in previous, simpler models, this repetition is intentional and necessary. This is the most complete model in the thesis, and having all the key elements described together in one place provides a comprehensive view of the entire system. We will introduce and derive the key equations that govern the dynamics of our system. We start with equations related to antibiotic diffusion in the porous medium and proceed to describe biofilm dynamics and nutrient transport. The explanation of the physical processes represented by each term is detailed in Section. 2.1. The mathematical framework governing antibiotic delivery from the implant medium follows the approach described in Section 5.1.2 [82], while the biofilm medium is modelled using a framework similar to that outlined in Section 4.2.2 [84].

The solid antibiotic concentration within the implant is defined by the following relation, although this expression is not used directly in solving the model [82]

$$C_p(x,t) \quad = \quad C_0, \quad \text{for} \quad -L_d < x < -L_1(t),\ t > 0. \tag{5.67}$$

The diffusion and dissolution dynamics of the antibiotic within the porous medium $(-L_1(t), 0)$, are governed by the following equations which are similar to the equations of Model 10 in Section 5.1.2.

$$(C_p)_t \quad = \quad D_a (C_p)_{xx}, \quad -L_1(t) < x < 0,\ t > 0, \tag{5.68}$$

$$C_b \quad = \quad \frac{\phi C_p}{\phi_b K}. \tag{5.69}$$

Here, D_a represents the apparent diffusion coefficient, defined as

$$D_a = \frac{1}{\phi(1+\frac{1}{K})} D_e = \frac{1}{\tau(1+\frac{1}{K})} \frac{\phi_e}{\phi} D_c, \tag{5.70}$$

where D_e is the effective diffusion coefficient and $K = \frac{k_d}{k_a}$ is the equilibrium dissociation constant. This constant, K, incorporates the interrelated effects of porosity, absorption, desorption, tortuosity, and constrictivity within the medium. In our model, D_a remains constant throughout both space and time.

To ensure volume conservation within the biofilm, a constraint is imposed that maintains the sum of all volume fractions equal to one

$$1 = \phi_{bio} + \frac{B + B_p + B_d}{\rho_B} + \frac{E}{\rho_E}, \tag{5.71}$$

where ρ_B and ρ_E denote the densities of bacterial cells and EPS, respectively and ϕ_{bio} represents the water volume fraction within the biofilm, which modulates the effective transport and availability of nutrients [84].

Within the biofilm medium, the dynamics of the antibiotic concentration are governed by the advection-diffusion-reaction equation

$$\phi_{bio} C_t + \phi_{bio}(vC)_x = \phi_{bio} D_C C_{xx} - k_c \phi_{bio} C, \quad 0 < x < L(t),\ t > 0. \tag{5.72}$$

Here, k_c represents the rate of antibiotic degradation within the biofilm, D_C is the diffusion coefficient of the antibiotic, and v denotes the advective velocity.

We model the dynamics of the nutrient and bacterial populations using advection-diffusion-reaction equations, which capture the changes in nutrient concentration and bacterial populations due to biochemical interactions. The equation governing nutrient dynamics is expressed as:

$$\phi_{bio} S_t + \phi_{bio}(vS)_x = \phi_{bio} D_S S_{xx} - \frac{\mu \phi_{bio} S}{k_S + \phi_{bio} S} B, \quad 0 < x < L(t),\ t > 0. \tag{5.73}$$

Here, $\frac{\mu \phi_{bio} S}{k_S + \phi_{bio} S} B$ quantifies the consumption of nutrients by proliferative bacteria. This term is derived from Monod kinetics, where μ represents the maximum rate of nutrient uptake, S is the nutrient concentration, k_S is the half-saturation constant, and B denotes the concentration of proliferative bacteria. The equation balances the effects of advection and diffusion of nutrients with their consumption by bacteria within the biofilm.

The dynamics of the proliferative bacteria concentration within the biofilm are governed by the following equation

$$\begin{aligned} B_t + (vB)_x &= D_B B_{xx} + (k_B - \kappa \phi_{bio} C) \frac{\mu \phi_{bio} S}{k_S + \phi_{bio} S} B - \max(\alpha_1 \phi_{bio} C - \alpha_2, 0) B - bB \\ &\quad - \max\left(k_F \frac{S_2 - S}{S_2 - S_1}, 0 \right) B \\ &\quad + \max\left(k_R \frac{S - S_1}{S_2 - S_1}, 0 \right) B_p, \quad 0 < x < L(t),\ t > 0. \end{aligned} \tag{5.74}$$

Here, bacterial growth is represented by a Monod term, $(k_B - \kappa \phi_{bio} C) \frac{\mu \phi_{bio} S}{k_S + \phi_{bio} S} B$, which is modulated by the antibiotic concentration at a rate κ. The term $\max(\alpha_1 \phi_{bio} C - \alpha_2, 0) B$ quantifies death due to the antibiotic in the absence of nutrient, while bB denotes the natural death rate.

Additionally, the dynamics of bacterial state transitions are influenced by nutrient thresholds, with $\max\left(k_F \frac{S_2-S}{S_2-S_1}, 0\right) B$ describing the formation of persister bacteria when nutrient levels fall below S_2, and $\max\left(k_R \frac{S-S_1}{S_2-S_1}, 0\right) B_p$ accounting for the reversion from persister to proliferative bacteria when nutrient levels exceed S_1.

The dynamics of remaining biomass constituents are described by the following equations

$$\begin{aligned}
(B_p)_t + (vB_p)_x &= D_{B_p}(B_p)_{xx} + \max\left(k_F \frac{S_2 - S}{S_2 - S_1}, 0\right) B \\
&\quad - \max\left(k_R \frac{S - S_1}{S_2 - S_1}, 0\right) B_p, \quad 0 < x < L(t),\ t > 0, && (5.75) \\
(B_d)_t + (vB_d)_x &= D_{B_d}(B_d)_{xx} + \kappa \phi_{bio} C \frac{\mu \phi_{bio} S}{k_S + \phi_{bio} S} B \\
&\quad + \max(\alpha_1 \phi_{bio} C - \alpha_2, 0) B + bB, \quad 0 < x < L(t),\ t > 0, && (5.76) \\
E_t + (vE)_x &= D_E E_{xx} + k_E \frac{\mu \phi_{bio} S}{k_S + \phi_{bio} S} B, \quad 0 < x < L(t),\ t > 0. && (5.77)
\end{aligned}$$

Here, equation (5.77) illustrates the production of EPS by proliferative bacteria facilitated by nutrient availability.

The advective velocity of biofilm constituents is determined as follows

$$v_x = \frac{1}{1 - \phi_{bio}} \left(\frac{k_B}{\rho_B} + \frac{k_E}{\rho_E} \right) \frac{\mu \phi_{bio} S}{k_S + \phi_{bio} S} B, \quad 0 < x < L(t),\ t > 0. \qquad (5.78)$$

Equation (5.78) has been derived in the same manner as equation (3.28) for Model 8.

Finally, the biofilm-bulk fluid interface or the biofilm thickness is governed by the ordinary differential equation

$$\frac{dL}{dt} = v(L),\ t > 0. \qquad (5.79)$$

This describes the rate of biofilm expansion over time and corresponds to the velocity of the biomass at the point $x = L$.

Initial and boundary conditions

The initial conditions for the implant medium have been chosen as

$$\begin{aligned}
C_p(x,0) &= C_{in} + (C_S - C_{in}) \frac{x^2}{L_{1,0}^2}, \quad \text{for} \quad -L_1(0) < x < 0, && (5.80) \\
C_b(x,0) &= \frac{\phi C_p(x,0)}{\phi_b K}, \quad \text{for} \quad -L_1(0) < x < 0, && (5.81) \\
L_1(0) &= L_{1,0}, && (5.82)
\end{aligned}$$

where $L_{1,0}$ is a small initial value for $L_1(t)$. The initial condition for the concentration variable C_p within the domain $-L_1(t) < x < 0$ is spatially dependent, ensuring consistency with the boundary conditions, thereby contributing to a well-posed model. Typically, this initial condition would be constant. This alignment is crucial for achieving an efficient numerical solution of the equations. A similar approach is adopted for the initial conditions of bacterial phenotypes and EPS, maintaining coherence with the boundary conditions. The initial conditions for nutrient, antibiotic, and biomass concentrations in the biofilm medium are defined as follows.

$$\begin{aligned}
C(x,0) &= C_{in}, \quad 0 < x < L(0), && (5.83)\\
S(x,0) &= S_0, \quad 0 < x < L(0), && (5.84)\\
B(x,0) &= B_0 e^{\frac{v(x,0)}{D_B}x}, \quad 0 < x < L(0), && (5.85)\\
B_p(x,0) &= B_{p0} e^{\frac{v(x,0)}{D_{B_p}}x}, \quad 0 < x < L(0), && (5.86)\\
B_d(x,0) &= B_{d0} e^{\frac{v(x,0)}{D_{B_d}}x}, \quad 0 < x < L(0), && (5.87)\\
E(x,0) &= E_0 e^{\frac{v(x,0)}{D_E}x}, \quad 0 < x < L(0), && (5.88)\\
L(0) &= L_0. && (5.89)
\end{aligned}$$

The boundary condition for C_p entails the continuity of antibiotic concentration at the interface between the implant and the biofilm. We also show the solubility condition at the moving boundary of the antibiotic for our first scenario and a zero-flux condition at the same boundary for our second scenario. These conditions are expressed as

$$\begin{aligned}
C_p(-L_1(t),t) &= C_s, \quad \text{when} \quad t < t_{L_1=L_d}, && (5.90)\\
C_p(0,t) &= C(0,t),\ t > 0. && (5.91)
\end{aligned}$$

The flux conditions for the antibiotic concentrations are

$$\begin{aligned}
-D_a(C_p)_x &= -\frac{dL_1}{dt}(C_s - C_0), \quad \text{at} \quad x = -L_1(t), \quad \text{for} \quad t < t_{L_1=L_d}, && (5.92)\\
(C_p)_x &= 0, \quad \text{at} \quad x = -L_1(t) = -L_d, \quad \text{for} \quad t < t_{L_1=L_d}, && (5.93)\\
-D_e(C_p)_x &= -D_C C_x, \quad \text{at} \quad x = 0,\ t > 0. && (5.94)
\end{aligned}$$

The Stefan boundary condition (5.92) is employed as the evolution equation governing the moving boundary $L_1(t)$, while equation (5.94) serves as the boundary condition for C at $x = 0$.

At the implant-biofilm interface, the concentration of nutrient and biomass constituents is subjected to a zero-flux boundary condition, while the advective velocity is assumed to be zero at this boundary.

$$-D_S S_x = -D_B B_x = -D_{B_p}(B_p)_x \quad = \quad -D_{B_d}(B_d)_x$$

$$= \quad -D_E E_x = 0, \quad \text{at } x = 0,\, t > 0, \tag{5.95}$$

$$v \quad = \quad 0, \quad \text{at } x = 0,\, t > 0. \tag{5.96}$$

We adopt an infinite sink condition for C at $x = L(t)$, as indicated by

$$C \quad = \quad 0, \quad \text{at} \quad x = 0,\, t > 0. \tag{5.97}$$

This boundary condition reflects the rapid depletion of antibiotic at the biofilm edge, where the antibiotic quickly diffuses away into the surrounding fluid, effectively preventing any accumulation at this interface.

Finally, the biomass constituents adhere to a zero-flux condition at the biofilm-bulk fluid interface ($x = L(t)$), whereas the nutrient concentration is governed by a Dirichlet boundary condition at the same interface.

$$\begin{aligned}
S &= S_0, \quad \text{at } x = L(t),\, t > 0, && (5.98)\\
-D_B B_x + vB = -D_{B_p}(B_p)_x + vB_p &= -D_{B_d}(B_d)_x + vB_d && \\
&= -D_E E_x + vE = 0, \quad \text{at } x = L(t),\, t > 0. && (5.99)
\end{aligned}$$

The description and values of the parameters are given in Table 2.2 and the description of the variables are given in Table 2.1.

5.2.3 Non-dimensionalisation

We use the following non-dimensionalisation:

$$\overline{B} = \frac{B}{k_S}, \quad \overline{B}_p = \frac{B_p}{k_S}, \quad \overline{B}_d = \frac{B_d}{k_S}, \quad \overline{E} = \frac{E}{k_S}, \quad \overline{S} = \frac{S}{k_S}, \quad \overline{C} = \frac{C}{C_S}, \quad \overline{C}_p = \frac{C_p}{C_S}, \quad \overline{C}_b = \frac{C_b}{C_S},$$

$$\bar{t} = bt, \quad \overline{v} = \frac{v}{bL_0}, \quad \overline{x} = \frac{x}{L_0}.$$

Now after applying the above non-dimensionalisations to the equations (5.68)-(5.79) we get,

$$\begin{aligned}
(\overline{C}_p)_{\bar{t}} &= \overline{D}_a(\overline{C}_p)_{\overline{xx}}, \quad -\overline{L}_1(\bar{t}) < \overline{x} < 0,\, \bar{t} > 0, && (5.100)\\
\overline{C}_b &= \frac{\phi \overline{C}_p}{\phi_b K}, && (5.101)\\
1 &= \phi_{bio} + \frac{\overline{B} + \overline{B}_p + \overline{B}_d}{\overline{\rho}_B} + \frac{E}{\overline{\rho}_E}, && (5.102)\\
\phi_{bio}\overline{C}_{\bar{t}} + \phi_{bio}(\overline{v}\overline{C})_{\overline{x}} &= \phi_{bio}\overline{D}_C(\overline{C})_{\overline{xx}} - \beta_4 \phi_{bio}\overline{C}, \quad 0 < \overline{x} < \overline{L}(\bar{t}),\, \bar{t} > 0, && (5.103)\\
\phi_{bio}\overline{S}_{\bar{t}} + \phi_{bio}(\overline{v}\overline{S})_{\overline{x}} &= \phi_{bio}\overline{D}_S\overline{S}_{\overline{xx}} - G_3\frac{\phi_{bio}\overline{S}}{1 + \phi_{bio}\overline{S}}\overline{B}, \quad 0 < \overline{x} < \overline{L}(\bar{t}),\, \bar{t} > 0, && (5.104)
\end{aligned}$$

$$\begin{aligned}
\overline{B}_{\overline{t}}+(\overline{v}\overline{B})_{\overline{x}} &= \overline{D}_B\overline{B}_{\overline{xx}}+(G_1-G_4\phi_{bio}\overline{C})\frac{\phi_{bio}\overline{S}}{1+\phi_{bio}\overline{S}}\overline{B}-\max(\beta_1\phi_{bio}\overline{C}-\beta_5,0)\overline{B} \\
&\quad -\overline{B}-\max\left(\beta_2\frac{\overline{S}_2-\overline{S}}{\overline{S}_2-\overline{S}_1},0\right)\overline{B} \\
&\quad +\max\left(\beta_3\frac{\overline{S}-\overline{S}_1}{\overline{S}_2-\overline{S}_1},0\right)\overline{B}_p, \quad 0<\overline{x}<\overline{L}(\overline{t}),\ \overline{t}>0, \qquad (5.105) \\
(\overline{B}_p)_{\overline{t}}+(\overline{v}\overline{B}_p)_{\overline{x}} &= \overline{D}_{B_p}(\overline{B}_p)_{\overline{xx}}+\max\left(\beta_2\frac{\overline{S}_2-\overline{S}}{\overline{S}_2-\overline{S}_1},0\right)\overline{B} \\
&\quad -\max\left(\beta_3\frac{\overline{S}-\overline{S}_1}{\overline{S}_2-\overline{S}_1},0\right)\overline{B}_p, \quad 0<\overline{x}<\overline{L}(\overline{t}),\ \overline{t}>0, \qquad (5.106) \\
(\overline{B}_d)_{\overline{t}}+(\overline{v}\overline{B}_d)_{\overline{x}} &= \overline{D}_{B_d}(\overline{B}_d)_{\overline{xx}}+G_4\phi_{bio}\overline{C}\frac{\phi_{bio}\overline{S}}{1+\phi_{bio}\overline{S}}\overline{B} \\
&\quad +\max(\beta_1\phi_{bio}\overline{C}-\beta_5,0)\overline{B}+\overline{B}, \quad 0<\overline{x}<\overline{L}(\overline{t}),\ \overline{t}>0, \qquad (5.107) \\
\overline{E}_{\overline{t}}+(\overline{v}\overline{E})_{\overline{x}} &= \overline{D}_E\overline{E}_{\overline{xx}}+G_2\frac{\phi_{bio}\overline{S}}{1+\phi_{bio}\overline{S}}\overline{B}, \quad 0<\overline{x}<\overline{L}(\overline{t}),\ \overline{t}>0, \qquad (5.108) \\
\overline{v}_{\overline{x}} &= \frac{1}{1-\phi_{bio}}\left(\frac{k_B}{\overline{\rho}_B}+\frac{k_E}{\overline{\rho}_E}\right)G_3\frac{\phi_{bio}\overline{S}}{1+\phi_{bio}\overline{S}}\overline{B}, \ 0<\overline{x}<\overline{L}(\overline{t}),\ \overline{t}>0, \qquad (5.109) \\
\frac{d\overline{L}}{d\overline{t}} &= \overline{v}(\overline{L}), \quad \overline{t}>0. \qquad (5.110)
\end{aligned}$$

We apply the same transformations to our initial and boundary conditions (5.80)-(5.99). The dimensionless initial conditions are

$$\begin{aligned}
\overline{C}_p(\overline{x},0) &= \overline{C}_{in}+\frac{L_0^2}{L_{1,0}^2}(1-\overline{C}_{in})\overline{x}^2, \quad \text{for } -\overline{L}_1(0)<\overline{x}<0, \qquad (5.111) \\
\overline{C}_b(\overline{x},0) &= \frac{\phi\overline{C}_p(\overline{x},0)}{\phi_b K}, \quad \text{for } -\overline{L}_1(0)<\overline{x}<0, \qquad (5.112) \\
\overline{L}_1(0) &= \overline{L}_{1,0}, \qquad (5.113) \\
\overline{C}(\overline{x},0) &= \overline{C}_{in}, \quad \text{for } 0<\overline{x}<\overline{L}(0), \qquad (5.114) \\
\overline{S}(\overline{x},0) &= \overline{S}_0, \quad \text{for } 0<\overline{x}<\overline{L}(0), \qquad (5.115) \\
\overline{B}(\overline{x},0) &= \overline{B}_0 e^{\frac{\overline{v}(\overline{x},0)}{\overline{D}_B}\overline{x}}, \quad \text{for } 0<\overline{x}<\overline{L}(0), \qquad (5.116) \\
\overline{B}_p(\overline{x},0) &= \overline{B}_{p0} e^{\frac{\overline{v}(\overline{x},0)}{\overline{D}_{B_p}}\overline{x}}, \quad \text{for } 0<\overline{x}<\overline{L}(0), \qquad (5.117) \\
\overline{B}_d(\overline{x},0) &= \overline{B}_{d0} e^{\frac{\overline{v}(\overline{x},0)}{\overline{D}_{B_d}}\overline{x}}, \quad \text{for } 0<\overline{x}<\overline{L}(0), \qquad (5.118) \\
\overline{E}(\overline{x},0) &= \overline{E}_0 e^{\frac{\overline{v}(\overline{x},0)}{\overline{D}_E}\overline{x}}, \quad \text{for } 0<\overline{x}<\overline{L}(0), \qquad (5.119) \\
\overline{L}(0) &= \overline{L}_0. \qquad (5.120)
\end{aligned}$$

The non-dimensionalised boundary conditions are

$$\overline{C}_p(-\overline{L}_1(\overline{t}),\overline{t}) = 1, \quad \text{when } \overline{t}<\overline{t}_{L_1=L_d}, \qquad (5.121)$$

$$
\begin{aligned}
\overline{C}_p(0,\bar{t}) &= \overline{C}(0,\bar{t}), \quad \bar{t}>0, && (5.122)\\
-\overline{D}_a(\overline{C}_p)_{\bar{x}} &= -\frac{d\overline{L}_1}{d\bar{t}}(1-Q), \text{ at } \bar{x}=-\overline{L}_1(\bar{t}), \text{ for } \bar{t}<\bar{t}_{L_1=L_d}, && (5.123)\\
(\overline{C}_p)_{\bar{x}} &= 0, \text{ at } \bar{x}=-\overline{L}_1(\bar{t})=-\overline{L}_d, \text{ for } \bar{t}\geq \bar{t}_{L_1=L_d}, && (5.124)\\
-\overline{D}_e(\overline{C}_p)_{\bar{x}} &= -\overline{D}_C\overline{C}_{\bar{x}}, \quad \text{at } \bar{x}=0, \bar{t}>0, && (5.125)\\
-\overline{D}_S\overline{S}_{\bar{x}}=-\overline{D}_B\overline{B}_{\bar{x}}=-\overline{D}_{B_p}(\overline{B}_p)_{\bar{x}} &= -\overline{D}_{B_d}(\overline{B}_d)_{\bar{x}} \\
&= -\overline{D}_E\overline{E}_{\bar{x}}=0, \quad \text{at } \bar{x}=0, \bar{t}>0, && (5.126)\\
\bar{v} &= 0, \quad \text{at } \bar{x}=0, \bar{t}>0, && (5.127)\\
\overline{C} &= 0, \quad \text{at } \bar{x}=\overline{L}(\bar{t}), \bar{t}>0, && (5.128)\\
\overline{S} &= \overline{S}_0, \quad \text{at } \bar{x}=\overline{L}(\bar{t}), \bar{t}>0, && (5.129)\\
-\overline{D}_B\overline{B}_{\bar{x}}+\bar{v}\overline{B}=-\overline{D}_{B_p}(\overline{B}_p)_{\bar{x}}+\bar{v}\overline{B}_p &= -\overline{D}_{B_d}(\overline{B}_d)_{\bar{x}}+\bar{v}\overline{B}_d \\
&= -\overline{D}_E\overline{E}_{\bar{x}}+\bar{v}\overline{E}=0, \quad \text{at } \bar{x}=\overline{L}(\bar{t}), \bar{t}>0. && (5.130)
\end{aligned}
$$

The dimensionless parameters for our above model equations (5.100)-(5.130) are

$$
\overline{D}_a=\frac{D_a}{bL_0^2}, \quad \overline{\rho}_B=\frac{\rho_B}{k_S}, \quad \overline{\rho}_E=\frac{\rho_E}{k_S}, \quad \overline{D}_C=\frac{D_C}{bL_0^2}, \quad \beta_4=\frac{k_c}{b}, \quad \overline{D}_S=\frac{D_S}{bL_0^2}, \quad G_3=\frac{\mu}{b},
$$

$$
G_1=\frac{k_B\mu}{b}, \quad G_4=\frac{C_s\kappa\mu}{b}, \quad \beta_1=\frac{\alpha_1 C_s}{b}, \quad \beta_5=\frac{\alpha_2}{b}, \quad \beta_2=\frac{k_F}{b}, \quad \beta_3=\frac{k_R}{b}, \quad \overline{D}_B=\frac{D_B}{bL_0^2},
$$

$$
\overline{D}_{B_p}=\frac{D_{B_p}}{bL_0^2}, \quad \overline{D}_{B_d}=\frac{D_{B_d}}{bL_0^2}, \quad \overline{D}_E=\frac{D_E}{bL_0^2}, \quad G_2=\frac{k_E\mu}{b}, \quad \overline{C}_{in}=\frac{C_{in}}{C_S}, \quad \overline{L}_{1,0}=\frac{L_{1,0}}{L_0}, \quad \overline{S}_0=\frac{S_0}{k_S},
$$

$$
\overline{B}_0=\frac{B_0}{k_S}, \quad \overline{B}_{p0}=\frac{B_{p0}}{k_S}, \quad \overline{B}_{d0}=\frac{B_{d0}}{k_S}, \overline{E}_0=\frac{E_0}{k_S}, \quad \overline{L}_0=\frac{L_0}{L_0}, \quad Q=\frac{C_0}{C_S}, \quad \overline{D}_e=\frac{D_e}{bL_0^2}, \quad \overline{L}_d=\frac{L_d}{L_0}.
$$

5.2.4 Boundary immobilisation

To accurately simulate the dynamics of the implant-biofilm interface and the antibiotic release process, we addressed the challenge of managing two moving boundaries in our model. This was accomplished by fixing the domain in the same way described in Section 5.1.4. Applying these transformations to the dimensionless model in 5.2.3, we get

$$
\begin{aligned}
(\overline{C}_p)_{\bar{t}}-\frac{\xi}{\overline{L}_1}\frac{d\overline{L}_1}{dt}(\overline{C}_p)_{\xi} &= \frac{\overline{D}_a}{\overline{L}_1^2}(\overline{C}_p)_{\xi\xi}, \quad -1<\xi<0, \bar{t}>0, && (5.131)\\
\overline{C}_b &= \frac{\phi\overline{C}_p}{\phi_b K}, && (5.132)\\
1 &= \phi_{bio}+\frac{\overline{B}+\overline{B}_p+\overline{B}_d}{\overline{\rho}_B}+\frac{E}{\overline{\rho}_E}, && (5.133)
\end{aligned}
$$

$$\phi_{bio}\overline{C}_{\bar{t}}+\phi_{bio}\frac{(\bar{v}\overline{C})_{\xi}}{\overline{L}}-\phi_{bio}\frac{\xi}{\overline{L}}\frac{d\overline{L}}{dt}\overline{C}_{\xi} = \phi_{bio}\frac{\overline{D}_C}{\overline{L}^2}\overline{C}_{\xi\xi}-\beta_4\phi_{bio}\overline{C}, \quad 0<\xi<1,\ \bar{t}>0, \tag{5.134}$$

$$\phi_{bio}\overline{S}_{\bar{t}}+\phi_{bio}\frac{(\bar{v}\overline{S})_{\xi}}{\overline{L}}-\phi_{bio}\frac{\xi}{\overline{L}}\frac{d\overline{L}}{dt}\overline{S}_{\xi} = \phi_{bio}\frac{\overline{D}_S}{\overline{L}^2}\overline{S}_{\xi\xi}-G_3\frac{\phi_{bio}\overline{S}}{1+\phi_{bio}\overline{S}}\overline{B}, \ 0<\xi<1,\ \bar{t}>0, \tag{5.135}$$

$$\begin{aligned}\overline{B}_{\bar{t}}+\frac{(\bar{v}\overline{B})_{\xi}}{\overline{L}}-\frac{\xi}{\overline{L}}\frac{d\overline{L}}{dt}\overline{B}_{\xi} &= \frac{\overline{D}_B}{\overline{L}^2}\overline{B}_{\xi\xi}+(G_1-G_4\phi_{bio}\overline{C})\frac{\phi_{bio}\overline{S}}{1+\phi_{bio}\overline{S}}\overline{B}\\ &\quad -\max(\beta_1\phi_{bio}\overline{C}-\beta_5,0)\overline{B}-\overline{B}\\ &\quad -\max\left(\beta_2\frac{\overline{S}_2-\overline{S}}{\overline{S}_2-\overline{S}_1},0\right)\overline{B}\\ &\quad +\max\left(\beta_3\frac{\overline{S}-\overline{S}_1}{\overline{S}_2-\overline{S}_1},0\right)\overline{B}_p, \quad 0<\xi<1,\ \bar{t}>0,\end{aligned} \tag{5.136}$$

$$\begin{aligned}(\overline{B}_p)_{\bar{t}}+\frac{(\bar{v}\overline{B}_p)_{\xi}}{\overline{L}}-\frac{\xi}{\overline{L}}\frac{d\overline{L}}{dt}(\overline{B}_p)_{\xi} &= \frac{\overline{D}_{B_p}}{\overline{L}^2}(\overline{B}_p)_{\xi\xi}+\max\left(\beta_2\frac{\overline{S}_2-\overline{S}}{\overline{S}_2-\overline{S}_1},0\right)\overline{B}\\ &\quad -\max\left(\beta_3\frac{\overline{S}-\overline{S}_1}{\overline{S}_2-\overline{S}_1},0\right)\overline{B}_p, \quad 0<\xi<1,\ \bar{t}>0,\end{aligned} \tag{5.137}$$

$$\begin{aligned}(\overline{B}_d)_{\bar{t}}+\frac{(\bar{v}\overline{B}_d)_{\xi}}{\overline{L}}-\frac{\xi}{\overline{L}}\frac{d\overline{L}}{dt}(\overline{B}_d)_{\xi} &= \frac{\overline{D}_{B_d}}{\overline{L}^2}(\overline{B}_d)_{\xi\xi}+G_4\phi_{bio}\overline{C}\frac{\overline{S}}{1+\overline{S}}\overline{B}+\overline{B}\\ &\quad +\max(\beta_1\phi_{bio}\overline{C}-\beta_5,0)\overline{B}, \ 0<\xi<1,\ \bar{t}>0,\end{aligned} \tag{5.138}$$

$$\overline{E}_{\bar{t}}+\frac{(\bar{v}\overline{E})_{\xi}}{\overline{L}}-\frac{\xi}{\overline{L}}\frac{d\overline{L}}{dt}\overline{E}_{\xi} = \frac{\overline{D}_E}{\overline{L}^2}\overline{E}_{\xi\xi}+G_2\frac{\phi_{bio}\overline{S}}{1+\phi_{bio}\overline{S}}\overline{B}, \quad 0<\xi<1,\ \bar{t}>0, \tag{5.139}$$

$$\frac{\bar{v}_{\xi}}{\overline{L}} = \frac{1}{1-\phi_{bio}}\left(\frac{k_B}{\overline{\rho}_B}+\frac{k_E}{\overline{\rho}_E}\right)G_3\frac{\phi_{bio}\overline{S}}{1+\phi_{bio}\overline{S}}\overline{B}, \ 0<\xi<1,\ \bar{t}>0, \tag{5.140}$$

$$\frac{d\overline{L}}{d\bar{t}} = \bar{v}(\overline{L}), \quad \bar{t}>0. \tag{5.141}$$

The transformed initial conditions are as follows

$$\overline{C}_p(\xi,0) = \overline{C}_{in}+(1-\overline{C}_{in})\xi^2, \quad \text{for } -1<\xi<0, \tag{5.142}$$

$$\overline{C}_b(\xi,0) = \frac{\phi\overline{C}_p(\xi,0)}{\phi_b K}, \quad \text{for } -1<\xi<0, \tag{5.143}$$

$$\overline{L}_1(0) = \overline{L}_{1,0}, \tag{5.144}$$

$$\overline{C}(\xi,0) = \overline{C}_{in}, \quad \text{for } 0<\xi<1, \tag{5.145}$$

$$\overline{S}(\xi,0) = \overline{S}_0, \quad \text{for } 0<\xi<1, \tag{5.146}$$

$$\overline{B}(\xi,0) = \overline{B}_0 e^{\frac{\bar{v}(\xi,0)\overline{L}_0}{\overline{D}_B}\xi}, \quad \text{for } 0<\xi<1, \tag{5.147}$$

$$\overline{B}_p(\xi,0) = \overline{B}_{p0} e^{\frac{\bar{v}(\xi,0)\overline{L}_0}{\overline{D}_{B_p}}\xi}, \quad \text{for } 0<\xi<1, \tag{5.148}$$

$$\overline{B}_d(\xi,0) = \overline{B}_{d0} e^{\frac{\bar{v}(\xi,0)\overline{L}_0}{\overline{D}_{B_d}}\xi}, \quad \text{for } 0<\xi<1, \tag{5.149}$$

$$\overline{E}(\xi,0) = \overline{E}_0 e^{\frac{\bar{v}(\xi,0)\overline{L}_0}{\overline{D}_E}\xi}, \quad \text{for } 0<\xi<1, \tag{5.150}$$

$$\overline{L}(0) = \overline{L}_0. \tag{5.151}$$

Now applying the same transformations to the boundary conditions (5.121)-(5.130) we get

$$\overline{C}_p(-1,\bar{t}) = 1, \quad \text{when } \bar{t} < \bar{t}_{L_1=L_d}, \tag{5.152}$$

$$\overline{C}_p(0,\bar{t}) = \overline{C}(0,\bar{t}), \quad \bar{t} > 0, \tag{5.153}$$

$$-\frac{\overline{D}_a}{\overline{L}_1}(\overline{C}_p)_\xi = -\frac{d\overline{L}_1}{d\bar{t}}(1-Q), \text{ at } \xi = -1, \text{ for } \bar{t} < \bar{t}_{L_1=L_d}, \bar{t} > 0, \tag{5.154}$$

$$(\overline{C}_p)_\xi = 0, \quad \text{at } \xi = -1, \text{ for } \bar{t} \geq \bar{t}_{L_1=L_d}, \bar{t} > 0, \tag{5.155}$$

$$-\frac{\overline{D}_e}{\overline{L}_1}(\overline{C}_p)_\xi = -\frac{\overline{D}_C}{\overline{L}}\overline{C}_\xi, \quad \text{at } \xi = 0, \bar{t} > 0, \tag{5.156}$$

$$\begin{aligned} -\overline{D}_S\overline{S}_\xi = -\overline{D}_B\overline{B}_\xi = -\overline{D}_{B_p}(\overline{B}_p)_\xi &= -\overline{D}_{B_d}(\overline{B}_d)_\xi \\ &= -\overline{D}_E\overline{E}_\xi = 0, \quad \text{at } \xi = 0, \bar{t} > 0, \end{aligned} \tag{5.157}$$

$$\bar{v} = 0, \quad \text{at } \xi = 0, \bar{t} > 0, \tag{5.158}$$

$$\overline{C} = 0, \quad \text{at } \xi = 1, \bar{t} > 0, \tag{5.159}$$

$$\overline{S} = \overline{S}_0, \quad \text{at } \xi = 1, \bar{t} > 0, \tag{5.160}$$

$$\begin{aligned} -\frac{\overline{D}_B}{\overline{L}}\overline{B}_\xi + \bar{v}\overline{B} = -\frac{\overline{D}_{B_p}}{\overline{L}}(\overline{B}_p)_\xi + \bar{v}\overline{B}_p &= -\frac{\overline{D}_{B_d}}{\overline{L}}(\overline{B}_d)_\xi + \bar{v}\overline{B}_d \\ &= -\frac{\overline{D}_E}{\overline{L}}\overline{E}_\xi + \bar{v}\overline{E} = 0, \quad \text{at } \xi = 1, \bar{t} > 0. \end{aligned} \tag{5.161}$$

5.2.5 Results and discussions

This model is solved in COMSOL using a methodology similar to that described in Section 5.1.5. The additional equations for bacterial phenotypes (eq. (5.136), (5.137), (5.138)) and EPS (eq. (5.139)) are handled using the 'General Form PDE' module. The volume constraint equation (5.133) is implemented via a submodule called 'Pointwise Constraint' within the EPS module. It is important to note that this approach can be applied within any of the biomass modules as well. This constraint does not function as an additional equation that would overdetermine the model; rather, it serves as a relationship among variables to reduce the solution space. COMSOL enforces this constraint using numerical methods, such as Lagrange multipliers, to maintain mathematical consistency in the system. A sensitivity analysis is performed for varying nutrient concentrations coming from the biofilm-bulk fluid boundary. The model also identifies distinct phases of biofilm behaviour that remain consistent across various parameter sets, and we examine the impact of different parameters on these phases. At any given time, the total concentration of a biofilm component denotes the integral of its concentration across the biofilm thickness, representing the component's mass per area, an areal concentration. All baseline parameter values are given in Table 2.2. It is important to note that all results are presented in non-dimensional form, although the overline notation is omitted in the figures for clarity.

Effect of varying nutrient concentration (S_0)

In the Figs. 5.7-5.9, we explore how the nutrient concentration coming from the biofilm-bulk fluid interface (S_0), influences the dynamics of bacterial populations and EPS production within the biofilm. The scenarios are represented by three distinct cases: **nutrient-rich environment** ($S_1 < S_2 < S_0$, red line), where the nutrient concentration at the biofilm-bulk fluid interface is above S_2; **intermediate nutrient environment** ($S_1 < S_0 < S_2$, black line), where the nutrient concentration lies between S_1 and S_2; and **nutrient-poor environment** ($S_0 < S_1 < S_2$, blue line), where the nutrient concentration is below S_1. These nutrient conditions dictate the transitions between proliferative and persister bacterial states, ultimately affecting the overall biofilm structure and resilience. All plots are for a final time of 15 days. This time was chosen because, although the biofilm had not yet reached a steady state, it exhibited prominent behaviours and structures by this point. Unlike Model 10, which used a 10-day final time, this model incorporates both bacterial and EPS dynamics, leading to more complex growth behaviours that take longer to develop.

We have not compared the results for different nutrient availability in this model to the similar results (Fig. 4.14-4.17) of Model 3 in Section 4.2.4. This is mainly because the behaviours of the bacterial phenotypes, EPS, and biofilm thickness are substantially different due to the controlled antibiotic release in this model, whereas Model 3 had continuous antibiotic exposure. However, aside from the total proliferative bacteria and total persister bacteria, the distribution pattern, for example, where the highest nutrient level results in the highest biofilm thickness and the lowest nutrient level results in the lowest biofilm thickness, remains consistent between the two models across the different nutrient cases for the other plots. This similarity in the ordering of nutrient cases highlights the influence of nutrient availability on biofilm dynamics, even though the mechanisms of antibiotic exposure differ.

Fig. 5.7(a) illustrates the dynamics of proliferative bacteria concentrations under three distinct nutrient conditions. In the nutrient-rich environment, the initial sharp increase in proliferative bacteria concentration is due to the abundance of nutrients that support rapid bacterial growth and division. This environment provides ideal conditions for bacteria to proliferate, leading to a rapid ascent to a high maximum concentration. However, as the bacteria continue to consume nutrients, the available resources begin to deplete, causing the proliferative bacteria population to decline. This decline is further influenced by the conversion of proliferative bacteria to persisters as the environment becomes less favourable, to dead bacteria by natural death or bacterial death due to antibiotics or to EPS. In the intermediate nutrient environment, the initial increase in proliferative bacteria is more moderate compared to the nutrient-rich environment. This is because the nutrient levels, while sufficient to support growth, are not as abundant, leading to a balanced state where some bacteria continue to proliferate while others convert to the persister state. This balance results in a lower proliferative concentration, as not all bacteria remain in the proliferative state. The subsequent decline in this environment is more gradual, reflecting a slower rate of nutrient depletion and a more stable bacterial population that can partially sustain itself for a longer period before decreasing. In the nutrient-poor environment, the initial increase in proliferative bacteria is low, as the limited nutrient availability forces most bacteria to remain in the persister state to survive. The peak concentration of proliferative bacteria is the lowest among all three conditions, as the scarcity of nutrients severely restricts bacterial growth. The very gradual decline following the peak reflects the limited bacterial activity in this environment, where the few proliferative bacteria that exist consume nutrients at a much slower rate, leading to a minimal reduction in their numbers over time.

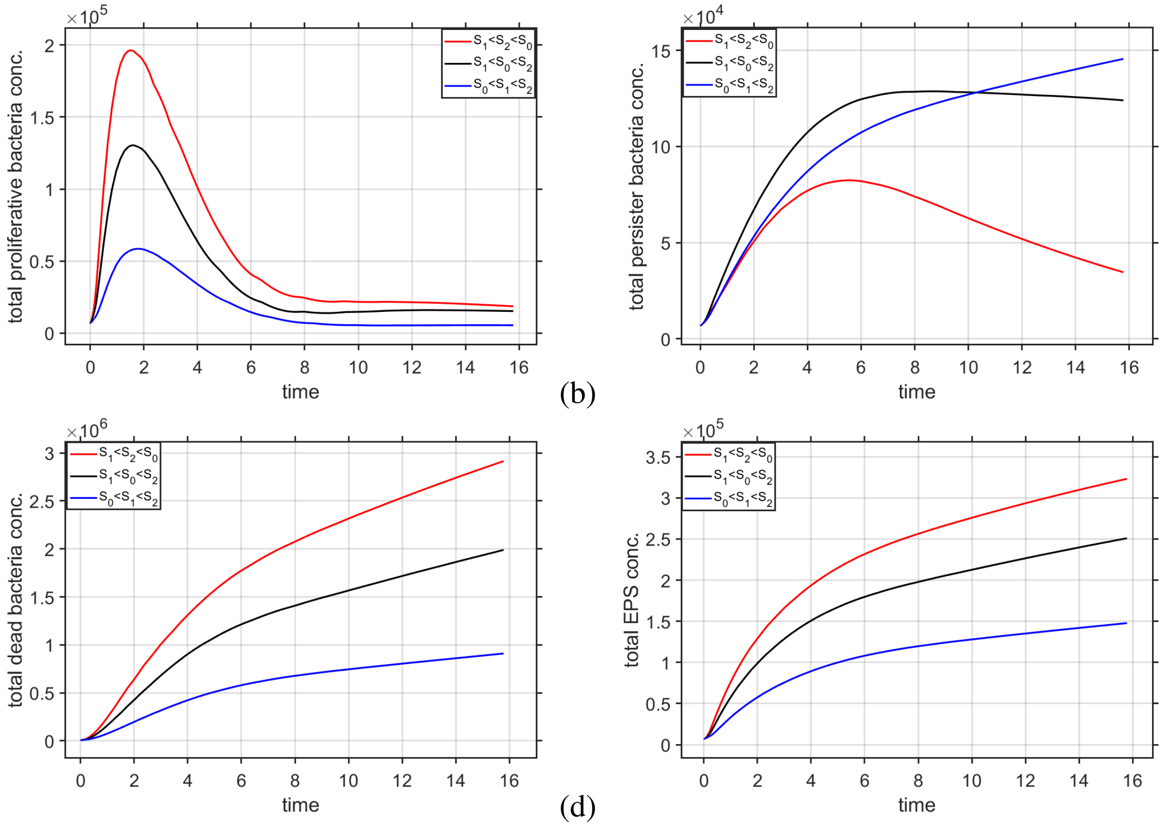

(a) (b) (c) (d)

Figure 5.7: Effect of varying nutrient concentration (S_0) on (a) temporal variation of total proliferative bacteria concentration, (b) temporal variation of total persister bacteria concentration, (c) temporal variation of total dead bacteria concentration, (d) temporal variation of total EPS concentration.

Fig. 5.7(b) presents the behaviour of persister bacteria concentrations under the same nutrient conditions. In the nutrient-rich environment, the persister concentration initially increases slowly. Despite the abundance of nutrients, not all bacteria immediately convert to the proliferative state; some remain as persisters due to variability in the bacterial population or temporary localised nutrient limitations within the biofilm. However, as the environment continues to support proliferation, the persister concentration reaches the lowest peak among the three conditions. This is because the nutrient-rich environment favours bacterial growth and proliferation over persistence, leading to a higher conversion of persisters into proliferative bacteria. As time progresses, the nutrient concentration gradually increases due to the reduced number of proliferative bacteria. Consequently, the persister population declines further as more bacteria either revert to the proliferative state. In the intermediate nutrient environment, the persister concentration increases more significantly than in the nutrient-rich environment. This is because the nutrient levels are sufficient to support some bacterial growth, but also induce persister formation. The peak persister concentration is higher than in the nutrient-rich environment, as the balance between nutrient availability and bacterial survival leads to a greater proportion of the bacterial population converting to or remaining in the persister state. After the peak, the persister concentration begins to decline as the nutrient levels become sufficient to sustain all bacteria, causing some persisters to revert to proliferative bacteria. Initially, the black line exhibits the highest persister concentration, followed by the blue and red lines. This is because the intermediate nutrient environment allows for a rapid initial increase in persisters, driven by the balance between moderate nutrient availability and the need for some bacteria to survive. However, after a certain time, the persister concentration in the nutrient-poor environment surpasses that of the intermediate environment. This crossing occurs because, in the nutrient-poor environment, the prolonged lack of nutrients forces nearly all bacteria to adopt the persister state. The continuous stress of low nutrients ensures that the persister population keeps increasing, eventually leading to the highest persister concentration over time, as the bacteria adapt to the harsh conditions and prioritise survival over growth. This behaviour exemplifies the resilience characteristic of biofilms.

Fig. 5.7(c) depicts the dynamics of dead bacteria concentrations across the different nutrient environments. In the nutrient-rich environment, the dead bacteria concentration increases rapidly due to the high turnover of the large proliferative bacterial population. The rapid growth of bacteria, driven by abundant nutrient availability, leads to a significant number of bacteria reaching the end of their life cycle or succumbing to external factors such as antibiotics. This results in a steep and continuous rise in dead bacteria concentration, reflecting the ongoing death of the initially large proliferative population. In the intermediate nutrient environment, the increase in dead bacteria is slower and more gradual. This is because the bacterial growth rate is lower than in the nutrient-rich environment, resulting in a smaller proliferative population and, consequently, a lower turnover rate. The sustained rise in dead bacteria concentration in this environment indicates a steady but slower rate of bacterial death, consistent with the balanced growth and survival strategies adopted by the bacteria in response to intermediate nutrient availability. In the nutrient-poor environment, the dead bacteria concentration increases the slowest among all conditions. This occurs because of the predominance of the persister state, which is characterised by a reduced metabolic rate and a lack of susceptibility to cell death, in contrast to the proliferative state. The gradual increase in dead bacteria concentration in this environment reflects the limited bacterial activity and slower turnover of the small proliferative population, resulting in the lowest overall dead bacteria concentration. In all three cases, we observe a reduced rate of increase in dead bacteria beginning around the time when the proliferative bacteria starts to decline.

Fig. 5.7(d) shows the dynamics of EPS concentrations in relation to nutrient availability. In the nutrient-rich environment, EPS production increases rapidly, driven by the high metabolic activity of proliferative bacteria. The nutrient-rich environment provides abundant resources, allowing bacteria to produce and accumulate large amounts of EPS, leading to the highest EPS concentration. This sustained high level of EPS reflects the continuous biofilm formation and maintenance supported by the ample nutrient supply. In the intermediate nutrient environment, EPS production is more moderate, as the bacterial growth rate as well as the EPS production rate are slower and there is a balance between proliferative and persister states. The rate of EPS production is lower than in the nutrient-rich environment due to the reduced availability of nutrients. The sustained increase in EPS concentration in this environment indicates ongoing biofilm activity, but at a lower level than in the nutrient-rich environment, reflecting the intermediate nutrient availability and the balanced bacterial response. In the nutrient-poor environment, EPS production is the slowest among all conditions. This is consistent with the limited growth of proliferative bacteria and the predominance of the persister state, which is in our model, not metabolically active and do not produce EPS. The lowest EPS concentration observed in this environment reflects the minimal biofilm formation and maintenance due to the restricted availability of nutrients, leading to reduced bacterial activity and EPS production. In all three cases, we observe a reduced rate of increase in EPS, mirroring the trend in dead bacteria concentration, starting around the time when the proliferative bacteria begin to decline.

Fig. 5.7 collectively illustrate how nutrient availability governs bacterial behaviour within a biofilm, influencing the dynamics of proliferative bacteria, persister bacteria, dead bacteria, and EPS production. In nutrient-rich environments, rapid bacterial growth and EPS production are maximised, leading to high peaks in proliferative bacteria and EPS concentrations, along with significant bacterial death resulting in a rapid increase in dead bacteria. The abundance of nutrients suppresses persister formation, leading to a low peak and subsequent decline in persister concentration as the environment continues to favour proliferation over persistence. In contrast, intermediate and nutrient-poor environments promote the formation of persisters, resulting in higher persister concentrations over time. In the intermediate nutrient environment, a balance between proliferation and persistence is maintained, leading to a moderate increase in persister concentration and a sustained level of EPS production. However, as nutrient levels decrease further, as seen in the nutrient-poor environment, the bacterial population shifts predominantly towards persistence, leading to the highest persister concentration as time progresses. The interplay between these factors highlights the adaptive strategies bacteria employ to survive under varying environmental conditions, with nutrient availability serving as the key driver of biofilm dynamics. Fig. 5.7 underscores the critical role of nutrient levels in dictating the balance between bacterial growth, survival, and biofilm formation, ultimately shaping the structure and function of the biofilm community.

Fig. 5.8(a) illustrates the evolution of biofilm thickness over time under three different nutrient conditions. In the nutrient-rich environment, the biofilm thickness increases rapidly and continuously, reflecting the high availability of nutrients that support bacterial growth and EPS production. As the bacteria proliferate and produce dead bacteria and EPS, they contribute to the expansion of the biofilm matrix, resulting in a steep increase in thickness. The red line shows that biofilm thickness reaches the highest level among all conditions, which is expected because the abundant nutrients facilitate the growth of proliferative bacteria, the production of EPS and transition to dead bacteria, all of which are critical for biofilm development. In the intermediate nutrient environment, the biofilm thickness also increases over time but at a slower rate compared to the nutrient-rich environment. This is due to the reduced availability of nutrients, which slows down biomass production. The black line indicates a moderate increase in biofilm thickness, reaching a level that is lower than in the nutrient-rich environment but higher than in the nutrient-poor environment. This intermediate growth is consistent with the balanced bacterial activity in this environment, where both proliferative and persister bacteria coexist in a balance, contributing to biofilm formation at a moderate pace. In the nutrient-poor environment, the increase in biofilm thickness is the slowest, as shown by the blue line. This environment severely limits dead bacteria and EPS production due to the lack of sufficient nutrients. Most bacteria remain in the persister state, leading to minimal biofilm expansion. Consequently, the biofilm thickness reaches the lowest level among all three conditions, reflecting the constrained bacterial activity and limited resources available for biofilm development.

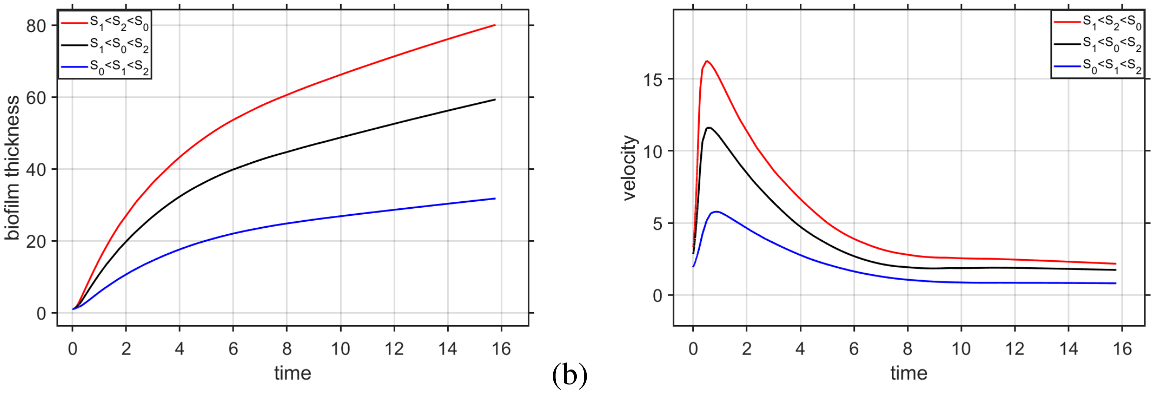

(a) (b)

Figure 5.8: Effect of varying nutrient concentration (S_0) on (a) temporal variation of biofilm thickness, (b) temporal variation of velocity at the biofilm-bulk fluid interface.

Fig. 5.8(b) presents the velocity of the biofilm-bulk fluid interface, which represents the rate of change in biofilm thickness, under the same nutrient conditions. The initial velocity in each scenario is different because it directly depends on the initial nutrient concentration available to the bacteria at the biofilm-bulk fluid interface. In the nutrient-rich environment, the initial velocity is very high, indicating a rapid increase in biofilm thickness due to the abundant nutrients that drive vigorous bacterial growth, death and EPS production. The velocity reaches a peak early on because the biofilm expands quickly as the bacteria proliferate and produce EPS at an accelerated rate. However, as the biomass constituents starts to reach a steady state, the velocity starts to decline. Notably, this slowing down of the biofilm growth rate occurs roughly around the same time that the growth of proliferative bacteria, production of dead bacteria, and EPS production begin to slow down, indicating a comprehensive shift in the biofilm dynamics as the system transitions from rapid growth to a more stable state (see Fig. 5.7(a),(c) and (d)). Over time, the velocity stabilises at a low level as the biofilm reaches a more mature state, where growth is balanced by the depletion of nutrients. In the intermediate nutrient environment, the velocity also increases initially but to a lesser extent than in the nutrient-rich environment. The peak velocity is lower, reflecting the slower rate of biofilm expansion due to the moderate availability of nutrients. After reaching this lower peak, the velocity decreases as well, following a similar pattern to the nutrient-rich environment but at a slower rate. The decline in velocity also begins around the same time that proliferative bacterial growth, dead bacteria production, and EPS production slow down, indicating a synchronised response to the decreasing nutrient availability. This decline indicates a gradual slowdown in biofilm growth as the nutrient levels continue to drop, reducing the bacteria's ability to proliferate and produce EPS. In the nutrient-poor environment, the initial velocity is the lowest among all conditions, corresponding to the slowest rate of biofilm expansion. The peak velocity is reached later than the other two cases and is much lower than in the other two environments because the limited nutrients severely restrict bacterial activity. The subsequent decline in velocity is also more gradual, reflecting the minimal growth of the biofilm as the bacteria prioritise survival in the persister state over active proliferation and EPS production. Similar to the other conditions, the slowdown in velocity coincides with the reduced growth of proliferative bacteria, decreased production of dead bacteria, and lower EPS production, all of which are linked to the limited nutrient availability. Over time, the velocity stabilises at a very low level, indicating that the biofilm has reached a state of minimal growth due to the ongoing nutrient scarcity.

Fig. 5.8 provide a comprehensive view of the biofilm's growth dynamics under different nutrient conditions. In the nutrient-rich environment, the biofilm grows rapidly, as evidenced by both the increasing thickness and the high initial velocity. The abundant availability of nutrients drives the rapid proliferation of bacteria and the production of EPS, leading to a thick and robust biofilm structure. As the nutrients deplete, the growth rate slows down, resulting in a decrease in the velocity of the biofilm-bulk fluid interface, and the biofilm thickness eventually stabilises at a high level. This slowdown in biofilm growth corresponds with the time when the growth of proliferative bacteria, the production of dead bacteria, and EPS production all begin to decline, indicating a coordinated response to diminishing nutrient levels. In the intermediate nutrient environment, the biofilm grows at a moderate pace, with both the biofilm thickness and the velocity peaking at lower levels than in the nutrient-rich environment. The balance between nutrient availability and bacterial activity results in a steady but slower biofilm expansion, which is reflected in the moderate final biofilm thickness and the gradually declining velocity as the biofilm matures. The decrease in velocity, like in the nutrient-rich environment, occurs around the same time that other biofilm-related processes slow down, underscoring the interdependence of these factors. In the nutrient-poor environment, the biofilm grows very slowly, with the lowest final thickness and velocity observed among all conditions. The limited nutrients force most bacteria into the persister state, resulting in minimal biomass production and a slow rate of biofilm expansion. The low initial velocity and its gradual decline indicate that the biofilm is barely growing, and the final thickness remains minimal due to the severe nutrient constraints. The timing of the slowdown in velocity aligns with the reduced growth and activity of the bacteria, reinforcing the critical role of nutrient availability in regulating biofilm development. This joint interpretation underscores the importance of nutrient levels in determining the rate and extent of biofilm growth, with more nutrients leading to faster and more substantial biofilm development, while nutrient scarcity limits growth and results in thinner biofilm structures and slower expansion rates.

Fig. 5.9(a) illustrates the spatial variation of proliferative bacteria concentration through the biofilm at the final time, which refers to the last time point simulated in this study, under three different nutrient conditions. Since the nutrient supply originates from the biofilm-bulk fluid interface, which is represented on the right side of the x-axis, the concentration of nutrients is highest at the interface and decreases as one moves deeper into the biofilm, which is towards the implant-biofilm interface $(x = 0)$. For all three nutrient conditions, the concentration of proliferative bacteria is highest at the biofilm-bulk fluid interface and decreases as we move further into the biofilm towards the implant. This trend occurs because proliferative bacteria rely on nutrient availability for growth and reproduction. The highest concentration of nutrients is at the interface, where the nutrient influx occurs, providing an ideal environment for bacterial proliferation. As the distance from the nutrient source increases, the nutrient concentration diminishes due to diffusion limitations and consumption by bacteria, leading to a corresponding decrease in proliferative bacteria concentration. Interestingly, the concentration of proliferative bacteria is highest in the intermediate nutrient condition, followed by the nutrient-rich environment, and is lowest in the nutrient-poor condition. This pattern can be explained by the balance between nutrient availability and the biological response of bacteria. In a nutrient-rich environment, the abundance of nutrients initially drives higher proliferation, which eventually results in an increased conversion rate to the dead bacteria state over time. In the intermediate nutrient environment, the balance between available nutrients and bacterial growth is more optimal, leading to sustained proliferative activity across the biofilm, hence the higher concentration. In the nutrient-poor environment, the low nutrient availability severely restricts bacterial growth, resulting in the lowest concentration of proliferative bacteria across the biofilm.

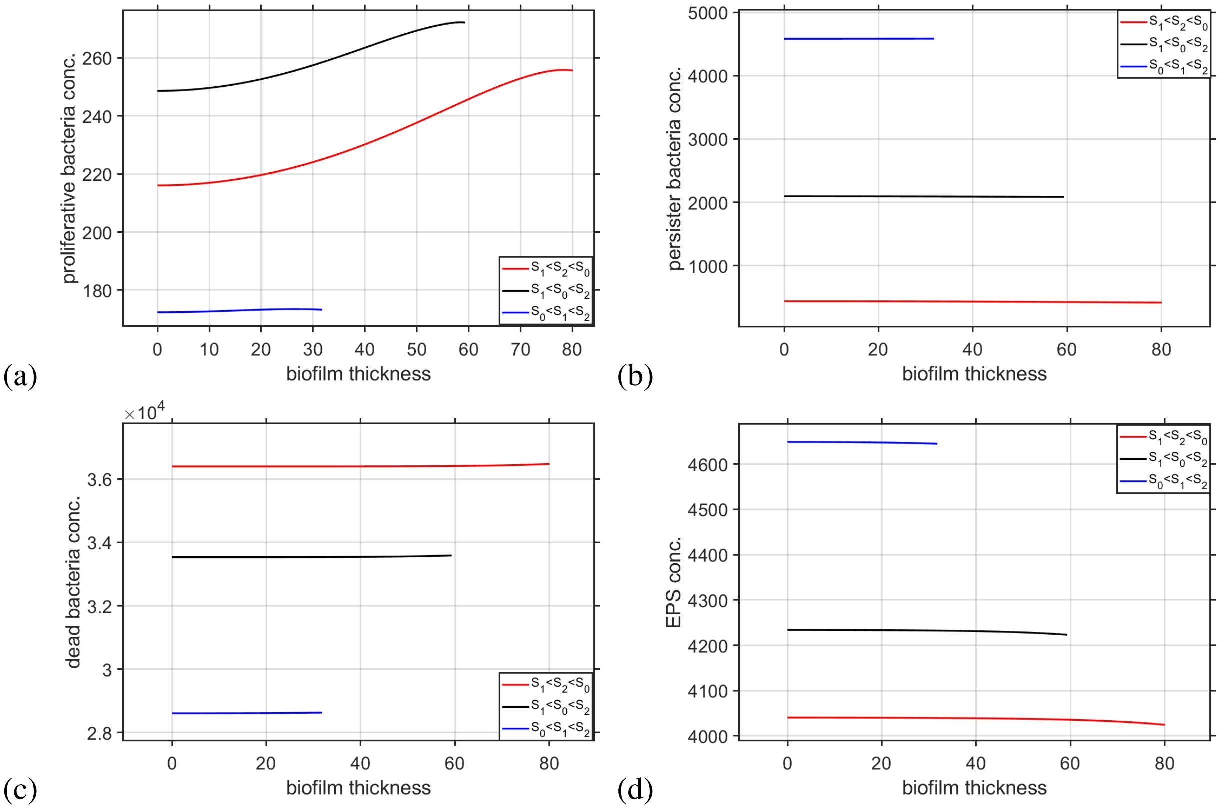

Figure 5.9: Effect of varying nutrient concentration (S_0) on (a) spatial variation of proliferative bacteria concentration at final time, (b) spatial variation of persister bacteria concentration at final time, (c) spatial variation of dead bacteria concentration at final time, (d) spatial variation of EPS concentration at final time.

Fig. 5.9(b) shows the spatial variation of persister bacteria concentration at the final time under the same nutrient conditions. Persister bacteria display a distinct concentration profile compared to proliferative bacteria. The concentration of persister bacteria is highest in the nutrient-poor environment, followed by the intermediate nutrient condition, and is lowest in the nutrient-rich environment. In the nutrient-poor environment, most bacteria are forced into the persister state to survive due to the lack of nutrients to sustain proliferative growth. This leads to the highest concentration of persisters across the biofilm. This shows resilience towards adverse environmental effects showed by biofilm. In the intermediate nutrient environment, the concentration of persister bacteria is lower than in the nutrient-poor condition but still significant. Here, some bacteria switch to the persister state as a survival strategy in response to moderate nutrient levels, balancing between growth and survival. The concentration is lower than in the nutrient-poor environment because the nutrient levels are not as restrictive, allowing for a higher proportion of bacteria to remain in the proliferative state. In the nutrient-rich environment, the concentration of persister bacteria is the lowest because the abundant nutrients support continued bacterial proliferation and reversion of persister to proliferative, rather than the formation of persisters.

Fig. 5.9(c) presents the spatial variation of dead bacteria concentration at the final time. Dead bacteria accumulate in the biofilm due to natural bacterial death and environmental stressors like antibiotic. The concentration of dead bacteria is highest in the nutrient-rich environment, followed by the intermediate nutrient condition, and lowest in the nutrient-poor environment. This trend can be attributed to the high initial proliferative activity in nutrient-rich conditions, which leads to more bacterial growth and, consequently, more bacterial death over time. In the intermediate nutrient environment, the concentration of dead bacteria is lower than in the nutrient-rich environment but still significant. The moderate bacterial growth in this environment leads to a steady accumulation of dead bacteria, though at a lower rate compared to the nutrient-rich condition. This reflects the balance between growth and death in a moderately nutrient-limited environment. In the nutrient-poor environment, the concentration of dead bacteria is the lowest, as fewer bacteria are proliferating and more are in the persister state. Consequently, fewer bacteria die, resulting in a lower overall concentration of dead bacteria.

Fig. 5.9(d) shows the spatial variation of EPS concentration at the final time. EPS is essential for maintaining the structure and stability of the biofilm and is closely linked to bacterial activity and nutrient availability. The concentration of EPS is highest in the nutrient-poor environment, followed by the intermediate nutrient condition, and is lowest in the nutrient-rich environment. This trend occurs because, over time, in nutrient-poor conditions, bacteria prioritise EPS production to stabilise the biofilm structure and protect themselves from environmental stressors, despite the limited nutrient availability. In our model, this can be attributed to the fact that in a nutrient-poor environment, the rate of EPS production is higher than the proliferation rate, primarily due to the antibiotic's inhibitory effect on bacterial proliferation. In the intermediate nutrient environment, EPS production is moderate, reflecting the balance between bacterial growth and biofilm stabilisation. The concentration of EPS is lower than in the nutrient-poor environment because the nutrient levels, while limited, still support some bacterial growth, leading to a distribution of resources between growth and EPS production. In the nutrient-rich environment, the concentration of EPS is the lowest because bacteria focus more on growth and proliferation rather than biofilm stabilisation. This occurs because, in this scenario, the proliferative bacteria population increases due to the higher growth rate and reversion from the persister state, leading to a higher rate of transition to dead bacteria. Although not directly modelled, it can be inferred that abundant nutrients reduce the emphasis on EPS production, as the bacteria can thrive without the need for extensive biofilm formation to protect against environmental stresses. Interestingly, EPS concentration shows a slight increase as we move deeper into the biofilm, towards the implant, across all nutrient conditions. This can be explained by the spatial distribution of bacterial activities within the biofilm. Closer to the nutrient influx at the biofilm-bulk fluid interface, bacterial growth is more dominant, resulting in higher concentrations of proliferative bacteria. As one moves deeper into the biofilm, where nutrient availability decreases, proliferative bacteria will produce more EPS and persister. This shows the shift of their focus from growth to stabilisation of the biofilm matrix, leading to an increase in EPS production in these regions.

Fig. 5.9 collectively reveal the intricate relationship between nutrient availability and the spatial distribution of bacterial states and EPS production. The nutrient-rich environment promotes intermediate concentrations of proliferative bacteria. However, the total concentration of proliferative bacteria is highest for this scenario due to the biofilm's larger thickness, even though spatial concentrations may be lower. A thicker biofilm can have higher total concentrations despite lower spatial concentrations. The nutrient-rich environment leads to a significant accumulation of dead bacteria at final time due to the rapid death associated with high initial growth rates. Conversely, in the nutrient-poor environment, bacteria predominantly switch to the persister state to survive the nutrient scarcity, leading to the highest concentration of persisters. The intermediate nutrient environment presents a balanced scenario reflecting an equilibrium between growth and survival mechanisms. The spatial distribution within the biofilm further emphasises the adaptive responses of bacteria to their environment. Proliferative bacteria are most concentrated at the nutrient-rich interface, declining deeper into the biofilm where nutrients are less available. In contrast, EPS concentration slightly increases deeper into the biofilm, suggesting a shift in bacterial focus from growth to structural maintenance as nutrient availability decreases. This interplay between bacterial states and biofilm structure across different nutrient conditions underscores the complexity of biofilm dynamics, where nutrient gradients drive the spatial organisation of bacterial communities and the stability of the biofilm matrix.

Fig. 5.10 shows the spatial structure of the different biomass constituents (proliferative bacteria, persister bacteria, dead bacteria, and EPS) across the biofilm at the final time for various nutrient concentrations (S_0). In previous analyses in Fig. 5.9, we examined how S_0 influenced concentration levels, where the concentrations appeared relatively constant. These figures aim to provide a clearer view of the spatial structure by normalising the concentrations at each point by the value at $x = 0$ (the implant-biofilm boundary), allowing for the identification of spatial trends across the biofilm. This analysis reveals key distribution patterns for the biomass constituents, showing how they are distributed from the implant-biofilm boundary (left) to the biofilm-bulk fluid boundary (right).

The spatial structures in this figure are largely similar to those in Fig. 4.17 of Model 3, with the exception of the dead bacteria (see Fig. 5.10(c)), which shows a different spatial pattern compared to Model 3 (see Fig. 4.17(c)). To avoid redundancy, we will focus on discussing the spatial structure of the dead bacteria, as the other biomass constituents follow similar trends to those in Fig. 4.17, though the patterns are more pronounced in the current model. The more pronounced spatial structure observed here is mainly due to the controlled antibiotic release. In Model 3 (Section 4.2), with continuous antibiotic administration, biofilm growth and consequently, the growth of all biomass constituents, was consistently suppressed. However, in this model, the

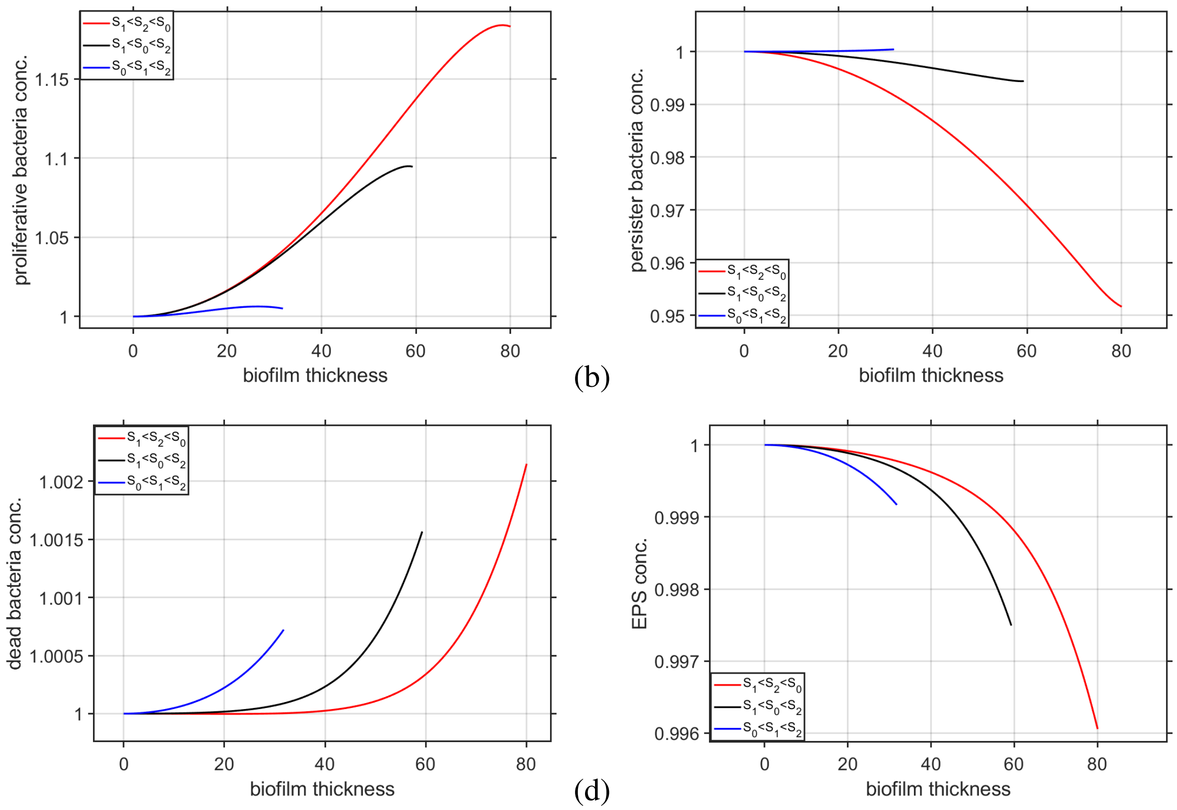

(a) (b)

(c) (d)

Figure 5.10: Spatial variation of (a) proliferative bacteria, (b) persister bacteria, (c) dead bacteria, and (d) EPS at the final time, shown for varying nutrient concentrations (S_0). In each plot, the concentrations are scaled by dividing the value at each spatial point by the concentration at $x = 0$.

antibiotic is nearly exhausted by the final time, allowing the biofilm and its constituents more time to grow, leading to a more defined spatial structure at the final time. This also explains the different distribution of dead bacteria. In Model 3, where the antibiotic was present throughout the time, the highest accumulation of dead bacteria occurred at the implant-biofilm interface, with a decrease as the antibiotic concentration decreased further from the interface, resulting in a dip and a slight increase near the biofilm-bulk fluid interface due to increased proliferative activity. In contrast, in this model, with almost all antibiotics exhausted from the biofilm, the highest accumulation of dead bacteria is now observed near the biofilm-bulk fluid interface, where proliferative bacteria are most concentrated.

Phases of biofilm growth

Now we explore the dynamic processes governing biofilm growth in the context of controlled antibiotic release from a porous implant. The definition of the phases discussed here is a culmination of the knowledge gained from all the biofilm growth models developed throughout this thesis. Previous results, such as those in Fig. 4.14 and 4.15, support the idea of these phases being integral to the growth cycle. In particular, the two-phase behaviour of the biomass constituents, where an initial phase marked by rapid changes due to antibiotics is followed by a stabilisation phase, sets the stage for the more detailed study of biofilm growth phases explored in this chapter. We identified five distinct phases that capture the key stages of biofilm development: Antibiotic delivery phase, Rapid acceleration of growth phase, Growth of proliferative bacteria phase, Tip formation phase, and Steady tip propagation phase. These phases are observed consistently across a range of model parameters, indicating their fundamental role in biofilm growth dynamics.

Antibiotic delivery phase (phase 1)-The antibiotic delivery phase marks the initial stage of biofilm development, beginning at $t = 0$ and continuing until the total antibiotic concentration in the system falls below 1% of its initial value. This phase is critical as it sets the initial conditions that will influence the subsequent growth of the biofilm. In our model, the antibiotic primarily suppresses bacterial growth and increases cell death among the proliferative bacterial population. Proliferative bacteria, being metabolically active, are vulnerable to the antibiotic, whereas persister bacteria, in a dormant state, are not affected. This differential susceptibility between proliferative and persister cells defines the initial distribution of bacterial phenotypes, influencing the biofilm's early structure and preparing for subsequent growth phases.

It is important to note that this phase's definition is based on the specific type of antibiotic action assumed in our model, which primarily targets proliferative cells by suppressing their growth and increasing mortality. If a different type of antibiotic were used, one capable of affecting persister cells, for example, the dynamics of this phase could change. In such cases, the phase may need to be defined differently to account for the altered interaction between the antibiotic and the bacterial phenotypes within the biofilm, potentially impacting the entire growth trajectory of the biofilm.

Rapid acceleration of growth phase (phase 2)-As the antibiotic concentration decreases during the antibiotic delivery phase, the biofilm enters the rapid acceleration of growth phase. This phase is characterised by a significant increase in the biofilm's growth rate, driven by the proliferation of bacteria and the accumulation of EPS. We define the end of this phase as being marked by the time at which the velocity of the biofilm-bulk fluid interface, or the biofilm thickness, reaches its maximum value.

The rapid acceleration observed during this phase is primarily due to the reduced antibiotic exposure, which allows proliferative bacteria to multiply rapidly. The availability of nutrients further fuels this growth, leading to a sharp increase in biofilm thickness. The EPS, produced by the bacteria, provides structural support to the growing biofilm, contributing to its mechanical stability and resilience to external stresses.

The velocity at the biofilm-bulk fluid interface represents the rate at which the biofilm expands. The maximum velocity during this phase indicates the peak of biofilm expansion, after which the growth rate begins to stabilise as the system transitions to the next phase.

Growth of proliferative bacteria phase (phase 3)-The growth of proliferative bacteria phase is marked by bacteria continuously growing within the biofilm, increasing the total number of proliferative cells. This phase ends when the total concentration of proliferative bacteria reaches its maximum value, signaling the peak of bacterial activity within the biofilm.

During this phase, the biofilm becomes more complex, with proliferative bacteria dominating the microbial community. The high concentration of proliferative bacteria in this phase also means that the biofilm is metabolically active, consuming nutrients and producing persister and dead bacteria as well as EPS. This phase represents a critical stage in biofilm maturation, where the biofilm's structure and function are fully established.

Before defining the tip formation phase and the steady tip propagation phase, it is crucial to visually establish the presence of a tip structure during biofilm growth and its movement. Fig. 5.11 offer valuable insights into the spatial distribution of proliferative bacteria across the biofilm, revealing how the tip forms and subsequently propagates.

In Fig. 5.11(a), the concentration of proliferative bacteria is plotted across the biofilm, both before the onset of the tip formation phase (phase 4) and during it. The concentrations are normalised by their respective maximum values over the entire time course, resulting in a range from 0 to 1. This normalisation ensures that the comparisons are meaningful across different time points. Before phase 4 begins, as indicated by the dashed line, the concentration of proliferative bacteria decreases monotonically from the biofilm-bulk fluid interface (on the right side of the x-axis) towards the implant-biofilm interface (on the left side of the x-axis). This gradient is typical of earlier biofilm growth phases, where bacterial activity is highest near the nutrient-rich biofilm-bulk fluid interface and diminishes deeper within the biofilm, where nutrients are more limited. This spatial distribution reflects the biofilm's adaptation to its microenvironment, where proliferative bacteria prioritise regions with more accessible resources. However, as the biofilm transitions into phase 4, the spatial profile of proliferative bacteria undergoes a significant change. The solid line in Fig. 5.11(a) shows that, during this phase, a localised increase in bacterial concentration emerges at the biofilm-bulk fluid interface, resulting in the formation of a rounded tip. This tip is a critical structural feature, representing a focal point of intense bacterial activity where the biofilm is actively expanding. The formation of this tip indicates that the biofilm is reorganising its structure to optimise growth at the interface, which is now becoming the primary driver of biofilm expansion. As time progresses during this phase, the concentration of proliferative bacteria at each spatial point within the biofilm starts to decrease. This decrease suggests a redistribution of bacterial resources, as the biofilm adjusts to maintain the tip structure while potentially reducing the density of bacteria in other regions to support this localised growth.

Fig. 5.11(b) continues the analysis into the steady tip propagation phase (phase 5), where the biofilm has further evolved. The concentrations in this figure are also normalised, allowing for a direct comparison between the start of phase 5 (dotted line), at 90 days (dashed line) and at 120 days (solid line).

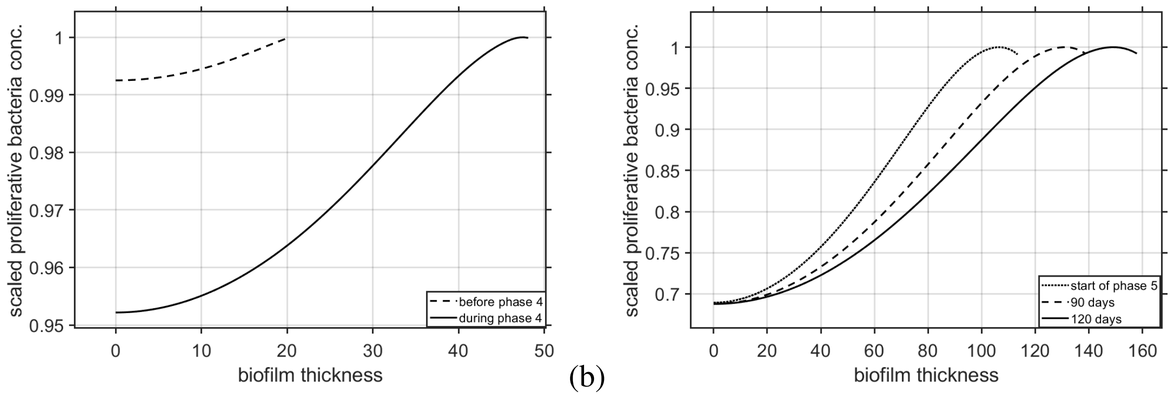

(a) (b)

Figure 5.11: (a) Comparison of the spatial behaviour of scaled proliferative bacteria concentration before and during phase 4. The plot shows a distinct tip forms at the biofilm-bulk fluid interface during phase 4. (b) Comparison of the spatial behaviour of scaled proliferative bacteria concentration at the start of phase 5, at 90 days and at 120 days. The plot shows the formed tip at the biofilm-bulk fluid interface propagates outward as the biofilm thickness increases over time. For both subfigures, the concentrations represent the total values throughout the entire biofilm at each specific time point, normalised by their respective maximum values over the entire time course, with values ranging from 0 to 1.

As the biofilm enters phase 5, the tip that formed during the previous phase begins to propagate outward steadily. This outward movement is clearly depicted by the shifting of the concentration profile towards greater biofilm thicknesses over time. The propagation of the tip signifies that the biofilm is continuing to expand, with the most significant growth occurring at the biofilm-bulk fluid interface. The proliferative bacteria are concentrated in this tip, which is driving the expansion of the biofilm. One particularly noteworthy observation is the stability of the proliferative bacteria concentration in the deeper regions of the biofilm, closer to the implant side. Despite the outward growth of the tip, the concentration of proliferative bacteria deep within the biofilm remains almost unchanged over time, as indicated by the close overlap of the dashed and solid lines in these regions. This stability suggests that the internal structure of the biofilm has reached a mature state, where changes in bacterial concentration are minimal. The deeper regions of the biofilm, having already undergone significant development in earlier phases, are now largely unaffected by the ongoing expansion at the tip. This stabilisation is crucial for maintaining the biofilm's overall integrity and resilience, ensuring that the biofilm remains robust even as it continues to grow at the periphery.

These detailed spatial insights provide a more comprehensive understanding of the mechanisms that govern biofilm expansion, particularly during its later stages of development. By analysing these spatial profiles, we gain valuable knowledge about the biofilm's structural adaptations and the factors that contribute to its sustained growth and robustness in diverse environments.

Tip formation phase (phase 4)-The tip formation phase represents a significant structural transition in the biofilm, as illustrated in Fig. 5.11(a). During this phase, the concentration of proliferative bacteria shifts, forming a rounded tip at the biofilm-bulk fluid interface. This tip becomes the focal point for biofilm expansion.

In earlier phases, bacterial concentration decreases smoothly from the bulk-fluid interface toward the implant. In phase 4, this distribution reorganises, with a localised increase at the interface, forming the characteristic tip.

We define the end of this phase by the condition $\left|\frac{\partial B}{\partial t}\frac{1}{B}\right| < 0.1$ at both the biofilm-bulk fluid boundary ($x = L(t)$) and the implant-biofilm boundary ($x = 0$). This condition signifies that the rate of change in the concentration of proliferative bacteria has slowed significantly across the entire biofilm, indicating the completion of the tip formation process and the transition to the next phase.

Steady tip propagation phase (phase 5)-As illustrated in Fig. 5.11(b), the steady tip propagation phase is defined by the continuous outward movement of the rounded tip that formed in the previous phase. During this phase, biofilm growth is concentrated at the biofilm-bulk fluid interface, while deeper regions of the biofilm remain structurally stable.

This outward propagation marks the mature stage of biofilm development, where growth is localised at the boundary, but the stability of the proliferative bacteria concentration in the deeper regions reflects a mature and established structure. This steady growth dynamic ensures the resilience of the biofilm to external changes, including antibiotic pressure, while maintaining its overall integrity.

These five phases collectively describe the complex and dynamic process of biofilm growth in the presence of controlled antibiotic release. Each phase represents a distinct stage in the biofilm's development, from the initial exposure to antibiotics through to the mature stage of steady growth and structural differentiation. Understanding these phases is essential for developing effective strategies to control biofilm-associated infections. These phases are illustrated and analysed through a series of figures, each focussing on different aspects of the biofilm dynamics. All plots are for 90 days. This is a comparatively longer final time than the other models in order to capture the steady tip propagation phase.

Fig. 5.12 provides a comprehensive view of the dynamic interactions between various components of the biofilm, proliferative bacteria, persister bacteria, dead bacteria, EPS, nutrient concentrations, and antibiotic concentrations along with the biofilm's growth rate, as indicated by the velocity at the biofilm-bulk fluid interface. These interactions are depicted across the first four phases of biofilm development, each of which is visually distinguished by a different background colour in the plot: green for the first phase, magenta for the second, grey for the third, and red for the fourth. This colour-coding helps clarify the transitions between phases and highlights the key processes occurring in each. The concentrations plotted represent the total values throughout the entire biofilm at each specific time point, normalised by their respective maximum values over the entire time course, resulting in a range from 0 to 1. The velocity curve reflects the velocity at the biofilm-bulk fluid interface, scaled by the maximum velocity observed at this interface across all time points. It is important to note that the fifth (final) phase is not shown in this plot, as it begins at a much later time. Including this phase would limit our ability to capture the distinct behaviours observed in the initial four phases. The behaviours associated with the final phase, as well as the earlier phases, are discussed in detail in Fig. 5.13.

During the antibiotic delivery phase, indicated by the green background, antibiotic concentration rapidly declines as it diffuses into the biofilm, suppressing proliferative bacteria growth. As a result, persister bacteria and EPS production remain low, and there is only a slight increase in dead bacteria, due to limited proliferative bacteria. Nutrient concentration rises due to reduced bacterial activity, while biofilm growth is slow but begins to accelerate as the antibiotic concentration decreases.

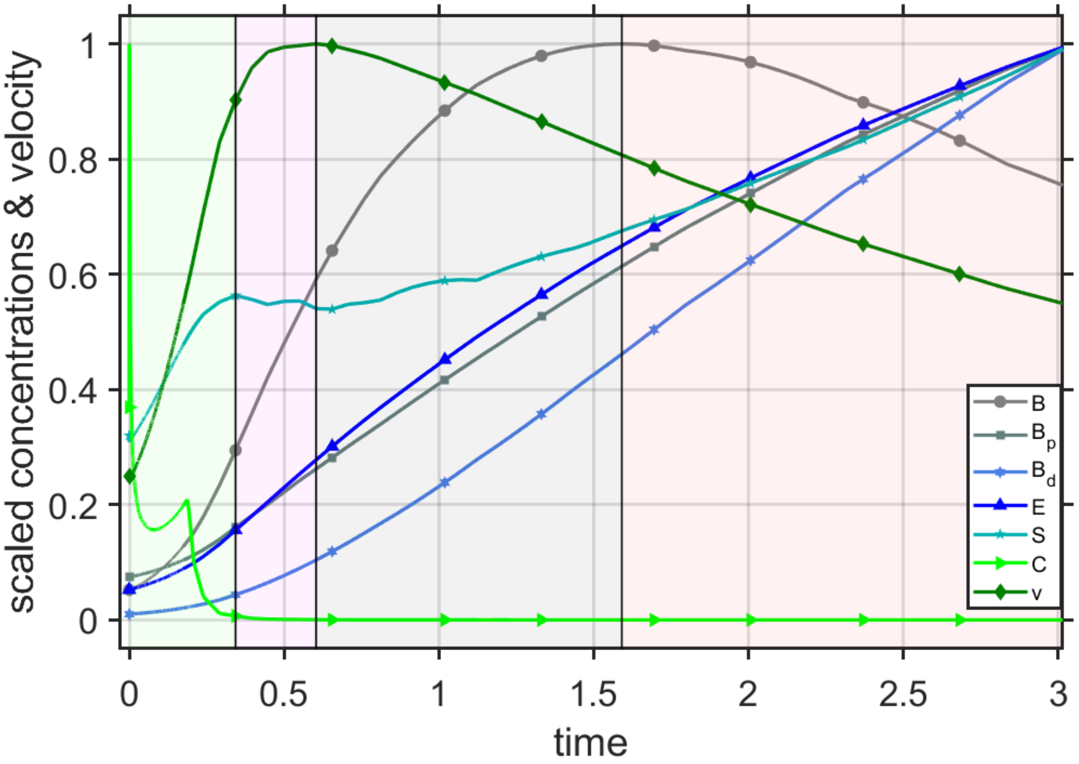

Figure 5.12: Dynamics of the first four phases of biofilm growth. The plot illustrates the scaled concentrations of proliferative bacteria (B), persister bacteria (B_p), dead bacteria (B_d), EPS (E), nutrient concentrations (S), and antibiotic concentrations (C), along with the scaled velocity (v) at the biofilm-bulk fluid interface, all plotted against time. The concentrations represent the total values throughout the entire biofilm at each specific time point, normalised by their respective maximum values over the entire time course, resulting in a range from 0 to 1. The velocity curve reflects the velocity at the biofilm-bulk fluid interface, scaled by the maximum velocity observed at this interface across all time points.

As the antibiotic concentration falls below a critical threshold, the biofilm enters the rapid acceleration of growth phase, marked by the magenta background. In this phase, proliferative bacteria grow rapidly, fuelled by nutrient consumption. This growth boosts EPS production, supporting biofilm structure, and increases persister bacteria. Dead bacteria also rise as some proliferative cells die. Nutrient concentration decreases slightly due to consumption by the growing bacterial population, and the velocity at the biofilm-bulk fluid interface peaks, marking the maximum biofilm expansion rate.

During the growth of proliferative bacteria phase, depicted with a grey background, proliferative bacteria reach their maximum concentration, driving continued EPS production and solidifying the biofilm structure. As the biofilm matures, persister bacteria increase, and dead bacteria accumulate due to stress from nutrient depletion and waste buildup. The biofilm's expansion rate slows, reflected by a decrease in velocity, while nutrient concentration rises as bacterial growth slows, indicating a shift in metabolic activity.

Finally, in the tip formation phase, shown with a red background, the biofilm undergoes a structural transition as proliferative bacteria concentration decreases, redistributing activity and resources to form a rounded tip at the biofilm-bulk fluid interface. EPS production continues, driving further expansion, while persister bacteria increase more slowly, maintaining a balance between active and dormant cells. Dead bacteria accumulate as natural death persist and the growth rate of the biofilm slows, indicated by decreasing velocity. Nutrient concentration rises more sharply as bacterial growth slows, reflecting reduced nutrient uptake.

Throughout these phases, the interplay between proliferative bacteria, persister bacteria, EPS, nutrients, and antibiotic concentration defines the biofilm's structural and functional evolution. Proliferative bacteria drive growth and EPS production, influencing the formation of persister and dead bacteria. This adaptive capability, including the formation of a protective EPS matrix and maintaining persister cells, highlights the biofilm's resilience in hostile environments like those with antibiotics. The formation of the tip during the tip formation phase marks a key step in biofilm maturation, enabling steady expansion despite internal and external stresses. The decrease in velocity and rise in nutrient concentration during the latter phases signal a transition from rapid growth to a more stable, mature structure.

To thoroughly understand the dynamics of biofilm growth and maturation, we must closely examine the actual changes in total concentrations and velocity, as the previous plot was normalised and focused on overall behaviour rather than absolute concentration levels. The next figure (see Fig. 5.13) provides these critical insights, showing how the total concentrations of proliferative bacteria (B), persister bacteria (B_p), dead bacteria (B_d), EPS (E), and the velocity (v) at the biofilm-bulk fluid interface evolve across the different phases. Fig. 5.13 highlight not only the trends but also the magnitude of changes, revealing how each component contributes to biofilm growth and structural stability over time. Due to the significant difference in scaling, the velocity is displayed on the right y-axis, while the biomass components are represented on the left y-axis.

Fig. 5.13(a) represents the antibiotic delivery phase (phase 1). During this phase, the biofilm is initially exposed to high antibiotic concentrations, which suppresses bacterial growth. As the antibiotic diffuses and reacts within the biofilm, its concentration gradually decreases, allowing bacterial activity to resume. As the antibiotic concentration decreases, the bacteria begin to proliferate. In this phase, B exhibits the highest concentration among all components. This is because, with the antibiotic concentration gradually decreasing, the bacteria that survive start to resume their growth. The proliferative bacteria are primarily responsible for driving the early expansion of the biofilm, as they are the most active in terms of growth. This early dominance of B reflects the biofilm's ability to rapidly respond to decreasing antibiotic levels by increasing bacterial proliferation. The concentration of persister bacteria increases slowly, and it remains the lowest among all components during this phase. This slow rise indicates that only a small fraction of the bacterial population transitions into the dormant state during the early stages of biofilm development. This occurs because the primary focus of the biofilm at this stage is on establishing and expanding its structure using up the available nutrient, rather than conserving cells in a dormant state. The concentration of dead bacteria is initially higher than both E and B_p, reflecting the natural attrition within the bacterial population as some cells succumb to the antibiotic or natural death. The moderate increase in B_d during this phase suggests that while some bacteria are dying due to the initial high antibiotic concentration, the overall biofilm remains largely viable as the surviving bacteria begin to proliferate. EPS production begins to increase during this phase, though its concentration is lower than both B and B_d. The rise in E indicates that proliferative bacteria are secreting EPS to support the structural development of the biofilm, but the focus is still primarily on bacterial proliferation. EPS is crucial for forming the biofilm's protective matrix, which helps in the initial stabilisation and protection of the bacterial community as it grows. The velocity at the biofilm-bulk fluid interface begins to increase, reflecting the initial stages of biofilm expansion. The rising velocity is a direct indicator of this expansion, driven by the increase in bacteria and EPS production. The biofilm's expansion at this stage is still relatively slow, corresponding to the biofilm's focus on overcoming the initial antibiotic pressure and establishing a foothold for more rapid growth in the next phase. This phase is characterised by the biofilm's adaptation to the presence of the antibiotic, with bacterial growth resuming as the antibiotic concentration decreases. The dominance of B over B_d, E, and B_p indicates that proliferative bacteria are the primary drivers of biofilm growth at this stage, as the biofilm focusses on increasing its cellular biomass and establishing a structural foundation.

Fig. 5.13(b) depicts the rapid acceleration of growth phase (phase 2), where the biofilm experiences a significant increase in growth rate. This phase is marked by a rapid escalation in the concentrations of B, B_p, B_d, and E, as well as a peak in (v) at the biofilm-bulk fluid interface. The concentration of proliferative bacteria continues to rise sharply during this phase, maintaining its position as the highest concentration among all components. This rapid increase occurs because the biofilm is now entering a phase where it can fully exploit the reduced antibiotic pressure and abundant nutrient availability. The sharp rise in B signifies that the biofilm is undergoing rapid expansion, with bacterial cells actively contributing to the overall growth of the

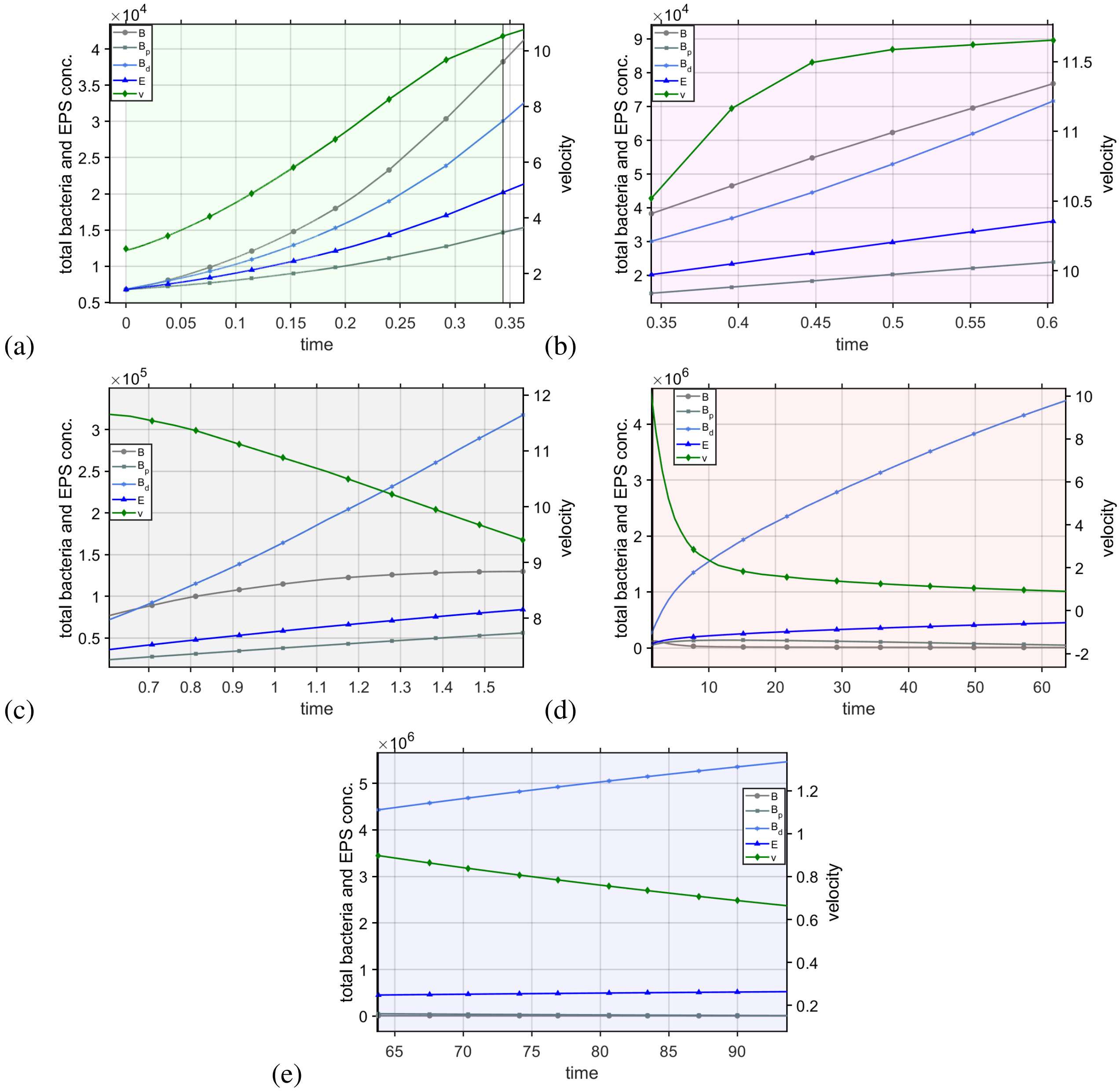

Figure 5.13: Temporal variation of total concentrations of proliferative bacteria (B), persister bacteria (B_p), dead bacteria (B_d), EPS (E) and the velocity at the biofilm-bulk fluid interface (v) during (a) phase 1, (b) phase 2, (c) phase 3, (d) phase 4, (e) phase 5.

biofilm. This aggressive growth is necessary to establish a strong and resilient biofilm structure that can withstand future challenges. The concentration of persister bacteria continues to rise, though it remains the lowest among all components. The gradual increase in B_p suggests that while most bacteria are actively proliferating, a subset is transitioning into the dormant state due to localised pockets of low nutrient. The presence of persister cells in this phase indicates that the biofilm is developing resilience, with a fraction of the population prepared to survive any unexpected environmental changes, such as a sudden decrease in overall nutrient concentration. The concentration of dead bacteria increases significantly, becoming the second-highest concentration after B. This rise in B_d reflects the natural death within the bacterial population, as some cells die due to competition for resources, accumulation of metabolic byproducts. It can also reflect the residual antibiotic effects. The increasing B_d during this phase is indicative of the intense bacterial activity within the biofilm, where rapid growth is accompanied by natural death. EPS production increases notably during this phase, ranking third in concentration after B and B_d. The sharp rise in E indicates that the bacteria are secreting large amounts of EPS to support the expanding biofilm structure. The increase in EPS is essential for sustaining the rapid expansion of the biofilm by providing a stable matrix that holds the biofilm together as it grows. The velocity at the biofilm-bulk fluid interface reaches its peak during this phase, reflecting the maximum rate of biofilm expansion. The high velocity suggests that the biofilm is rapidly growing, driven by the combined increase in bacterial biomass and EPS production. This rapid expansion is characteristic of the biofilm's aggressive growth strategy during this phase, as it seeks to maximise its coverage and establish dominance in its environment. In summary, this phase represents the biofilm's most vigorous period of growth, characterised by rapid bacterial proliferation, increased EPS production, and significant biofilm expansion. The dominance of B over B_d, E, and B_p underscores the continued importance of proliferative bacteria in driving biofilm expansion during this phase. The biofilm's strategy during this phase is to grow as quickly as possible, establishing a robust structure that can protect the community from future challenges.

Fig. 5.13(c) illustrates the growth of proliferative bacteria phase (phase 3), where the concentration of proliferative bacteria (B) initially remains high but becomes surpassed by the concentration of dead bacteria (B_d), very quickly afterwards, as the phase progresses. This phase marks a transition from rapid growth to the stabilisation of the biofilm structure. During this phase, the concentration of proliferative bacteria reaches its peak. At the beginning of this phase, the concentration of proliferative bacteria remains the highest, indicating that bacterial activity is still robust. However, as the phase progresses, B is overtaken by B_d, reflecting a shift in the biofilm's dynamics. The initial dominance of B suggests that bacterial proliferation continues to be a major driver of biofilm growth, but as nutrient limitations increase, the growth rate of B slows down. This shift occurs because the biofilm is now reaching a critical mass, where the available resources within the biofilm become limiting factors, reducing the rate of proliferation. The concentration of persister bacteria continues to increase gradually, remaining the lowest among all components. This slow rise indicates that while some bacteria are transitioning into the dormant state, the overall focus is still on maintaining a stable balance between growth and dormancy. The gradual increase in B_p reflects the biofilm's strategy of preserving a portion of its population in a dormant state, driven by the reduced nutrient concentration that resulted from high proliferation in earlier phases. The concentration of dead bacteria continues to rise sharply and eventually surpasses B to become the highest concentration in this phase. This significant increase in B_d reflects the biofilm's natural attrition as bacterial death rates exceed proliferation. This is a critical part of the biofilm's lifecycle, where the focus shifts from rapid expansion to the maintenance of a stable and resilient structure, even as some bacteria inevitably die off. EPS production continues to increase steadily, ranking third in concentration after B_d and B. The sustained rise in E suggests that the bacteria are still actively contributing to the biofilm matrix, even as bacterial growth slows. The velocity at the biofilm-bulk fluid interface begins to decrease during this phase, indicating that the rapid expansion observed in the previous phase is slowing. As the biofilm matures, the biofilm expansion slows, and the biofilm focuses more on maintaining its structure rather than continuing to expand rapidly. This phase represents a critical transition in the biofilm's lifecycle, where the initial dominance of B gives way to B_d as the biofilm matures. The decrease in velocity and the shift in the balance between growth and death indicate that the biofilm is moving towards a more stable, mature state. This phase is crucial for the biofilm as it begins to prioritise long-term survival over rapid expansion, with the increased B_d signifying the natural death of the bacterial population.

Fig. 5.13(d) focuses on the tip formation phase (phase 4), where the biofilm undergoes a significant structural transition. During this phase, the concentration of proliferative bacteria (B) decreases steadily, eventually becoming the lowest concentration among all components. This phase is characterised by the reorganisation of the biofilm's structure, particularly at the biofilm-bulk fluid interface, where a rounded tip begins to form. The concentration of proliferative bacteria decreases steadily throughout this phase, reflecting a redistribution of bacterial activity within the biofilm. Initially, total concentration B ranks second after B_d, but as the phase progresses, it very quickly becomes the lowest concentration. This decrease suggests that the biofilm is reallocating its resources to focus bacterial growth and activity at the biofilm-bulk fluid interface, where the tip is forming. The reduction in B indicates that the biofilm is prioritising structural reorganisation over further bacterial proliferation. This shift is critical for the formation of the tip, which will drive the biofilm's controlled expansion in the next phase. The concentration of persister bacteria stabilises during this phase, eventually decreasing slightly, but it remains higher than B by the end of the phase. This stabilisation indicates a balance between proliferative and persister states, with the biofilm maintaining its resilience by keeping a portion of the population in a dormant state. The slight decrease in B_p suggests that as the proliferative bacteria decreases, persister cells diminishes slightly. The concentration of dead bacteria remains the highest throughout this phase, reflecting ongoing bacterial death. The increase in B_d is likely due to natural death within the biofilm. EPS production continues to increase during this phase, eventually surpassing both B_p and B. The sustained increase E indicates that bacteria are actively secreting EPS to reinforce the deeper biofilm structure, especially as proliferative bacteria form a rounded tip at the biofilm-bulk fluid interface. The increase in EPS during this phase is crucial for the biofilm's ability to maintain its structure as it reorganises and prepares for the next phase of controlled expansion. The velocity at the biofilm-bulk fluid interface continues to decrease, indicating that the expansion of the biofilm is stabilising. The decrease in velocity reflects the biofilm's focus on structural reorganisation rather than rapid expansion. The formation of the tip is a key adaptation that allows the biofilm to prepare for steady, controlled growth in the subsequent phase. The reduced velocity also suggests that the biofilm is becoming more compact and structured, focussing on internal stability over expansion. This phase is critical for the biofilm's structural maturation, as the formation of the rounded tip facilitates further expansion in the steady tip propagation phase. The initial hierarchy of B_d, B, E, and B_p shifts to B_d, E, B_p, and B very quickly, reflecting the biofilm's evolving priorities as it matures. The structural changes that occur during this phase are essential for setting the stage for the biofilm's long-term stability and continued growth in a controlled manner.

Fig. 5.13(e) represents the steady tip propagation phase (phase 5), where the biofilm has possibly reached a mature state, and the tip formed in the previous phase begins to propagate outward steadily. This phase is characterised by the stabilisation of the biofilm structure and the continued controlled expansion driven by the tip at the biofilm-bulk fluid interface. The concentration of proliferative bacteria stabilises at a lower level during this phase, eventually overlapping with B_p. This stabilisation reflects the biofilm's shift towards maintaining its established structure rather than rapid proliferation. The decrease and eventual overlap with B_p indicate that the biofilm's growth is now more controlled and less dependent on active bacterial proliferation. The concentration of persister bacteria also decreases slightly and eventually overlaps with B. This overlap suggests that the biofilm is maintaining a balanced population of active and dormant bacteria, ensuring its long-term resilience. The decrease in B_p indicates that the biofilm's focus is shifting away from dormancy as the structure stabilises. This occurrs due to the lower proliferative concentration, resulting in a reduced transition to the persister state. However, the presence of persister cells remains important for the biofilm's ability to withstand future environmental changes. The concentration of dead bacteria continues to rise significantly, becoming the dominant component in the biofilm. The substantial increase in B_d reflects ongoing bacterial death. The dominance of B_d underscores the biofilm's natural death as it reaches a mature state. This increase in B_d is a natural consequence of the biofilm's lifecycle, and the structure is maintained through the production of new EPS and the continued growth at the biofilm-bulk fluid interface. EPS production continues to rise steadily during this phase, becoming the second-highest concentration after B_d. The increase in E suggests that the bacteria are still contributing to the biofilm matrix, ensuring its stability and resilience as the tip propagates outward. The continued rise in E is crucial for maintaining the biofilm's structural integrity as it grows. EPS is essential for the biofilm's long-term stability, providing the matrix that holds the biofilm together and protects the bacterial cells within it. The velocity at the biofilm-bulk fluid interface remains low, reflecting the steady, controlled expansion of the biofilm. The low velocity indicates that the biofilm is no longer rapidly expanding, but rather growing in a more stable, sustained manner. The steady propagation of the tip ensures that the biofilm continues to expand while maintaining its structural integrity. This controlled expansion is crucial for the long-term survival of the biofilm, as it allows the biofilm to grow without overextending its resources or destabilising its structure. This phase represents the biofilm's mature state, where growth continues steadily, and the structure is maintained. The dominance of B_d and E over B_p and B, along with the eventual overlap of B and B_p, indicates that the biofilm is in a balanced state, poised for long-term survival and resilience.

Fig. 5.13 illustrates the dynamic processes that drive biofilm growth and maturation across different phases. In the antibiotic delivery phase, the biofilm adapts to the presence of antibiotics, setting the stage for rapid growth in the rapid acceleration of growth phase. The growth of the proliferative bacteria phase marks the peak of bacterial activity, after which the biofilm undergoes structural reorganisation in the tip formation phase. Finally, the steady tip propagation phase represents the biofilm's mature state, where growth continues steadily, and the structure is maintained. The detailed examination of these phases provides valuable insights into the biofilm's lifecycle, highlighting the interplay between bacterial phenotypes, EPS production, and the biofilm's structural dynamics. This understanding is essential for developing strategies to control biofilm growth and persistence in various environments.

Manipulating critical times

The identification and understanding of these distinct phases of biofilm growth are crucial, as they remain consistent between varying sets of parameters. This consistency offers the opportunity to manipulate biofilm growth to achieve specific outcomes. By changing parameter values to affect the critical times, those time points where one phase transitions into the next, we can potentially control the biofilm's development, either by slowing it down, stopping it altogether, or even eradicating the biofilm. Such manipulations potentially provide a powerful tool for biofilm management, particularly in scenarios where inhibition of further growth or elimination of the biofilm is desirable.

To explore how these critical times can be influenced, we examine the effects of varying important model parameters. First, we focus on S_0, which represents the nutrient concentration coming from the bulk fluid. Nutrient availability plays a fundamental role in biofilm dynamics, as it regulates the transition between proliferative and persister bacterial states. In previous analyses in Section 4.2.4 and 5.2.5, we observed significant and essential changes in the characteristics of the biofilm when S_0 was altered. Therefore, we will first investigate how varying S_0 affects the critical times of each phase, as this could provide insights into how nutrient control can be leveraged to manage biofilm growth. Next, we turn our attention to the non-dimensional parameter Q, which is the ratio of the initial antibiotic concentration loaded into the implant to the antibiotic's solubility in the biofilm. This parameter captures a vital characteristic of the implant's ability to deliver the antibiotic effectively into the biofilm. By varying Q, we aim to understand whether and how this parameter influences the critical times. Discovering any dependency between Q and the transitions between the biofilm growth phases could inform strategies to optimise antibiotic delivery systems to disrupt biofilm formation or enhance biofilm eradication efforts. Thus, by analysing the effects of these parameters on the critical phase transition times, we aim to identify practical approaches to manipulating biofilm dynamics for targeted control and eradication.

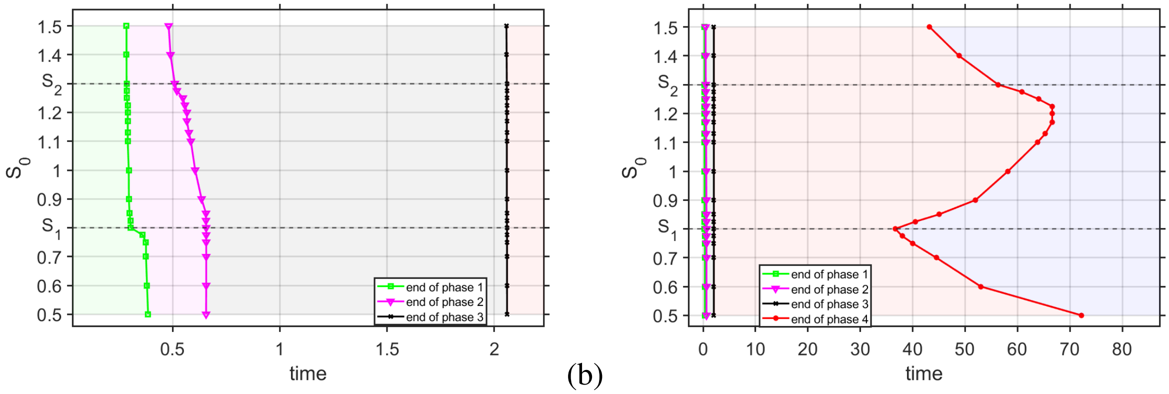

(a) (b)

Figure 5.14: Influence of varying S_0 on the critical times marking the end of biofilm growth phases. (a) Variation of the first three critical times (end of phase 1, end of phase 2, and end of phase 3), (b) Variation of all four critical times, focusing on the final critical time (end of phase 4).

Fig. 5.14 examines the effects of varying S_0, on the critical times that distinguish the transitions between different biofilm growth phases. The non-dimensional parameter S_0 ranges from 0.5 to 1.5, with non-dimensional $S_1 = 0.8$ and $S_2 = 1.3$ acting as critical thresholds for the availability of nutrients. In this model, when $S_0 \leq S_1$ is classified as insufficient nutrient conditions, $S_1 < S_0 < S_2$ as intermediate nutrient levels, and $S_0 \geq S_2$ as sufficient nutrient availability. It's important to note that antibiotic only affects the proliferative bacteria in this system, and nutrient levels directly regulate the transitions between proliferative and persister states. This understanding frames the interpretation of the critical times, focussing on how nutrient availability controls these transitions and, consequently, the biofilm's structural and dynamic properties.

Fig. 5.14(a) provides a detailed view of the critical times for the first three phases, phase 1 (antibiotic delivery phase), phase 2 (rapid acceleration of growth phase), and phase 3 (growth of proliferative bacteria phase), as functions of S_0. These early critical times reflect how nutrient availability impacts the biofilm's initial growth and interaction with the antibiotic.

The green curve represents the time at which phase 1 ends. As S_0 increases from 0.5 to 1.5, we observe a decrease in the critical time for the end of phase 1. At low values of S_0, there is insufficient nutrient availability to support significant bacterial proliferation, which results in lower concentrations of proliferative bacteria. Since the antibiotic primarily affects proliferative bacteria, fewer antibiotics are required to eliminate them in nutrient-poor conditions, and the antibiotic remains in the biofilm for a longer time. This leads to a longer critical time for the end of phase 1 at lower S_0. As S_0 increases, the nutrient concentration allows for a greater number of proliferative bacteria to form, which in turn means that higher concentration of antibiotics are required to target and eliminate them. As a result, the antibiotic is exhausted from the system more quickly and the biofilm moves on to the next phase sooner. This explains the sharper decrease in the critical time for the end of phase 1 as S_0 approaches S_1. However, beyond S_1, the decrease in the critical time becomes less pronounced because the proliferative bacteria have more consistent access to nutrients, stabilising their population and the time required to deplete the antibiotic.

The magenta curve tracks the end of phase 2, which marks the conclusion of the rapid acceleration of biofilm growth. This curve exhibits a steeper decline as S_0 increases compared to the green curve for phase 1, particularly in the intermediate nutrient range between S_1 and S_2. The sharper decrease in the critical time for phase 2 occurs because, in this phase, nutrient availability becomes increasingly important for sustaining the rapid bacterial proliferation that characterises this period of biofilm development. As S_0 increases, the biofilm has access to more nutrients. This abundance of nutrients fuels the biofilm's ability to grow quickly, shortening the duration of this phase. The availability of nutrients facilitates rapid bacterial division, and the biofilm expands at a faster rate, which is why we see a more pronounced decline in the critical time for phase 2. In the intermediate nutrient range, where $S_1 < S_0 < S_2$, the availability of nutrients is sufficient to fuel rapid bacterial growth, and the biofilm can move through the rapid growth phase quickly. However, as S_0 increases beyond S_2, the critical time begins to stabilise. At these higher nutrient concentrations, the biofilm reaches a point where further increases in nutrient availability no longer significantly impact the growth rate. This stabilisation occurs because, beyond S_2, the nutrient concentration is no longer the limiting factor for biofilm growth. The bacteria have access to sufficient nutrients to sustain their rapid growth, and further increases in S_0 do not accelerate this process any further. This explains why the critical time for the end of phase 2 decreases more steeply in the intermediate nutrient range and then begins to level off at higher nutrient concentrations.

The black curve represents the critical time for the end of phase 3, which marks the peak concentration of proliferative bacteria in the biofilm. Unlike the green and magenta curves, this curve shows only a slight decrease as S_0 increases, indicating that varying nutrient availability has little effect on when the proliferative bacteria reach their peak total concentration. The reason for this behaviour is that, by the time the biofilm reaches the end of phase 3, the growth of proliferative bacteria is its maximum, and the nutrient levels no longer play as significant a role in determining the total concentration of proliferative bacteria. Although increasing S_0 supports faster bacterial growth in the earlier phases, the overall population of proliferative bacteria reaches a peak relatively quickly. Once this peak is reached, additional nutrients do not substantially impact the timing of this peak. This explains why the decrease in the critical time for phase 3 is much less pronounced than for the earlier phases. Essentially, the biofilm's dynamics in phase 3 are less dependent on nutrient availability because the proliferative bacteria have already reached a point where they are growing at their maximum potential. Additionally, this subtle decrease in the black curve suggests that the biofilm's growth dynamics have reached a more stable phase by the time phase 3 occurs. The total population of proliferative bacteria is less sensitive to variations in S_0, indicating that the biofilm has stabilised its growth. The lower sensitivity of phase 3 to changes in nutrient availability implies that the biofilm's structural integrity and the balance between proliferative and persister cells are becoming more established at this point, leading to a more consistent critical time for the end of this phase.

Fig. 5.14(b) shows how all four critical times (the end of phases 1, 2, 3, and 4) vary with S_0. However, the primary focus is on the final critical time, representing the end of phase 4 (tip formation phase), as there is a large time difference between the earlier critical times and this one. The red curve in Figure 2 illustrates the behaviour of the final critical time across different nutrient levels.

At low S_0 values (below S_1), the nutrient availability is insufficient to support the structural changes necessary for tip formation. In this phase, the biofilm requires a stable structure to begin propagating the rounded tip at the biofilm-bulk fluid interface, and lower S_0 values mean that the number of proliferative bacteria is too low to drive these changes. As a result, tip formation, and by extension, steady tip propagation, takes much longer at lower S_0, delaying the biofilm's transition to a mature, stable state. This explains why the critical time for the end of phase 4 decreases sharply as S_0 increases from 0.5 towards S_1. In the intermediate nutrient range ($S_1 < S_0 < S_2$), the critical time for the end of phase 4 shows a more complex, non-monotonic behaviour. Initially, as S_0 increases beyond S_1, the critical time increases, reaching a maximum around $S_0 = 1.2$. This can be explained by the balance between proliferative and persister bacteria. In this nutrient range, although more nutrients promote the growth of proliferative bacteria, they also encourage the transition of proliferative bacteria into persisters. This rapid transition between states destabilises the biofilm's structural integrity, delaying the onset of steady tip propagation. As the nutrient availability increases, the biofilm requires more time to achieve a stable balance between proliferative and persister cells, leading to a longer critical time for the end of phase 4. At higher nutrient concentrations above $S_0 = 1.2$, the critical time for the end of phase 4 decreases once again. In this almost sufficient or sufficient nutrient range, the biofilm can support a higher concentration of proliferative bacteria, which leads to a rapid increase in structural integrity. The transition from persister to proliferative becomes more dominant, and the biofilm can complete tip formation and enter the steady tip propagation phase much sooner. As a result, the critical time for the end of phase 4 decreases rapidly as S_0 increases through this range.

The behaviours observed in Fig. 5.14 can be interpreted in terms of the balance between nutrient availability, bacterial proliferation, and structural changes in the biofilm. For the early phases, increases in S_0 shorten the critical times because more nutrients support faster bacterial growth and more rapid antibiotic consumption. However, once nutrient availability exceeds certain thresholds (such as S_1 and S_2), further increases in S_0 have diminishing returns, and the biofilm's growth rate stabilises. The more complex behaviour seen in phase 4 reflects the biofilm's structural dynamics, which are strongly influenced by the balance between proliferative and persister bacteria. In the intermediate nutrient range, this balance is highly dynamic, leading to longer critical times as the biofilm struggles to stabilise its structure. Once S_0 increases into the sufficient nutrient range, the biofilm rapidly reaches a mature state, and the critical time decreases. The final critical time (end of phase 4) is particularly sensitive to variations in S_0, indicating that the biofilm's structural maturation is heavily dependent on nutrient availability and the transitions between proliferative and persister states. This phase also has a much more pronounced response to nutrient variation than the earlier phases, which suggests that biofilm maturation is more dependent on nutrient-driven transitions between bacterial phenotypes than on the early dynamics of bacterial growth and antibiotic consumption.

Fig. 5.14 show that controlling nutrient levels can have significant effects on the timing of key biofilm growth transitions, particularly in the later phases where structural changes are crucial. Understanding these dynamics can help in developing strategies to manipulate biofilm growth and potentially delay or accelerate biofilm maturation for therapeutic purposes.

Fig. 5.15 illustrates the influence of varying the parameter Q, on the critical times that mark the transitions between different phases of biofilm growth. As the antibiotic affects proliferative bacteria, changing Q directly impacts the biofilm's growth dynamics, particularly the critical times for the various growth phases. In this analysis, we examine the behaviour of the critical times for each phase and explain how increasing Q affects biofilm formation and antibiotic efficiency.

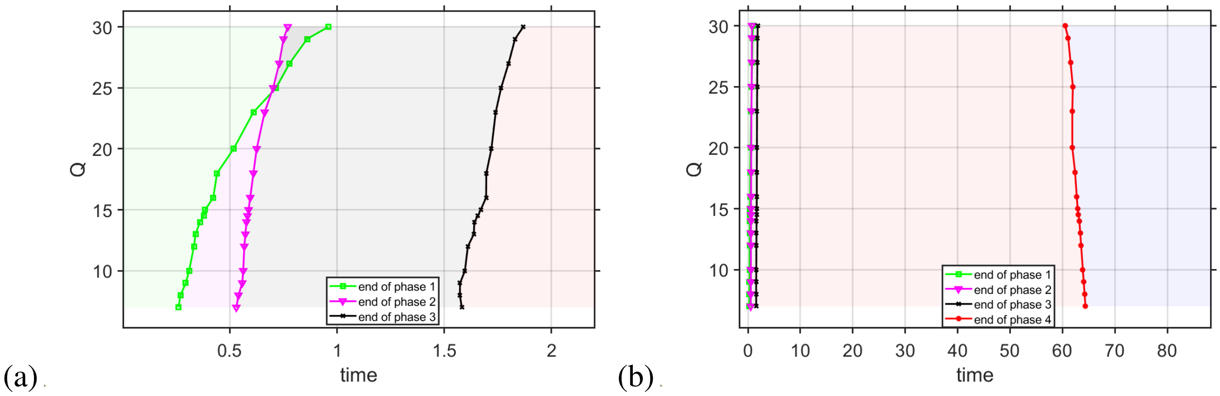

(a) (b)

Figure 5.15: Influence of varying Q on the critical times marking the end of biofilm growth phases. (a) Variation of the first three critical times (end of phase 1, end of phase 2, and end of phase 3), (b) Variation of all four critical times, focusing on the final critical time (end of phase 4).

The green curve in Fig. 5.15(a) shows how the critical time for the end of phase 1 increases as Q increases. As Q increases, the solid antibiotic concentration in the implant increases or the solubility of the antibiotic decreases. Consequently, the antibiotic takes longer to be depleted, which prolongs the time required for the antibiotic to reach 1% of its initial total concentration.

This explains why the duration of the antibiotic delivery phase increases with increasing Q, as higher Q prolongs the release time of antibiotic.

The magenta curve in Fig. 5.15(a) represents the critical time at which the velocity of the biofilm-bulk fluid interface reaches its peak, marking the end of phase 2. As Q increases, the critical time associated with this phase also increases. This behaviour indicates that as the solid antibiotic concentration increases or the solubility decreases, the biofilm takes longer to reach its peak growth velocity. This is because a higher Q means more antibiotic is present to kill proliferative bacteria, slowing down biofilm growth overall. It could also mean lower solubility which prolongs antibiotic presence in the biofilm leading to slower biofilm growth. Since proliferative bacteria contribute to the production of EPS, dead bacteria, and persister cells, the slower growth of proliferative bacteria results in a slower overall accumulation of biofilm biomass, which delays the time at which the biofilm reaches its maximum growth velocity.

Around $Q = 25$, we observe the green curve crossing the magenta curve. This suggests that as Q increases, the biofilm reaches its peak growth velocity before the total antibiotic concentration falls below 1% of the initial total antibiotic concentration. One might expect the biofilm to reach its peak velocity after the antibiotic has been depleted, as the antibiotic actively suppresses bacterial growth. However, despite the significant presence of the antibiotic, the biofilm still manages to attain its peak growth velocity. This behaviour indicates that, while the antibiotic is still killing proliferative bacteria, the biofilm is likely entering a phase where other factors, such as the accumulation of persister bacteria, dead bacteria and EPS, begin to dominate the dynamics. These biomass constituents are not directly affected by the antibiotic, allowing the biofilm to continue growing and reaching its peak velocity despite the presence of the antibiotic. Notably, this crossover is not a critical threshold, as if we define the end of phase 1 to occur when the antibiotic concentration falls below 5% of the initial total antibiotic concentration instead of 1%, the green curve would shift leftward. This would result in the critical time for the end of phase 1 occurring much earlier, showing that the crossover does not represent a strict limit but is dependent on how we define the antibiotic exhaustion point.

The black curve in Fig. 5.15(a) represents the critical time for the end of phase 3, which is the time at which the total concentration of proliferative bacteria reaches its peak. As Q increases, the critical time for this phase also increases. This is because a higher initial solid antibiotic concentration or lower antibiotic solubility means that the antibiotic release duration is prolonged. So, more proliferative bacteria are being killed by the antibiotic. As a result, it takes longer for the population of proliferative bacteria to reach its maximum concentration, as the antibiotic is constantly reducing their numbers. This increase in critical time with higher Q values occurs because the biofilm's proliferative bacteria are the main target of the antibiotic, and more antibiotic in the system leads to a more significant suppression of the bacterial population. Consequently, the peak in proliferative bacteria concentration is delayed as the system struggles to balance bacterial growth against the effects of the antibiotic.

The red curve in in Fig. 5.15(b) shows the critical time for the end of phase 4, marking the transition to the steady tip propagation phase, where the biofilm reaches a mature state. As Q increases, the critical time decreases, which means that the biofilm matures more quickly. Although in this case, longer antibiotic presence in the biofilm as seen by the green curve leads to more proliferative bacteria being killed, which might suggest that biofilm growth would slow down, the biofilm actually matures faster. This is because the elimination of proliferative bacteria allows the structure of the biofilm to stabilise more quickly. Once proliferative bacteria are killed, the remaining components of the biofilm, dead bacteria, persistent bacteria, and EPS, take over and solidify the structure of the biofilm. As a result, the biofilm transitions to a mature, stable state earlier. This earlier maturation is facilitated by faster suppression of proliferative bacteria at higher Q values. Eliminating proliferative bacteria prevents new biomass from being added, allowing the biofilm to reach its steady state more quickly. The earlier transition to the steady tip propagation phase indicates that the biofilm stabilises faster at higher Q, even though the overall biofilm growth might be suppressed due to the reduced number of proliferative bacteria.

Fig. 5.15 illustrates the complex relationship between antibiotic availability and biofilm growth dynamics. Higher Q values prolong the early stages of biofilm growth by delaying the exhaustion of the antibiotic and extending the time for peak biofilm velocity and proliferative bacteria concentration. However, this leads to a quicker transition to biofilm maturity, marked by earlier onset of steady tip propagation in the later stages. Understanding these dynamics is crucial for designing effective antibiotic delivery systems for biofilm eradication.

5.3 Initial optimisation of the antibiotic delivery

In this section, an optimisation framework for antibiotic delivery is introduced by modifying the initial concentration of the antibiotic stored within the implant. The goal is to explore how spatially dependent initial antibiotic concentrations can impact antibiotic delivery and biofilm behaviour. In particular, by understanding how the different phases of biofilm growth occur, it might be possible to target each phase with a different concentration of antibiotic through spatial patterning. This approach aims to optimise the timing and dosage of antibiotic delivery to disrupt biofilm development more effectively.

Model 2 can be modified to optimise antibiotic delivery, and this section demonstrates an example by making small changes. In the original model, the solid antibiotic concentration within the implant was assumed to be uniform over space. It was defined as:

$$C_p(x,t) = C_0, \quad \text{for} \quad -L_d < x < -L_1(t)$$

However, in this new approach, the concentration is spatially dependent, allowing for a more tailored antibiotic release profile. The spatial dependence of the antibiotic concentration is introduced using a step function that divides the implant into two sub-regions with different antibiotic concentrations. We modify the equation to:

$$C_p(x,t) = C_0(x), \quad \text{for} \quad -L_d < x < -L_1(t),\, t > 0,, \tag{5.162}$$

where

$$C_0(x) = C_{01} H\left(\frac{L_d}{2} - L_1\right) + C_{02} H\left(L_1 - \frac{L_d}{2}\right). \tag{5.163}$$

Here, H denotes the Heaviside function and C_{01} and C_{02} represent the antibiotic concentrations in the two sub-domains $[-L_d/2, -L_1(t)]$ and $[-L_d, -L_d/2]$, respectively.

The parameters C_{01} and C_{02} are not arbitrary but are related to the solid antibiotic concentration, C_0, in Model 2. We introduce a perturbation δ' to explore different delivery profiles. So these parameters are defined as

$$C_{01} = C_0 + \delta, \quad C_{02} = C_0 - \delta. \tag{5.164}$$

This perturbation introduces an optimisation variable that can be tuned to investigate how changes in the antibiotic concentration distribution affect the overall antibiotic delivery profile and its efficacy. The parameter δ serves as a control parameter in the optimisation framework. It is important to note that the total mass of the solid antibiotic concentration in the implant remains constant which is C_0 regardless of the value of δ; only the spatial distribution of the antibiotic changes.

This spatial dependence represents the simplest form of optimisation of the antibiotic concentration distribution. However, this is merely an initial exploration of optimisation techniques, and one could further develop more complex spatial dependencies to investigate the effects of varying antibiotic concentrations within different regions of the implant. Such refinements could provide even more targeted antibiotic delivery based on the reaction within the biofilm. In any expression where C_0 is involved in Model 2, it will now be replaced by $C_0(x)$ for this model. All other governing equations, as well as the other initial and boundary conditions, remain the same as those in Model 2, described in Section. 5.2.2. Fig. 5.16 illustrates how the antibiotic is stored in the implant, released into the dissolved state, and diffuses into the biofilm.

The new antibiotic concentration as well as the entire model is non-dimensionalised and boundary immobilised using the same scaling factors as in Model 2, in Section. 5.2.3 and 5.2.4. This leads to the transformed equation:

$$\overline{C}_p(\xi,\bar{t}) \;=\; Q(\xi), \quad \text{for} \quad -\frac{\overline{L}_d}{\overline{L}_1} < \xi < -1,\, \bar{t} > 0 \tag{5.165}$$

$$\tag{5.166}$$

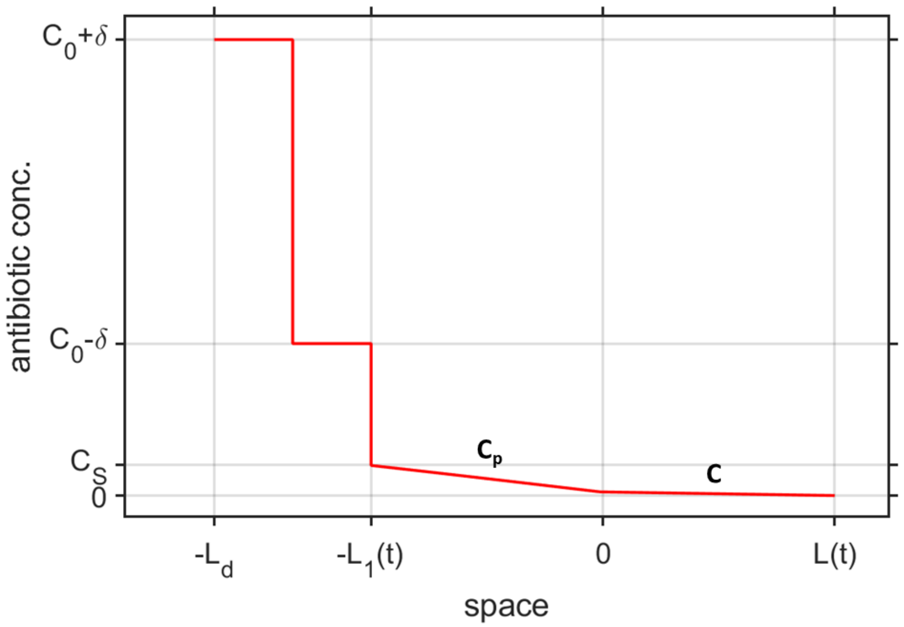

Figure 5.16: Schematic representation of antibiotic concentration profile along the implant and biofilm. The region from $-L_d$ to $-L_1(t)$ represents the solid antibiotic stored in the implant, where the concentration is $C_0+\delta$ for $-L_d$ to $-L_d/2$ and $C_0-\delta$ for $-L_d/2$ to $-L_1$. δ is considered negative for this figure. Between $-L_1(t)$ and 0, the antibiotic is dissolved, with a concentration C_p, limited by the solubility of the antibiotic (C_s). The region from 0 to $L(t)$ corresponds to the biofilm, where the antibiotic concentration is C. This profile illustrates the transition of the antibiotic from the solid form in the implant to its dissolved state and subsequent diffusion into the biofilm.

where

$$Q(\xi) = Q_1 H\left(\frac{\overline{L}_d}{2\overline{L}_1} - 1\right) + Q_2 H\left(1 - \frac{\overline{L}_d}{2\overline{L}_1}\right). \tag{5.167}$$

Here,

$$Q_1 = Q + \overline{\delta}, \quad Q_2 = Q - \overline{\delta}. \tag{5.168}$$

The non-dimensional parameters for the above expressions are

$$Q_1 = \frac{C_{01}}{C_S}, \quad Q_2 = \frac{C_{02}}{C_S}, \quad Q = \frac{C_0}{C_S}, \quad \overline{\delta} = \frac{\delta}{C_S}.$$

5.3.1 Results and Discussions

The model was solved using COMSOL, following a methodology similar to that described in Section 5.2.5. The new equation was implemented in COMSOL by defining the variable $Q(\xi)$ that represents the spatially dependent antibiotic concentration. This variable was then used within the modules to solve the dependent variables for antibiotic concentration and biofilm dynamics. To ensure convergence of this model, we adjusted the default settings in COMSOL for the ’Method and Termination’ under the ’Fully Coupled’ section, switching from ’Constant (Newton)’ to ’Automatic (Newton)’. This modification was essential for both studies (see Section 5.1.5). All other settings remained unchanged.

A sensitivity analysis was performed on the parameter δ to observe how varying solid antibiotic distributions affect the phases of biofilm dynamics. It is important to note that all results are based on non-dimensionalised variables, with the overline notation omitted in the figures for clarity.

The behaviour observed in Fig. 5.17 can be explained by closely examining how varying the parameter δ affects the distribution of antibiotic concentration in the implant and its impact on the different phases of biofilm growth. It is important to note that the total mass of initial solid antibiotic concentration in the implant remains the same regardless of the value of δ; only the spatial distribution of the antibiotic changes. δ determines how the antibiotic is spatially distributed between the two halves of the implant. We varied it from -5 to 10 to cover a range of cases for the spatially dependent antibiotic concentration. For $\delta < 0$, a lower antibiotic concentration is initially released, followed by a higher concentration when L_1 crosses $L_d/2$, which is the point where the antibiotic release front reaches halfway through the porous implant.. For $\delta = 0$, the antibiotic is uniformly distributed across the implant. In contrast, for $\delta > 0$, a higher concentration is released initially, followed by a lower concentration in the latter half of the release. When $\delta = 10$, the concentration drops to zero for $L_1 > L_d/2$. So, increasing δ means the initial solid antibiotic concentration in the half of the implant near the implant-biofilm interface increases, while the concentration in the farther half decreases. This distribution strongly influences how quickly the antibiotic is released into the biofilm, which in turn affects the biofilm dynamics in each phase.

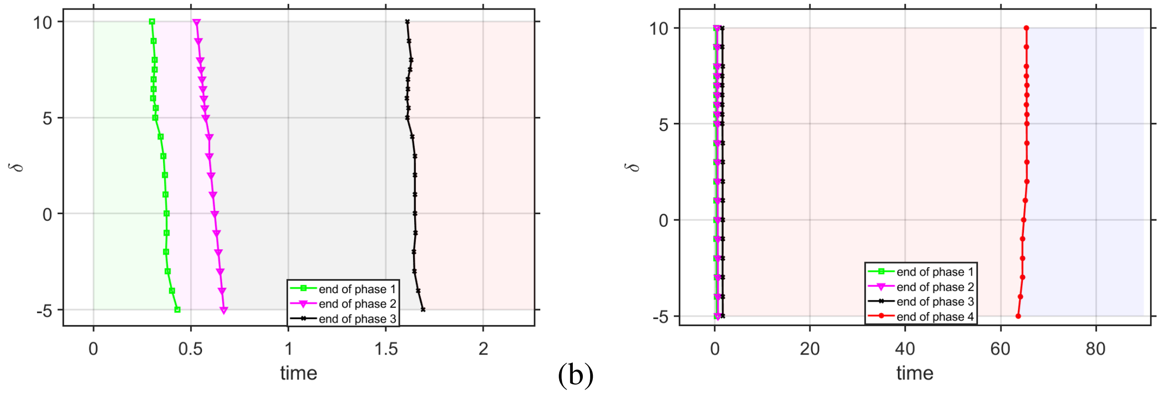

(a) (b)

Figure 5.17: Influence of varying δ on the critical times marking the end of biofilm growth phases. (a) Variation of the first three critical times (end of phase 1, end of phase 2, and end of phase 3), (b) Variation of all four critical times, focusing on the final critical time (end of phase 4).

In Fig. 5.17(a), the green curve, which represents the end of phase 1, clearly shows that as δ increases, the critical time decreases. This indicates that the antibiotic delivery phase becomes shorter as δ increases. Physically, this is because a larger δ means more antibiotic is concentrated near the implant-biofilm interface, where it can more rapidly dissolve. As a result, the biofilm is exposed to a higher concentration of antibiotic early on, leading to faster antibiotic delivery and quicker depletion of the available antibiotic in the system. The movement of the boundary L_1, which governs the region of undissolved antibiotic, is directly affected by this concentration. With more antibiotic near the interface, the higher concentration gets released faster, causing L_1 to recede more quickly, accelerating the antibiotic release process. This explains why the biofilm progresses through the antibiotic delivery phase more rapidly as δ increases, because the antibiotic is consumed faster, leaving less time for phase 1 to continue. In contrast, when δ is negative, meaning a smaller amount of antibiotic is initially available, the antibiotic delivery phase is prolonged. The lower initial solid antibiotic concentration means that less antibiotic diffuses into the biofilm at the start, leading to a slower depletion of the antibiotic. Consequently, the biofilm remains in phase 1 for a longer period because it takes more time for the antibiotic to be used up. This slower release of the antibiotic at lower δ values is responsible for the longer critical times seen in the green curve for negative δ.

The magenta curve, which tracks the end of phase 2, follows a similar trend, with the critical time decreasing as δ increases. The reason for this is that as δ increases and more antibiotics get available near the biofilm, the early killing of proliferative bacteria is more effective. Proliferative bacteria are the main target of the antibiotic, and with a higher antibiotic concentration near the biofilm, a larger number of proliferative bacteria are killed earlier. This reduces the overall biomass available to sustain the rapid acceleration of growth, which is characteristic of phase 2. As a result, the biofilm cannot sustain this rapid growth phase for as long, leading to an earlier end to phase 2 as δ increases. Additionally, because proliferative bacteria are also the source of persister cells and EPS, killing more of them early on means there is less transfer to persister cells and reduced EPS production. Both persister cells and EPS contribute to the biomass velocity. Therefore, the reduction in these biomass components caused by higher initial solid antibiotic concentrations further accelerates the transition out of phase 2.

The black curve, which represents the end of phase 3, also shows a decrease in critical time as δ increases, but this decrease is less pronounced than for the green and magenta curves. By the time the biofilm reaches phase 3, most of the antibiotic has already been consumed. While a higher initial solid antibiotic concentration near the biofilm interface affects the overall number of proliferative bacteria, the impact is less direct at this stage. As a result, the critical time decreases more gradually as δ increases. The biofilm has already experienced significant bacterial reduction in earlier phases, so the effect of further changes in antibiotic concentration is muted, leading to a slower rate of decrease in critical time for phase 3 compared to earlier phases.

In Fig. 5.17(b), we see the behaviour of the red curve, which represents the end of phase

4. Here, the critical time behaves differently compared to the earlier phases, it increases as δ increases. This indicates that the biofilm reaches a mature, steady state later when δ is larger. When δ is large, most of the antibiotic is concentrated near the implant-biofilm interface, leading to rapid depletion of the antibiotic early on. However, because the second half of the implant contains much less antibiotic, or none at all (as is the case when $\delta = 10$), there is insufficient antibiotic to effectively control the biofilm growth in the earlier stages. The steady tip propagation phase, which marks the biofilm's structural maturation, requires a stable structure composed of proliferative bacteria, persister cells, and EPS. Since proliferative bacteria are killed off more quickly with higher δ, fewer persister cells are formed, and less EPS is produced. Both persister cells and EPS are crucial for building and maintaining the biofilm's structure, so their reduction along with less proliferative bacteria weakens the biofilm. This structural weakening delays the onset of steady tip propagation, as the biofilm requires more time to reach a state where it can support steady growth at the biofilm-bulk fluid interface. This explains why the critical time for the end of phase 4 increases as δ increases. The biofilm's structure takes longer to stabilise due to the reduced biomass components contributing to its growth. On the other hand, when δ is smaller, the antibiotic concentration is initially lower for the first half of the implant or near the implant-biofilm interface which leads to a more gradual dissolution of the antibiotic. This allows the biofilm to be exposed to the antibiotic over a longer period. This extended exposure helps the biofilm stabilise its structure earlier, as the biomass production is higher during the earlier stages, have more time to adjust and build a stable biofilm structure. Consequently, the biofilm reaches the steady tip propagation phase sooner when δ is smaller, and the critical time for phase 4 decreases. This is why the biofilm reaches maturity earlier at lower δ values.

This analysis suggests that shifting from a uniform antibiotic loading to a spatially dependent antibiotic loading is a significant first step towards optimising antibiotic delivery. The results clearly show that varying δ, which controls how the antibiotic is distributed across the implant, has a direct and measurable effect on the timing of critical biofilm growth phases. By increasing the antibiotic concentration near the implant-biofilm interface, the antibiotic is delivered more efficiently in the early stages, leading to faster bacterial killing and shorter biofilm growth phases. However, it also reveals that higher concentrations near the interface can deplete the antibiotic too quickly, leaving the biofilm less controlled in the later stages, thus delaying its maturation. This insight highlights the trade-offs between early and late-stage antibiotic availability and demonstrates that spatial control of antibiotic concentration can significantly influence biofilm dynamics.

While this approach may not yet fully optimise antibiotic delivery, it proves that spatially dependent loading is a powerful mechanism for influencing the timing and effectiveness of antibiotic release. The ability to adjust the antibiotic concentration across the implant provides a new layer of control that was not possible with uniform loading. This result suggests that further refinement of this method—such as fine-tuning the concentration gradient or balancing antibiotic release more evenly across the implant—could lead to more effective strategies for sustained and targeted antibiotic delivery. Thus, this model establishes a clear pathway towards more sophisticated antibiotic optimisation techniques by showing the tangible benefits of spatially controlled loading.

5.4 Summary

This chapter explored the influence of controlled antibiotic release from porous implants on biofilm growth and its composition, employing three models to progressively incorporate more complex interactions and phenomena. The modelling framework uniquely integrates both implant and biofilm domains, incorporating proliferative, persister, and dead bacteria, EPS production, and nutrient-regulated persister transitions, a combination which has not, to our awareness, been achieved in prior biofilm modelling literatures. The primary focus was on how the antibiotic delivery from a porous implant affects the biofilm's overall growth, bacterial phenotype transitions, EPS production, and nutrient availability. Model 10, addressed the general impact of antibiotic delivery from a porous implant on biofilm growth, focussing on parameters such as antibiotic effectiveness and the ratio of the initial solid antibiotic concentration to its solubility in the biofilm. Model 2 expanded this analysis to include bacterial phenotypes—proliferative, persister, and dead bacteria—and nutrient-dependent transitions, with an in-depth look at how nutrient availability coupled with controlled antibiotic delivery influences biofilm structure and growth. The third model introduced an initial optimisation approach by spatially varying the antibiotic concentration in the implant, demonstrating the potential of this method for improving antibiotic delivery strategies.

Model 10 focused on understanding how antibiotic delivery from a porous implant affects biofilm growth, with comparisons drawn against a baseline model (Model 11) without antibiotic influence. The results showed that while antibiotic delivery initially slows biofilm growth, this effect is transient. The antibiotic diffuses rapidly into the biofilm and is quickly depleted, leading to a resumption of biofilm growth at rates comparable to the baseline model. The biofilm eventually reaches the same final thickness as in the model without antibiotics, indicating that the antibiotic's impact is confined to its presence in the biofilm during the early growth phase. Sensitivity analysis was conducted to examine how varying antibiotic effectiveness and the ratio of initial solid antibiotic concentration in the implant to solubility in the biofilm, influenced biofilm growth. Increasing antibiotic effectiveness or solid antibiotic concentration, led to little to no change in biofilm growth. For higher solid antibiotic concentration, changes in antibiotic effectiveness became more pronounced, indicating an interplay between the two parameters. However, even with increased antibiotic concentrations and effectiveness, the biofilm eventually resumed normal growth, once the antibiotic was depleted from the system. The observation that even high antibiotic concentrations led to only temporary control was significant, underscoring the importance of understanding this dynamic for optimising long-term treatment strategies.

In Model 2, nutrient availability played a critical role in determining the biofilm structure and growth dynamics. Higher nutrient concentrations led to faster biofilm growth, with higher proliferative bacteria and EPS production. Conversely, in nutrient-poor environments, biofilm growth was significantly slower, and the biofilm adopted a survival strategy, with a greater proportion of persister cells. The nutrient-poor environment was characterised by slower biofilm maturation and reduced structural development, but persister cells remained dominant, making the biofilm more resilient to antibiotic effects. This model revealed five distinct phases of biofilm growth: antibiotic delivery phase, rapid acceleration of growth, growth of proliferative bacteria, tip formation, and steady tip propagation. Sensitivity analysis on nutrient concentration and the ratio of initial antibiotic loading to the solubility of the antibiotic revealed intricate dynamics governing the transitions between biofilm growth phases. Increasing nutrient concentrations led to shorter critical times for the initial growth phases (antibiotic delivery and rapid acceleration), but the transition to biofilm maturity (steady tip propagation) was delayed under intermediate nutrient conditions, reflecting the biofilm response to nutrient availability and how it affects the balance between different bacterial phenotypes. The higher Q values prolonged the early growth phases, but led to faster biofilm stabilisation and earlier onset of the steady tip propagation phase, suggesting that while the antibiotic delays early growth, it accelerates biofilm maturity by reducing the proliferative bacterial population and stabilising the biofilm structure. The identification of these phases and the systematic analysis of how they shift with nutrient and antibiotic parameters represent a novel contribution that enhances interpretability of biofilm evolution in therapeutic contexts. It will be important to see if these behaviours can help inform optimised antibiotic delivery in future biofilm models.

The final model in this chapter introduced an initial approach to optimise antibiotic delivery by varying the spatial distribution of the antibiotic concentration in the implant, instead of an uniform distribution. The analysis explored how changing the distribution of antibiotic between the implant-biofilm interface and the deeper regions of the implant impacted biofilm growth phases. When more antibiotic was concentrated near the implant-biofilm interface, the antibiotic was released faster, leading to a shorter antibiotic delivery phase and quicker suppression of biofilm growth in the early stages. However, this rapid release also resulted in faster depletion of the antibiotic, which left the biofilm less controlled in the later stages, delaying its maturation. In contrast, when the antibiotic was more evenly distributed or concentrated away from the implant-biofilm interface, the release was more gradual, allowing the antibiotic to remain active over a longer period. This resulted in slower initial suppression of the biofilm, but more consistent control over time, enabling the biofilm to mature earlier. This trade-off between immediate bacterial killing and sustained control over biofilm growth offers a new perspective on optimising antibiotic delivery strategies, suggesting that spatial control over antibiotic release could significantly improve biofilm management. This modelling and analysis of spatially optimised antibiotic loading strategies introduces a new approach to spatial control within the implant to influence biofilm outcomes. This spatial control offers a promising step towards optimising antibiotic delivery for more effective biofilm management.

The work in this chapter opens several avenues for future exploration and refinement. First, the spatial distribution of the antibiotic within the implant could be further optimised by employing more sophisticated gradients in the solid antibiotic concentration. For example, a multi-gradient distribution could prolong the effectiveness of the antibiotic over time. Additionally, making the antibiotic release rate spatially variable by designing implants with a spatially varying porosity could enhance control over antibiotic diffusion. In a porous implant, regions with higher porosity could facilitate faster antibiotic release near the biofilm, while lower porosity areas would slow down release, extending the antibiotic's impact over longer periods.

Another key future direction would involve introducing oral antibiotics alongside the antibiotics delivered from the porous implant. This combined approach could mitigate biofilm growth more effectively by targeting different bacterial populations and reducing the risk of bacterial resistance developing within the biofilm. The interaction between systemic and localised antibiotics would also provide insights into the most effective multi-pronged strategies for biofilm eradication.

Chapter 6

Conclusion and future work

The central aim of this thesis was to address the significant clinical problem of biofilm formation on medical implants, a challenge that persists due to the inherent resistance of biofilms to conventional antibiotic treatments. Additionally, this work sought to bridge existing knowledge gaps by incorporating bacterial phenotypes, nutrient dynamics, and localised controlled antibiotic delivery into a cohesive modelling framework, advancing our understanding of biofilm resilience and potential treatment strategies. Biofilms, once established on implant surfaces, can lead to chronic infections and severely complicate patient outcomes, as they offer a protective environment that shields bacteria from systemically delivered antibiotics and immune responses. This research was motivated by the pressing need to find more effective methods to control biofilm growth, particularly by optimising antibiotic delivery systems within implants to disrupt biofilm formation and prevent infection.

The overarching goal of this research was to investigate how controlled antibiotic release from a implant could impact biofilm growth and composition. By focussing on the intricate dynamics between antibiotic diffusion, bacterial phenotypic transitions, and nutrient availability, this study sought to improve the current understanding of how these factors interact and influence the effectiveness of treatments aimed at biofilm eradication. Ultimately, the research aimed to provide insights that could lead to the development of better therapeutic strategies for preventing biofilm-related infections in clinical settings.

To achieve this, the research set out to explore several key questions. First, it sought to determine how the release of antibiotics from a porous implant affects biofilm growth over time, especially in relation to bacterial proliferation, the formation of persister cells, and the production of the EPS that reinforces biofilm stability. Understanding the temporal dynamics of biofilm suppression in response to antibiotic exposure is crucial for identifying optimal treatment windows and dosages. Another objective was to examine the role of nutrient availability at the biofilm-bulk fluid interface in shaping biofilm structure and resilience. Since nutrient levels directly influence bacterial growth and survival strategies, this aspect of the research was aimed to reveal how variations in nutrient concentrations could alter the balance between proliferative bacteria and persistent cells, ultimately affecting the biofilm's ability to resist treatment. In addition, this thesis paved the way for potential optimisations for the antibiotic delivery strategy to counteract biofilm infection. For example, rather than relying on a uniform release of antibiotics, the study investigated whether spatially dependent antibiotic loading could enhance biofilm suppression by controlling the timing and location of antibiotic delivery. This approach was intended to optimise the interaction between the antibiotic and the biofilm, with the goal of improving the effectiveness of both immediate and long-term treatment.

6.1 Conclusion

Chapter 2 laid the foundation for understanding biofilm dynamics by developing and systematically simplifying a detailed biofilm growth model. This model incorporated bacterial phenotypes, EPS production, nutrient availability, and antibiotic delivery from porous implant. This chapter developed a hierarchy of models that captured essential biofilm behaviours while simplifying the complexities. The primary implication of this chapter lies in the flexibility offered by the hierarchical model simplifications. This approach provides a more customisable modelling framework for biofilm-related studies, enabling researchers to selectively incorporate or omit specific biofilm dynamics depending on the needs of their investigation. This flexibility allows for an accurate representation of critical factors, such as nutrient interactions and phenotypic transitions, while maintaining focus on the aspects most relevant to the specific research objectives. The chapter also offers a framework for modellers seeking computationally efficient solutions to biofilm problems, demonstrating that critical biofilm dynamics can be isolated and studied in detail without requiring overly complex modelling approaches. These insights suggest that future biofilm research can benefit from this flexibility, particularly when developing real-time biofilm control methods in resource-limited environments or systems requiring rapid computational turnaround. The systematic approach to model simplification provides a blueprint for how researchers might approach the challenge of modelling complex biological systems like biofilms, balancing the need for accuracy with the practicality of computational efficiency. Rather than collapsing the model into a single version, the thesis presents an adaptable framework where various aspects of biofilm behaviour can be isolated or emphasised based on specific research or application needs.

Chapter 3 focused on developing and analysing biofilm growth models in non-antibiotic environments to establish a baseline understanding of the mechanisms driving biofilm formation. This groundwork was essential for later comparing the effects of antibiotics. The chapter examined biofilm growth in relation to nutrient availability, bacterial proliferation, and EPS production, providing a foundation for more complex models that include antibiotic interactions.

The first section introduced Model 11, a simplified framework capturing key biofilm processes such as nutrient diffusion, biomass accumulation, and detachment. This model follows a similar framework to [2]. Results indicated that biofilm thickness is highly sensitive to the balance between bacterial death and growth rates, as well as the detachment rate. Lower death-to-growth ratios led to thicker biofilms, while higher detachment rates thinned biofilms more rapidly, underscoring the importance of mechanical detachment in controlling biofilm structure. The analysis also revealed that higher nutrient availability at the biofilm-bulk fluid interface accelerated growth, leading to faster steady-state biofilm thickness. This finding highlights nutrient supply as a major driver of biofilm development, with implications for controlling biofilm growth through nutrient limitation. These results align with existing literature on nutrient supply as a major driver of biofilm development, suggesting potential avenues for controlling biofilm growth through nutrient limitation.

In the second part, Model 8 added complexity by incorporating EPS production and unsteady bacterial growth. The results showed that nutrient diffusion and consumption rates significantly influenced both biofilm thickness and EPS production. Higher nutrient diffusion led to faster biofilm growth initially, but also caused nutrient depletion in deeper biofilm layers, prompting bacteria to prioritise EPS production for structural stability. This adaptation to nutrient scarcity was an interesting and informative outcome, as it demonstrates biofilms' resilience in maintaining long-term survival despite growth limitations. This finding partially inspired the nutrient dependencies modelled in the next chapter, highlighting how biofilms may shift strategies based on nutrient availability. The findings emphasise the trade-offs between rapid growth and long-term biofilm stability. Higher nutrient diffusion rates promote fast growth but lead to nutrient exhaustion, while slower diffusion fosters more stable, sustained growth. Additionally, the maximal nutrient consumption rate (μ) played a crucial role: higher μ led to rapid bacterial growth followed by nutrient depletion and increased EPS production, while lower μ supported more uniform bacterial growth and less EPS production.

This chapter offered valuable insights into biofilm behaviour in natural environments, providing a framework for predicting biofilm growth under various conditions. These models paved the way for designing interventions, such as limiting nutrient access or altering consumption rates, to manage biofilm growth. This baseline understanding set the stage for future exploration of biofilm responses to external interventions, particularly antibiotics, and supports the development of more effective strategies for biofilm management.

Chapter 4 shifted focus to the complexities of biofilm dynamics under constant antibiotic pressure, introducing two models, Model 5 and Model 3, designed to investigate how biofilms composed of proliferative, persister, and dead bacteria respond to continuous antibiotic exposure and varying nutrient conditions. The goal was to understand how bacterial phenotypes interact under antibiotic stress and how nutrient availability influences biofilm resilience and structural integrity.

Model 5 followed a biofilm modeling framework similar to that in [84], and it produced interesting insights into biofilm composition under antibiotic pressure. A constant concentration of antibiotics significantly affected biofilm growth. Higher antibiotic levels reduced proliferative bacteria and increased dead cells, while the biofilm adapted by relying more on persister cells, which are tolerant to antibiotics. This shift towards persister dominance illustrated the resilience of biofilms, which can survive antibiotic exposure by transitioning to a state of persistence. Even as proliferative cells died, the biofilm persisted, which underscored the challenge of eradicating biofilms with antibiotics alone. Interestingly, the analysis showed that higher antibiotic concentrations led to decreased EPS production, a crucial component for biofilm stability. Lower antibiotic concentrations allowed for more proliferative bacteria and increased EPS production, resulting in thicker, more robust biofilms. This suggested that low antibiotic concentration can allow biofilms to maintain their structural integrity, making them more difficult to eliminate.

Model 3 introduced the novel aspect of nutrient-dependent transition rates between persister and proliferative states, simulating biofilm behavior under variable nutrient conditions. This nutrient dependency offered new perspectives on biofilm adaptation, aligning well with experimental insights [7, 99] but now providing a formal mathematical framework to study these dynamics. In nutrient-rich environments, rapid bacterial proliferation increased the vulnerability of the biofilm to antibiotics, leading to more dead cells. Despite initial growth, nutrient-rich biofilms were more susceptible to collapse under antibiotic treatment due to their dependence on proliferative cells. In contrast, nutrient-poor environments promoted a survival strategy characterised by increased persister cells and EPS production, despite reduced bacterial activity. This highlighted biofilms' adaptability to stress, with nutrient-poor biofilms showing enhanced resistance to antibiotics. This has significant implications for clinical settings, where biofilms in environments with limited nutrients, such as medical implants, are often more resistant to treatments.

By comparing the two models, it became evident that nutrient availability plays a critical role in biofilm dynamics. Model 5, with fixed transition rates, showed a static response to antibiotics, where persister cells ensured biofilm resilience at the cost of reduced thickness. Model 3, with nutrient-dependent transitions, offered a more adaptive biofilm structure. In nutrient-rich conditions, biofilms grew rapidly but were vulnerable to collapse. In nutrient-poor conditions, biofilms shifted towards persistence and structural stability, allowing them to better withstand environmental stressors. The findings emphasised that both antibiotic concentration and nutrient availability are key factors in biofilm behaviour. In nutrient-rich environments, biofilms grew quickly, but were more prone to collapse under antibiotic treatment. In nutrient-poor environments, biofilms adopted a defensive strategy, forming more persister cells and producing more EPS, making them more resistant to environmental stressors.

These insights contribute to understanding biofilm resilience, particularly in challenging environments like medical devices. They suggest that biofilm treatment strategies should account for both antibiotic pressure and nutrient conditions. Combining antibiotics with approaches that limit nutrient access may be more effective in weakening biofilm structures and making them more susceptible to eradication.

Chapter 5 explored the effects of controlled antibiotic release from porous implants on biofilm dynamics, introducing two models, Model 10 and Model 2, and a model exploring initial optimisations of antibiotic delivery strategy, to evaluate the impact of antibiotic delivery, nutrient availability, and bacterial phenotype transitions on biofilm growth. The chapter aimed to understand how controlled antibiotic release interacts with biofilms over time, influencing bacterial survival strategies, biofilm structure, and long-term stability.

Model 10 explored controlled antibiotic delivery in a simplified biofilm setting to establish a clear understanding of the antibiotic release mechanism. This approach of release mechanism aligns with the method in [82]. While controlled antibiotic release initially suppressed biofilm growth, the antibiotic was rapidly depleted, allowing biofilm growth to resume at a comparable rate to the non-antibiotic model (Model 11). If the antibiotic in this model had the additional effect of killing bacterial cells rather than only inhibiting growth, the outcomes might have differed, potentially achieving greater biofilm reduction. Sensitivity analyses revealed that increasing the antibiotic effectiveness rate in a high initial antibiotic concentration loaded in the implant to antibiotic solubility ratio scenario slowed biofilm growth, but did not prevent regrowth after antibiotic exhaustion. This suggests that controlled release alone is insufficient for prolonged biofilm suppression, highlighting the need for sustained antibiotic presence or combination therapies to prevent biofilm resurgence in medical implants.

Model 2 added complexity by incorporating transitions in the bacterial phenotype (proliferative, persistent, and dead bacteria) and the availability of nutrients. In this model, the antibiotic suppresses bacterial growth and increases the number of dead cells. In nutrient-rich environments, biofilm growth accelerated, with more proliferative bacteria and EPS production, but the biofilm became more vulnerable to antibiotics, leading to greater cell death. In contrast, nutrient-poor environments favoured persister cells, resulting in slower growth but greater resilience to antibiotic effects. This model identified five distinct phases of biofilm growth, marking a new insight into biofilm dynamics. Sensitivity analyses revealed that higher nutrient concentrations led to faster transitions through early growth phases, while intermediate nutrient conditions delayed biofilm maturity. Increased ratio of initial antibiotic concentration to the antibiotic solubility, delayed early growth phases but accelerated biofilm stabilisation, indicating that while antibiotics initially slow growth, they can also promote faster biofilm maturity.

The final model explored optimising antibiotic delivery by varying the spatial distribution of antibiotic concentration within the implant. Sensitivity analysis on the parameter, which controls this distribution, showed that concentrating antibiotics near the implant interface resulted in faster initial suppression but rapid depletion, leaving biofilms uncontrolled later. Conversely, distributing the antibiotic farther from the interface led to sustained suppression over time. These findings suggest that spatially optimised antibiotic loading could balance short-term bacterial suppression with long-term biofilm control, offering potential for improved medical device design.

Overall, Chapter 5 highlighted the complexities of biofilm treatment in real-world applications. Although controlled antibiotic release provided initial suppression, it is insufficient for long-term biofilm control without sustained release or adjunct strategies. Biofilms in nutrient-rich environments grew quickly but are more vulnerable to antibiotics, whereas biofilms in nutrient-poor environments were more resistant due to the dominance of persister cells. These insights emphasise the importance of accounting for both nutrient availability and antibiotic distribution when designing treatment strategies for biofilm infections, suggesting that combining antibiotic treatments with approaches like nutrient deprivation or targeting persister cells may improve long-term biofilm control. Furthermore, spatially dependent antibiotic loading offered a promising avenue for optimising antibiotic delivery systems. Together, these models offer a novel mathematical framework bridging the interactions between antibiotic delivery strategies, nutrient availability, and biofilm composition.

6.2 Future work

The research conducted in this thesis has laid the groundwork for several promising directions that could further advance our understanding of biofilm dynamics and optimise antibiotic delivery systems. One critical avenue for future investigation is the refinement of antibiotic spatial distribution within porous implants. The current study demonstrated the potential of spatially dependent antibiotic loading, but further optimisation could be achieved by introducing more complex, multi-gradient distributions of the antibiotic. For example, this could be achieved by defining a multi step-wise function or even an exponential gradient. Such gradients could be tailored to deliver higher concentrations of antibiotics to critical areas of the biofilm, such as the regions near the biofilm-implant interface, while maintaining lower concentrations in other regions to prolong the overall effectiveness of the treatment. This approach could help sustain antibiotic presence over a longer duration.

Furthermore, making the antibiotic release rate spatially variable by designing implants with controlled variations in porosity represents another promising direction. Porosity affects the diffusion of the antibiotic in the implant, and a spatially varying porosity could be used to control antibiotic release kinetics across different regions of the implant. Mathematically, this could be modelled by introducing a spatially variable diffusion coefficient of the antibiotic in the implant medium. By adjusting the porosity and hence the diffusion coefficients in different regions of the implant, faster release could be achieved near the biofilm-implant interface, where immediate antibiotic action is critical, while slower release from areas farther from the interface could provide a sustained supply of the antibiotic over time. This strategy would extend the therapeutic window, maintaining antibiotic efficacy throughout the biofilm growth phases and preventing regrowth after initial suppression. A detailed investigation into the optimal spatial arrangement of porosity and antibiotic concentration could significantly enhance the efficiency of antibiotic delivery systems in implant-related infections. Additionally, the parameters related to the diffusion rate and porosity will need careful calibration to ensure that the antibiotic concentration does not drop too quickly or stay too high for too long, as both scenarios can lead to ineffective biofilm control and could make the biofilm more resilient through adaptation or persister cell formation.

Another potential area of improvement is the introduction of pulse dosing of antibiotics from the implant, which could be a game-changing approach in sustaining the antibiotic's effectiveness over time. In this strategy, the implant could be structured with alternating layers of antibiotics and biodegradable polymers. The antibiotics in the first layer would be released in a controlled manner, followed by a delay as the polymer layer degrades, and then a second layer of antibiotics would be released. This could be modelled by making the initial antibiotic concentration in the implant dependent on both the spatial position and the temporal progression of polymer biodegradation. The biodegradation of the polymer could be modelled using a degradation rate constant, which could be linked to the thickness of the polymer layer and its chemical properties. The antibiotic release would be triggered when the polymer concentration drops below a certain threshold. This would allow for controlled, sequential antibiotic release, effectively creating multiple steps of pulse dosing. However, the parameters governing the timing and dosage of each pulse must be carefully optimised to avoid excessive antibiotic exposure between pulses, which could inadvertently enhance biofilm resilience.

Pulse dosing offers a strategy to counteract the rapid depletion of antibiotics observed in spatially uniform models. By releasing antibiotics in bursts, the biofilm is periodically exposed to high concentrations of antibiotics, preventing bacterial populations from recovering or adapting between doses. This approach could also help to manage bacterial populations at different stages of growth, addressing both proliferative and persister cells more effectively. The multiple steps of pulse dosing would extend the duration of antibiotic exposure and reduce the chances of biofilm regrowth, making it a highly promising method for improving long-term biofilm control.

Another promising direction for future research involves the integration of systemic antibiotic administration, such as oral or intravenous antibiotics, alongside localised delivery from porous implants. This combined therapeutic strategy could offer a more comprehensive approach to biofilm control, as systemic antibiotics would target dispersed bacterial populations and bloodstream infections, while localised antibiotics from the implant would directly address the biofilm at the infection site. The simplest way to include this in our model is to modify the infinite sink boundary condition for the antibiotic at the biofilm-bulk fluid interface (Eq. (5.97)) to a time-dependent Dirichlet condition. This allows us to model the fluctuating concentration of the antibiotic over a specific time period, reflecting the patient's oral intake schedule. For example, instead of setting $C = 0$ at the biofilm-bulk fluid interface ($x = L$) for all time, we can model the concentration as follows: Initially, $C = 0$ for a certain period, but after the oral intake at time

t_{dose} starts, the concentration changes to $C = C_{\text{dose}}$, representing the antibiotic concentration in the fluid stream due to oral intake. This concentration remains until time t_{off}, after which C returns to zero, to model the clearance of the antibiotic. This approach also allows us to introduce multiple oral doses over the course of the treatment. Additionally, we can model the antibiotic concentration in the fluid, $C_{\text{dose}}(t)$, as a time-dependent function to capture the gradual increase and subsequent decrease in concentration, reflecting the pharmacokinetics of the oral antibiotic. Optimising the timing of oral antibiotic administration and cessation can be an effective strategy to improve antibiotic delivery and combat biofilm infections. By carefully tuning the intervals for antibiotic intake and clearance, the antibiotic concentration can be maintained at therapeutic levels during critical periods, maximising its effectiveness while minimising resistance.

Another avenue for future research is the exploration of alternative antibiotics that target different aspects of bacterial physiology. For instance, antibiotics that can affect persister cells or specifically disrupt the EPS matrix could have a significant impact on biofilm resilience. Such treatments could be especially useful during the later phases of biofilm growth when persister cells and EPS contribute to increased biofilm stability and antibiotic resistance. Additionally, combining antibiotics with agents that can disperse biofilm structure or enhance bacterial susceptibility to antibiotics could create a more effective, multipronged approach to biofilm control.

To further enhance the realism and predictive power of biofilm models, future studies should incorporate additional biofilm behaviours, such as quorum-sensing mechanisms, which are known to regulate bacterial communication and biofilm development. Quorum sensing plays a key role in coordinating biofilm growth, and the transition between bacterial phenotypes. Including this mechanism in future models through growth rates and transition rates would provide a deeper understanding of how bacterial communities respond to antibiotic stress, potentially revealing new intervention points for disrupting biofilm stability.

Additionally, future models should account for detachment processes driven by mechanical forces such as shear stress, which can influence biofilm dispersal in clinical settings. In natural environments, biofilms frequently experience detachment due to shear forces from fluid flow, especially in devices such as catheters and stents. Modelling these detachment events would allow for a more dynamic representation of biofilm evolution and resilience, offering insights into how biofilms regrow or spread after partial removal during medical interventions. Although this approach has been modelled in the thesis for simpler biofilm growth models, such as Models 10 and 11, incorporating it into more generalised models such as Model 2 could significantly enhance the design of effective mechanical cleaning or sterilisation protocols. By integrating these dynamics into broader models, we can better simulate real-world conditions and optimise treatment strategies.

Environmental stressors, such as fluctuations in pH, oxygen levels, and other local conditions, should also be explored in future biofilm models. These factors are known to significantly affect biofilm structure and function, particularly in challenging clinical environments like chronic wounds or implanted medical devices. By simulating how biofilms respond to these stressors, we can better understand the conditions that promote biofilm resilience and devise strategies that exploit these vulnerabilities, such as manipulating environmental conditions to weaken biofilm defences before applying antibiotic treatments.

Finally, a major area for future development is the extension of the current models to two or three dimensions. The 1D models used in this thesis have provided valuable insights into biofilm growth and antibiotic diffusion; however, biofilms in real-world scenarios exhibit complex three-dimensional structures that significantly impact nutrient distribution, antibiotic penetration, and bacterial interactions. Extending the model to 2D and 3D would allow exploration of biofilm curvature, shape, and localised growth patterns, which are critical to understanding how biofilms develop in heterogeneous environments. A 3D model could capture key spatial features, such as the formation of mushroom-like biofilm structures, the presence of hollow voids, and the influence of microfluidic flow patterns on antibiotic delivery. These higher-dimensional models would offer a more realistic simulation of biofilm behaviour, providing clearer insights into biofilm resilience and the mechanisms by which antibiotics penetrate or fail to penetrate biofilm matrices.

In conclusion, this thesis represents a significant advancement in our understanding of biofilm dynamics and the potential for optimised antibiotic delivery through porous implants. The models developed herein provide a comprehensive framework for simulating biofilm growth and composition. By systematically exploring the effects of nutrient availability and antibiotic concentration, this research has highlighted the complex interplay between biofilm structure and treatment efficacy. Importantly, the insights gained from this work underscore the critical need for fine-tuned, targeted strategies that balance rapid bacterial suppression with long-term control, avoiding the pitfalls of overexposure that can promote biofilm resilience. Looking ahead, the potential for further optimisation, through more sophisticated spatial antibiotic loading, pulse dosing, or the integration of systemic antibiotics, opens new avenues for improving clinical outcomes. These innovations, combined with future experimental validation and multidimensional modelling, offer a promising path towards more effective and sustainable biofilm management strategies. Ultimately, the work presented in this thesis lays the groundwork for developing advanced patient-specific treatment solutions that have the potential to significantly improve infection control in medical implants and other biofilm-related challenges in clinical settings.

Appendix A

Comparison of biofilm growth models with variable and constant biofilm porosity

This appendix provides a detailed comparison between two biofilm models, one with a variable water volume fraction and the other with a constant water volume fraction, based on the Simplification strategy 1 described in Section. 2.2. The first model, referred to as Model 1, incorporates a dynamic ϕ_{bio}, where the porosity evolves over time and space and this model is described in Section 2.1. The second model, Model 2, assumes a constant ϕ_{bio} and is detailed, along with its formulation and results, in Section 5.2.

The main goal of this appendix is to investigate the differences between biofilm models with a variable versus a constant water volume fraction. By comparing these models under the same conditions, the analysis aims to determine how the assumption of a constant ϕ_{bio} affects predictions related to biofilm growth and bacterial dynamics. A key aim is to assess whether simplifying the model by assuming a constant ϕ_{bio} leads to significant deviations from the more complex variable ϕ_{bio} model, thus guiding the decision on whether this simplification can be adopted without substantial loss of accuracy in further studies.

Outline

The appendix is structured as follows. The first section presents the mathematical framework for the biofilm model with variable ϕ_{bio}, including the governing equations and relevant boundary and initial conditions. The second section simplifies the governing equations using dimensionless variables. In the third section, we address the challenges posed by the two moving boundaries and use the boundary immobilisation method to provide a mathematical solution and enable accurate simulation. The final section contains a detailed comparison of the two models, examining biofilm thickness, velocity of biomass, biomass distribution and nutrient concentration. To ensure a comprehensive analysis, we perform the comparison for three different initial values of the water volume fraction (ϕ_{bio0}), allowing us to evaluate the models across a range of conditions and make an informed decision on whether the simplification to a constant ϕ_{bio} is valid.

A.0.1 Governing equations for Model 1

This section provides a structured mathematical framework for Model 1, as explained in Section 2.1. The framework mirrors that of Model 2 in Section 5.2.2, with the addition of the variable ϕ_{bio}. To avoid redundancy, only the PDE equation for ϕ_{bio} along with its boundary and initial condition are mentioned here, as they differ from Model 2. All other equations remain the same as in Model 2 and are explained in detail in Section 5.2.2.

Following the same concept in [141], the water volume fraction (ϕ_{bio}) will follow an unsteady advection reaction equation.

$$\begin{aligned}
(\phi_{bio})_t + (v\phi_{bio})_x &= \frac{\phi}{1-\phi}\left(\frac{\text{R.H.S. of } B + \text{R.H.S. of } B_p + \text{R.H.S. of } B_d}{\rho_B}\right) \\
&\quad + \frac{\phi}{1-\phi}\left(\frac{\text{R.H.S. of } E}{\rho_E}\right), \\
&= \frac{\phi}{1-\phi}\left(\frac{k_B}{\rho_B} + \frac{k_E}{\rho_E}\right)\frac{\mu\phi_{bio}S}{k_S + \phi_{bio}S}B, \quad 0 < x < L(t),\ t > 0. \qquad \text{(A.1)}
\end{aligned}$$

We have ignored the diffusion terms because they are significantly smaller compared to the reaction terms, allowing us to simplify the calculations without compromising the accuracy of the model.

Initial and boundary conditions

The initial and boundary conditions for this model remain unchanged from Model 2, except for ϕ_{bio}. For a detailed description of the rest of the initial and boundary conditions, refer to Section 5.2.2.

The initial conditions for ϕ_{bio} has been chosen as

$$\phi_{bio}(x,0) = \phi_{bio0}, \quad 0 < x < L(0). \qquad \text{(A.2)}$$

At the implant-biofilm interface, the water volume fraction is governed by a Dirichlet boundary condition at this interface.

$$\phi_{bio} = \phi_{bio0}, \quad \text{at} \quad x = 0,\ t > 0. \qquad \text{(A.3)}$$

Finally, the water volume fraction adhere to a zero-flux condition at the biofilm-bulk fluid interface ($x = L(t)$).

$$(\phi_{bio})_x = 0, \quad \text{at} \quad x = L(t),\ t > 0. \qquad \text{(A.4)}$$

All the parameters used in this model are described with appropriate values in Table. 2.2.

A.0.2 Non-dimensionalisation

We use the same non-dimensional variables as Model 2 in Section. 5.2.3. Only the modified equations for water volume fraction (equation (A.1)) and the initial and boundary conditions (equation (A.2)-(A.4)) have been non-dimensionalised here.

$$(\phi_{bio})_{\bar{t}} + (\bar{v}\phi_{bio})_{\bar{x}} \quad = \quad \frac{\phi}{1-\phi}\left(\frac{k_B}{\bar{\rho}_B} + \frac{k_E}{\bar{\rho}_E}\right)\frac{\mu\phi_{bio}\bar{S}}{k_S + \phi_{bio}\bar{S}}\bar{B}, \quad 0 < \bar{x} < \bar{L}(\bar{t}),\ \bar{t} > 0. \tag{A.5}$$

The dimensionless initial condition is

$$\phi_{bio}(\bar{x}, 0) \quad = \quad \phi_{bio0}, \quad \text{for} \quad 0 < \bar{x} < \bar{L}(0). \tag{A.6}$$

The non-dimensionalised boundary conditions are

$$\phi_{bio} \quad = \quad \phi_{bio0}, \quad \text{at} \quad \bar{x} = 0,\ \bar{t} > 0, \tag{A.7}$$

$$(\phi_{bio})_{\bar{x}} \quad = \quad 0, \quad \text{at} \quad \bar{x} = \bar{L}(\bar{t}),\ \bar{t} > 0. \tag{A.8}$$

The dimensionless parameters for this model are identical to those in Model 2 from Section 5.2.3, with no additional dimensionless parameters introduced.

A.0.3 Boundary immobilisation

To accurately simulate the dynamics of the implant-biofilm interface and the antibiotic release process, we addressed the challenge of managing two moving boundaries in our model. This was accomplished by fixing the domain in the same way as described in Section 5.2.4. Since all the other equations remains the same as in Section 5.2.4, we only apply these transformations to the dimensionless model in Section A.0.2.

$$(\phi_{bio})_{\bar{t}} + \frac{(\bar{v}\phi_{bio})_{\xi}}{\bar{L}} - \frac{\xi}{\bar{L}}\frac{d\bar{L}}{dt}(\phi_{bio})_{\xi} \quad = \quad \frac{\phi}{1-\phi}\left(\frac{k_B}{\bar{\rho}_B} + \frac{k_E}{\bar{\rho}_E}\right)\frac{\mu\phi_{bio}\bar{S}}{k_S + \phi_{bio}\bar{S}}\bar{B}, \quad 0 < \xi < 1,\ \bar{t} > 0. \tag{A.9}$$

The transformed initial condition is as follows

$$\phi_{bio}(\xi, 0) \quad = \quad \phi_{bio0}, \quad \text{for} \quad 0 < \xi < 1. \tag{A.10}$$

Now applying the same transformations to the boundary conditions A.7-A.8 we get

$$\phi_{bio} \quad = \quad \phi_{bio0}, \quad \text{at} \quad \xi = 0,\ \bar{t} > 0, \tag{A.11}$$

$$(\phi_{bio})_{\xi} \quad = \quad 0, \quad \text{at} \quad \xi = 1,\ \bar{t} > 0. \tag{A.12}$$

A.0.4 Results and discussions

Following the methodology outlined in Section 5.2.5, we numerically solve the model using COMSOL. The additional equation for water volume fraction (eq. (A.9)) are handled using the 'General Form PDE' module. All results presented are based on non-dimensionalised variables, with the overline notation omitted from the figures for clarity. To evaluate the impact of different modelling assumptions, we conduct a comparative analysis between two biofilm growth models, Model 1 and Model 2, under controlled antibiotic release conditions. The key difference between the models lies in the treatment of the water volume fraction in the biofilm, ϕ_{bio}, where Model 1 includes an evolution equation for ϕ_{bio} and Model 2 assumes ϕ_{bio} is constant throughout the biofilm. It is important to note that, in Model 2, the value of ϕ_{bio} is fixed at the same initial value ϕ_{bio0} used in Model 1. Additionally, we will consider three different values for ϕ_{bio0}, 0.7, 0.8 and 0.9, to provide a broader perspective on the comparison and ensure that our decision regarding the treatment of ϕ_{bio} is well-informed. This comparison aims to determine whether incorporating the evolution of ϕ_{bio} significantly affects the results. Based on this analysis, we will decide whether to adopt ϕ_{bio} as a constant or variable for all subsequent models in the remainder of the thesis. All baseline parameter values are given in Table 2.2. The total time computed is 10 days unless otherwise stated.

Fig. A.1, A.2. A.3 present a detailed comparison between Model 1 and Model 2. This comparison is made for three different initial water volume fraction values, ϕ_{bio0}, 0.9 (red line), 0.8 (black line) and 0.7 (blue line). The solid lines in each figure represent Model 2, while the dashed lines represent Model 1.

In Fig. A.1(a), which shows the biofilm thickness over time, the dashed and solid lines start almost identically for all three values of ϕ_{bio0}, indicating that both models predict nearly the same biofilm growth behaviour in the early stages. This close agreement suggests that, initially, the constant ϕ_{bio} assumption in Model 2 provides a very accurate approximation of biofilm thickness when compared to the more complex Model 1, where ϕ_{bio} varies over time. As time progresses, slight differences begin to appear between the models. The solid lines generally predict a slightly higher biofilm thickness than the dashed lines, with this discrepancy becoming more noticeable as the value of ϕ_{bio0} increases. At $\phi_{bio0} = 0.9$, the solid line shows a somewhat faster biofilm growth compared to the dashed line. However, these differences are quite modest overall, with the two models showing a similar trend in biofilm growth throughout the simulation. The consistent overlap of the solid and dashed lines at earlier stages, followed by only minor deviations later, suggests that Model 2 is highly effective at approximating biofilm thickness, even under conditions where ϕ_{bio} might be expected to vary.

In Fig. A.1(b), which displays the velocity at the biofilm-bulk fluid interface, the solid and dashed lines are again almost indistinguishable during the initial time period across all ϕ_{bio0} values. This indicates that both models predict nearly identical early-stage velocity behaviour, confirming that the assumption of a constant ϕ_{bio} in Model 2 captures the essential early dy-

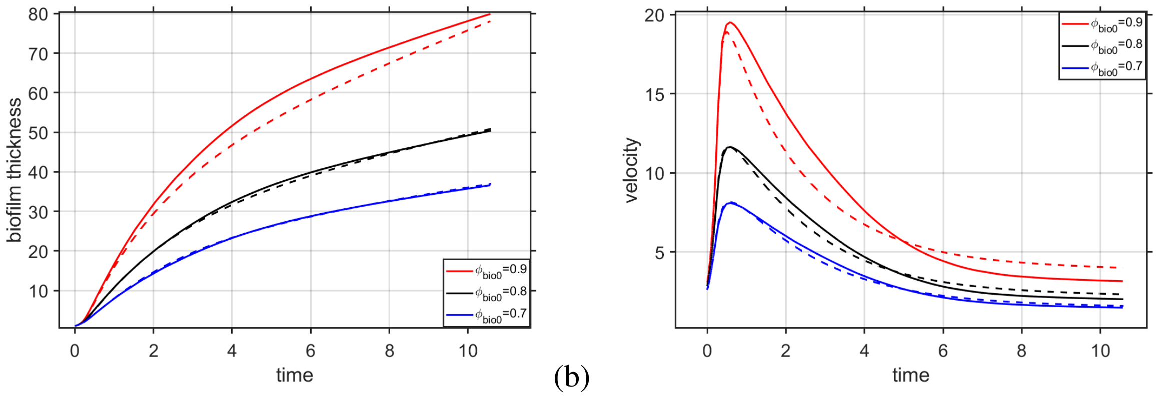

(a) (b)

Figure A.1: Comparison of Model 2 and Model 1, focusing on the temporal variation of (a) biofilm thickness and (b) velocity at the biofilm-bulk fluid interface. The analysis includes three different initial water volume fractions (ϕ_{bio0} = 0.7, 0.8, and 0.9). Solid lines correspond to Model 2 (constant ϕ_{bio}), while dashed lines correspond to Model 1 (variable ϕ_{bio}).

namics of biofilm growth with high accuracy. As time progresses, a slight separation between the lines occurs. The dashed lines begin to rise above the solid lines, suggesting that biofilm growth in Model 1, where ϕ_{bio} varies, proceeds at a slightly faster rate during the later stages of the process. This difference in velocity implies that biofilm growth in Model 1 continues for a longer period before reaching a steady state compared to Model 2. The solid lines show a more rapid decline in velocity. However, even in these later stages, the differences between the two models remain relatively small. The overall trend of decreasing velocity over time is consistent between the models.

The effect of varying ϕ_{bio0} is visible in both Fig. A.1(a) and (b). Higher values of ϕ_{bio0}, lead to faster biofilm growth and higher initial velocities, while lower values of ϕ_{bio0}, correspond to slower biofilm growth and lower initial velocities. This is expected since higher ϕ_{bio0} values correspond to greater initial water content in the biofilm, which accelerates growth and increases fluid interaction. The black lines lie between the blue and red lines, showing intermediate growth rates and velocities. Despite this variation across ϕ_{bio0} values, the differences between the solid and dashed lines remain small, demonstrating that Model 2 provides a close approximation to Model 1 for all ϕ_{bio0} cases.

Overall, the comparison between the the two models regarding biofilm thickness and velocity, demonstrates that while there are some quantitative differences between the models, particularly at later stages and higher ϕ_{bio0} values, these differences are minimal. Both models produce similar qualitative results. The constant ϕ_{bio} assumption in Model 2 does not significantly alter the predictions of biofilm thickness or velocity when compared to the variable ϕ_{bio} approach in Model 1.

In Fig. A.2(a), the total proliferative bacteria concentration over time is plotted for both models. Initially, Model 2 and Model 1 follow nearly the same trajectory for all values of ϕ_{bio0}. This close agreement during the early stages indicates that the assumption of constant

ϕ_{bio} in Model 2 does not significantly affect the short-term dynamics of proliferative bacterial growth. In this phase, the biofilm structure is still forming and the initial conditions dominate the dynamics, leading to similar growth patterns in both models. As time progresses, the dashed lines begin to rise above the solid lines, particularly at the peak of the proliferative bacteria concentration. This behaviour is most prominent for higher initial water volume fractions. The higher peak in Model 1 can be attributed to the evolving ϕ_{bio}, which allows the biofilm to adapt its internal structure, leading to a more favourable environment for bacterial growth. However, after the peak, the difference between the two models begins to shrink. The reason for this convergence is that, after a certain point, the proliferative bacteria begin to die off or transform into persister cells, and both models reach a steady-state decline. Although the dashed lines remain slightly higher, indicating that varying ϕ_{bio} allows for marginally higher bacterial activity, the overall trends remain very similar. This suggests that while Model 1 may predict slightly more proliferative bacteria at its peak, the constant ϕ_{bio} assumption in Model 2 provides an accurate qualitative approximation of the overall dynamics.

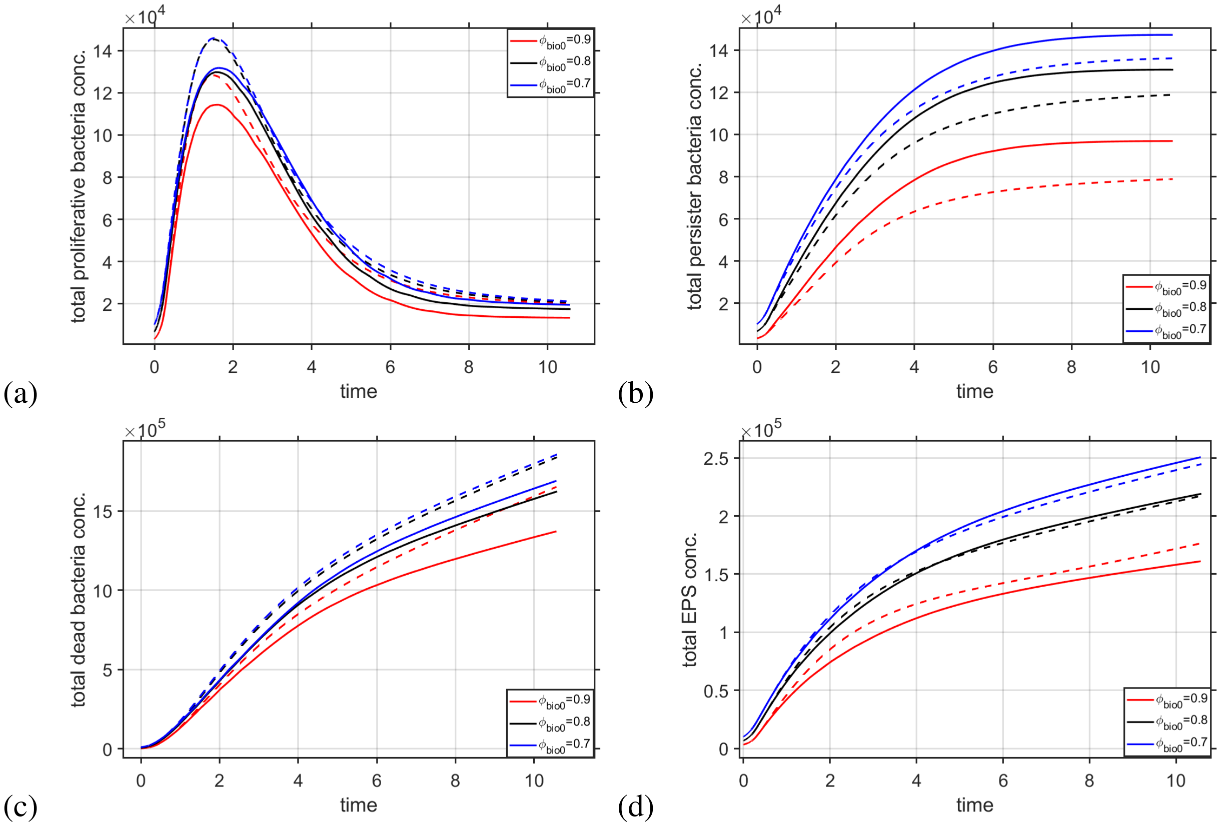

Figure A.2: Comparison of Model 2 and Model 1, focusing on the temporal variation of total concentrations of (a) proliferative bacteria, (b)persister bacteria, (c)dead bacteria and (d) EPS. The analysis includes three different initial water volume fractions (ϕ_{bio0} = 0.7, 0.8, and 0.9). Solid lines correspond to Model 2 (constant ϕ_{bio}), while dashed lines correspond to Model 1 (variable ϕ_{bio}).

In Fig. A.2(b), the total persister bacteria concentration is plotted over time. Similarly to

Fig. A.2(a), the solid and dashed lines almost overlap in the initial stages across all ϕ_{bio0} values, indicating that both models predict comparable early-stage behaviour for persister bacteria. This consistency again stems from the fact that the early biofilm dynamics is largely governed by the initial conditions, and both models begin from distinct but highly similar starting points. As time progresses, the solid lines gradually rise above the dashed lines, indicating that the constant ϕ_{bio} assumption leads to a slightly higher accumulation of persister bacteria in the later stages of biofilm development. This behaviour can be explained by the different growth environments provided by the two models. In Model 2, where ϕ_{bio} is constant, the structure within the biofilm is more stable, allowing for the continuous growth of persister cells over time. In contrast, the evolving ϕ_{bio} in Model 1 likely introduces fluctuations that slightly hinder persister cell accumulation. This trend is most pronounced for higher ϕ_{bio0} values, where the solid lines diverge more from the dashed lines. However, despite this divergence, the overall pattern remains the same, with both models predicting a steady increase in persister bacteria concentration. The minor differences in magnitude do not significantly alter the general biofilm behaviour, justifying the use of Model 2 in cases where computational efficiency is prioritised.

Fig. A.2(c) shows the total dead bacteria concentration as a function of time. Both models produce nearly identical results during the early stages, indicating that the initial dynamics of dead bacteria accumulation are similar regardless of whether ϕ_{bio} is treated as variable or constant. This similarity occurs because the biofilm is still in its initial stages and cell death rates are relatively low during this time. As the biofilm matures, the dashed lines begin to rise above the solid lines, especially for higher ϕ_{bio0} values. This indicates that the variable ϕ_{bio} in Model 1 leads to a slightly faster accumulation of dead bacteria. The evolving biofilm structure in Model 1 allows for more cell death, as it can create conditions in which proliferative bacteria are less able to survive over time, leading to a higher death rate. In contrast, Model 2, with its stable ϕ_{bio}, supports a more gradual accumulation of dead bacteria. However, while Model 1 predicts slightly higher concentrations of dead bacteria, the overall trends between the two models remain very similar. Both show a steady rise in dead bacteria concentration over time, with only minor differences in magnitude. These results reinforce the idea that the constant ϕ_{bio} assumption in Model 2 is an acceptable approximation, as the differences in predicted dead bacteria concentrations are not large enough to significantly affect the dynamics of the biofilm.

In Fig. A.2(d), the total EPS concentration is plotted as a function of time. Both models produce nearly identical results during the early stages of biofilm development, reflecting similar short-term predictions for EPS production. As time progresses, the dashed lines rise above the solid lines, indicating that the variable ϕ_{bio} in Model 1 leads to slightly faster accumulation of EPS, particularly for higher ϕ_{bio0} values. This can be attributed to the evolving nature of ϕ_{bio} in Model 1, which creates a more dynamic environment conducive to higher EPS production. EPS plays a critical role in maintaining the structure of the biofilm and promoting cell adhesion, and the variable ϕ_{bio} in Model 1 enhances these processes. However, an interesting behaviour occurs for lower ϕ_{bio0} values ($\phi_{bio0} = 0.7$ and 0.8). After a certain point, the solid lines rise above the dashed lines, indicating that, in these cases, the constant ϕ_{bio} assumption in Model 2 supports more EPS production in the later stages of biofilm growth. Nonetheless, the differences between the models are small, and both follow the same general trends, with a steady increase in EPS concentration over time. This further supports the idea that Model 2 is a valid approximation, even when predicting EPS production.

The initial water volume fraction (ϕ_{bio0}) has a significant effect on the total concentrations of proliferative, persister, and dead bacteria, as well as EPS. For Fig. A.2, which represent the total concentrations of proliferative bacteria, persister bacteria, dead bacteria, and EPS respectively, lowest ϕ_{bio0} leads to the highest concentrations of these components over time for both the models, followed by $\phi_{bio0} = 0.8$, and finally $\phi_{bio0} = 0.9$ (red lines), which yields the lowest concentrations. This behaviour can be explained by the relationship between water volume fraction and the initial concentration of bacteria and EPS in the biofilm. When the water volume fraction is low, the biofilm is denser, containing more bacteria and EPS. This higher initial bacterial concentration in a denser biofilm leads to faster accumulation of proliferative, persister, and dead bacteria as well as EPS over time. The denser biofilm structure helps retain these components, allowing them to accumulate more effectively. Cells proliferate rapidly, more EPS is produced, and dead cells accumulate within the biofilm, resulting in higher concentrations over time. In contrast, with a higher water volume fraction, the initial concentration of bacteria and EPS is lower because the biofilm has more water and less solid biomass. This dilutes the biofilm, allowing bacteria and EPS to spread out, leading to a slower rate of accumulation over time. Since the bacteria start from a lower base concentration, it takes longer for the biofilm to build up similar concentrations of these components. Thus, biofilms with lower water volume fractions tend to retain more bacteria and EPS over time, leading to higher overall concentrations, while biofilms with higher water volume fractions have more dispersed components and slower accumulation, resulting in lower concentrations.

In Fig. A.3(a), the total nutrient concentration over time is shown. Initially, the values for Model 1 and Model 2 overlap, indicating that both models predict nearly identical nutrient dynamics in the early stages of biofilm growth. However, as time progresses, a key divergence emerges. The solid lines rise above the dashed lines for each ϕ_{bio0} case, particularly for higher ϕ_{bio0} values. This indicates that the constant ϕ_{bio} assumption in Model 2 allows for a more sustained nutrient consumption within the biofilm over time. The lower nutrient concentrations predicted by Model 1 could be due to the evolving biofilm structure including higher proliferative bacteria, which may allow for faster nutrient consumption compared to the more stable biofilm in Model 2. This difference becomes more pronounced as ϕ_{bio0} increases, with the $\phi_{bio0} = 0.9$ case showing the largest discrepancy. Despite this, the general upward trend remains consistent between the two models, suggesting that both capture the essential nutrient dynamics, even though Model 2 predicts a higher total nutrient concentration as time progresses.

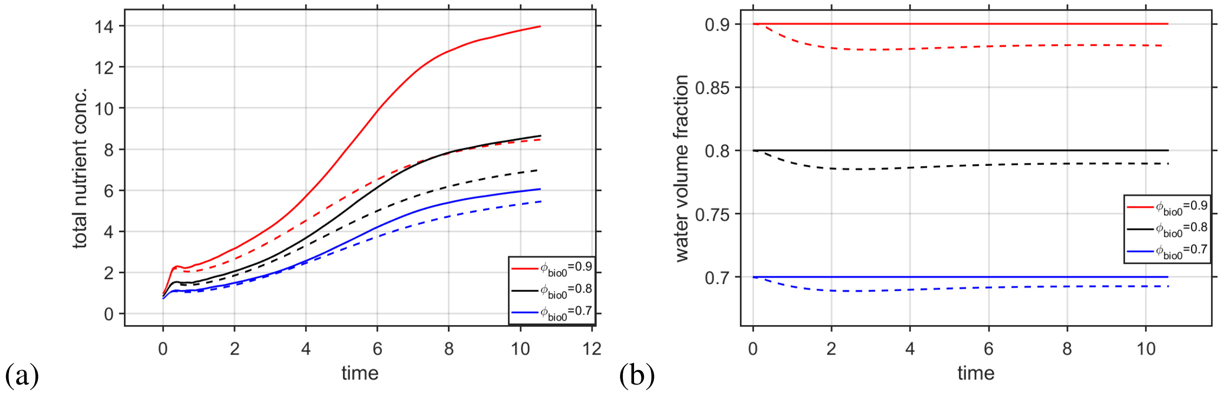

Figure A.3: Comparison of Model 2 and Model 1, focusing on the temporal variation of (a) the total nutrient concentrations and (b) water volume fraction at the biofilm-bulk fluid interface. The analysis includes three different initial water volume fractions (ϕ_{bio0} = 0.7, 0.8, and 0.9). Solid lines correspond to Model 2 (constant ϕ_{bio}), while dashed lines correspond to Model 1 (variable ϕ_{bio}).

In Fig. A.3(b), the water volume fraction (ϕ_{bio}) is plotted over time at the biofilm-bulk fluid interface. In Model 2, ϕ_{bio} is constant by definition, so the solid lines remain flat at their initial values. For Model 1, ϕ_{bio} is allowed to vary over time. In the early stages, the dashed lines drop slightly before stabilising, indicating that the water content of the biofilm initially decreases as the bacterial cells grow and the biofilm consolidates. This slight fluctuation is more pronounced for higher ϕ_{bio0} values, but it remains small overall. In later stages, ϕ_{bio} stabilises near its initial value in Model 1, demonstrating that the dynamic variation in the water volume fraction is relatively minor. This further supports the use of the constant ϕ_{bio} assumption in Model 2, as the differences between the two models are minimal.

The comparison across Fig. A.2 and A.3 illustrates that while there are small differences between Model 1 and Model 2, particularly in the later stages of biofilm development and for higher ϕ_{bio0} values, these differences are not significant enough to alter the overall trends. Both models predict similar qualitative dynamics for bacterial concentrations, EPS production, nutrient uptake, and water volume fraction.

In Fig. A.4(a), the proliferative bacteria concentration across biofilm at the final time is compared between the two models. Model 2 show a relatively uniform distribution of proliferative bacteria across the biofilm, although slightly increasing towards the biofilm-bulk fluid interface. This uniformity indicates that the constant water volume fraction assumption in Model 2 supports a stable environment throughout the biofilm, leading to minimal spatial variation in proliferative bacteria concentration. Conversely, for Model 1, there is a clear gradient of proliferative bacteria across the biofilm thickness. Notably, the dashed lines are higher near the biofilm-bulk fluid interface, particularly for higher ϕ_{bio0} values. This indicates that the evolving ϕ_{bio} enhances bacterial growth in regions closer to the biofilm surface. The biofilm-bulk fluid interface provides a more favourable environment due to increased nutrient availability and less competition for space, which results in higher bacterial proliferation. However, deeper in the biofilm, closer to the implant-biofilm interface, the proliferative bacteria concentration decreases and the dashed lines fall below the solid lines. This suggests that the evolving ϕ_{bio} creates a less favourable environment in these regions, potentially due to reduced nutrient penetration, and higher competition for resources. In Model 2, the constant ϕ_{bio} ensures that proliferative bacteria concentrations are sustained even in the deeper layers, which results in a more uniform distribution compared to the notable spatial variation seen in Model 1. This behaviour, where the solid line is higher in deeper regions and the dashed line is higher near the surface, is consistent across all ϕ_{bio0} values. Despite these differences in bacterial distribution between the two models, the overall trends remain quite similar, with both models showing the expected increase in bacterial concentration near the biofilm surface and comparable final distributions.

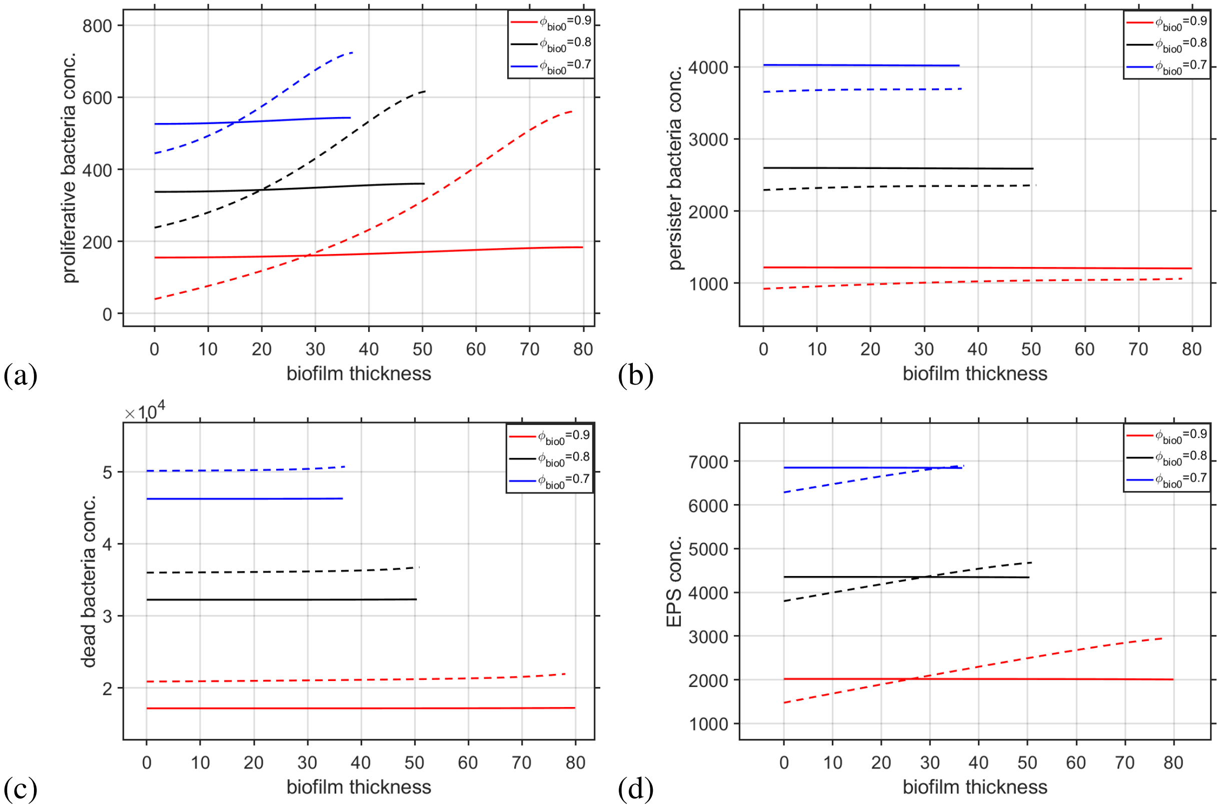

Figure A.4: Comparison of Model 2 and Model 1, focusing on the spatial variation of the concentrations of (a) proliferative bacteria, (b)persister bacteria, (c)dead bacteria and (d) EPS. The analysis includes three different initial water volume fractions (ϕ_{bio0} = 0.7, 0.8, and 0.9). Solid lines correspond to Model 2 (constant ϕ_{bio}), while dashed lines correspond to Model 1 (variable ϕ_{bio}).

In Fig. A.4(b), the persister bacteria concentration across biofilm thickness is depicted. Unlike proliferative bacteria, the distribution of persister cells is fairly uniform across the biofilm for both models, which is consistent with the idea that persister cells are more dormant and less dependent on local environmental conditions than proliferative cells. However, in Model 2 the concentration is consistently higher than that of Model 1 for all ϕ_{bio0} cases. This suggests that the constant ϕ_{bio} assumption in Model 2 leads to a more conducive environment for the accumulation of persister cells. The uniform and stable water volume fraction in Model 2 provides steady conditions throughout the biofilm, which may allow more bacteria to transition into the persister state and survive longer. On the other hand, in Model 1, the variable ϕ_{bio} introduces fluctuations that slightly reduce the number of persister cells across the biofilm. Despite the slightly higher persister bacteria concentration in Model 2, both models predict almost identical distributions of persister cells, showing that the constant ϕ_{bio} assumption in Model 2 yields a very similar outcome to the more complex Model 1.

In Fig. A.4(c), the dead bacteria concentration across biofilm thickness is shown. Both models predict an almost flat distribution of dead bacteria across the biofilm, with a slight increase around the biofilm-bulk fluid interface, indicating that bacterial death rates are relatively uniform across the thickness, regardless of the spatial point in the biofilm. This aligns with the expectation that as biofilm growth stabilises, dead cell accumulation reaches a steady state throughout the structure. However, a noticeable difference is that the dashed lines are higher than the solid lines for all ϕ_{bio0} cases. This indicates that the evolving ϕ_{bio} in Model 1 results in a higher accumulation of dead bacteria. This outcome could be due to the less stable environment in Model 1, where the variable water volume fraction can create localised conditions of stress, nutrient limitation, or increased bacterial competition, leading to higher death. The dynamic nature of ϕ_{bio} in Model 1 might reduce the capacity for bacterial populations to survive long-term, thus increasing the dead cell count. On the other hand, the constant ϕ_{bio} in Model 2 results in a more stable and predictable environment, leading to a lower accumulation of dead bacteria. While the exact number of dead cells is higher in Model 1, both models show similar profiles and trends in bacterial death across biofilm thickness, confirming that Model 2 is still an effective approximation.

In Fig. A.4(d), the EPS concentration across biofilm thickness is plotted. EPS plays a crucial role in maintaining biofilm structure, as it provides the matrix that holds the biofilm together and protects the bacterial cells. Both models predict an increase through biofilm thickness in EPS concentration. The concentration for Model 2 is generally higher than that of Model 1 across most of the biofilm, suggesting that the constant ϕ_{bio} assumption in Model 2 supports higher EPS production. The stable water content in Model 2 likely allows for more continuous EPS synthesis, leading to higher concentrations throughout most of the biofilm. In contrast, the dynamic ϕ_{bio} in Model 1 introduces fluctuations that may reduce EPS production in some areas, leading to lower overall concentrations. However, around the biofilm-bulk fluid interface, the dashed lines cross the solid lines and become higher. This crossing occurs deeper into the biofilm as ϕ_{bio0} increases. This behaviour suggests that the evolving ϕ_{bio} in Model 1 promotes higher EPS production near the biofilm surface, where conditions may be more favourable for EPS synthesis. The variable ϕ_{bio} could lead to localised increases in bacterial activity and EPS secretion in these regions. Despite the crossover near the biofilm surface, both models show similar trends and magnitudes for EPS production, confirming that Model 2 is a strong approximation for biofilm matrix formation.

In Fig. A.5(a), the nutrient concentration is plotted across the biofilm thickness. Nutrient diffusion from the bulk fluid into the biofilm is a critical factor in biofilm growth, and both models show steep nutrient gradients, with the highest concentrations near the biofilm-bulk fluid interface and progressively lower concentrations deeper into the biofilm. The solid lines are generally higher than the dashed lines at any spatial point in the biofilm for most ϕ_{bio0} cases. This indicates that the constant ϕ_{bio} assumption supports a more sustained and uniform nutrient consumption within the biofilm. This can be validated by the uniform spatial behaviour of proliferative bacteria for Model 2. In Model 1, the dynamic ϕ_{bio} may result in more efficient nutrient consumption or transport, leading to slightly lower nutrient concentrations throughout the biofilm. However, for the highest ϕ_{bio0} value, the dashed line crosses the solid line and becomes slightly higher near the biofilm-bulk fluid interface. This suggests that the evolving ϕ_{bio} enhances nutrient consumption in regions near the surface for higher water content environments. Nevertheless, for the majority of the biofilm thickness, the nutrient concentration remains higher in Model 2, reinforcing the stability of nutrient distribution in the constant ϕ_{bio} model. Although Model 1 slightly enhances nutrient availability near the surface for higher ϕ_{bio0}, both models exhibit comparable nutrient gradients, validating the accuracy of Model 2 in simulating nutrient uptake.

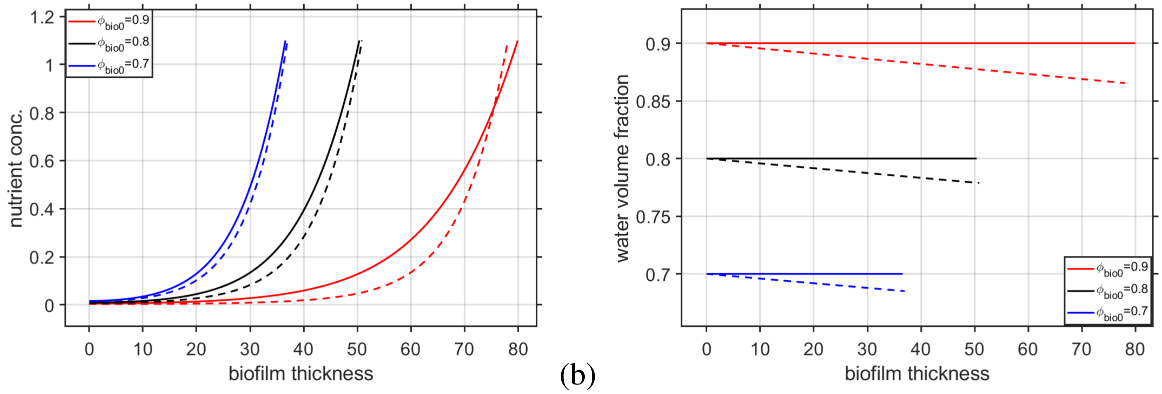

(a) (b)

Figure A.5: Comparison of Model 2 and Model 1, focusing on the spatial variation of (a) the nutrient concentration and (b) water volume fraction final time. The analysis includes three different initial water volume fractions (ϕ_{bio0} = 0.7, 0.8, and 0.9). Solid lines correspond to Model 2 (constant ϕ_{bio}), while dashed lines correspond to Model 1 (variable ϕ_{bio}).

In Fig. A.5(b), the water volume fraction (ϕ_{bio}) is shown across the biofilm thickness. As expected, for Model 2 it remains constant across the biofilm thickness, reflecting the assumption that the water content is uniform throughout the biofilm in this model. In Model 1, the water volume fraction decreases through the biofilm, maintaining the lowest water volume fraction at the biofilm-bulk fluid interface. This decrease is more pronounced for higher ϕ_{bio0} values.

This behaviour can be attributed to the fact that higher concentrations of bacteria and EPS near the biofilm surface occupy more space within the biofilm matrix, thereby reducing the available water content in these regions. The dynamic nature of ϕ_{bio} in Model 1 allows for localised reductions in water content where bacterial growth and EPS production are highest. Despite the slight drop in water volume fraction in Model 1, the overall similarity in water distribution across biofilm thickness in both models strongly supports the validity of Model 2.

The comparison across Fig. A.4 and A.5 illustrates that while there are small differences between Model 1 and Model 2, particularly in the distribution of proliferative bacteria, EPS, and nutrients across the biofilm thickness, these differences are not significant enough to alter the overall trends. Both models predict similar qualitative dynamics for bacterial concentrations, EPS distribution, nutrient uptake, and water volume fraction. The constant ϕ_{bio} assumption in Model 2 proves to be a reasonable and computationally efficient alternative to the more complex Model 1, and can be confidently used for subsequent analysis without sacrificing accuracy.

A.0.5 Summary

This chapter provides a thorough comparison between two biofilm models, Model 1, which uses a variable water volume fraction (ϕ_{bio}) that evolves over time and space, and Model 2, which assumes a constant ϕ_{bio}. The key objective of this comparison was to assess whether the simpler Model 2 can reproduce the results of Model 1 with sufficient accuracy, thereby allowing the use of a constant ϕ_{bio} without compromising the model's reliability or predictive power.

The comparison focused on critical biofilm characteristics, including biofilm thickness, the concentrations of proliferative, persister, and dead bacteria, nutrient concentration, and EPS distribution. Across all these metrics, Model 2 consistently produced results that matched qualitatively those of Model 1.

For biofilm thickness, both models showed nearly identical predictions during the early stages of growth. Over time, small differences appeared, with Model 2 predicting slightly faster growth, particularly for higher initial water volume fractions (ϕ_{bio0}). However, these differences were minor, and the overall growth trends in both models were nearly indistinguishable. Regarding bacterial dynamics, both models predicted very similar behaviour. For proliferative bacteria, Model 1, with its evolving ϕ_{bio}, showed slightly higher concentrations near the biofilm-bulk fluid interface, while Model 2 predicted a more uniform distribution throughout the biofilm. Despite this difference, the overall trends were consistent. For persister bacteria, the two models produced almost identical results, with only minimal variation. Dead bacteria concentrations were also very similar between the two models, with Model 1 showing a slightly higher concentration, but not to a degree that would significantly alter the model's predictions. In terms of nutrient concentration, both models exhibited similar spatial profiles, with nutrient levels decreasing as one moved deeper into the biofilm. Model 2 predicted slightly higher nutrient concentrations throughout, but this difference did not affect the overall behaviour of the system. The distribution of EPS followed a similar pattern, both models predicted increasing EPS concentrations through the biofilm, with Model 1 showing slightly higher EPS near the biofilm-bulk fluid interface.

For the water volume fraction, as expected, Model 2 showed a constant ϕ_{bio} throughout the time and space. In contrast, Model 1 showed a slight decrease near the biofilm-bulk fluid interface as the biofilm developed and also a slight decrease over time, particularly for higher initial values. This decrease reflected the increase in bacterial and EPS content, which slightly reduced the available water volume. However, the variation was small, and the overall water distribution remained close to its initial value, confirming that the constant ϕ_{bio} assumption in Model 2 closely approximated the behaviour observed in Model 1.

In conclusion, this chapter demonstrates that Model 2, with its constant ϕ_{bio}, can accurately replicate the results of the more complex Model 1 across all key biofilm characteristics. The small differences observed between the models are negligible and do not significantly affect the overall trends or predictions. This analysis supports the conclusion that Model 2 can be confidently used in future studies without losing important model attributes.

Bibliography

[1] C. Abad and A. Haleem. Prosthetic joint infections: an update. *Current Infectious Disease Reports*, 20:1–13, 2018.

[2] F. Abbas, R. Sudarsan, and H. J. Eberl. Longtime behavior of one-dimensional biofilm models with shear dependent detachment rates. *Mathematical Biosciences & Engineering*, 9(2):215, 2012.

[3] R. D. Acemel, F. Govantes, and A. Cuetos. Computer simulation study of early bacterial biofilm development. *Scientific Reports*, 8(1):1–9, 2018.

[4] U. Ahmed and K. Vafai. Analysis of biofilm growth in the presence of osmotic pressure and temperature effects. *International Journal of Heat and Mass Transfer*, 55(21-22):5709–5721, 2012.

[5] E. Alpkvist, C. Picioreanu, M. C. Van Loosdrecht, and A. Heyden. Three-dimensional biofilm model with individual cells and continuum eps matrix. *Biotechnology and Bioengineering*, 94(5):961–979, 2006.

[6] E. Alpkvista and I. Klapper. A multidimensional multispecies continuum model for heterogeneous biofilm development. *Bulletin of Mathematical Biology*, 69:765–789, 2007.

[7] S. M. Amato and M. P. Brynildsen. Nutrient transitions are a source of persisters in escherichia coli biofilms. *PloS One*, 9(3):e93110, 2014.

[8] K. Anguige, J. King, and J. Ward. Modelling antibiotic-and anti-quorum sensing treatment of a spatially-structured pseudomonas aeruginosa population. *Journal of Mathematical Biology*, 51:557–594, 2005.

[9] K. Anguige, J. King, and J. Ward. A multi-phase mathematical model of quorum sensing in a maturing pseudomonas aeruginosa biofilm. *Mathematical Biosciences*, 203(2):240–276, 2006.

[10] C. R. Arciola, D. Campoccia, and L. Montanaro. Implant infections: adhesion, biofilm formation and immune evasion. *Nature Reviews Microbiology*, 16(7):397–409, 2018.

[11] B. Atkinson and I. Davies. The overall rate of substrate uptake (reaction) by microbial films. part i-a biological rate equation. *Trans. Inst. Chem. Eng*, 52:260–268, 1974.

[12] B. P. Ayati and I. Klapper. A multiscale model of biofilm as a senescence-structured fluid. *Multiscale Modeling & Simulation*, 6(2):347–365, 2007.

[13] L. Bacakova, E. Filova, M. Parizek, T. Ruml, and V. Svorcik. Modulation of cell adhesion, proliferation and differentiation on materials designed for body implants. *Biotechnology Advances*, 29(6):739–767, 2011.

[14] E. Ben-Jacob, O. Schochet, A. Tenenbaum, I. Cohen, A. Czirok, and T. Vicsek. Generic modelling of cooperative growth patterns in bacterial colonies. *Nature*, 368(6466):46–49, 1994.

[15] R. Bernardes, J. A. Ferreira, M. Grassi, M. Nhangumbe, and P. de Oliveira. Fighting opportunistic bacteria in drug delivery medical devices. *SIAM Journal on Applied Mathematics*, 79(6):2456–2478, 2019.

[16] H. Beyenal, S. N. Chen, and Z. Lewandowski. The double substrate growth kinetics of pseudomonas aeruginosa. *Enzyme and Microbial Technology*, 32(1):92–98, 2003.

[17] H. Beyenal and Z. Lewandowski. Modeling mass transport and microbial activity in stratified biofilms. *Chemical Engineering Science*, 60(15):4337–4348, 2005.

[18] J. Bigger et al. Treatment of staphyloeoeeal infections with penicillin by intermittent sterilisation. *Lancet*, pages 497–500, 1944.

[19] N. Billings, A. Birjiniuk, T. S. Samad, P. S. Doyle, and K. Ribbeck. Material properties of biofilms—a review of methods for understanding permeability and mechanics. *Reports on Progress in Physics*, 78(3):036601, 2015.

[20] M. Böl, A. E. Ehret, A. Bolea Albero, J. Hellriegel, and R. Krull. Recent advances in mechanical characterisation of biofilm and their significance for material modelling. *Critical reviews in biotechnology*, 33(2):145–171, 2013.

[21] M. Böl, R. B. Möhle, M. Haesner, T. R. Neu, H. Horn, and R. Krull. 3d finite element model of biofilm detachment using real biofilm structures from clsm data. *Biotechnology and Bioengineering*, 103(1):177–186, 2009.

[22] S. Bottero, T. Storck, T. J. Heimovaara, M. C. van Loosdrecht, M. V. Enzien, and C. Picioreanu. Biofilm development and the dynamics of preferential flow paths in porous media. *Biofouling*, 29(9):1069–1086, 2013.

[23] A. Braem, L. Van Mellaert, T. Mattheys, D. Hofmans, E. De Waelheyns, L. Geris, J. Anné, J. Schrooten, and J. Vleugels. Staphylococcal biofilm growth on smooth and porous titanium coatings for biomedical applications. *Journal of Biomedical Materials Research Part A: An Official Journal of The Society for Biomaterials, The Japanese Society for Biomaterials, and The Australian Society for Biomaterials and the Korean Society for Biomaterials*, 102(1):215–224, 2014.

[24] J. D. Bryers. Biofilm formation and chemostat dynamics: pure and mixed culture considerations. *Biotechnology and Bioengineering*, 26(8):948–958, 1984.

[25] K. Bush, P. Courvalin, G. Dantas, J. Davies, B. Eisenstein, P. Huovinen, G. A. Jacoby, R. Kishony, B. N. Kreiswirth, E. Kutter, et al. Tackling antibiotic resistance. *Nature Reviews Microbiology*, 9(12):894–896, 2011.

[26] C. A. Chapman, E. A. Cuttaz, J. A. Goding, and R. A. Green. Actively controlled local drug delivery using conductive polymer-based devices. *Applied physics letters*, 116(1), 2020.

[27] N. Cogan. Effects of persister formation on bacterial response to dosing. *Journal of theoretical biology*, 238(3):694–703, 2006.

[28] N. Cogan and J. P. Keener. The role of the biofilm matrix in structural development. *Mathematical Medicine and Biology*, 21(2):147–166, 2004.

[29] S. Cometta, D. W. Hutmacher, and L. Chai. In vitro models for studying implant-associated biofilms-a review from the perspective of bioengineering 3d microenvironments. *Biomaterials*, page 122578, 2024.

[30] J. W. Costerton, Z. Lewandowski, D. E. Caldwell, D. R. Korber, and H. M. Lappin-Scott. Microbial biofilms. *Annual Review of Microbiology*, 49(1):711–745, 1995.

[31] M. Crouzet, C. Le Senechal, V. S. Brözel, P. Costaglioli, C. Barthe, M. Bonneu, B. Garbay, and S. Vilain. Exploring early steps in biofilm formation: set-up of an experimental system for molecular studies. *BMC microbiology*, 14:1–12, 2014.

[32] E. L. Cussler. *Diffusion: mass transfer in fluid systems*. Cambridge university press, 2009.

[33] B. D'ACUNTO, L. Frunzo, V. Luongo, and M. R. Mattei. Invasion moving boundary problem for a biofilm reactor model. *European Journal of Applied Mathematics*, 29(6):1079–1109, 2018.

[34] B. D'Acunto, L. Frunzo, and M. Mattei. Qualitative analysis of the moving boundary problem for a biofilm reactor model. *Journal of Mathematical Analysis and Applications*, 438(1):474–491, 2016.

[35] B. Daşbaşı and İ. Öztürk. Mathematical modelling of bacterial resistance to multiple antibiotics and immune system response. *SpringerPlus*, 5:1–17, 2016.

[36] M. E. Davey and G. A. O'toole. Microbial biofilms: from ecology to molecular genetics. *Microbiology and molecular biology reviews*, 64(4):847–867, 2000.

[37] D. Davies. Understanding biofilm resistance to antibacterial agents. *Nature Reviews Drug Discovery*, 2(2):114–122, 2003.

[38] D. De Beer, R. Srinivasan, and P. S. Stewart. Direct measurement of chlorine penetration into biofilms during disinfection. *Applied and Environmental Microbiology*, 60(12):4339–4344, 1994.

[39] I. De-la Pinta, M. Cobos, J. Ibarretxe, E. Montoya, E. Eraso, T. Guraya, and G. Quindós. Effect of biomaterials hydrophobicity and roughness on biofilm development. *Journal of Materials Science: Materials in Medicine*, 30:1–11, 2019.

[40] R. Dillon, L. Fauci, A. Fogelson, and D. Gaver III. Modeling biofilm processes using the immersed boundary method. *Journal of Computational Physics*, 129(1):57–73, 1996.

[41] B. D'Acunto and L. Frunzo. Qualitative analysis and simulations of a free boundary problem for multispecies biofilm models. *Mathematical and Computer Modelling*, 53(9-10):1596–1606, 2011.

[42] B. D'Acunto, L. Frunzo, and M. R. Mattei. Moving boundary problem for the detachment in multispecies biofilms. *Ricerche di Matematica*, 67(2):683–698, 2018.

[43] H. Eberl, E. Morgenroth, D. Noguera, C. Picioreanu, B. Rittmann, M. van Loosdrecht, and O. Wanner. *Mathematical modeling of biofilms*. International Water Association Publications, 2006.

[44] H. Eberl, C. Picioreanu, J. Heijnen, and M. Van Loosdrecht. A three-dimensional numerical study on the correlation of spatial structure, hydrodynamic conditions, and mass transfer and conversion in biofilms. *Chemical Engineering Science*, 55(24):6209–6222, 2000.

[45] H. J. Eberl, D. F. Parker, and M. C. Van Loosdrecht. A new deterministic spatio-temporal continuum model for biofilm development. *Computational and Mathematical Methods in Medicine*, 3(3):161–175, 2001.

[46] F. El Moustaid, A. Eladdadi, and L. Uys. Modeling bacterial attachment to surfaces as an early stage of biofilm development. *Mathematical Biosciences & Engineering*, 10(3):821, 2013.

[47] M. Erkihun, Z. Asmare, K. Endalamew, B. Getie, T. Kiros, and A. Berhan. Medical scope of biofilm and quorum sensing during biofilm formation: Systematic review. *Bacteria*, 3(3):118–135, 2024.

[48] A. Fayzullin, A. Bakulina, K. Mikaelyan, A. Shekhter, and A. Guller. Implantable drug delivery systems and foreign body reaction: Traversing the current clinical landscape. *Bioengineering*, 8(12):205, 2021.

[49] J. A. Ferreira, P. de Oliveira, P. M. da Silva, and M. Grassi. From life-saving to life-threatening: A mathematical model to simulate bacterial infections in surgical procedures. *SIAM Journal on Applied Mathematics*, 81(3):1226–1247, 2021.

[50] H.-C. Flemming and J. Wingender. The biofilm matrix. *Nature reviews microbiology*, 8(9):623–633, 2010.

[51] M. R. Frederick, C. Kuttler, B. A. Hense, and H. J. Eberl. A mathematical model of quorum sensing regulated eps production in biofilm communities. *Theoretical Biology and Medical Modelling*, 8:1–29, 2011.

[52] V. Fröjd, L. Chávez de Paz, M. Andersson, A. Wennerberg, J. Davies, and G. Svensäter. In situ analysis of multispecies biofilm formation on customized titanium surfaces. *Molecular Oral Microbiology*, 26(4):241–252, 2011.

[53] V. Fröjd, V. Franke-Stenport, L. Meirelles, and A. Wennerberg. Increased bone contact to a calcium-incorporated oxidized commercially pure titanium implant: an in-vivo study in rabbits. *International journal of Oral and Maxillofacial Surgery*, 37(6):561–566, 2008.

[54] H. Fujikawa. Diversity of the growth patterns of bacillus subtilis colonies on agar plates. *FEMS microbiology ecology*, 13(3):159–167, 1994.

[55] H. J. Gaebler and H. J. Eberl. A simple model of biofilm growth in a porous medium that accounts for detachment and attachment of suspended biomass and their contribution to substrate degradation. *European Journal of Applied Mathematics*, 29(6):1110–1140, 2018.

[56] M. Gasik, L. Van Mellaert, D. Pierron, A. Braem, D. Hofmans, E. De Waelheyns, J. Anné, M.-F. Harmand, and J. Vleugels. Reduction of biofilm infection risks and promotion of osteointegration for optimized surfaces of titanium implants. *Advanced Healthcare Materials*, 1(1):117–127, 2012.

[57] D. P. Gnanadhas, M. Elango, S. Janardhanraj, C. Srinandan, A. Datey, R. A. Strugnell, J. Gopalan, and D. Chakravortty. Successful treatment of biofilm infections using shock waves combined with antibiotic therapy. *Scientific reports*, 5(1):17440, 2015.

[58] C. Gordon, N. Hodges, and C. Marriott. Antibiotic interaction and diffusion through alginate and exopolysaccharide of cystic fibrosis-derived pseudomonas aeruginosa. *Journal of Antimicrobial Chemotherapy*, 22(5):667–674, 1988.

[59] C. W. Hall and T.-F. Mah. Molecular mechanisms of biofilm-based antibiotic resistance and tolerance in pathogenic bacteria. *FEMS Microbiology Reviews*, 41(3):276–301, 2017.

[60] S. Hogan, M. Zapotoczna, N. Stevens, H. Humphreys, J. O'Gara, and E. O'Neill. Potential use of targeted enzymatic agents in the treatment of staphylococcus aureus biofilm-related infections. *Journal of Hospital Infection*, 96(2):177–182, 2017.

[61] M. Jafari, P. Desmond, M. C. van Loosdrecht, N. Derlon, E. Morgenroth, and C. Picioreanu. Effect of biofilm structural deformation on hydraulic resistance during ultrafiltration: A numerical and experimental study. *Water Research*, 145:375–387, 2018.

[62] J. Jass, S. Surman, and J. Walker. *Medical biofilms: detection, prevention and control*. John Wiley & Sons, 2003.

[63] S. Karimifard, X. Li, C. Elowsky, and Y. Li. Modeling the impact of evolving biofilms on flow in porous media inside a microfluidic channel. *Water Research*, 188:116536, 2020.

[64] E. Karunakaran, J. Mukherjee, B. Ramalingam, and C. A. Biggs. "biofilmology": a multidisciplinary review of the study of microbial biofilms. *Applied Microbiology and Biotechnology*, 90(6):1869–1881, 2011.

[65] W. Khan, S. Farah, and A. J. Domb. Drug eluting stents: developments and current status. *Journal of controlled release*, 161(2):703–712, 2012.

[66] Z. Khatoon, C. D. McTiernan, E. J. Suuronen, T.-F. Mah, and E. I. Alarcon. Bacterial biofilm formation on implantable devices and approaches to its treatment and prevention. *Heliyon*, 4(12), 2018.

[67] D. King and S. McGinty. Assessing the potential of mathematical modelling in designing drug-releasing orthopaedic implants. *Journal of Controlled Release*, 239:49–61, 2016.

[68] J. C. Kissel, P. L. McCarty, and R. L. Street. Numerical simulation of mixed-culture biofilm. *Journal of Environmental Engineering*, 110(2):393–411, 1984.

[69] I. Klapper and J. Dockery. Finger formation in biofilm layers. *SIAM Journal on Applied Mathematics*, 62(3):853–869, 2002.

[70] G. M. Knight, N. G. Davies, C. Colijn, F. Coll, T. Donker, D. R. Gifford, R. E. Glover, M. Jit, E. Klemm, S. Lehtinen, et al. Mathematical modelling for antibiotic resistance control policy: do we know enough? *BMC infectious diseases*, 19(1):1–9, 2019.

[71] K. Lewis. Riddle of biofilm resistance. *Antimicrobial Agents and Chemotherapy*, 45(4):999–1007, 2001.

[72] K. Lewis. Persister cells, dormancy and infectious disease. *Nature Reviews Microbiology*, 5(1):48–56, 2007.

[73] K. Lewis. Multidrug tolerance of biofilms and persister cells. *Bacterial Biofilms*, pages 107–131, 2008.

[74] K. Lewis. Persister cells. *Annual Review of Microbiology*, 64:357–372, 2010.

[75] Y. Liu, Y. Li, and L. Shi. Controlled drug delivery systems in eradicating bacterial biofilm-associated infections. *Journal of Controlled Release*, 329:1102–1116, 2021.

[76] B. Martin, Z. Tamanai-Shacoori, J. Bronsard, F. Ginguené, V. Meuric, F. Mahé, and M. Bonnaure-Mallet. A new mathematical model of bacterial interactions in two-species oral biofilms. *PloS One*, 12(3):e0173153, 2017.

[77] A. Mašić, J. Bengtsson, and M. Christensson. Measuring and modeling the oxygen profile in a nitrifying moving bed biofilm reactor. *Mathematical Biosciences*, 227(1):1–11, 2010.

[78] J. P. Masters, N. A. Smith, P. Foguet, M. Reed, H. Parsons, and A. P. Sprowson. A systematic review of the evidence for single stage and two stage revision of infected knee replacement. *BMC musculoskeletal disorders*, 14:1–12, 2013.

[79] MathWorks. Solve boundary value problems in matlab. `https://uk.mathworks.com/help/matlab/math/boundary-value-problems.html`, 2024.

[80] S. McGinty, S. McKee, R. M. Wadsworth, and C. McCormick. Modelling drug-eluting stents. *Mathematical medicine and biology: a journal of the IMA*, 28(1):1–29, 2011.

[81] S. McGinty, S. McKee, R. M. Wadsworth, and C. McCormick. Modeling arterial wall drug concentrations following the insertion of a drug-eluting stent. *SIAM Journal on Applied Mathematics*, 73(6):2004–2028, 2013.

[82] S. McGinty, T. T. Vo, M. Meere, S. McKee, and C. McCormick. Some design considerations for polymer-free drug-eluting stents: a mathematical approach. *Acta Biomaterialia*, 18:213–225, 2015.

[83] E. Medilanski, K. Kaufmann, L. Y. Wick, O. Wanner, and H. Harms. Influence of the surface topography of stainless steel on bacterial adhesion. *Biofouling*, 18(3):193–203, 2002.

[84] J. K. Miller, J. S. Brantner, C. Clemons, K. Kreider, A. Milsted, P. Wilber, Y. H. Yun, W. J. Youngs, G. Young, H. T. Badawy, et al. Mathematical modelling of pseudomonas aeruginosa biofilm growth and treatment in the cystic fibrosis lung. *Mathematical Medicine and Biology: a Journal of the IMA*, 31(2):179–204, 2014.

[85] N. Möker, C. R. Dean, and J. Tao. Pseudomonas aeruginosa increases formation of multidrug-tolerant persister cells in response to quorum-sensing signaling molecules. *Journal of Bacteriology*, 192(7):1946–1955, 2010.

[86] C. Multiphysics. Livelink$^{\text{TM}}$ for matlab$^{®}$user's guide. *COMSOL Multiphysics*, ©2009-2018.

[87] V. Nandakumar, S. Chittaranjan, V. M. Kurian, and M. Doble. Characteristics of bacterial biofilm associated with implant material in clinical practice. *Polymer journal*, 45(2):137–152, 2013.

[88] J. R. Nebeker, R. Virmani, C. L. Bennett, J. M. Hoffman, M. H. Samore, J. Alvarez, C. J. Davidson, J. M. McKoy, D. W. Raisch, B. K. Whisenant, et al. Hypersensitivity cases associated with drug-eluting coronary stents: a review of available cases from the research on adverse drug events and reports (radar) project. *Journal of the American College of Cardiology*, 47(1):175–181, 2006.

[89] I. Olsen. Biofilm-specific antibiotic tolerance and resistance. *European Journal of Clinical Microbiology & Infectious Diseases*, 34:877–886, 2015.

[90] N. C. Overgaard. Application of variational inequalities to the moving-boundary problem in a fluid model for biofilm growth. *Nonlinear Analysis: Theory, Methods & Applications*, 70(10):3658–3664, 2009.

[91] M. Peszynska, A. Trykozko, G. Iltis, S. Schlueter, and D. Wildenschild. Biofilm growth in porous media: experiments, computational modeling at the porescale, and upscaling. *Advances in Water Resources*, 95:288–301, 2016.

[92] C. Picioreanu, M. C. Van Loosdrecht, and J. J. Heijnen. A new combined differential-discrete cellular automaton approach for biofilm modeling: Application for growth in gel beads. *Biotechnology and Bioengineering*, 57(6):718–731, 1998.

[93] C. Picioreanu, M. C. Van Loosdrecht, and J. J. Heijnen. Effect of diffusive and convective substrate transport on biofilm structure formation: A two-dimensional modeling study. *Biotechnology and Bioengineering*, 69(5):504–515, 2000.

[94] C. Picioreanu, J. Xavier, and M. C. van Loosdrecht. Advances in mathematical modeling of biofilm structure. *Biofilms*, 1(4):337–349, 2004.

[95] T. Pintelon, D. Graf von der Schulenburg, and M. Johns. Towards optimum permeability reduction in porous media using biofilm growth simulations. *Biotechnology and Bioengineering*, 103(4):767–779, 2009.

[96] G. Pizarro, C. Garcia, R. Moreno, and M. Sepulveda. Two-dimensional cellular automaton model for mixed-culture biofilm. *Water Science and Technology*, 49(11-12):193–198, 2004.

[97] F. P. Pons-Faudoa, A. Ballerini, J. Sakamoto, and A. Grattoni. Advanced implantable drug delivery technologies: transforming the clinical landscape of therapeutics for chronic diseases. *Biomedical microdevices*, 21:1–22, 2019.

[98] M. Pousti, M. P. Zarabadi, M. A. Amirdehi, F. Paquet-Mercier, and J. Greener. Microfluidic bioanalytical flow cells for biofilm studies: a review. *Analyst*, 144(1):68–86, 2019.

[99] M. Prax and R. Bertram. Metabolic aspects of bacterial persisters. *Frontiers in cellular and infection microbiology*, 4:148, 2014.

[100] S. N. Qasim, A. Swann, and R. Ashford. The dair (debridement, antibiotics and implant retention) procedure for infected total knee replacement–a literature review. *SICOT-J*, 3, 2017.

[101] K. Quan, J. Hou, Z. Zhang, Y. Ren, B. W. Peterson, H.-C. Flemming, C. Mayer, H. J. Busscher, and H. C. van der Mei. Water in bacterial biofilms: pores and channels, storage and transport functions. *Critical reviews in microbiology*, 48(3):283–302, 2022.

[102] M. A. Rather, K. Gupta, and M. Mandal. Microbial biofilm: formation, architecture, antibiotic resistance, and control strategies. *Brazilian Journal of Microbiology*, pages 1–18, 2021.

[103] M. Revilla, B. Galán, and J. R. Viguri. An integrated mathematical model for chemical oxygen demand (cod) removal in moving bed biofilm reactors (mbbr) including predation and hydrolysis. *Water Research*, 98:84–97, 2016.

[104] B. E. Rittmann and P. L. McCarty. Model of steady-state-biofilm kinetics. *Biotechnology and Bioengineering*, 22(11):2343–2357, 1980.

[105] P. A. Roberts, R. M. Huebinger, E. Keen, A.-M. Krachler, and S. Jabbari. Predictive modelling of a novel anti-adhesion therapy to combat bacterial colonisation of burn wounds. *PLoS Computational Biology*, 14(5):e1006071, 2018.

[106] P. A. Roberts, R. M. Huebinger, E. Keen, A.-M. Krachler, and S. Jabbari. Mathematical model predicts anti-adhesion–antibiotic–debridement combination therapies can clear an antibiotic resistant infection. *PLoS Computational Biology*, 15(7):e1007211, 2019.

[107] S. N. Rothstein, W. J. Federspiel, and S. R. Little. A unified mathematical model for the prediction of controlled release from surface and bulk eroding polymer matrices. *Biomaterials*, 30(8):1657–1664, 2009.

[108] M. Rozis, D. S. Evangelopoulos, and S. G. Pneumaticos. Orthopedic implant-related biofilm pathophysiology: a review of the literature. *Cureus*, 13(6), 2021.

[109] J. Sankaran, N. J. Tan, K. P. But, Y. Cohen, S. A. Rice, and T. Wohland. Single microcolony diffusion analysis in pseudomonas aeruginosa biofilms. *npj Biofilms and Microbiomes*, 5(1):35, 2019.

[110] K. Sauer, P. Stoodley, D. M. Goeres, L. Hall-Stoodley, M. Burmølle, P. S. Stewart, and T. Bjarnsholt. The biofilm life cycle: expanding the conceptual model of biofilm formation. *Nature Reviews Microbiology*, 20(10):608–620, 2022.

[111] J. Siepmann and F. Siepmann. Mathematical modeling of drug delivery. *International journal of pharmaceutics*, 364(2):328–343, 2008.

[112] P. S. Stewart. Diffusion in biofilms. *Journal of bacteriology*, 185(5):1485–1491, 2003.

[113] P. S. Stewart and J. W. Costerton. Antibiotic resistance of bacteria in biofilms. *The lancet*, 358(9276):135–138, 2001.

[114] P. S. Stewart and M. J. Franklin. Physiological heterogeneity in biofilms. *Nature Reviews Microbiology*, 6(3):199–210, 2008.

[115] S. A. Stewart, J. Domínguez-Robles, R. F. Donnelly, and E. Larrañeta. Implantable polymeric drug delivery devices: classification, manufacture, materials, and clinical applications. *Polymers*, 10(12):1379, 2018.

[116] P. Stoodley, D. DeBeer, and Z. Lewandowski. Liquid flow in biofilm systems. *Applied and Environmental Microbiology*, 60(8):2711–2716, 1994.

[117] S. Subramanian, R. C. Huiszoon, S. Chu, W. E. Bentley, and R. Ghodssi. Microsystems for biofilm characterization and sensing–a review. *Biofilm*, 2:100015, 2020.

[118] I. W. Sutherland. The biofilm matrix–an immobilized but dynamic microbial environment. *Trends in microbiology*, 9(5):222–227, 2001.

[119] B. Szomolay. Analysis of a moving boundary value problem arising in biofilm modelling. *Mathematical Methods in the Applied Sciences*, 31(15):1835–1859, 2008.

[120] D. Taherzadeh, C. Picioreanu, and H. Horn. Mass transfer enhancement in moving biofilm structures. *Biophysical Journal*, 102(7):1483–1492, 2012.

[121] A. Tam. *Mathematical modelling of pattern formation in yeast biofilms*. PhD thesis, 2019.

[122] S. W. Taylor and P. R. Jaffé. Biofilm growth and the related changes in the physical properties of a porous medium: 1. experimental investigation. *Water Resources Research*, 26(9):2153–2159, 1990.

[123] A. Teillant, S. Gandra, D. Barter, D. J. Morgan, and R. Laxminarayan. Potential burden of antibiotic resistance on surgery and cancer chemotherapy antibiotic prophylaxis in the usa: a literature review and modelling study. *The Lancet Infectious Diseases*, 15(12):1429–1437, 2015.

[124] J. S. Temenoff and A. G. Mikos. *Biomaterials: the intersection of biology and materials science*, volume 1. Pearson/Prentice Hall Upper Saddle River, 2008.

[125] S. Tolman, P. Meakin, and M. Matsushita. Cluster-size distribution in the incremental growth of dla clusters. *Journal of the Physical Society of Japan*, 58(8):2721–2726, 1989.

[126] B. W. Towler, A. Cunningham, P. Stoodley, and L. McKittrick. A model of fluid–biofilm interaction using a burger material law. *Biotechnology and Bioengineering*, 96(2):259–271, 2007.

[127] G. K. Triantafyllopoulos, V. Soranoglou, S. G. Memtsoudis, and L. A. Poultsides. Implant retention after acute and hematogenous periprosthetic hip and knee infections: whom, when and how? *World Journal of Orthopedics*, 7(9):546, 2016.

[128] M. G. Trulear and W. G. Characklis. Dynamics of biofilm processes. *Journal (Water Pollution Control Federation)*, pages 1288–1301, 1982.

[129] I. Tsujino, J. Ako, Y. Honda, and P. J. Fitzgerald. Drug delivery via nano-, micro and macroporous coronary stent surfaces. *Expert Opinion on Drug Delivery*, 4(3):287–295, 2007.

[130] A. R. Tzafriri, A. Groothuis, G. S. Price, and E. R. Edelman. Stent elution rate determines drug deposition and receptor-mediated effects. *Journal of controlled release*, 161(3):918–926, 2012.

[131] C. Uruén, G. Chopo-Escuin, J. Tommassen, R. C. Mainar-Jaime, and J. Arenas. Biofilms as promoters of bacterial antibiotic resistance and tolerance. *Antibiotics*, 10(1):3, 2020.

[132] W. J. Van der Giessen, A. M. Lincoff, R. S. Schwartz, H. M. Van Beusekom, P. W. Serruys, D. R. Holmes, S. G. Ellis, and E. J. Topol. Marked inflammatory sequelae to implantation of biodegradable and nonbiodegradable polymers in porcine coronary arteries. *Circulation*, 94(7):1690–1697, 1996.

[133] A. D. Verderosa, J. Harris, R. Dhouib, M. Totsika, and K. E. Fairfull-Smith. Eradicating uropathogenic escherichia coli biofilms with a ciprofloxacin–dinitroxide conjugate. *MedChemComm*, 10(5):699–711, 2019.

[134] D. Verotta, J. Haagensen, A. M. Spormann, and K. Yang. Mathematical modeling of biofilm structures using comstat data. *Computational and Mathematical Methods in Medicine*, 2017, 2017.

[135] N. J. Vickers. Animal communication: when i'm calling you, will you answer too? *Current Biology*, 27(14):R713–R715, 2017.

[136] T. Vladkova. Surface modification approach to control biofouling. Springer, 2008.

[137] H. Wallace, L. Li, and F. Davidson. The effect of cell death on the stability of a growing biofilm. *Mathematical Modelling of Natural Phenomena*, 11(5):33–48, 2016.

[138] Q. Wang and T. Zhang. Review of mathematical models for biofilms. *Solid State Communications*, 150(21-22):1009–1022, 2010.

[139] O. Wanner. *Mathematical modeling of biofilms*. International Water Association Publications, 2006.

[140] O. Wanner and W. Gujer. A multispecies biofilm model. *Biotechnology and Bioengineering*, 28(3):314–328, 1986.

[141] O. Wanner and P. Reichert. Mathematical modeling of mixed-culture biofilms. *Biotechnology and Bioengineering*, 49(2):172–184, 1996.

[142] J. Ward, J. Wattis, S. Jabbari, J. Siggers, R. Kabayashi, J. Armitage, S. Godfrey, and H. Packer. Modelling the development and formation of biofilms. *Mathematics in Medicine Study Group*, 2005.

[143] C. M. Watters, T. Burton, D. K. Kirui, and N. J. Millenbaugh. Enzymatic degradation of in vitro staphylococcus aureus biofilms supplemented with human plasma. *Infection and drug resistance*, pages 71–78, 2016.

[144] H. Wu, C. Moser, H.-Z. Wang, N. Høiby, and Z.-J. Song. Strategies for combating bacterial biofilm infections. *International journal of oral science*, 7(1):1–7, 2015.

[145] J. B. Xavier, C. Picioreanu, S. A. Rani, M. C. van Loosdrecht, and P. S. Stewart. Biofilm-control strategies based on enzymic disruption of the extracellular polymeric substance matrix–a modelling study. *Microbiology*, 151(12):3817–3832, 2005.

[146] S. Yazdi, A. M. Ardekani, and A. Borhan. Locomotion of microorganisms near a no-slip boundary in a viscoelastic fluid. *Physical Review E*, 90(4):043002, 2014.

[147] T. C. Zhang and P. L. Bishop. Density, porosity, and pore structure of biofilms. *Water Research*, 28(11):2267–2277, 1994.

[148] W. Zhang, S. Wang, S. Ge, J. Chen, and P. Ji. The relationship between substrate morphology and biological performances of nano-silver-loaded dopamine coatings on titanium surfaces. *Royal Society Open Science*, 5(4):172310, 2018.

[149] H. Q. Zhao, D. Jayasinghe, S. Hossainy, and L. B. Schwartz. A theoretical model to characterize the drug release behavior of drug-eluting stents with durable polymer matrix coating. *Journal of Biomedical Materials Research Part A*, 100(1):120–124, 2012.

[150] S. Zheng, M. Bawazir, A. Dhall, H.-E. Kim, L. He, J. Heo, and G. Hwang. Implication of surface properties, bacterial motility, and hydrodynamic conditions on bacterial surface sensing and their initial adhesion. *Frontiers in Bioengineering and Biotechnology*, 9:643722, 2021.

[151] X. Zhu, D. W. Pack, and R. D. Braatz. Modelling intravascular delivery from drug-eluting stents with biodurable coating: investigation of anisotropic vascular drug diffusivity and arterial drug distribution. *Computer methods in biomechanics and biomedical engineering*, 17(3):187–198, 2014.